The development and application of Uranium, Molybdenum, and Vanadium stable isotope ratios as redox-proxies in samples from modern times and the Early Earth

Von der Naturwissenschaftlichen Fakultät der

Gottfried Wilhelm Leibniz Universität Hannover

zur Erlangung des Grades

Doktorin der Naturwissenschaften (Dr. rer. nat.)

genehmigte Dissertation

von

Annika Neddermeyer, geb. Brüske, M. Sc.

2019

Referent: Prof. Dr. Stefan Weyer

Korreferent: Prof. Dr. Ronny Schoenberg

Tag der Promotion: 06.05.2019

Acknowledgements

Doubtlessly, I would not have written this thesis without the support and assistance of many people who I wish to thank at the beginning.

My deepest thanks go to Prof. Dr. Stefan Weyer and Dr. Stephan Schuth for initiating this project and giving me the opportunity to be a part of it. I thank you for your support during my PhD years and for shaping my scientific focus. You have always answered my questions and gave me new ideas when I was stuck in a stagnant project. I have learned a lot from you and will always commemorate my great PhD time.

I especially thank Prof. Dr. Ronny Schoenberg for being my co-referee and providing me with samples and productive discussions and Prof. Dr. Heimhofer for participating in and chairing my Examination Board.

I thank my colleagues at the Leibniz University of Hannover who have supported me with their help and guidance through this time. My special thanks go to Dr. Nadja Pierau, who taught me to transform from a chemist into a geochemist and guided me through my first clean-lab and mass spectrometric experiences. Thank you, Nadja, for being patient and kind to me and making me feel welcome in our working group. Dr. Ingo Horn is thanked for teaching me how to operate the machines throughout all their issues so that I was able to understand and solve the encountered problems myself. I thank all the others from our working group, who have been great colleagues and supported me during my PhD: Dr. Marina Lazarov, Alexandra Tangen, Katharina Rabe, Dr. Martin Oeser-Rabe, Dr. Moritz Albrecht, Dr. Mona Weyrauch, Yvonne Röbbert, Lena Steinmann, Lili Meier, Dr. Maria Kirchenbaur, and Dr. Ashley Martin. I especially thank Lena and Yvonne for sharing all the frustration and a lot of chocolate when we were room-mates. Of course, I am also thankful to all colleagues from the Institute of Mineralogy in Hannover who have shared this exciting time with me. Thank you, Dongmei Qi, for sharing your office with me, even though it was only a short time.

I thank all my collaboration partners from the University of Tübingen, Leibniz Institute for Baltic Sea Research (IOW), University of Oldenburg, Jacobs University Bremen, Alfred-Wegener Institut Bremerhaven (AWI), Yale University, UC-Riverside, Goethe-University Frankfurt, University of Johannesburg, and the University of Bern, who have supported me by providing samples and helpful discussions during thy PhD time.

Ohne Frage bin ich heute dort, wo ich bin, da ich eine mich unglaublich liebende und unterstützende Familie und Freunde um mich herum habe. Meine Eltern haben mich immer unterstützt, moralisch, finanziell und emotional, und mir damit die Basis für ein tolles Leben bereitet. Ohne euch hätte ich mein Studium nicht beenden können, danke, dass ihr immer für mich da seid. Meinen Geschwistern danke ich für ihre Zuneigung und Unterstützung über all die Jahre. Ihr seid einfach super! Auch die weitere Familie, egal ob blutsverwandt oder angeheiratet, gibt mir immer Halt und unterstützt mich, wo sie nur kann. Außerdem habe ich einige sehr gute Freunde, auf die ich mich immer verlassen und stützen kann. Mit solchen Menschen um mich herum kann ich mich wirklich glücklich schätzen.

Wie einsam wäre das Leben ohne die Liebe und Unterstützung durch einen Partner an meiner Seite, der all die Hochs und Tiefs mit mir durchlebt. Torben, ich danke dir für die fantastische Zeit, die wir bis jetzt hatten und freue mich darauf, mein restliches Leben mit dir zu verbringen.

Abstract

The metals Molybdenum (Mo), Uranium (U), and Vanadium (V) belong to the group of redox-sensitive elements and may be used to track redox processes in geological samples. They all show characteristic isotope fractionation that may be captured and preserved in marine sediments so that precise and accurate measurements may reveal past environmental changes of the depositional redox conditions in the oceans. Reconstructing past redox conditions must always rely on a solid understanding of causal present-day processes and hence, their investigation is the basis for reliable interpretations. In this thesis, the isotope fractionation of Mo, U, and V is investigated to improve our understanding of present-day processes during their geochemical cycling and to apply this knowledge to gain information on past environments.

The behavior of V in seawater highly depends on speciation, pH and Eh and V isotopes are likely a very sensitive proxy for redox changes in the aquatic environment. In order to use V isotopes for this purpose, the V isotope composition of seawater needs to be analyzed. The first part of this thesis deals with a new method development to separate V from a seawater matrix, purifying this fraction and optimizing mass spectrometric measurements. Therefore, different separation procedures were tested, such as a Fe co-precipitation and ion-chromatographic exchange both followed by additional ion-exchange especially optimized for seawater samples. The final ion-exchange method was applied repeatedly to North Sea seawater and yielded a $\delta^{51}V_{Nist-3165}$ = -0.62 ‰ ± 0.25 ‰ (n = 17 single analyses from 6 separately processed aliquots) which is in agreement with a recently published V isotope composition of open-ocean seawater within analytical error (Wu et al., 2019). The results show that, compared to other measured environmental compartments, V isotopes exhibit a high isotope signature in seawater. An additional seawater sample from the Southern Ocean resulted in a $\delta^{51}V_{Nist-3165}$ = -2.53 ‰ ± 0.21 ‰ (n = 5), which shows a significantly fractionated signature compared to open-ocean and North Sea. These first-order results need further confirmation and ultimately will help to apply V isotopes as an additional tool in paleo-oceanography.

The second part of this thesis targets the investigation of Mo and U isotope fractionation in sediments from the Black Sea and the Cariaco Basin, which are the modern analogues for marine anoxic depositional conditions during past times. Both isotope proxies have been used extensively as single proxies and here, their inter-relationships and responses to the same conditions are aimed to be understood. Hence, both signatures on the same samples were analyzed. The results show that Mo scavenging is mainly controlled by water column sulfide

chemistry, whereas U immobilization mainly occurs at the sediment-water interface and upper cm of the sediment pile. The feedback between U isotope ratios of the water column and the sediment stems from the seawater δ^{238}U controlling the sediment δ^{238}U. Although both elements show highly different removal pathways, the isotope signatures of sediments exhibit an inverse correlation in the Black Sea and the Cariaco Basin, with the Cariaco Basin trend being generally lower in δ^{238}U and δ^{98}Mo. This correlation indicates a direct relationship between the responses of Mo and U to surrounding conditions and removal efficiencies which are mainly controlled by sulfate reduction rates and resulting dissolved sulfide concentrations. The results are reproduced in a coupled water column and reactive transport model and the different slopes of the correlation in both basins can be explained with varying degrees of basin restriction, sulfate reduction rates, and isotope compositions of the respective water columns. Hence, the coupled application of Mo and U isotopes will also strengthen results in paleo-redox studies.

The third part of this thesis discusses the application of the U isotope proxy for the reconstruction of Archean and Early Proterozoic anoxic conditions. Here, U isotope fractionation may help to disentangle the complex evolution of molecular oxygen during the Archean and Proterozoic times. The Archean is characterized by overall anoxic conditions in the atmosphere and hydrosphere, however, the temporal and spatial evolution of free oxygen is highly debated among scientists. Several lines of evidence indicate a change to slightly oxic conditions around 2.46 Ga to 2.33 Ga (Bekker et al., 2004; Luo et al., 2016; Gumsley et al., 2017) and this period has been named the Great Oxidation Event (GOE). The increase in free oxygen ultimately resulted in oxidative weathering of continental crust and caused geochemical cycling of redox-sensitive elements. Authigenic enrichment of U in marine anoxic organic-rich or Fe-rich sediments as well as marine carbonates is monitored relative to Post-Archean Average Shale (PAAS) and indicates an increase in U cycling during the late Archean. Interestingly, this increased authigenic U enrichment is accompanied with considerably fractionated δ^{238}U values, mainly towards lower values compared to continental crust. These low U isotope compositions are best explained by U isotope fractionation as a consequence of the onset of partial U mobilization during oxidative weathering of uraninite, just before the GOE, i.e. roughly at ~2.5 Ga. After the GOE, the observed δ^{238}U values indicate the onset of modern-style weathering of uraninite and other U-bearing minerals with quantitative U mobilization and limited U isotope fractionation in a continuously anoxic deep ocean.

Zusammenfassung

Die Metalle Molybdän (Mo), Uran (U) und Vanadium (V) gehören zu den redox-sensitiven Elementen und werden als Redox Proxys in geologischen Proben verwendet. Sie zeigen charakteristische Isotopenfraktionierung, welche in marinen Sedimenten erhalten bleiben kann, sodass ihre präzise und akkurate Messung vergangene Redox Schwankungen während der Ablagerung in den Ozeanen aufzeigen kann. Dabei beruht die Rekonstruktion vergangener Bedingungen immer auf einem soliden Verständnis der heutigen Prozesse. In dieser Dissertation wurde die Isotopenfraktionierung von Mo, U und V untersucht, um das Verständnis der heutigen Fraktionierungsprozesse zu erweitern und dieses Wissen anzuwenden, um vergangene Umweltbedingungen zu rekonstruieren.

Das Verhalten von V in Meerwasser hängt von der Speziierung, dem pH- und eH-Wert ab und V Isotope sind vermutlich ein sensitiver Anzeiger für Redox-Schwankungen im marinen Bereich. Um V Isotope für diese Anwendung zu verwenden, muss die Isotopie des Meerwassers bestimmt werden. Dafür wurde zu Beginn dieser Promotion eine neue Methode entwickelt, welche die Trennung des V von der Meerwassermatrix, die Aufreinigung dieser Fraktion und ein optimiertes massenspektrometrisches Messprotokoll enthält. Die unterschiedlichen Methoden der Eisen-Kofällung und der ionen-chromatographischen Trennung wurden speziell für eine Meerwassermatrix getestet. Beide Methoden sind gefolgt von der matrixangepassten ionen-chromatographischen Aufreinigung der V Fraktion. Die endgültige ionen-chromatographische Trennmethode wurde wiederholt an Nordseewasser angewendet und ergab einen $\delta^{51}V_{Nist-3165}$ = -0.62 ‰ ± 0.25 ‰ (n = 17 Einzelanalysen an sechs Teilproben), welcher innerhalb der analytischen Unsicherheit mit der kürzlich publizierten V Isotopie des offenen Ozeans von Wu et al. (2019) übereinstimmt. Im Vergleich mit anderen Reservoiren zeigen die Ergebnisse, dass die V Isotopie von Meerwasser eine schwere Signatur besitzt. Zusätzlich wurde eine weitere Probe aus dem Südlichen Ozean analysiert, welche einen $\delta^{51}V_{Nist-3165}$ = -2.53 ‰ ± 0.21 ‰ (n = 5) zeigt und signifikant fraktioniert ist gegenüber der Nordsee und dem offenen Ozean. Weitere Untersuchungen sind nötig, um diese ersten Ergebnisse zu bestätigen und V schlussendlich als Paleo-Redox Proxy anzuwenden.

Der zweite Teil dieser Dissertation beschäftigt sich mit der Untersuchung von Mo und U Isotopenfraktionierung in Sedimenten des Schwarzen Meeres und des Cariaco Beckens, welche die modernen Analoga für marine anoxische Bedingungen der Vergangenheit sind. Beide Isotopensysteme wurden schon ausgiebig einzeln als Redox Proxys verwendet und sollen nun auf ihre Zusammenhänge und Resonanz auf die gleichen Ablagerungsbedingungen

analysiert werden. Dafür wurden beide Proxys an den gleichen Sedimenten angewendet. Die Ergebnisse zeigen, dass die Ausfällung von Mo hauptsächlich durch die Sulfidkonzentration der Wassersäule kontrolliert wird, wohingegen U in erster Linie an der Wasser-Sediment und in den oberen cm des Sediments ausfällt. Die U Isotopensignatur des Sediments wird dabei schlussendlich durch die Isotopensignatur des Wassers bestimmt. Obwohl Mo und U sehr unterschiedliche Ablagerungsmechanismen haben, sind die Isotopensignaturen der Sedimente im Schwarzen Meer und im Cariaco Becken jeweils invers korreliert, wobei das Cariaco Becken generell leichtere δ^{238}U und δ^{98}Mo zeigt. Diese Korrelation deutet auf einen direkten Zusammenhang zwischen der Mo und U Ablagerung hin, welche schlussendlich durch die Sulfatreduktionsrate und daraus resultierende gelöste Sulfidkonzentration kontrolliert wird. Die Ergebnisse wurden in einem kombinierten Modell der Wassersäule und des reaktiven Transports reproduziert und die unterschiedlichen Steigungen der Korrelationen können mit Hilfe der Beckenrestriktion, Sulfatreduktionsrate und Isotopenzusammensetzung der jeweiligen Wassersäule erklärt werden. Die kombinierte Anwendung von Mo und U Isotopenvariationen kann folglich Ergebnisse in Paleo-Redox Studien verstärken.

Der dritte Teil dieser Dissertation befasst sich mit der Anwendung des U Isotopen Proxys für die Rekonstruktion anoxischer Bedingungen im Archaikum und frühen Proterozoikum. Die Analyse der U Isotopenfraktionierung kann dabei helfen, den komplexen Anstieg der molekularen Sauerstoffkonzentrationen zu verstehen. Das Archaikum ist durch weitreichende anoxische Bedingungen in der Atmosphäre und Hydrosphäre charakterisiert, und der zeitliche und örtliche Anstieg des molekularen Sauerstoffs wird zahlreich diskutiert. Verschiedene Indikatoren weisen auf einen Anstieg des Sauerstoffgehalts der Atmosphäre ab 2.46 Ga bis 2.33 Ga hin (Bekker et al., 2004; Luo et al., 2016; Gumsley et al., 2017), daher wird diese Zeit das Große Oxidations Ereignis (GOE) genannt. Der Anstieg von molekularem Sauerstoff hat schlussendlich zur oxidativen Verwitterung der kontinentalen Kruste geführt, sodass redox-sensitive Elemente mobilisiert wurden. Die in dieser Studie gemessene authigene Anreicherung von U in anoxischen Organik-reichen oder Fe-reichen Sedimenten und marinen Karbonaten wurde relativ zum post-archaischen durchschnittlichen Schiefer (PAAS) berechnet und diese Werte zeigen einen Anstieg der U Mobilisierung im späten Archaikum. Interessanterweise wird die U Anreicherung von fraktionierten δ^{238}U Werten begleitet. Diese zeigen hauptsächlich leichtere Werte als heutige kontinentale Kruste und können mit Hilfe der U Mobilisierung und einhergehender Isotopenfraktionierung während der oxidativen Verwitterung kurz vor dem GOE erklärt werden. Nach dem GOE abgelagerte Sedimente zeigen moderne Verwitterung von U Mineralen mit quantitativer U Mobilisierung und geringer U Isotopenfraktionierung in einem weiterhin anoxischen tiefen Ozean.

Key words: Paleo-redox proxy, Molybdenum, Uranium, Vanadium, sedimentary archives, seawater, modern times, Early Earth, stable isotope fractionation

Schlüsselwörter: Paläo-Redox Proxy, Molybdenum, Uranium, Vanadium, Sedimentäre Archive, Meerwasser, Moderne Zeit, Frühe Erde, stabile Isotopenfraktionierung

Table of Contents

Chapter III: Correlated molybdenum and uranium isotope signatures in modern anoxic sediments

Chapter IV: The onset of oxidative weathering traced by uranium isotopes

Chapter I: Introduction

1. Metal stable isotopes as redox proxies

The analysis of metal stable isotope ratios in geological samples has emerged to be a powerful tool in geo-sciences and especially in paleo-oceanography. Metal stable isotopes are frequently fractionated by bio-geochemical processes in nature and these signatures can be captured and preserved in the rock record, also over geological timescales. Hence, these archives can serve to reconstruct and understand past conditions and processes. Precise and accurate analyses of these signatures can provide information about, e.g., bio-geochemical cycling due to redox variations, complexation, diffusion, evaporation, precipitation, ad- and desorption, and biological uptake (see overview by Wiederhold, 2015). Advances in mass-spectrometric measurement techniques (multiple-collector inductively coupled mass spectrometers) have resulted in the observation of metal stable isotope fractionation throughout the periodic table of the elements and have enabled the scientific geochemical community to understand and address the processes mentioned above.

Stable isotope fractionation is caused by mass differences between two isotopes of an element and results in their unequal distribution between two compartments (Anbar and Rouxel, 2007). Mass differences are responsible for different physicochemical properties of the respective isotopes and are described by kinetic and equilibrium effects. Kinetic fractionation effects occur in uni-directional processes and result from faster reaction rates of light isotopes compared to heavy isotopes. Processes that can cause kinetic isotope fractionation are diffusion, evaporation, or biological uptake (Wiederhold, 2015). Equilibrium isotope fractionation occurs during exchange reactions between two reactants and results from different bonding environments of light and heavy isotopes. In general, heavy isotopes feature lower zero-point energies compared to light isotopes and hence enrich heavier isotopes over lighter ones in compounds with stiffer bonds, such as higher redox states or lower coordination numbers (Anbar and Rouxel, 2007; Wiederhold, 2015).

Apart from mass-dependent isotope fractionation, some elements (e.g. S, O) also show mass-independent fractionation (MIF) that results from molecular symmetry or self-shielding processes, for example during photo-chemical gaseous reactions(Wiederhold, 2015). For heavy isotopes, such as U, Tl or Hg, mass-independent isotope fractionation is explained by nuclear field shift effects that result from the large volume of the nucleus and shielding of orbitals during reactions. Hence, they can occur during kinetic and equilibrium fractionation and go in the same or opposite direction of mass-dependent fractionation effects. During the reduction of U(VI) to U(IV) the nuclear field shift overcomes the mass dependent effects. The final net isotope fractionation is in opposite to mass-dependent fractionation and, hence, reduced species are enriched in heavy isotopes (Bigeleisen, 1996; Moynier et al., 2013). Magnetic isotope effects (MIE) can occur due to nuclear spin and magnetic moment and are

completely independent of the isotope's mass, however, their relevance to natural processes in unclear (Wiederhold, 2015).

In this thesis, the focus lies on the application of stable metal isotope fractionation during redox transformations to understand modern and past redox processes. Redox reactions of many elements cause isotope fractionation and have been extensively studied and applied to trace the redox evolution of the present-day and past environment (see reviews of Severmann and Anbar, 2009, and Wiederhold, 2015, and references therein). The reconstruction of past conditions always relies on a solid understanding of present-day processes that cause isotope fractionation during geochemical cycling between different reservoirs, such as the geosphere, biosphere, atmosphere, and hydrosphere. Hereby, oxygen fluctuations can affect isotope fractionation directly (e.g. direct reduction-oxidation processes) or indirectly when oxygen concentrations affect processes that then themselves involve isotope fractionation (e.g. biological uptake of Fe) (Severmann and Anbar, 2009).

Among many others, the elements Molybdenum (Mo), Uranium (U) and Vanadium (V) attract special interest due to their redox-sensitive characters and resulting enrichment in reducing sediments. Hereby, they undergo specific isotope fractionation and different environmental reservoirs are reasonably well characterized for Mo and U. Hence, their isotope fractionation behavior during global environmental cycling at present-day is applied commonly as redox-proxies (see recent reviwes by Andersen et al., 2017, and Kendall et al., 2017), however, detailed understanding of processes and inter-relationships are lacking. In opposite, the analysis of V isotope fractionation in nature has just recently grown due to several methodical issues that complicate the analyses of V isotopes (Nielsen et al., 2011; Prytulak et al., 2011; Nielsen et al., 2016; Wu et al., 2016; Schuth et al., 2017; Teng et al., 2017). The present-day geochemical reservoirs need to be fully characterized to merge V isotopes into a promising additional proxy that may strengthen results in multi-isotope proxy studies (Prytulak et al., 2013; Nielsen et al., 2014; Brüske, 2015; Ventura et al., 2015; Wu et al., 2015; Gao et al., 2017; Prytulak et al., 2017; Schuth et al., 2017).

1.2 Molybdenum

Molybdenum (atomic number 41) is a transition metal that occurs in various oxidation states and its partitioning behavior highly depends on the surrounding redox conditions and hence, it shows respective siderophile, chalcophile and lithophile character (Greaney et al., 2018). In the upper continental crust, it occurs with an average content of 1.1 µg g^{-1} (Rudnick and Gao, 2003). In opposite to its igneous scarcity, Mo is required by most living organisms as an essential micronutrient for catalysis in enzymes (Bittner and Mendel, 2010). Generally, on the Earth's surface and in aqueous environments, Mo occurs in its hexavalent, oxidized, state as

molybdate MoO_4^{2-} being very mobile and well soluble. In this state it is very unreactive and consequently, Mo's present-day ocean residence time is 440 ky (Miller et al., 2011) which results in conservative behavior and leads to the relative enrichment of Mo with an average oceanic concentration of 105 nmol l^{-1} (Collier, 1985). Under reducing conditions, Mo occurs in its tetravalent state and is highly particle-reactive and, hence, quickly immobilized. In the global oceanic cycle, Mo is introduced into the oceans via rivers and to a low extent (~5 %) via low-temperature hydrothermal fluids (Miller et al., 2011). Its main sinks from the oceans are ferromanganese oxides (crusts, nodules and pelagic sediments, 30 % - 50 % removal of Mo), reduced organic rich anoxic and euxinic sediments such as black shales or saprolites (6 % - 15 % removal of Mo) and intermediate sediments (suboxic or sulfidic at depths, 50 % - 65 % removal of Mo) at continental shelfs (Kendall et al., 2017).

Mo has seven stable isotopes (^{92}Mo, ^{94}Mo, ^{95}Mo, ^{96}Mo, ^{97}Mo, ^{98}Mo, ^{100}Mo) with similar abundances between 9.55 % to 24.13 % (Figure 1). However, several of them suffer from isobaric interferences with Zr- (on masses 92, 94 and 96) or Ru isotopes (on masses 96, 98 and 100).
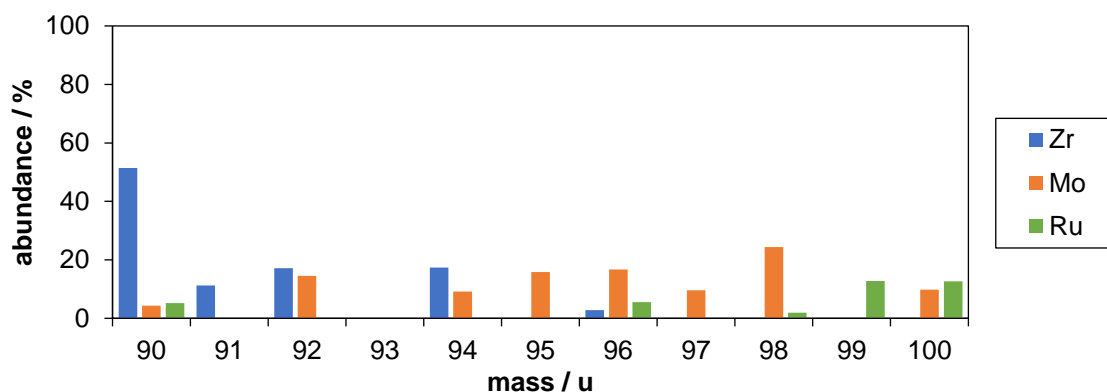
Figure 1: Natural abundances of Mo, Ru and Zr isotopes in the range from 90 to 100 u (Berglund and Wieser, 2011).

Molybdenum is introduced to the oceans mainly by rivers that have a wide range in isotope signatures from δ^{98}Mo$_{rivers}$ of 2.3 to -0.1 ‰ with an average δ^{98}Mo$_{river}$ of 0.7 ‰ (Archer and Vance, 2008). Rivers are sourced by weathered material from the continental crust which has a calculated average δ^{98}Mo$_{cont.\ crust}$ of 0.3 ‰ (Voegelin et al., 2014). The bulk silicate Earth (BSE, mantle + crust) has an average of δ^{98}Mo$_{BSE}$ of 0.04 ‰, with the mantle being isotopically homogenous, however, the crust shows isotopic deviations between the different zones.

As all three major oceanic sinks enrich light Mo isotopes, this results in a heavy (and uniform) δ^{98}Mo of oxic seawater (+2.34 ‰ ± 0.10 ‰, Siebert et al., 2003; Nakagawa et al., 2012).

Isotope fractionation between seawater and Fe-Mn-oxides (oxic sink) was observed to be largest with lighter Mo isotopes being adsorbed onto oxide particle surfaces and resulting in Δ^{98}Mo between the solid and the dissolved phase of ~3 ‰ depending on the mineralogy and pH (Barling et al., 2001; Siebert et al., 2003; Goldberg et al., 2009). Isotope fractionation in reduced sediments that were deposited under mildly oxygenated to anoxic but non-sulfidic conditions (H_2S conditions below 11 µmol l^{-1} (Neubert et al., 2008) is highly variable with Δ^{98}Mo between solid and dissolved phase between 1 - 3 ‰. Isotope fractionation in such environments depends on a variety of factors, including Fe-Mn oxide contents and crystallinity and the amount of H_2S in pore-waters (Siebert et al., 2006; Poulson Brucker et al., 2009).

Under strongly reducing conditions with concentrations of H_2S_{aq} > 11 µmol kg^{-1} ("action point of switch" APS) (Helz et al., 1996; Erickson and Helz, 2000) molybdate is quantitatively converted to thio-molybdate which is very particle reactive. The particle reactive oxythio-molybdates are adsorbing onto solid mineral particles or organic matter particles and are almost quantitatively removed from the water column. Molybdate adsorbs readily onto Fe-Mn oxy-hydroxide particles that form at the chemocline and which act as particulate shuttle for a variety of metals, including Mo, into deeper waters. At anoxic conditions at the sediment-water interface, the particles re-dissolve thereby releasing trapped molybdate that is either diffusing back into the water column or scavenged into the sediment by other carrier phases. During the operation of such a particulate shuttle, Mo can be more efficiently enriched in sediments compared to elements that are less affine to Fe-Mn oxy-hydroxides (e.g. U). This mechanism may be very important in restricted basins with weakly sulfidic deep waters where the chemocline fluctuates vertically thus enabling reductive dissolution of Fe-Mn particles in bottom waters and Mo release at the sediment/water interface where it is accumulated. Accordingly, this "Mo-pump" may be especially important in the Cariaco basin and the Saanich inlet (Algeo and Tribovillard, 2009; Dellwig et al., 2010).

The removal of thio-molybdates may also happen within the water column (hypothesized for the Black Sea) or within the sulfidic pore-waters, however, quantitative removal results in minor net isotope fractionation. Varying δ^{98}Mo signatures can be observed at lower or only intermittently high H_2S concentrations because of slow or incomplete reaction to thiomolybdates (Arnold et al., 2004; Dahl et al., 2010; Nägler et al., 2011; Nägler et al., 2005). During periods of enhanced seafloor anoxia, more Mo was likely removed from the ocean with minor isotope fractionation, resulting in a shift of δ^{98}Mo of seawater, and with that of all Mo sinks, towards lower values, thus making Mo isotopes an important tool to decipher past anoxia extents (Gordon et al., 2009; Proemse et al., 2013; Kendall et al., 2015).

1.2 Uranium

Uranium (atomic number 92) is the heaviest primordially occurring element on Earth, it belongs to the group of actinides and is radioactive. It has an average content of 2.7 µg g^{-1} in the upper continental crust resulting from its refractory and lithophile character and making the crust a large U reservoir (~30 % of all U on Earth) (Rudnick and Gao, 2003). Usually, U occurs in two oxidation states, U^{IV} and U^{VI}. Uranium^{V} is believed to exist as well, however, it disproportionates quickly and is therefore uncommon in nature (Renshaw et al., 2005). The main species of U under current near-surface conditions is the uranyl cation (UO$_2^{2+}$) that preferably forms carbonate complexes (e.g. UO$_2$(CO$_3$)$_3^{4-}$) in water. Its rather unreactive behavior leads to relative enrichment in seawater with concentrations of 13 nmol l^{-1} and long ocean residence times of 250 – 500 ky (Ku et al., 1977; Emerson and Huested, 1991). Under reducing conditions, U^{VI} is reduced to U^{IV} as uraninite (UO$_2$, U$_3$O$_7$, U$_3$O$_8$) and precipitates from aqueous solution. Uranium enters the oceans via riverine input which makes up 80 - 100 % of total U input (Dunk et al., 2002). Major sinks in the U marine geochemical cycle are the reduction and following precipitation of U^{IV} species in anoxic and euxinic settings and at continental shelves, that become anoxic with depth, biogenic carbonates and hydrothermally altered basalts. Other minor sinks are metalliferous sediments, pelagic clays and opaline silica (Andersen et al., 2017).

Uranium has no stable isotopes, however, two of its isotopes, ^{235}U and ^{238}U, are primordial, i.e. have long half-lives (0.7038x10^9 years and 4.468x10^9 years, respectively (Weyer et al., 2008).
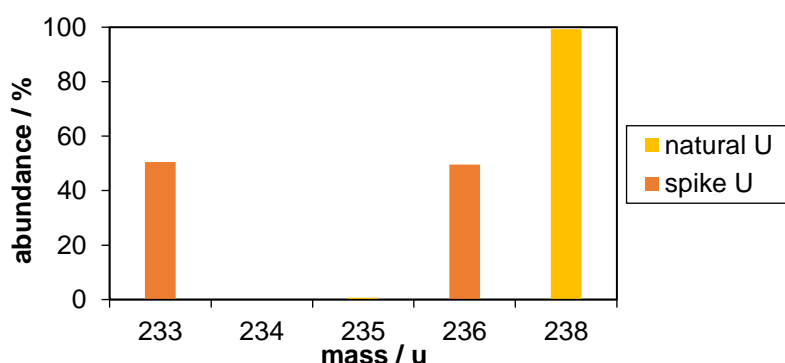
Figure 2: Uranium abundances of natural and synthetic spike isotopes (Verbruggen et al., 2008; Berglund and Wieser, 2011).

Their abundances differ significantly with ^{238}U being much more abundant (99.28 %) than ^{235}U (0.71 %) (Figure 2). The isotope ^{234}U is a decay product of ^{238}U and is also occurring in nature in very low abundances of 0.0054 % because of its short half-life of 2.46x10^5 years (Cheng et al., 2013). Alpha-recoil processes during the decay of ^{238}U to ^{234}U can damage the crystal

lattice in minerals. This process results in preferential mobilization of loosely bound ^{234}U and with that fractionation of the $^{234}U/^{238}U$ ratios from secular equilibrium (atomic $^{234}U/^{238}U_{sec.eq.}$ = 0.000054887 (Cheng et al., 2000)). Hence, precise measurements of $^{234}U/^{238}U$ may, e.g., be used to track weathering processes, in order to reject respective samples for paleo-redox studies (Andersen et al., 2004; Stirling et al., 2007; Andersen et al., 2014).

As a consequence of the volume dependent $^{238}U/^{235}U$ isotope fractionation during U reduction, oxidized seawater has a uniform $\delta^{238}U_{seawater}$ = -0.39 ± 0.06 ‰, slightly isotopically lighter than that of river water (~ -0.3 ‰; Stirling et al., 2007; Weyer et al., 2008; Tissot and Dauphas, 2015; Noordmann et al., 2016; Andersen et al., 2016; Rolison et al., 2017), the dominant source of oceanic U. Rivers, on the other hand, are sourced from weathering continental materials, and the continental crust has a $\delta^{238}U_{cont. crust}$ ranging from -0.2 ‰ to -0.4 ‰ (Tissot and Dauphas, 2015; Noordmann et al., 2016). The main marine sinks are anoxic sediments, e.g. black shales from anoxic or euxinic oceans, that display the largest U isotope fractionation relative to seawater with $\delta^{238}U_{anoxic sed.}$ = -0.2 to 0.4 ‰ (Weyer et al., 2008; Andersen et al., 2014; Andersen et al., 2017). Hypoxic sediments derived from continental margins with oxic overlying water columns, for example off Peru and Washington State, show an average $\delta^{238}U_{hypoxic sed.}$ = -0.24 ‰ (Weyer et al., 2008; Andersen et al., 2016). Marine carbonates can be fairly enriched in U and diagenetically unaltered biogenic carbonates display seawater-like isotope signature of $\delta^{238}U_{carbonates}$ = -0.4 ‰ (Romaniello et al., 2013; Chen et al., 2017). This makes carbonates a promising additional proxy to record the seawater isotope composition of past oceans in paleo-oceanography (Brennecka et al., 2011; Lau et al., 2017). During removal of U at mid-ocean ridges, U is fractionated in altered oceanic crust (AOE) that displays $\delta^{238}U_{AOE}$ = -0.47 to 0.27 ‰ (Andersen et al., 2017). A small oceanic sink in the global U cycle are metalliferous sediments such as Fe-Mn crusts and nodules that display an average $\delta^{238}U_{met. sed.}$ = -0.62 ‰ (Weyer et al., 2008; Goto et al., 2014). Similar as Mo isotopes, the global U isotopic mass balance is shifted during periods of enhanced seafloor anoxia, and these shifts can be used to reconstruct past extents and durations of seafloor anoxia and oxygen evolution.

1.3 Vanadium

Vanadium (atomic number 23) is a transition metal that belongs to the group of redox-sensitive metals. Due to its highly variable behavior as a mildly incompatible, refractory, and lithophilic element it is widely distributed in igneous and sedimentary rocks, however, metallic occurrences are very rare (Huang et al., 2015). The upper continental crust contains 97 µg g^{-1} and V can be found in a large number of different minerals (e.g. sulfides, sulfates, silicates, oxides, phosphates, or vanadates) (Rudnick and Gao, 2003; Gustafsson, 2019). In the deep subsurface as well as in the aqueous environment, V is very redox-sensitive and occurs in

several oxidation states in nature (V^{III}, V^{IV} vanadyl VO^{2+}, and V^V usually vanadate $H_nVO_4^{(3-n)-}$) (Takeno, 2005; Gustafsson, 2019). Vanadium^{II} may also occur in nature, however, is not stable in the boundary field of water (Gustafsson, 2019). Vanadium speciation highly depends on surrounding pH, Eh, solution chemistry and also biology, and it may also polymerize at higher concentrations as vanadate oligomers (Gustafsson, 2019). Under present-day ambient conditions, V^V is dominant at the surface and in the oceans, and primarily exists as mobile and well-soluble $H_2VO_4^-$ and HVO_4^{2-} (Wehrli and Stumm, 1989; Takeno, 2005; Huang et al., 2015; Gustafsson, 2019).

The dissolved V concentration is highly variable and also depends on anthropogenic inputs (Gustafsson, 2019). Its oceanic concentration varies between 30 to 50 nmol l^{-1} (Jeandel et al., 1987; Holland et al., 2004; Beck et al., 2012; Poehle et al., 2015) which corresponds to an average value of 1.8 µg l^{-1} (Schlesinger et al., 2017). Vanadium generally behaves conservative, however, surface waters may show a slight V depletion (Emerson and Huested, 1991; Huang et al., 2015; Ho et al., 2018) and a seasonal variability in coastal areas has been observed (Kowalski et al., 2009; Wang and Sañudo Wilhelmy, 2009). Its oceanic residence time has been estimated to be 130 ky with respect to riverine input and, hence, V is well-balanced in the oceans. Besides the high impact that humans have on the global V cycle and hence anthropogenically increasing the flux of V in rivers, the consideration of further V input from the atmosphere and oxic sediments results in a decrease of the oceanic residence time to 42 ky (Schlesinger et al., 2017). Anthropogenic influence is mainly caused by the extensive use of V-containing fossil fuels and further applications in the steel and electronic industries or as a catalyzer (Schlesinger et al., 2017). In the marine realm, V is mainly buried in suboxic inorganic sediments, e.g. at passive continental margins, and to a lesser extent deposited at hydrothermal vent systems. Additionally, minor V is retained in reducing sediments because of its affinity for organic matter (Schlesinger et al., 2017).

Vanadium has only two stable isotopes, ^{50}V and ^{51}V, with respective abundances of 0.25 % and 99.75 % (Berglund and Wieser, 2011) (Figure 3). In addition to this high difference in abundances, the occurrence of isobaric (^{50}Cr and ^{50}Ti) and molecular interferences complicate the measurement of stable V isotopes. New protocols for the measurement of V isotope ratios have only recently been established with multiple collector inductively coupled mass spectrometry (MC-ICP-MS) (Nielsen et al., 2011; Prytulak et al., 2011; Nielsen et al., 2016; Wu et al., 2016; Schuth et al., 2017). However, the use of different reference materials to calculate and present $\delta^{51}V$ values remains an issue (Schuth et al., 2017). In this thesis, $\delta^{51}V$ are given relative to a pure Nist-3165 solution if not denoted otherwise (following literature data has been re-calculated given the comparative values from Schuth et al., 2017).
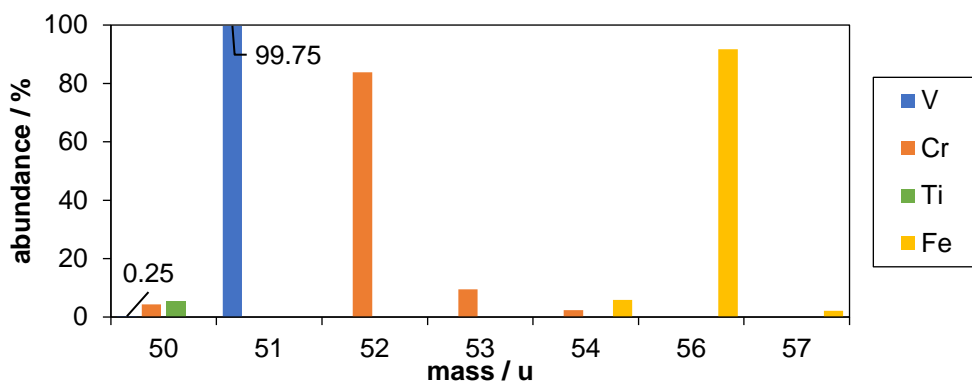
Figure 3: Natural abundances of Ti, V, Cr, and Fe isotopes in the range from mass 50 to mass 57 (Berglund and Wieser, 2011).

The bulk silicate Earth (BSE) has been characterized with a $\delta^{51}V_{BSE} = $ -1.37 ‰ ± 0.2 ‰ (Prytulak et al., 2013) and average values for several meteorites display values of $\delta^{51}V_{meteorites} = $ -2.37 ‰ ± 0.2 ‰ (Nielsen et al., 2014). Crude oils have been found to range over 2 ‰ (Ventura et al., 2015; Gao et al., 2017). Magmas from different settings have been found to vary within 2 ‰, indicative that the redox-state as well as the bonding environment plays a major role in V isotope fractionation (Prytulak et al., 2017). Additionally, V minerals have been found to show variations of up to 1.5 ‰ (Schuth et al., 2017). Only recently, the oceanic V isotope signature of seawater was identified to be $\delta^{51}V_{open\ ocean} = $ -0.47 ‰ ± 0.15 ‰ (Wu et al., 2019) which is heavier than other so far observed values and which is needed to understand the global cycling of V isotopes and the resulting global mass balance.

2. Aims of the thesis

This thesis is separated into three main chapters that aim at answering different objectives by using stable Mo, U, and V isotope analyses. Chapter II contains the set up and application of a new method for the precise and accurate measurement of the V isotope signature of natural seawater for applying this proxy in future redox-reconstruction studies. Therefore, V must be separated from the salt matrix and interfering Cr, Ti, Fe and other matrix elements while ensuring isotope homogeneity and efficient V recovery. The first approach is based on a Fe co-precipitation method that is applied on synthetic and natural seawater. Iron is added in excess, then the solution is alkalized and during the formation of Fe-hydroxides, other metals co-precipitate. Additionally, an ion chromatography (Chelex-100 resin) purification method both with synthetic and natural seawater is tested. Therefore, three previously published methods are repeated and then modified and adapted for the purpose of V isotope measurements of natural seawater samples. The final V fractions of seawater are purified in an ion-exchange column method and measured with a Neptune and Neptune Plus ICP-MS.

Chapter III aims at improving our understanding on the application of Mo and U isotopes as redox proxies. Both isotope systems have been extensively studied, however, a systematic comparison and investigation of their responses to the same conditions lacks from the literature as there are only limited data for Mo and U isotope compositions analyzed on the same samples. In this study, the Mo and U isotope compositions of sediments from the Black Sea and the Cariaco Basin, which are the type modern localities for restricted marine basins with euxinic deep water columns, is investigated. Sediments from drill cores as well as core top surface sediments from different water depths are analyzed for their Mo and U isotope compositions to investigate isotope fractionation under highly (sulfidic) euxinic conditions (central Black Sea), moderately euxinic (Cariaco Basin), and suboxic to only weakly euxinic (such as along the slopes of Black Sea and Cariaco Basin). The study addresses the influence of ocean and pore-water chemistry by analyzing samples from different burial depths along the slope and deep portions of both basins and finally, analyze deeper drill cores through various sediment units to refine the historical evolution of sedimentation in the Black Sea and Cariaco Basin.

Chapter IV applies the U isotope redox proxy on Archean and Early Proterozoic shales, carbonates, and selected iron-rich sediments to identify the onset of U isotope fractionation along with the evolution of oxygen on Earth. The so-called Great Oxidation Event (GOE) was introduced to be the transition from an overall anoxic world to slightly oxidizing conditions that initiated first oxidative weathering and geochemical cycling of redox-sensitive elements (Bekker et al., 2004). Here, the focus lies specifically on the time period before the GOE to gain a better understanding of local or global processes and environmental changes that induced first U isotope fractionation. Mainly drill core samples are chosen and samples are selected carefully based on their authigenic U enrichment. Older samples from the meso-Archean are used as references to compare with younger deposited units.

(*Bibliography at the end of Chapter II*)

Chapter II:

Determining the isotope composition of

Vanadium (^{51}V/^{50}V) in seawater

Abstract

The application of the redox-sensitive trace metal V and its isotopes as a redox-indicator requires the characterization of all respective environmental compartments in order to understand its global cycling. Therefore, a new method to determine the isotope composition of Vanadium ($^{51}V/^{50}V$) of seawater by separation of the V fraction from the seawater matrix, purification of this fractions and subsequent measurement with ICP-MS, is presented. For the first separation tests, a Fe co-precipitation method was tested with synthetic and natural seawater. These tests showed incomplete V yields of 61 %, 75 %, and 81 % for Elba, Corfu and Madeira seawater, respectively, and 75 % and 60 % V yield for synthetic seawater A and B. The natural samples showed a high V loss during the following ion-exchange purification of the precipitated fractions and most variations occurred within the Fe co-precipitation and the main cleanup. Hence, the Fe co-precipitation did not seem a sufficient approach to separate V from a seawater matrix and an additional method, utilizing the chelating ion-exchange resin Chelex-100 was set up. First, three methods from publications were tested with synthetic seawater and then method (1) was applied to Maldive Islands natural seawater. The separation of V from Maldive Islands seawater resulted in 84 % V yield in the Chelex-100, however, during the following cleanup steps, V was significantly lost into the matrix (final V yield 36 %). The tested Chelex-100 methods were modified into one new method adopting the advantages of all tested methods. To evaluate systematic methodical errors within this method, several natural samples from the North Sea were processed repeatedly. The cleaned seawater matrices were doped with known reference standards to evaluate the reproducibility of V isotope compositions during the procedures. The natural North Sea seawater samples (n = 8 out of 9) and most doped seawater matrix samples (n = 6 out of 7) were processed successfully during the Chelex-100 separation and following cleanup steps, however, V yield was found to be only 74 % in average for natural samples. Doped matrices, on the other hand, showed 93 % V yield in average. Most V loss can be ascribed to non-quantitative sorption of V onto the Chelex-100 resin and/or sample loss during many different handling steps, like additional evaporation, re-filling and dilution. Even though some processed pure reference materials showed V isotope fractionation during the procedure, the natural samples were measured for their V isotope compositions. The V isotope signature of North Sea seawater was determined with a $\delta^{51}V_{Nist-3165}$ = -0.62 ‰ ± 0.25 ‰ (n = 17 single analyses from 6 different and separately processed sample aliquots). This value agrees with the previously reported value for open-ocean seawater by Wu et al. (2019) within analytical uncertainty. Finally, the method was applied to further natural seawater samples from the Pacific, Indian, Arctic, and Southern Ocean, as well as an additional North Sea sample. All samples were processed successfully in the Chelex-100 separation, however, due to high V loss and a possible lab blank

contamination of Cr and Ti (indicated by low $^{51}V/^{52}Cr$ and $^{51}V/^{49}Ti$ during additional cleanup steps), only one sample could be measured successfully for its V isotope compositions (named 'Antarctic' from the Southern Ocean). This sample showed a $\delta^{51}V_{Nist-3165}$ = -2.53 ‰ ± 0.21 ‰ (n = 5) which is significantly lower compared to the measured North Sea and published open-ocean value, however, a possible remaining Cr or Ti contamination from high lab blanks cannot be ruled out.

1. Introduction

Vanadium is a transition metal that gains more and more interest in the field of geochemistry due to its highly variable behavior as a mildly incompatible, refractory, and lithophilic element and is, hence, widely distributed in igneous and sedimentary rocks (Huang et al., 2015). In the aqueous environment, V is very redox-sensitive and of special interest because it occurs in several oxidation states in nature. Vanadium speciation highly depends on surrounding pH, Eh, solution chemistry and also biology, however, the main natural oxidation states are +III, +IV, and +V with the last one being dominant in present-day oxidized oceans as $H_2VO_4^{4-}$ and HVO_4^{2-} (Wehrli and Stumm, 1989; Takeno, 2005; Huang et al., 2015). Its oceanic concentration varies between 30 to 50 nmol l^{-1} (Jeandel et al., 1987; Holland et al., 2004; Poehle et al., 2015) because it mainly behaves conservative, however, surface waters may show a slight V depletion (Emerson and Huested, 1991; Huang et al., 2015) and a seasonal variability in coastal areas has been observed (Kowalski et al., 2009; Wang and Sañudo Wilhelmy, 2009).

Vanadium has only two stable isotopes, ^{50}V and ^{51}V, with respective abundances of 0.25 % and 99.75 % (Berglund and Wieser, 2011). Because of this high difference in abundances and the occurrence of isobaric (^{50}Cr and ^{50}Ti) as well as molecular interferences, the measurement of stable V isotopes is not trivial. Plus, the double-spike technique cannot be applied as V has only those two isotopes. Due to the latest advances within plasma mass spectrometry V isotopes can now be measured precisely and accurately in multi-collector inductively-coupled mass spectrometry (MC-ICP-MS) (Nielsen et al., 2011; Prytulak et al., 2011; Nielsen et al., 2016; Wu et al., 2016; Schuth et al., 2017). Within the last years, V isotopic differences between several natural reservoirs have been observed and hence, V isotopes may be generally applied to the reconstruction of past redox conditions, to gain information about cycling and alteration of magmas, as a redox tracer for crust and mantle processes, and to track cycling between different environmental compartments (Prytulak et al., 2013; Nielsen et al., 2014; Brüske, 2015; Ventura et al., 2015; Wu et al., 2015; Gao et al., 2017; Prytulak et al., 2017; Schuth et al., 2017). Only recently, the global oceanic V isotope signature of seawater was published (Wu et al., 2019) which is needed to understand the global cycling of V isotopes and the resulting global mass balance.

In this study, we aim at deciphering the V isotope signature of seawater by developing a method that withstands the demands on high precision V isotope measurements. In order to measure V isotopes with MC-ICP-MS, V must be separated and purified from the sample matrix. A main reason for this is the need to eliminate isobaric interferences of Cr and Ti on the low-abundant ^{50}V quantitatively. Also, matrix components need to be minimized as they would cause matrix effects in the plasma and disturb a measurement. The last reason is the necessity of a Fe clean solution because Fe is added as mass bias monitor with a known isotope composition, because the double-spike technique cannot be applied as V has only two stable isotopes. During all these steps, V recovery must be ensured, and V isotopes must not be fractionated. Because of the high salt matrix in seawater, the first step is to eliminate this salt matrix from the V fraction while preserving V recovery.

In a first approach (section 3), it was tested whether an Fe co-precipitation method can be applied for the separation of V from natural and synthetic seawater matrices. Co-precipitation with Fe-hydroxides is a method that has been applied for decades to pre-concentrate metals, such as U, from seawater matrices (Ku et al., 1977; Chou and Moffatt, 2000). Here, Fe is added in excess, the solution is made alkaline and Fe-hydroxides precipitate while taking other trace metals with it. The process of co-precipitation can be caused by surface adsorption, occlusion and inclusion, mixed crystal formation, and post-precipitation on altered precipitates (Inagaki et al., 2009). For V, the solution pH is expected to control V sorption onto goethite (and likely also other Fe-oxyhydroxides) because of the dependence of V speciation of the pH (Peacock and Sherman, 2004; Huang et al., 2015).

Alternatively, to this pre-concentration method, an ion chromatography (Chelex-100 resin) purification method both with synthetic and natural seawater was tested. Chelex-100 resin is a chelating exchange resin produced by Bio-Rad Laboratories that consists of styrene divinylbenzene copolymers that operate with iminodiacetate ions as chelating groups. These groups have a high preference for high-valent heavy metal cations over monovalent cations even in high salt matrices (Bio-Rad Laboratories, technical notes and manual). Chelex-100 has been used to pre-concentrate metals from salt matrices previously and thus, three of these published methods were chosen to be tested for the purpose of purifying V from seawater (section 4): (1) Abbasse et al. (2002), (2) Pai et al. (1990), and (3) Riley and Taylor (1968).

Any seawater metal fraction needs to be further purified in order to achieve the level of purity needed for V isotope measurements (Nielsen et al., 2011; Wu et al., 2016; Schuth et al., 2017). Here, different ion-exchange columns with ion-chromatography resins were tested to achieve highest V yields together with low Ti, Cr, and Fe residues in the final fractions. Therefore, concentrations in all separated fractions were monitored carefully to calculate yields and loss. After the tests for separating V from the matrix successfully, a modified ion-exchange method was set-up and adapted for the purpose of V isotope measurements of replicate analyses of

North Sea and several other seawater samples (sections 5 and 6). The final V isotope measurement protocol was optimized to suit the demands of measuring the signatures in seawater precisely and accurately and finally the V isotope signature of North Sea and Southern Ocean seawater were measured successfully.

2. Chemicals, samples and measurement methods

2.1 Chemicals and labware

Sample preparation and purification was carried out in a metal-free laboratory at Leibniz University Hannover in laminar flow benches. For contact with purified V fractions (during cleanup of the V fraction), only glass beakers were used. Within the first test of Fe co-precipitation, it was found that V adsorbs readily into PFA beakers and cannot be desorbed thus resulting in observable V loss in samples and permanent coloring of PFA beakers (Figure 1). For glass beakers, glass lids can be used, however, they do not close the beaker properly. For any other matrices or bulk samples, that needed to be heated with closed lids, Savillex® PFA beakers were used.
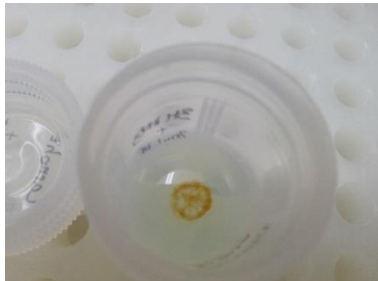
Figure 1: Image showing adsorbed V in a PFA beaker with supernatant solution.

In this study, either 18 MΩ de-ionized water, called MQ water, or desalinated water, called VE water, were used. Glass and teflon beakers were previously cleaned by leaching three days with alkaline soap, 6 M HCl, 7.5 M HNO_3 and MQ water, respectively. All plastic lab ware including 2 l PP bottles for seawater sample preparation and storage was leached with alkaline soap, 1 M HCl and MQ water each three days. Concentrated HCl and HNO_3 (37 % and 65 %, p.a., Carl Roth GmbH + Co. KG, Karlsruhe, Germany) were purified in-house via sub-boiling in a teflon and quartz distill, respectively. Concentrated HF (40%), acetic acid (100 %), NH_3 (25 %) and H_2O_2 (30 %) were purchased in suprapure grade from Merck KGaA, Darmstadt, Germany. Ammonium acetate (lot: SZBC0510V) was purchased from Sigma Aldrich, Germany. The solid chemicals NaCl (lot: K41620204047), $CaCl_2$*2 H_2O (lot: TA343182),

$NaHCO_3$ (lot: K43171129207), KCl (lot: B1039538431) and $FeCl_3*6\,H_2O$ (lot: B1039943410) were purchased from Merck KGaA, Darmstadt, Germany. $MgSO_4*7\,H_2O$ (lot: 1T002152) was purchased from AppliChem GmbH, Darmstadt, Germany. $MgCl_2*6\,H_2O$ (lot: 61601188) was purchased from Alfa Aesar, Karlsruhe, Germany. Ammonium acetate buffer solutions were prepared from MQ water, glacial acetic acid, and ammonia solution.

Chelex-100, biotechnology grade cation exchange resin, was purchased in sodium form, 1 % crosslinkage, 100 - 200 dry mesh size, 150 - 300 µm wet bead size, ~3,500 MW limit (Bio-Rad Laboratories, München, Germany). The resin was cleaned successively prior usage in a column flow method with four cv (cv = column reservoirs) of the respective eluting acid, four cv of MQ water, four cv of NH_3 solution, and 2 cv of ammonium acetate buffer, where it was also stored in for re-usage. Anion resin AG1x8 (BioRad laboratories, München), seizes 100 – 200 mesh and 200 – 400 mesh, was cleaned in a batch method with MQ, 2 M HCl, and 5 M HCl successively. After using anion resin for ion-exchange, it was discarded. For the separation of Ti and other high field strength elements (Münker et al., 2001) LN resin (Triskem, France) was used. It was cleaned in columns successively with 1 cv MQ water, 3 cv 6 M HCl, 1 cv MQ water, 3 cv 2 M HNO_3, 1 cv MQ water, 3 cv 2 M HF, 1 cv MQ water, and 1 cv 6 M HCl, then the resin was stored in 0.05 M HCl for re-usage.

For ion exchange, different columns were used, among them self-made pipette tip columns (frit made of high-density PE, 35 µm mesh, 1 mm thickness, Reichelt RCT Chemicals, Germany; total bed size of 0.15 ml and reservoir size of 1 ml), self-made pasteur pipette columns (low-density poly-ethylene, Brandt, Germany; frit made of high-density PE, 35 µm mesh, 1 mm thickness, Reichelt RCT Chemicals, Germany; total bed size of 0.5 ml and reservoir size of 5 ml), and polypropylene gravity ion-chromatography columns (15 cm length, 12 ml total volume, from Rockbourne, UK). All columns are successively cleaned before and after usage by soaking in alkaline soap and 5 % HCl.

Any pH adjustment was controlled by measurements with a pH-electrode (Mettler-Toledo FG2) that was previously calibrated using purchased calibrating solutions (Thermo Scientific, pH 4 and 7, traceable to NIST standard reference materials), rinsed in between usage with MQ water and stored in 1 M KCl. Tygon tubes (LMT-55, inner diameter 1.52 mm) were cleaned by letting 3 % HNO_3 and MQ water flow through them for several hours prior and after usage.

Two Alfa-Aesar solutions ('new' Specpure from 2015 lot: 865306AG, 'old' ca. 13 years old, Specpure lot no. 25331055), a pure V foil (Alfa-Aesar foil, dissolved in 3 M HNO_3, lot: H25X037), and a Nist-3165 solution (lot: 992706, National Institute of Standards and Technology, USA) served as reference materials for isotope measurements. Additionally, as in-house standard, the black shale sample XJT-6 was dissolved and measured repeatedly during Neptune Plus ICP-MS sessions. For mass bias correction, the Fe reference material

IRMM-014 was used. Standards for calibrating concentration measurements were prepared from multi-element solution standards (VHG labs) and solutions of Indium (CertiPur, Merck) and Iridium (specpure, Alfa-Aesar) served as internal standards. The certified river water standard TMDA-51.4 (lot 1011, Environment Canada) was used for precision and accuracy control during concentration measurements.

2.2 Synthetic seawater samples

In order to test new methods, synthetic seawater was prepared according to table 1 (Kester et al., 1976). Therefore, NaCl and KCl were dried at 100 °C in a drying furnace overnight. The next day, the respective bottle was filled with VE water, let stand for roughly an hour and rinsed again. It was left on a hotplate at 60 °C to dry completely. Then, the bottle was filled with the needed amount of VE water. Salts were weighed into small containers and added into the water. The bottle was shaken thoroughly and left standing with closed lid to equilibrate for several days. After that, oxygen was bubbled through the water for roughly 30 minutes and finally, the bottle was shaken again and stored with closed lid.

Table 1: Recipe for preparing 0.5 l artificial seawater, concentration with asterisk* according to Kester et al. (1976).

salts	M / g mol^{-1}	n / mol	cation / mg l^{-1}	anion / mg l^{-1}	weight / g for 0.5 l
NaCl	58.44	0.233	10706.49	16509.14	13.61
MgSO$_4$*7 H$_2$O	246.48	0.014	686.19	2712.11	3.48
MgCl$_2$*6 H$_2$O	203.3	0.013	610.81	1781.95	2.55
CaCl$_2$*2 H$_2$O	147.02	0.005	412.98	730.64	0.76
KCl	74.55	0.005	386.98	350.90	0.37
NaHCO$_3$	84	0.001	53.51	142.00	0.10
ions	M / g mol^{-1}	concentration / mg l^{-1}	Concentration* / g kg^{-1}		
Na$^+$	22.99	10760	10.760		
Mg^{2+}	24.305	1297	1.297		
Ca^{2+}	40.08	413	0.413		
K$^+$	39.1	387	0.387		
Cl$^-$	35.45	19373	19.353		
SO$_4^{2-}$	96.06	2712	2.712		
HCO$_3^-$	61.01	142	0.142		

2.3 Natural Seawater samples

Table 2 summarizes natural samples, and their sampling information, that were processed in this study. Elba and Corfu seawater were acidified after manual sampling and later filtered in the lab (acidified again), then they were subsampled to 1 l aliquots for the procedures. Maldives, Madeira, and Mauritius samples were only filtered and then acidified in the lab, as well as the professionally sampled Jub 16. Jub 14, Artic, Antarctic and Helgoland seawater were filtered already shipboard and later acidified in the lab. North Sea seawater (~19 l canister) was filtered and acidified shipboard. Samples with more than two liters of total volume (North Sea, Helgoland, and Jub 16) were subsampled to 2 l aliquots that were filled into cleaned 2 l (PP) bottles (cleaning detail in section 2.1). Filtration of samples from Elba, Corfu, Madeira, Maldive Islands, Jub 14, and Mauritius was performed at LUH each with a 0.45 µm cellulose nitrate filter with a Sartorius 16150 polycarbonate filtration tool. Filters of Elba, Corfu, Madeira and Maldives seawater were leached with 3 % nitric acid (total volume of 60 ml) for several days and measured for their elemental concentrations. On the premise of complete dissolution of the filtered fraction (no visible particles were left on the filters or in the leaching bottles) the measurements showed that the particulate concentrations were 0.48 ng l^{-1} V in Elba, 0.96 ng l^{-1} V in Maldives, 1.17 ng l^{-1} V in Corfu, and 2.55 ng l^{-1} V in Madeira seawater. These samples were manually sampled near-shore by swimming into the bay and collecting the water into pre-cleaned bottles. However, the measured values indicate that particulate V contents in the samples was low and negligible compared to dissolved contents (sections 3.4.2 and 4.7.1) with minor local variations.

Table 2: Summary of natural samples processed in this study. Manual sampling was performed by swimming out into the sea, diving and letting seawater flow into bottles. Professional sampling was performed shipboard with professional equipment. Med. Sea = Mediterranean Sea.

sample locality	vol. / l	sample aliquots	date of sampling	sampling info	filtered	acidified	Contact person
Elba, I, Capo Bianco, Med. Sea	3	Elba I, II, III	02.09.14	Manual sampling	0.45 µm	HCl (1 %)	Annika Neddermeyer (LUH)
Corfu, GR, Agios Giorgius, Med. Sea	2	Korfu I, II	27.09.14	Manual sampling	0.45 µm	HCl (1 %)	Nadja Neubert (LUH)
Madeira, P, Canico, Atlantic Ocean	2	Madeira I, II	08.10.14	Manual sampling	0.45 µm	HCl (1 %)	Stephan Schuth (LUH)
Maldives, Indian Ocean	2	Maldives	13.04.15	Manual sampling	0.45 µm	HCl (1 %)	Stephan Schuth (LUH)
North Sea, D, Spikeroog	~19	North Sea I, II, III, IV, V, VI, VII, VIII, IX	04.12.15	Professional sampling	0.45 µm	HCl (1 %)	Ann-Katrin Meinhardt (Uni Oldenburg)
Actic Ocean	2	Actic	n.a.	Professional sampling	0.2 µm	HCl (0.2 %)	Gernot Nehrke (AWI)
Antarctic, Southern Ocean	2	Antarctic	n.a.	Professional sampling	0.2 µm	HCl (0.2 %)	Gernot Nehrke (AWI)
Helgoland, D, North Sea	4	Helgoland A + B	n.a.	Professional sampling	0.2 µm	HCl (0.2 %)	Gernot Nehrke (AWI)
Pacific Ocean, 13°10.51' N, 119°12.19' W	2	Jub 14	14.09.15	Professional sampling at cruise Sonne 240, 1275 m above seafloor	0.45 µm	HCl (1 %)	Nathalie Tepe (Jacobs Uni Bremen)
Pacific Ocean, 7°7.524' S, 88°27.007' W	4	Jub 16 A + B	May/June 2015	Professional sampling at cruise Sonne 242, depth of 4126 m, circa 15 m above seafloor	0.45 µm	HCl (1 %)	Nathalie Tepe (Jacobs Uni Bremen)
Mauritius (Ile des deux Cocos), Indian Ocean	2	Mauritius	Sept. 2015	Manual sampling	0.45 µm	HCl (1 %)	Stephan Schuth (LUH)

2.4 ICP-OES concentration measurements

For high concentrated solutions the concentrations were measured with the Varian Vista inductively-coupled plasma optical emission spectrometer (ICP-OES). External calibration solutions were prepared from pure reference materials in the range of 1 – 15 µg g^{-1}. Samples were measured automatically using a Cetac ASX-510 autosampler and were calibrated with the external reference solutions. Washout of previous solutions was carried out with 3 % HNO_3. At the beginning of each sequence a blank was measured and subtracted automatically during the evaluation with the software. Following the calibration solutions and at the last position after measuring samples, an external standard was measured to monitor any potential drift during the sequence. The drift was highly variable for the different measured absorption lines, but in average was ~4 % for the first session and ~10 % for the second session. In the first session, the following absorption lines were calibrated Na 589.592, Mg 280.270, Ca 422.673, Ti 334.941, Ti 337,280, V 311.070, Cr 267.716, and Fe 238.204 and the original seawater of Elba, Madeira, and Corfu was measured. Within the second session, the following absorption lines were calibrated Na 588.995, Mg 280.270, Mg 279.553, Ca 393.366, Ti 334.941, Ti 337.280, V 311.837, Cr 267.716, and Fe 238.204 and the first V fraction of the synthetic seawater A and B (from the Fe co-precipitation) were measured.

2.5 ICP-MS concentration measurements

Concentration measurements are necessary to control column yield and purity of processed samples and were mostly performed with the Thermo-Scientific ELEMENT XR inductively-coupled mass spectrometer (ICP-MS). Due to the different matrices in the samples, e.g. either high salt content ('original seawater', 'doped seawater', 'seawater after Chelex-100 separation') or purified ion-exchange fractions (Fe precipitates, matrix, and V fractions after cleanups) different set-ups (sample introductory systems) were tested and used (Table 3). An ESI SC2 DX autosampler was always used. As Vanadium tends to accumulate on the cones during measurement sessions, cones were cleaned and re-installed regularly to keep the background low (V intensity should be below 300 cps in medium resolution). However, this could not be achieved in some sessions. The performance of the instrument was checked and optimized daily by using a 1 ng g^{-1} tune solution to yield a sensitivity of at least 1 million cps on ^{115}In in low resolution mode and a U/UO ratio of < 6 %. Each measurement session consisted of blocks beginning with an acid blank, followed by measurement of five to six external calibrations standards with concentrations from 0.1 ng g^{-1} to 100 ng g^{-1} and a maximal number of 25 samples. Washout of previous solutions was carried out with 3 % HNO_3 for four to five minutes. As an internal standard ^{115}In or ^{193}Ir were used to correct for any drift during analyses.

Table 3: Parameters for Element XR ICP-MS measurements.

Parameter	Set-up for purified solutions	Set-up for high-salt matrix fractions
Cones	Ni Jet or H sampler + H skimmer or Al H sampler + H skimmer	
Nebulizer	Teflon or glass with 100 ml min⁻¹ capillary	Glass with 100 ml min⁻¹ capillary
Spray chamber	Glass double-pass Scott design	Glass cyclon or double-pass Scott design
Rf power	~1200 W	
Cooling Ar	15.0 l min⁻¹	
Auxiliary Ar	0.75 – 0.9 l min⁻¹	
sample Ar	1.0 – 1.1 l min⁻¹	
Extraction voltage	2000 V	
Analysis mode	Dynamic (counting, analogue, and faraday)	
Data collection	3 runs x 3 passes, total collection time ~2 min	

The following isotopes were measured in low resolution mode because of their low concentrations in seawater ^{55}Mn, ^{85}Rb, ^{95}Mo, ^{97}Mo, ^{135}Ba, ^{137}Ba, ^{185}Re, ^{187}Re, and ^{238}U. Because of molecular interferences, the following isotopes were measured in medium resolution mode ^{47}Ti, ^{49}Ti, ^{51}V, ^{52}Cr, ^{53}Cr, ^{56}Fe and ^{57}Fe. Some isotopes (^{55}Mn, ^{88}Sr, ^{23}Na, ^{25}Mg, ^{42}Ca, and ^{44}Ca) were measured in medium resolution because of high concentrations in seawater or to control low resolution results. Note, however, that not all isotopes were measured in each session and especially Re and U were only measured during one session for the Fe co-precipitation approach.

To check accuracy and precision during measurements the certified river water standard TMDA-51.4 (diluted and with internal standards) was measured several times during each session, usually directly after measuring external calibration standards and at the end of each block. For the measured isotopes (except Re and U) the average value of all single analyses was always within the certified range of the respective isotopes even though a single session may show values out of the certified range (Table 4). The average calculated deviation between measured and certified values describes a respective error for each isotope. Total errors for measured concentrations in this study include internal measurement errors, deviation of certified reference materials, weighing, dilution and pipette uncertainties, however, the latter cannot be well quantified. For purified solutions (matrix and V fractions after cleanups) the external difference of TMDA-51.4 between measured and certified values (average of all single deviations) is higher than internal errors of the sample's measurements. Hence, this TMDA-51.4 deviation is given as average uncertainty in any results plots (average values for elements with multi-isotope determinations). For high salt matrix solutions ('original seawater', 'doped seawater', 'seawater after Chelex-100 separation', 'alkali matrix') the TMDA-51.4 is not a qualified reference material as the samples internal errors are usually higher due to the high matrix load. Hence, uncertainties on concentration data of salt matrix solutions are calculated

from the average internal errors (~15 % for V, Cr, Ti and Fe). However, most of the times, measuements of high salt containing solutions did not succeed at all. Limits of detection (LOD) were calculated from the standard deviation of ten repeated analyses of a blank solution (Table 4). This standard deviation was multiplied with three and divided by the slope of the calibration curve (DIN 32 645:2008-11, Deutsches Institut für Normung e. V., Beuth Verlag, Berlin). Measured concentrations that were below the respective LOD were not used for further interpretation of data.

Table 4: Deviation of measured TMDA-51.4 replicate analyses compared to the certificate from all measurement sessions. Only certified isotopes are shown. LOD = limit of detection.

isotope	resolution	LOD average ± 1 s.d. / ng g^{-1} (n = 7)	TMDA-51.4 certified ± 2-sigma / ng g^{-1}	Average measured ± 1 s.d. / ng g^{-1}	# TMDA measured	average deviation of all single TMDA-51.4 / % (= error purified sol.)
^{23}Na	medium	2.58 ± 1.79				
^{25}Mg	medium	7.13 ± 6.8				
^{44}Ca	medium	42.96 ± 34.48				
^{47}Ti	medium	0.171 ± 0.17	14.2 ± 0.99	13.98 ± 1.27	52	6.66
^{49}Ti	medium	0.236 ± 0.18	14.2 ± 0.99	13.89 ± 1.26	53	6.78
^{51}V	medium	0.006 ± 0.005	48 ± 3.7	48.81 ± 3.49	53	5.58
^{52}Cr	medium	0.010 ± 0.01	66.2 ± 4.7	66.92 ± 4.91	52	5.65
^{53}Cr	medium	0.094 ± 0.08	66.2 ± 4.7	66.79 ± 4.91	51	5.65
^{55}Mn	medium	0.003 ±0.003	84.3 ± 6.6	84.76 ± 6.09	49	5.46
^{56}Fe	medium	0.051 ± 0.04	118 ± 15.2	130.10 ± 9.43	52	11.62
^{57}Fe	medium	2.241 ± 1.79	118 ± 15.2	130.28 ± 9.25	53	11.75
^{88}Sr	medium	0.013 ± 0.02	116 ± 8.5	119.09 ± 6.86	44	5.08
^{55}Mn	low	0.003 ± 0.003	84.3 ± 6.6	86.20 ± 6.02	31	5.37
^{85}Rb	low	0.047 ± 0.04	15.5 ± n.a.	16.35 ± 1.61	45	8.78
^{95}Mo	low	0.014 ± 0.01	57.6 ± 4.5	55.71 ± 3.22	49	4.27
^{97}Mo	low	0.029 ± 0.01	57.6 ± 4.5	55.46 ± 3.13	48	4.32
^{135}Ba	low	0.091 ± 0.08	73.1 ± 5.1	74.35 ± 3.80	43	4.11
^{137}Ba	low	0.052 ± 0.05	73.1 ± 5.1	74.59 ± 3.73	44	4.17

2.6 ICP-MS isotope measurements

Isotope measurements were performed with the Thermo-Scientific Neptune and Neptune Plus inductively-coupled mass spectrometers. Both machines were connected to a Cetac Aridus II desolvating sample introduction system and an additional ESI SC2 DX autosampler for automated sample introduction can be attached. Samples were either measured with the autosampler system in an automated sequence or manually. A 100 ml min^{-1} capillary and teflon

nebulizer were installed and connected the Aridus and the injector. Standard nickel H sampler and nickel H skimmer cones were used to keep molecular interferences at a low level. Nickel Jet sampler and nickel X cones were tested and resulted in generally higher signal intensities (Nielsen et al., 2011; Nielsen et al., 2016; Wu et al., 2016), however, intensities of interferences of $^{38}Ar^{16}O^+$ and $^{40}Ar^{14}N^+$ were increased as well (especially N from the usage of the Aridus desolvator spraychamber). These interferences then yielded signal intensities > 50 V on mass 54. Compared to that the standard setup with H cones resulted in signal intensities of ~4.5 V for $^{40}Ar^{14}N^+$ (Figure 2) which is adequately low for successful measurements.

Later, the implementation of a spacer (a metal ring), that is inserted between the cones to enlarge their distance, was tested. Several tests at our laboratory with other isotope systems with a spacer have shown that with a dry plasma (from the Aridus desolvator spraychamber) a higher distance between the cones increases sensitivity, e.g. by ~20 % for U and 10 % for Ni (Weyrauch et al., 2017). For V isotope measurements the increase was ~10 % and a 0.7 mm or 0.8 mm copper spacer was used within the last sessions (~60 V/µg g^{-1} with H cones). All measurements were performed in high resolution mode to resolve molecular interferences on several of the measured isotopes ($^{38}Ar^{16}O^+$ and $^{40}Ar^{14}N^+$ on ^{54}Fe; $^{40}Ar^{13}C^+$ on ^{53}Cr; $^{36}Ar^{16}O^+$, $^{38}Ar^{14}N^+$, and $^{40}Ar^{12}C^+$ on ^{52}Cr; $^{38}Ar^{12}C^+$ on ^{51}V; $^{36}Ar^{14}N^+$ and $^{38}Ar^{12}C^+$ on ^{50}V) (Nielsen et al., 2016; Wu et al., 2016; Schuth et al., 2017). In order to avoid any molecular sulfur or chlorine species, chloric or sulfuric acids during sample preparation were not used (Nielsen et al., 2011).

The peaks of all measured isotopes need to be adjusted on top of each other and checked regularly in a so-called peakcenter measurement. Hereby, the center mass was defined to be on the left-hand shoulder of the peaks so that the plateau did not include molecular interferences (Figure 2) (Nielsen et al., 2016; Wu et al., 2016). Consequently, only ^{52}Cr or ^{53}Cr could be measured as one of the two was in the center cup that comprised a dummy mass (Table 5). The peaks of molecular and isobaric interferences needed to be checked in a blank solution as well to proof the correct position of the center mass. The abundance of peakcenter measurements was varied from each to every ~10th single measurement. However, sample and standard should always be measured with the same method, either both with peakcenter or without. Hence, an additional peakcenter method was applied during the seawater samples sequences which only contained the peakcenter protocol at the beginning and 5 cycles. Here, the measured center mass is allowed to vary within 5 – 10 % from the given values in the cup configuration and the software automatically re-adjusts the peaks should they have drifted. Therefore, seawater samples and their respective bracketing standards were measured quickly after each other and no sample solution was wasted during a peakcenter measurement.
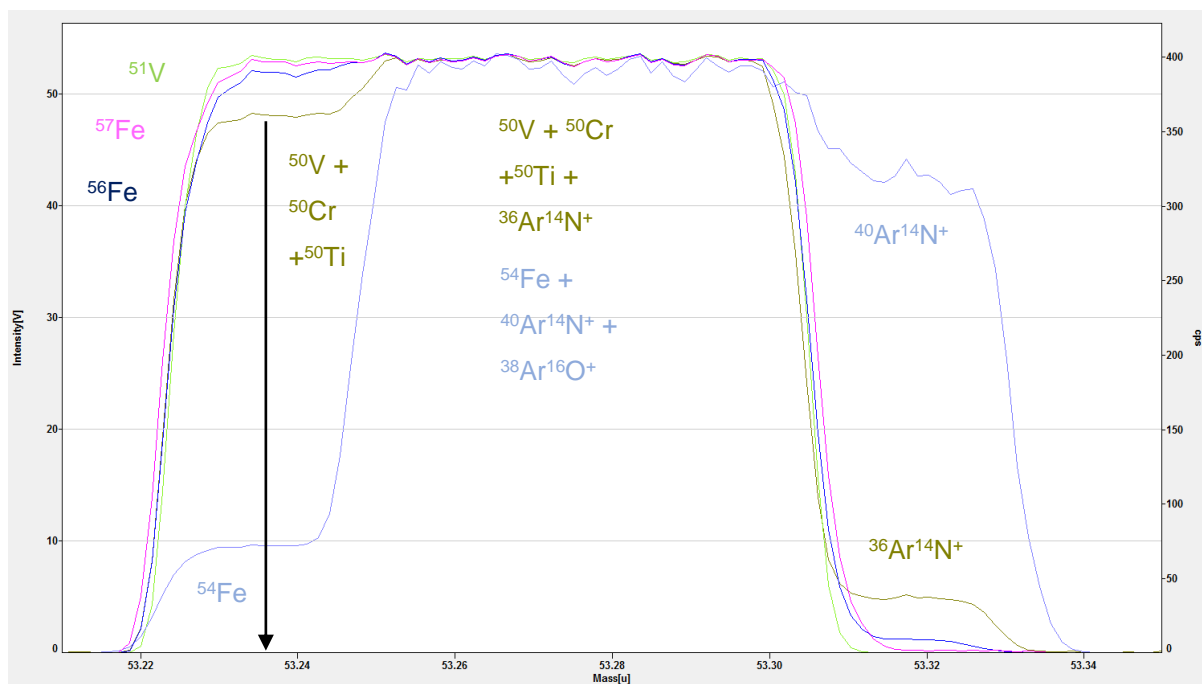
L4: mass 50 (factor 374.03)   L2: mass 51   H1: mass 54 (factor 9.79)

H2: mass 56 (factor 3.19)   H3: mass 57 (factor 136.76)

Figure 2: Peak scan showing measured isotopes and exemplarily molecular interferences with the Neptune Plus ICP-MS (according to final cup configuration, table 5). Arrow indicates the center mass to which all peaks are aligned to be measured on the left-hand shoulder without molecular interferences. No Cr and Ti was measured and hence, their peaks are not shown.

The setup of the Faraday detector cups and resistors and the corresponding measured isotopes are shown in table 5. Resistors are attached to faraday cups and define the measurable intensity range, with high resistance resulting in higher sensitivity and limitations to maximum endurable intensities (max. 50 mV for 10^{13} Ω resistor, max. 50 V for 10^{11} Ω resistor, max. 500 V for 10^{10} Ω resistor). Due to the possible use of $^{56}Fe/^{54}Fe$ or $^{57}Fe/^{56}Fe$ as mass bias monitor (see detailed explanations later) and the additional cup L5 in the Neptune Plus, different cup configurations for both machines are possible (Schuth et al., 2017). At the beginning of the study, the $^{56}Fe/^{54}Fe$ ratio was used with both machines and only the 10^{10} Ω and 10^{11} Ω resistors were attached to cups. The 10^{10} Ω resistor was always attached on the cup for measuring the ^{51}V isotope whenever its intensity increased above 40 V. After calibration of the 10^{13} Ω resistor and the ion counter (IC3A) these two were used for the very low intensities of the interfering isotopes ^{52}Cr and ^{49}Ti on the Neptune Plus (upper row 'final cup Neptune Plus' of table 5). Hence, the final cup configuration was used for all V isotope measurements of natural and doped seawater samples as well as processed standards from the lab procedures. Previous cup configurations were only used for qualitative sample screenings or measurements of pure reference materials. Sample screenings were performed

to test $^{51}V/^{49}Ti$ and $^{51}V/^{xx}Cr$ ratios prior to quantitative isotope measurements, because the Neptune and Neptune Plus are more sensitive than the Element XR ICP-MS. Sometimes the Element results indicate a pure V fractions which proofs to contain too much Cr and/or Ti during a Neptune screening.

Table 5: Overview of the different cup configurations used with the Neptune and Neptune Plus ICP-MS. Asterisks indicate a dummy mass on the center cup C. Only in the upper cup configuration, ^{57}Fe was used as mass bias monitor, otherwise ^{54}Fe was used.

detector	L5	L4	L3	L2	L1	C	H1	H2	H3	H4
final Neptune Plus (since sept. 2016 with IC and $10^{13}\,\Omega$ resistor, before with 10^{11})										
mass	^{49}Ti	^{50}V		^{51}V	^{52}Cr	*	^{54}Fe		^{56}Fe	^{57}Fe
resistor / Ω	Ion counter	10^{11}		10^{11} or 10^{10}	10^{13}	10^{11}	10^{11}		10^{11}	10^{11}
Neptune Plus (only 11.11.15 and 15.2.16)										
mass		^{49}Ti	^{50}V		^{51}V	*	^{53}Cr	^{54}Fe		^{56}Fe
resistor / Ω		10^{11}	10^{11}		10^{11} or 10^{10}	10^{11}	10^{11}	10^{11}		10^{11}
old Neptune										
mass	no L5	^{49}Ti	^{50}V		^{51}V	*	^{53}Cr	^{54}Fe		^{56}Fe
resistor / Ω		10^{11}	10^{11}		10^{11} or 10^{10}	10^{11}	10^{11}	10^{11}		10^{11}

Data collection during sample and standard measurements was performed with different integration times and cycles amounts (one cycle is the static measurement of the cup configuration for the respective integration time). Either 25 cycles each 8 s, 50 cycles each 4 s, or 60 cycles each 4 s were used. For any seawater samples measurements, the last setup with 60 cycles each 4 s was adopted. Washout was carried out with 3 % HNO_3 for at least 4 minutes or longer depending on blank levels during respective sessions. The application of an acid blank correction was tested several times and showed that blank internal variability was high even in 180 cycles each 4 s integration time because the $10^{11}\,\Omega$ resistors show high electronic noise in the low intensity area. Some $\delta^{51}V$ values of reference materials were calculated for comparison with and without blank subtraction and showed the same results, hence, the correction did not influence analytical precision. However, the blank correction increased the $^{51}V/^{49}Ti$ and $^{51}V/^{xx}Cr$ ratios because for the very low abundant Ti and Cr signals, that are measured with the sensitive $10^{13}\,\Omega$ resistor and ion counter, the difference between blank and sample signal intensities is less than 1000. These lower sample/blank ratios usually demand a blank correction, however, as the final $\delta^{51}V$ values are not influenced, the acid blank subtraction may be neglected. Nevertheless, every few single measurements a new acid blank was measured in 3 % nitric acid to monitor blank levels even though a systematic blank correction was not applied.

Instead, a precise baseline measurement (defining the background noise of the machine) was found to be very important due to the previously described minor differences between sample and background intensities of the low abundant Cr and Ti interferences. Different baseline protocols were tested within this study. At the beginning and by only using 10^{10} Ω and 10^{11} Ω resistors, the baseline was measured automatically with the software for 1 s integration time and 300 s total data collection once at the morning of each day. After calibration of the 10^{13} Ω resistor, it was found that due to the slow response time of the resistor, the baseline needed to be measured with 4 s integration time by using the method editor. A method was created that contained 180 cycles each with 4 s integration time and was measured at the beginning of each session. After starting the method, the software forces the machine to open the analyzer gate automatically and it needed to be shut down manually again. Before, all baseline values were set to 0 in the executive software and afterwards the measured values were copied in manually. This baseline remained stable during the course of a measurement day and was applied in the last sessions.

The performance of the machine was optimized daily using a ~0.5 µg g^{-1} pure Nist-3165 V solution to reach maximum intensities of V in accordance with low molecular interferences (especially nitrides contribution from the Aridus desolvator). Depending on the daily tuning, solutions were diluted to yield concentrations of 1.5 µg g^{-1} V to 0.4 µg g^{-1} V. Because of the high difference in abundances between ^{50}V and ^{51}V, a minimum intensity of 25 V on ^{51}V is necessary and needed to be achieved by adjusting the machine parameters (Nielsen et al., 2011). This intensity resulted in a minimal signal of ~50 mV on the ^{50}V+^{50}Ti+^{50}Cr peak. This intensity level should not be undercut due to decreasing counting statistics on the 10^{11} Ω resistor. All pure standard and sample solutions were matched to yield the same intensity within 10 %.

To correct for instrumental mass bias, due to space-charge effects in the plasma, an IRMM-014 Fe standard solution (~0.5 µg g^{-1} corresponding to ~20 V on ^{56}Fe) was added to the samples (Brüske, 2015; Schuth et al., 2017). Iron has three isotopes that can be measured along with V isotopes to be used as mass bias monitor (^{54}Fe, ^{56}Fe and ^{57}Fe). However, due to variety of other isotopes mentioned above that need to be measured and the limited number of Faraday detector cups, only the use of the ^{56}Fe/^{54}Fe ratio is possible with the Neptune (Table 5). Hence, this setup was applied with the Neptune and Neptune Plus at the beginning. Additionally, some measurements were performed without adding Fe to test the performance of the machine with less other elements (Fe in this case) in the plasma and at higher intensities, which would not be possible while measuring the ^{54}Fe isotope due to high molecular interferences (mainly ^{38}Ar^{16}O$^+$ and ^{40}Ar^{14}N$^+$) on it. Alternatively, by using the additional cup L5 of the Neptune Plus, the ^{57}Fe/^{56}Fe ratio may be used as mass bias monitor as well which was done in the later course of the study. Here, many high intense molecular interferences are

avoided by not measuring ^{54}Fe at all. Plus, no ^{54}Cr contamination on the signal of ^{54}Fe needs to be corrected, which should not be an issue in purified samples. Nevertheless, the use of ^{57}Fe simplifies the offline spreadsheet calculations. However, ^{57}Fe is less abundant than ^{54}Fe which is no a problem as IRMM-014 can be added in sufficient amounts to yield good signal intensities.

The mass bias correction can be either performed automatically with the software or manually offline in an Excel sheet. Due to the potential ^{54}Cr contamination on ^{54}Fe, the use of the $^{56}Fe/^{54}Fe$ ratio demands an offline correction whenever traces of Cr may occu (as in the case of real samples). Then, the ^{54}Cr contamination is ruled out by iteratively calculating a β_{Fe} by inserting the real $^{56}Fe/^{54}Fe = 15.69858$ of IRMM-014 (IRMM, 2008) into equation 1, where m(^{5X}Fe) and m(^{5X}Fe) describe the absolute masses of the respective isotopes (Schuth et al., 2017). In equation 1, the numerator is always the higher mass isotope. Then, the hypothetic $^{54}Cr/^{53}Cr$ ratio is mass bias corrected using the exponential law (equation 2, where A and B denote the two respective isotopes and m the respective absolute isotope mass), a hypothetic ^{54}Cr intensity is calculated and is then subtracted from the measured $^{54}Fe+^{54}Cr$ signal. After three iteration steps, a steady β_{Fe} value is achieved and used for the other isotopes for mass bias correction.

$$\beta_{Fe} = \frac{\left(\left(LN\left(^{5X}Fe/^{5X}Fe\right)_{true}\right)/\left(LN\left(^{5X}Fe/^{5X}Fe\right)_{measured}\right)\right)}{\left(LN(m(^{5X}Fe)/m(^{5X}Fe))\right)}$$ eqn. 1

$$A/B_{corrected} = ((A/B_{true})/(m(A)/m(B)))^{\beta_{Fe}}$$ eqn. 2

With $^{57}Fe/^{56}Fe$ the β_{Fe} can be directly calculated assuming a true $^{57}Fe/^{56}Fe = 0.023096$ of IRMM-014 (IRMM, 2008). During the manual offline correction, the order of calculation is mass bias calculation first, either applying an iteration or not, followed by interference correction. Hence, the mass bias correction was usually applied offline and manually during seawater sample analyses, however, for only measuring reference materials in overnight sequences the correction was also applied online (for both using the $^{56}Fe/^{54}Fe$ and $^{57}Fe/^{56}Fe$ ratios). To correct the isobaric interferences of ^{50}Cr and ^{50}Ti on the low abundant ^{50}V the isotopes ^{52}Cr or ^{53}Cr and ^{49}Ti were monitored (Table 5) (Schuth et al., 2017). The true ratios of $^{50}Cr/^{52}Cr = 0.051856$ and $^{50}Cr/^{53}Cr = 0.45732$ (Berglund and Wieser, 2011) and $^{50}Ti/^{49}Ti = 0.972537$ (Leya et al., 2007) were applied (Schuth et al., 2017). These ratios were mass bias corrected using the exponential law and β_{Fe} in a first step and then in a second step their theoretical contribution of ^{50}Cr and ^{50}Ti was subtracted from the measured $^{50}V+^{50}Ti+^{50}Cr$ signal (equation 2, where A and B denote the two respective isotopes). This procedure resulted in interference and mass bias corrected $^{51}V/^{50}V$ ratios which were used to calculate $\delta^{51}V$ values relative to a pure V

solution (either Alfa-Aesar or Nist-3156 as denoted) following equation 3 and the standard-sample-standard bracketing method.

$$\delta^{51}V = \left(\frac{\left(^{50}V/^{51}V\right)_{sample}}{\left(^{50}V/^{51}V\right)_{standard}} - 1 \right) * 1000 \qquad \text{eqn. 3}$$

During various Neptune Plus sessions, different external reference materials were measured to check accuracy and precision of the measurements. Table 6 lists all used reference materials and their measured and reported $\delta^{51}V$ values. Due to the above-mentioned different procedures, either the $^{51}V/^{53}Cr$ or $^{51}V/^{52}Cr$ was monitored. The interference correction on ^{50}V can only be applied until a certain level of Cr and Ti is reached which is given in the literature to be $^{51}V/^{49}Ti = 25,000$ and $^{51}V/^{53}Cr = 25,000$ (Wu et al., 2016). This translates into a $^{51}V/^{52}Cr = 2,800$ due to the different abundances of the Cr isotopes (Berglund and Wieser, 2011). In the literature, different bracketing standards were used and here, aliquots of these different materials were measured as well to proof inter-laboratory accuracy.

Table 6: Compilation of all measured pure reference materials in this study. They agree with previously reported values (from references cited in last column), # describes number of total δ51V analyses, δ51V are given as average between mass-bias and interference [mb+i] and only interference corrected [i] values (measured without Fe as mass bias monitor). Results are averages from both machines and different cup configurations, hence, only 51V/53Cr or 51V/52Cr was measured. Results for the Alfa-Aesar foil are cited from Schuth et al. (2017), indicated by an*, and re-calculated versus Alfa-Aesar solution and 51V/53Cr.

	$^{51}V/^{49}Ti$	$^{51}V/^{52}Cr$	$^{51}V/^{53}Cr$	δ51V bracketing standard	δ51V [mb+i] or [i]	δ51V 2 s.d.	δ51V #	References
Alfa-Aesar sol.	1,590,000	49,000		Nist-3165	-1.65	0.21	69	
Nist-3165	74,900	71,000	320,000	Alfa-Aesar sol.	1.66	0.25	41	
Nist-3165	66,000	52,000	890,000	old Alfa-Aesar sol.	0.48	0.25	33	
XJT-6	6,530,000		6,560,000	old Alfa-Aesar sol.	-0.52	0.08	3	Brüske (2015)
old Alfa-Aesar sol.	3,700,000	170,000	2,130,000	Alfa-Aesar sol.	1.10	0.15	7	Schuth et al. (2017)
BDH	520,000	31,000	520,000	Alfa-Aesar JP	-1.27	0.30	24	Nielsen et al. (2011) Wu et al. (2016) Schuth et al. (2017)
Alfa-Aesar JP	4,870,000		330,000	Alfa-Aesar sol.	0.97	0.12	5	Schuth et al. (2017)
Alfa-Aesar foil *	no Ti detected *	2,800,000 *	24,700,000	Alfa-Aesar sol.	2.38	0.07 *	10 *	Schuth et al. (2017)

3. Separation of V from seawater with an Fe co-precipitation approach

3.1 Application to synthetic seawater

The first Fe co-precipitation was performed with ~2 l of synthetic seawater which was produced as described in section 2.2 except that $NaHCO_3$ was not added into the synthetic seawater. The synthetic seawater was doped with pure single elemental standard solutions of U, V, Mo, and Re to yield final concentrations of ~10 µg g^{-1} (supplementary table S 1). These elements were chosen, because they belong to the group of redox-sensitive elements and may be of interest to be analyzed in real seawater samples. The two liters of doped synthetic seawater were split into two aliquots, named A (V = 1.1 l) and B (V = 1 l).

The protocol for the Fe co-precipitation of seawater is shown in table 7 it was modified from (Ku et al., 1977; Weisel et al., 1984; Chou and Moffatt, 2000). Dissolved $FeCl_3*6\,H_2O$ was added directly into both bottles with synthetic seawater to give final Fe amounts of ~35 mg. The bottles were shaken and left to equilibrate for one hour. Then, 2 – 3 ml of NH_3 solution (25 %) was added to yield a final pH of 9 – 10 and to precipitate Fe-hydroxides, indicated by a shiny orange color (Figure 3). The bottles were shaken for a minute and then left to equilibrate for one hour in turns of five times total.

Table 7: Protocol for Fe co-precipitation.

Step	Procedure
1	Add $FeCl_3 * 6\,H_2O$ to sample, so that total [Fe] = 35 mg
2	Shake for one minute, let stand for one hour
3	Add NH_3 (25 %), so that pH = 9 – 10
4	Shake for one minute, let stand for one hour, repeat 5x
5	Let precipitate accumulate overnight
6	Suck precipitate out with a glass pipette
7	Transfer the precipitate into 50 ml centrifuge tubes
8	Centrifuge at 3000 U for 20 minutes, decant the supernatant
9	Rinse the precipitate with ~10 ml of MQ water, shake and centrifuge again
10	Decant the supernatant and re-dissolve the precipitate in 6 M HCl

Overnight, the precipitates accumulated at the bottom of the bottles and were transferred carefully into centrifuge tubes with a glass pipette. All precipitates were centrifuged at 3000 U for 20 minutes. An aliquot of the supernatant was taken out to be measured qualitatively for its element composition and according to table 7 these aliquots are named *step 8*. The rest of the supernatant was transferred back into the original seawater bottles. The precipitates were rinsed with ~10 ml of MQ water and centrifuged again, whereby another aliquot of the

supernatant rinse solution was taken for elemental measurements (named *step 10*). The washed precipitates were re-dissolved in 6 M HCl and both, precipitates and rinse solutions were diluted to be measured for their elemental concentrations.

3.2 Application to natural seawater

The second Fe co-precipitation test was performed with natural seawater from Elba, Corfu, and Madeira that was split into aliquots of ~1 l yielding two samples from Corfu and Madeira, and three samples from Elba. For the co-precipitation with natural samples $FeCl_3*6 H_2O$ was pre-cleaned using anion resin AG1 X8 to avoid sample contamination from impurities of the iron-chloride. To do so, each portion of 10 % $FeCl_3*6 H_2O$ solution was dried in small PFA beakers and then re-dissolved in 6 M HCl. The anion resin cleaning followed the V-Fe separation protocol from Schuth et al. (2017). Here, the matrix rinses through the resin whereas Fe is retained with 6 M HCl. The final Fe fraction was washed off the resin by adding 7 M HNO_3. It was evaporated and re-dissolved in H_2O for the co-precipitation. The seawater samples were processed as described above for synthetic seawater and a time-series of the process in shown in figure 3. Samples from Corfu and Elba needed 7 ml of NH_3 to have a pH = 9 - 10, whereas samples from Madeira needed 16 ml. This is probably due to a lower starting pH because more HCl had been added for acidification of original seawater. At the end, the precipitates were treated with 5 ml of HNO_3 (65 %) and 0.5 ml of H_2O_2 (30 %) to get rid of any remaining organic seawater compounds. Then, the precipitates were finally dissolved in 6 M HCl for further purification.
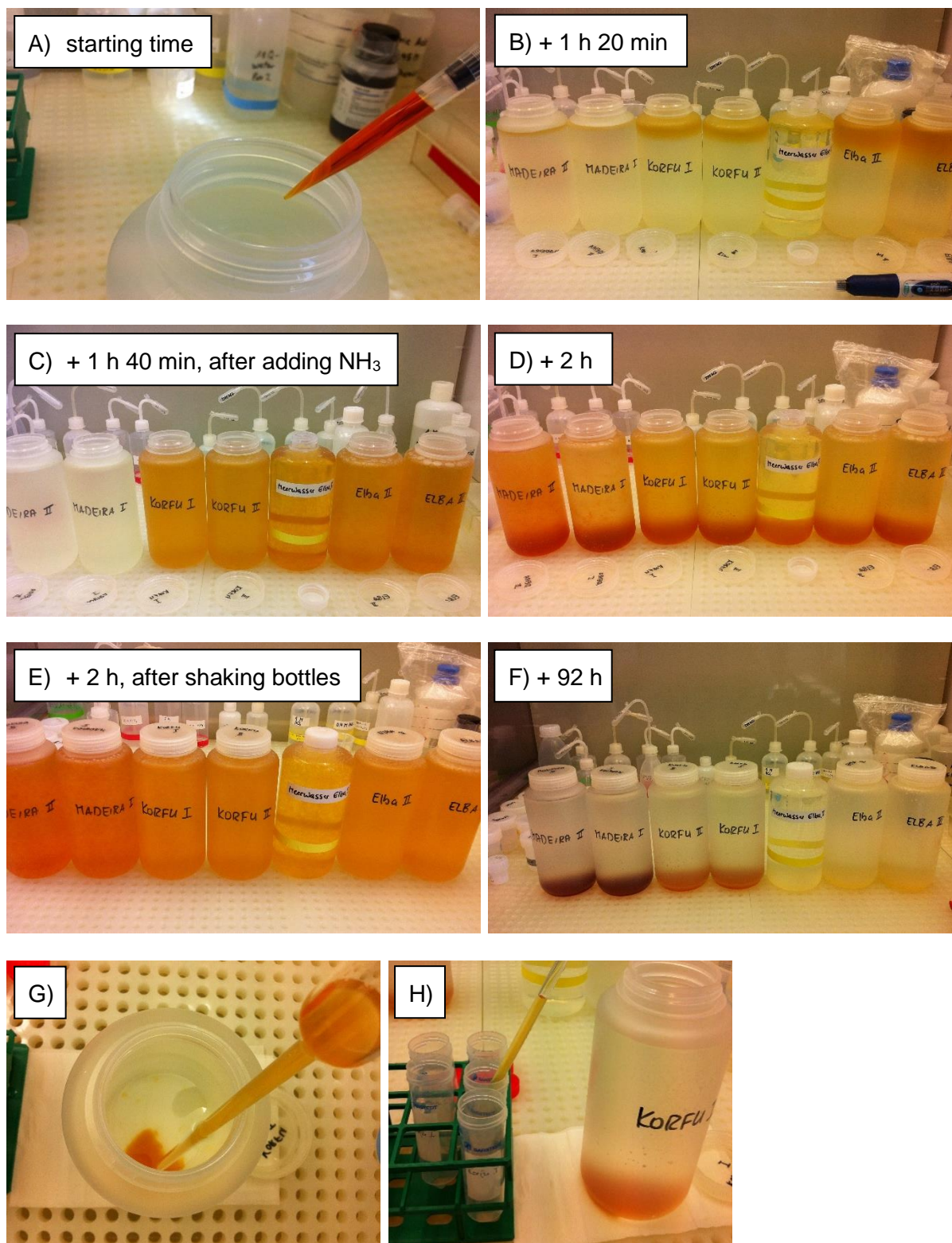
Figure 3: Time series of Fe-coprecipitation method for natural seawater samples. In A: FeCl$_3$*6 H$_2$O is added. In B: the first precipitates appear at the top. In C: NH$_3$ was added which induced more precipitation within Corfu and Elba samples. In D: also Madeira samples precipitated orange Fe(OH)$_3$. In E: all samples were shaken, and precipitation continues. In F: after 92 hours all precipitates accumulated at the bottom of the bottles, significant different colors of the precipitates can be observed. In G: the precipitates are carefully taken out with a glass pipette. In H: the precipitates are transferred into centrifuge tubes.

3.3 Purification of the V fractions after Fe co-precipitation

To separate the V from all other metals in the precipitates, all synthetic and natural metal fractions from Fe co-precipitation were cleaned with an ion-chromatography method according to Brüske (2015) and Schuth et al. (2017), which is shown in figure 4, see references for detailed descriptions. Instead of only applying the columns once (like in Schuth et al., 2017), they were processed repeatedly to ensure full separation of V from other metals and therefore, were checked for purity in between with ICP-MS. After each step, the respective fractions are dried down overnight and to oxidize any remaining resin, aqua regia is added and again vaporized the next morning. The Fe-V cleanup (BioRad AG 1X8 anion resin 200 – 400 mesh size in 1 ml pipette tip columns) was processed twice, one time with the whole metal fraction and then with the matrix from the first step. Due to the high Fe/V ratio in the precipitates, it seemed reasonable to separate V twice from the matrix and combine those V fractions afterwards. Moreover, to avoid an overloading of the Fe columns with Fe, the samples were split into aliquots for each Fe-V separation step. After separating the fractions, the respective aliquots were re-united to represent one sample from synthetic A, synthetic B, Elba, Corfu, and Madeira, respectively.

The second ion-chromatography column in Schuth et al. (2017) employs LN resin and the third step uses anion resin (called "main separation"). For our seawater samples, we decided to first apply the main separation (BioRad AG 1X8 anion resin 200 – 400 mesh in in self-made pasteur pipette columns) because it will remove remaining major ions (e.g. Na, Mg, Ca, and K) from the seawater matrix and then apply the LN column for Ti cleanup (LN resin in 1 ml pipette tip columns). Prior to any dilutions for measurements, a 1:1 mixture of MQ water and H_2O_2 (30 %) is added and carefully evaporated to avoid residues of concentrated acids in the samples.

The main separation was performed once with all samples. This resulted in a V fraction and a main matrix. These V fractions were checked on the Neptune Plus ICP-MS and did not show a steady and constant signal, which can be indicative of too much remaining matrix. Thus, they needed another major ion separation (main separation). Because of lower V concentrations in the V cut, a V loss during the Fe-V or first main separation was assumed and hence, the matrix fraction was processed as a sample as well to account for the first V loss. To quantify the V loss and impurities, all fractions were measured on the Element XR ICP-MS or ICP-OES concerning elemental concentrations. After that, a second main separation was applied to the V fraction and the 1. Matrix. This resulted in two matrices and two V fractions, called V-matrix and matrix-matrix as well as V-V and matrix-V fraction. Both final V fractions were purified for remaining Ti with a LN column as described in Schuth et al. (2017). After that, all resulting fractions were measured with the ICP-OES, (see section 2.4) or Element XR ICP-MS (see section 2.5) to quantify column yield and V loss.

1. Fe cleanup	2. Fe cleanup	1. main cleanup	2. main cleanup	Ti cleanup
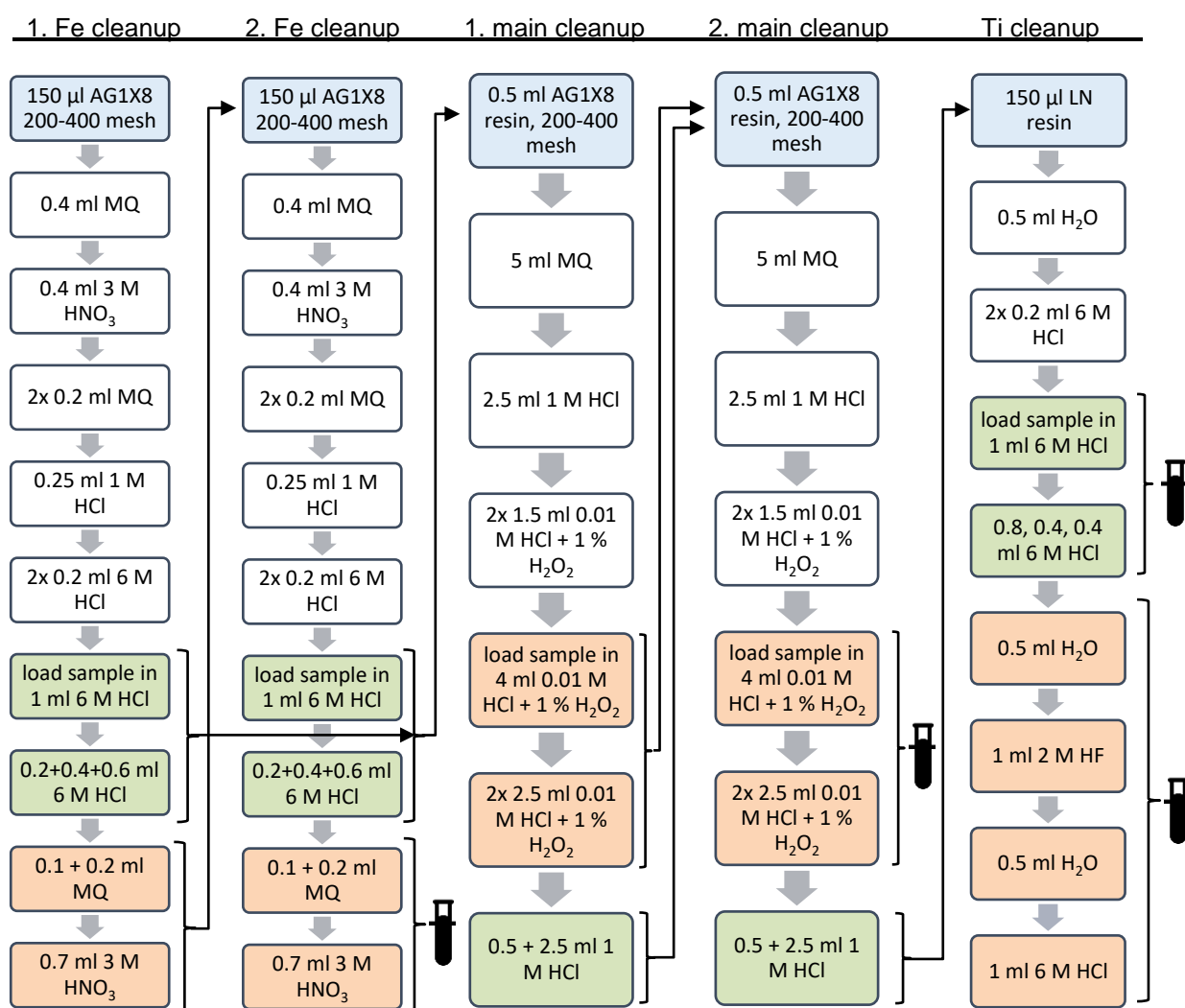
Figure 4: Scheme showing the five different purification steps of V from natural and synthetic seawater by ion-chromatography after Fe co-precipitation. Used resins are highlighted in blue, colorless squares depict resin cleaning prior to sample load, V elution is highlighted in green, and matrix elution in orange. Arrows indicate which fractions were cleaned in the next steps, whereby small test tubes indicate that a fraction is taken out for ICP-MS measurements. Modified from Brüske (2015) and Schuth et al. (2017).

3.4 Results and discussion of the Fe-coprecipitation method

3.4.1 Fe co-precipitation with synthetic seawater

The Fe co-precipitation method did not show a complete recovery of added V into synthetic seawater. For precipitate A the yield was ~75 % and for precipitate B the respective yield was ~60 % (Table 8). The differences between these numbers highlight, that even though both experiments were performed in the same manner, they are not representative and reproducible. The difference may be also due to uncertainties in concentration measurements. The calculated yield for the rinse solution from *step 8* and *step 10* is very low, but only describes

a portion of not precipitated metals because they were not weighed before dilution and measurements. Thus, the metals missing in the calculation were probably still in the synthetic seawater and did not co-precipitate with the Fe. To improve the yield in V-Fe co-precipitation, the used conditions may be adjusted because the yield highly depends on the amounts of precipitants used, the pH, the coexisting salts and the ageing time of precipitation (Terada, 2000).

The Fe co-precipitation was sufficient for U in both synthetic seawater samples A and B with yields of ~95 % and ~87 %, respectively (Table 8). For Mo and Re, however, the method did not work out as only minor amounts were found in the precipitates. Even though both elements are supposed to behave particle-reactive under certain conditions, these conditions were obviously not met in our experiment. In oxygenated water, e.g. as our synthetic seawater, Mo occurs as molybdate and behaves conservative. Only with enough sulfide around to transform it into thio-molybdates, will it become particle reactive and readily adsorb onto surfaces (Morford and Emerson, 1999; Erickson and Helz, 2000). Therefore, Mo co-precipitation with Fe is usually performed in the presence of sulfuric acids (Terada, 2000). Rhenium is supposed to adsorb onto Fe-oxy-hydroxides, however, its adsorption behavior increases under reducing conditions, similar to Mo (Morford et al., 2005). Our experiment, on the other hand, showed that Re co-precipitation with Fe under those experimental conditions was only minor.

Table 8: Results of Fe co-precipitation with synthetic seawater A and B. Note that step 8 and step 10 describe the rinse solutions after centrifugation and washing of the precipitate, however, they only include a portion of the respective solutions and were not back calculated to the total volume; indicated by *. 'Theo amount' describes the calculated amount based on gravimetrical doping of seawater.

	precipitate / mg	step 8 * / mg	step 10 * / mg	theo. / mg	yield in precipitate / %	yield in solutions 8+10 * / %
synthetic A						
Mo	0.26	1.28	0.11	10.49	2.45	13.22
Re	0.06	1.29	0.11	10.49	0.60	13.42
U	9.98	0.01	0.00	10.47	95.30	0.11
V	7.82	0.26	0.03	10.47	74.65	2.76
synthetic B						
Mo	0.22	0.92	0.08	9.54	2.29	10.44
Re	0.04	0.95	0.09	9.53	0.42	10.92
U	8.25	0.01	0.01	9.52	86.69	0.14
V	5.74	0.23	0.03	9.52	60.29	2.71

In general, co-precipitation follows different mechanisms, such as surface adsorption, occlusion and inclusion, mixed crystal formation, and post-precipitation on altered precipitate (Inagaki et al., 2009). Hence, the yield was likely higher if the conditions were matched for these elements. Also, the mentioned issues likely affect natural seawater in a different manner and thus, a second Fe co-precipitation test with natural seawater was necessary and performed.

3.4.2 Fe co-precipitation with natural seawater and cleanup of all fractions

Results for yields during the cleanup of synthetic seawater A and B are calculated relative to the measured V contents in the Fe precipitates (Table 9). The calculated amount of V prior to Fe co-precipitation is used as original seawater composition. To evaluate the Fe co-precipitation with natural samples, the original concentration in those samples needed to be measured. Because of the high salt matrix, this was done with the ICP-OES (marked with an asterisk in table 9) and resulted in V contents of $3.26\,\mu g\,l^{-1} \pm 1.12\,\mu g\,l^{-1}$ for Elba, $3.21\,\mu g\,l^{-1} \pm 1.07\,\mu g\,l^{-1}$ for Corfu, $3.11\,\mu g\,l^{-1} \pm 1.05\,\mu g\,l^{-1}$ for Madeira, respectively (see next paragraph for calculation of uncertainty). These values are significantly higher than published V contents of the Mediterranean Sea ($1.78\,\mu g\,l^{-1}$ to $2.5\,\mu g\,l^{-1}$, Jeandel et al., 1987, and Sherrell and Boyle, 1988) and Atlantic Ocean ($1.66\,\mu g\,l^{-1}$ to $2.46\,\mu g\,l^{-1}$ Jeandel et al., 1987, Van der Sloot et al., 1989, and Poehle et al., 2015). Most likely these offsets can be explained by high uncertainties of the ICP-OES measurements because they were performed in the low ppb-range and hence, are close to the detection limits (LOD) of the machine. Unsatisfactorily, LOD's were not quantified during this session and no external reference material was quantified neither. In addition, V was only quantified with one absorption line and may have been disturbed by spectral interferences of OH-absorption peaks. Consequently, the analytical uncertainty cannot be calculated precisely and is estimated. As all three samples were quantified in a similar range, the error is likely systematic. Taking the offsets between the measured and published values (maximum and minimum) into consideration, estimated errors for the measured V contents in Elba, Corfu, and Madeira seawater are in average 34 %, 33 %, and 34 %, for Elba, Corfu, and Madeira, respectively.

Hence, any calculated yields will suffer from these inaccurate measurements (indicated by '~'). On the other hand, V contents have been found to be influenced by particulate load which is significantly higher in rivers than in seawater (Van der Sloot et al., 1989). The measured values may be accurate due to higher V particulate load because of sampling near-shore. Additionally, all other fractions were measured with ICP-MS and the sum of these fractions (seawater after precipitation, Fe matrix, main matrix, and V fraction) is in the same order of magnitude than the measured original contents. Hence, the ICP-OES seawater contents seem sufficiently accurate even if measurement uncertainties remain rather high (rather qualitative than

quantitative determinations). The precipitates from Elba, Corfu and Madeira were not measured for their elemental concentrations, so that any V yield of V contents can only be calculated to their original contents. Nevertheless, the remaining seawater after precipitation was measured with ICP-MS and these analyses showed that 40 %, 25 %, and 19 % were left in the respective samples (estimated uncertainty 15 %, section 2.5). This in turn can be back calculated to a theoretical V yield in the precipitates of ~61 %, ~75 %, and ~81 % for Elba, Corfu and Madeira, respectively, which is in the same order of magnitude as synthetic seawater A and B (Table 9).

For the first cleanup round, which includes two Fe separations and one main separation, the yields of the first V fractions compared to the original seawater values are significantly too low with ~11 %, ~24 %, and ~56 % for Elba, Corfu, and Madeira, respectively. For Elba seawater, this is due to the failed main separation. For Corfu seawater, the main separation also lost a significant portion of V (28 %), however, for Madeira seawater the main separation was reasonably successful (3 %). This highlights that the main separation is highly sensitive to different factors and can easily be failed by the experimentalist. For example, the pH and sample matrix, especially Fe (Nielsen et al., 2011), play a major role in quantitative sorption of V onto the anion resin and in the formation of peroxide-complexes. Plus, due to buffer capacities of the sample matrix itself, the hydrogen peroxide may be easily decomposed, thus hindering V from sorption onto the resin. Hence, a speculative reason for the failed main cleanup of Elba seawater is most likely pH variability. Further detailed discussion about this issue can be found in section 7.1.

For synthetic seawater A and B, the V yields within the first cleanup round are 86 % and 109 % compared to the precipitates, respectively, which is sufficiently high. However, deviations can be observed between the sum of V found in the first main matrix and in the first V fraction and amount in the precipitates. Here, most likely these offsets in sum arise from the comparison of data from ICP-OES (1. V fraction) with ICP-MS (all other fractions) and their different individual uncertainties. Nevertheless, it can be observed that both Fe separations did not cause significant V loss as the Fe matrix only contained minor V. After these three first separation steps, a qualitative check of the sample purities with the Neptune ICP-MS was performed. This showed that, even without quantification, the signals of ^{52}Cr and ^{49}Ti were too high for precise V isotope measurements. Thus, a second cleanup round of a main and a Ti cleanup was performed. Therefore, the synthetic seawater was diluted 1:50 and this aliquot was further processed (column '2. V fraction' in table 9). Both cleanups of the V fraction went sufficiently successful with a yield for the second cleanup round of 102 %, 103 %, 77 %, 88 %, and 89 % for synthetic A and B, Elba, Corfu, and Madeira, respectively. It strikes that Elba seawater again had the lowest yield, likely indicative of a complex matrix still in the sample solutions. Finally, the yields of the last V fractions of the natural samples were ~8 %, ~21 %, and ~50 %

for Elba, Corfu, and Madeira in comparison to starting compositions, which shows that the whole procedure was very instable and not reproducible.

Table 9: Vanadium contents and yields of all cleanup steps for metal fractions from Fe co-precipitation of synthetic seawater A + B, and natural seawater from Elba, Corfu, and Madeira. Asterisks mark measured values from ICP-OES whereas all other values were obtained with the Element ICP-MS. Values in italic and brackets are probably inaccurate due to measurement artefacts. All contents are back-calculated to total sample amounts. See text for details on measured fractions.

1. Cleanup round							
Fe precipitates	Absolute volume / l	original seawater / µg	precipitate / µg	in seawater after precipitation/ µg	Fe matrix V conc / µg	1. main matrix / µg	1. V fraction / µg	V yield / %
synth. A	1.1	10470	7819		0.13	1562.1	6686 *	85.51
synth. B	1	9520	5741		0.07	1301.9	6233 *	108.58
Elba	3	9.8 *		3.9 (40 %)	0.36	8.09	1.08	11.08
Corfu	2	6.4 *		1.6 (25 %)	0.07	1.77	1.54	23.91
Madeira	2	6.2 *		1.2 (19 %)	0.77	0.20	3.50	56.33
2. Cleanup round							
1. V fraction	2. V fraction / µg	2. main matrix / µg	Ti cleanup matrix / µg	final V fraction / µg	2. V yield / %	total V yield / %	
synth. A	133.72	0.072	0.532	135.73	101.50		
synth. B	124.66	0.025	0.275	128.77	103.30		
Elba	1.08	0.058	0.001	0.83	76.8	8.4	
Corfu	1.54	0.106	0.002	1.35	88.0	21.1	
Madeira	3.50	0.282	0.005	3.12	89.1	50.4	
Cleanup of 1. Main separation matrix							
1. main matrix	1. main matrix / µg	2. main matrix / µg	Ti cleanup matrix / µg	V from 1. main matrix / µg	V yield / %		
synth. A	1562.1	*(2448.44)*	0.8447	373.145	23.89		
synth. B	1301.9	916.37	0.6612	175.236	13.46		
Elba	8.09	2.909	0.0019	0.251	3.10		
Corfu	1.77	1.4902	0.0029	0.397	22.44		
Madeira	0.20	0.0037	0.003	0.301	150.18		

Because the first main separation resulted in high V loss into the first main matrix, this matrix was purified in the second cleanup round as well (lowest part of table 9). The results show that also the second main matrix contained a significant portion of V whereas the second Ti cleanup was successful. It strikes that the sum of V in the second main matrix, Ti cleanup matrix and V fractions do not match the starting V content. This may be explained by measurement errors (ICP-MS V error 5.6 %, from section 2.5) and volumetric dilution of samples. Especially the

value for V in the second main matrix of synthetic seawater A is too high to be realistic. Due to higher matrix content in the matrix V fraction it was not combined with the final V fraction. The compositions of all fractions can be found in the supplementary section S 1.

In Summary, the Fe co-precipitation seems rather variable in yield in synthetic and natural seawater based on the samples processed in this study. Thus, the Fe co-precipitation method needs further improvement to achieve enough V yield by adjusting the experimental conditions, e.g. pH, amount of Fe added, or ageing time of the precipitates. Most variations within the method occur due to the Fe co-precipitation itself and the main separation, which can be improved by adjusting the pH and thus V-peroxide complex stability. However, high amounts of Fe may cause a failure in the main separation (Nielsen et al., 2011) which remains a risk during an Fe co-precipitation approach. Elba seawater did show the most unsuccessful separation which may also indicate its individual sample matrix influence. Elba seawater was sampled in a bay not too far away from the beach and thus, the particulate load in the water may have caused the problems even though the water was filtered several days after sampling. Corfu and Madeira seawater were also sampled by hand as well, however, it seems likely that regional variations in seawater composition influence the separation. Thus, it is advised to use open-ocean seawater for further tests of separating V from a seawater matrix.

4. Purification of V from seawater with an ion-chromatography approach using Chelex-100 resin according to published methods

4.1 Application of published literature methods to synthetic seawater

Table 10 shows the protocols of the chosen methods that are compared for the pre-concentration of V from seawater. Note that the main differences lay in the used eluting chemicals that differ between acid in (1) and (2) or base in (3). Also, (2) uses a pH buffer whereas both others only adjust the pH before the separation. A third major difference is the resin form that is used which is NH_4^+-form in (1) and (2), and H^+-form in (3). For testing the three methods, each 0.5 l of synthetic seawater was prepared according the protocol described in section 2.2. An aliquot form each seawater without metals was taken to serve as blank for these method tests (10 g out of 0.5 l). Then, the synthetic seawater samples were doped with Fe, V, Cr, and Ti pure single standard solutions to yield final concentrations of these elements of 0.1 µg kg^{-1}. Another aliquot was taken after doping with metals (10 g out of 0.5 l). Synthetic seawater was doped with all four respective elements to serve as a first test whether this method may also separate the metals and thus be V-sensitive. Also, the test was supposed to indicate whether Fe, Cr, or Ti may interfere with the quantitative V separation. The samples were shaken thoroughly before loading onto the Chelex-100 columns.

For method (2) the ammonium acetate buffer solution was cleaned with Chelex-100 prior to adding into the sample. Therefore, circa 5 ml of Chelex-100 resin (100 – 200 mesh, NH_4^+-form) was filled into polypropylene gravity ion-chromatography columns (15 cm length, 12 ml total volume). The buffer solution was dropped onto the resin at a flow rate of 2 ml min^{-1} and the first 20 ml were discarded whereas the rest of cleaned buffer was collected into a cleaned PP bottle. The pH was monitored before and afterwards.

For the separation of synthetic seawater samples, the before described PP columns were put into a self-made plastic rack to sit above the pre-cleaned collecting bottles, which were connected to the seawater with tygon tubing. Resin was given into the columns to give a final reservoir height of ~4 cm. The resin was successively cleaned according to the protocols. Then, seawater samples were dropped onto the resin with a peristaltic pump (Behr Labor Technik, PLP 380, 2-channel DG-2, PPH5062) at the respective drop rates (Table 10) without evolving an overlying water reservoir (and thus too much pressure) or disturbing the resin bed. During the elution of metals from resin (part 2 in table 10) all fractions were collected in separate PFA beakers (Figures 5, 6, and 7) and the V fractions were split into portions of 5 for (1), 7 for (2), and 6 cuts for (3) so that all cuts were measured separately with Element XR ICP-MS and elution curves could be produced.

Table 10: Comparison of tested methods for separating V from a seawater matrix. Cv = column volume.

Step	(1) Abbasse et al. (2002)		(2) Pai et al. (1990)		(3) Riley & Taylor (1968)	
	Used chemicals	Item for collection	Used chemicals	Item for collection	Used chemicals	Item for collection
Part 1: Preparation of Chelex-100 (100-200 mesh)						
Wash	25 ml 2 M HNO_3/0.5 M HCl		3 x cv 2 M HNO_3		20 ml 2 M HNO_3	
Wash	50 ml H_2O		5 x cv H_2O		H_2O until pH of rinse sol. = 4.5 (min 100 ml)	
Convert	15 ml 1 M NH_3		3 x cv 1 M NH_3			
Wash	25 ml H_2O		5 cv H_2O			
Part 2: Separation of V from seawater						
Load sample	sample (adjusted to pH = 5), flow rate 2 ml min^{-1}	PP bottle	sample (add 30 ml l^{-1} of 1 M ammonium acetate buffer, pH = 6.5)	PP bottle	sample with pH = 5.0 ± 0.2, flow rate 5 ml min^{-1}	PP bottle
Wash matrix			5 x 1 ml H_2O	7 ml PFA beaker		
wash matrix			4 x 5 ml 1 M buffer at pH = 5.5	60 ml PFA beaker		
wash			5 x 1 ml H_2O	7 ml PFA beaker	200 ml H_2O	250 ml PFA beaker
V elution	5 x 2 ml 2 M HNO_3/0.5 M HCl	5 x 7 ml PFA beakers	7 x 1 ml 2M HNO_3	7 x 7 ml PFA beakers	6 x 4 ml 1 M NH_3	6 x 7 ml PFA beakers
Regenerate resin	3 x cv 2 M HNO_3	60 ml PFA beaker	3 x cv 2 M HNO_3	60 ml PFA beaker	1 x cv H_2O	60 ml PFA beaker
Regenerate resin	5 x cv H_2O	60 ml PFA beaker	5 x cv H_2O		3 x cv 2 M HNO_3	
Regenerate resin	3 x cv 1 M NH_3	60 ml PFA beaker	3 x cv 1 M NH_3	60 ml PFA beaker	5 x cv H_2O	60 ml PFA beaker
Regenerate resin	5 x cv H_2O	60 ml PFA beaker	5 x cv H_2O		3 x cv 1 M NH_3	
Regenerate resin					5 x cv H_2O	

Also, resin regeneration solutions and seawater after the separation (aliquot of 10 g) were collected to be measured for their element contents. After finishing the separation, all matrix and V fractions were evaporated to dryness on a hotplate. They were treated with aqua regia (3:1, concentrated HCl and concentrated HNO_3) to destroy remaining organic components of the resin or from the original seawater. Alkali and resin cleaning fractions are prepared to be

measured concerning their element concentrations by diluting with 3% HNO$_3$ according to their expected salt contents (alkali matrix 1:100, resin cleaning fractions first 1:50, later 1:10). The internal standard for ICP-MS measurements is added as well.
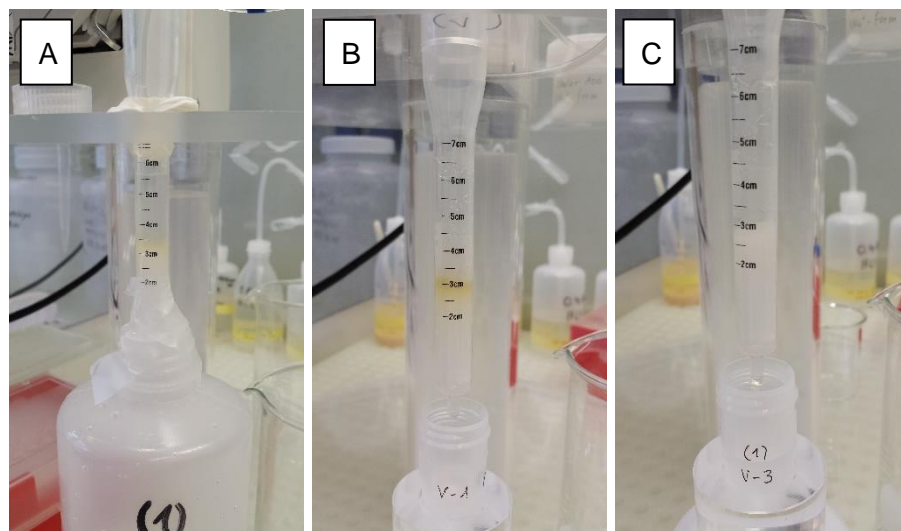
Figure 5: Separation of metals from synthetic seawater according to method (1). In A: the sample is dropping onto the resin and the metals are indicated by the yellowish coloring of the resin. In B: the first ml of V fraction is eluted. In C: the third V ml is eluted, and the yellowish color has already vanished.
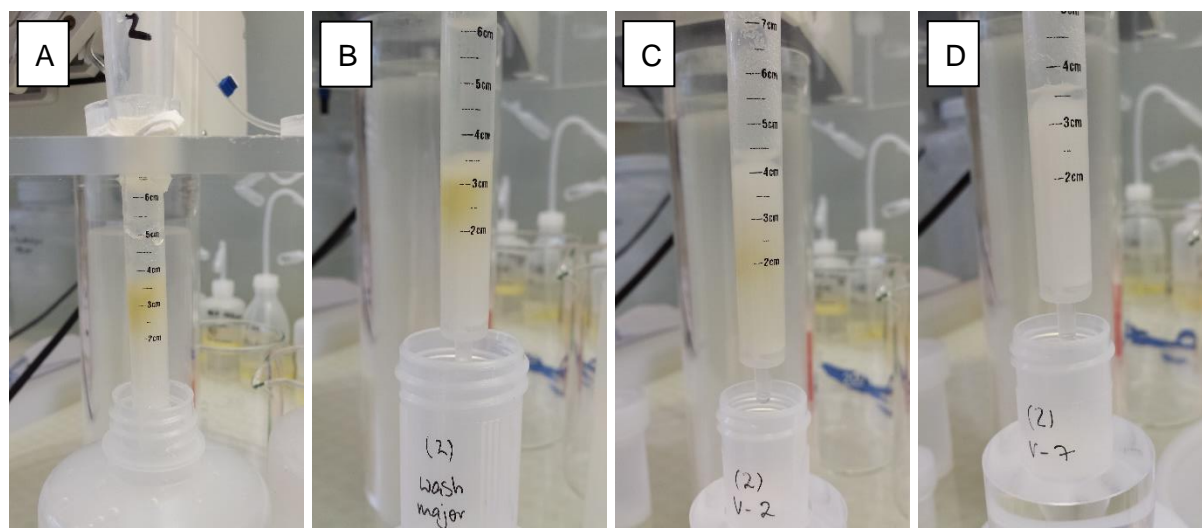
Figure 6: Separation of metals from synthetic seawater according to method (2). In A: the sample is dropping onto the resin and the metals are indicated by the yellowish coloring of the resin. In B: the resin is washed with buffer solution. In C: the second ml of V fraction is eluted; the metals are moving down the resin. In D: the last V ml is eluted, and the yellowish color has vanished.
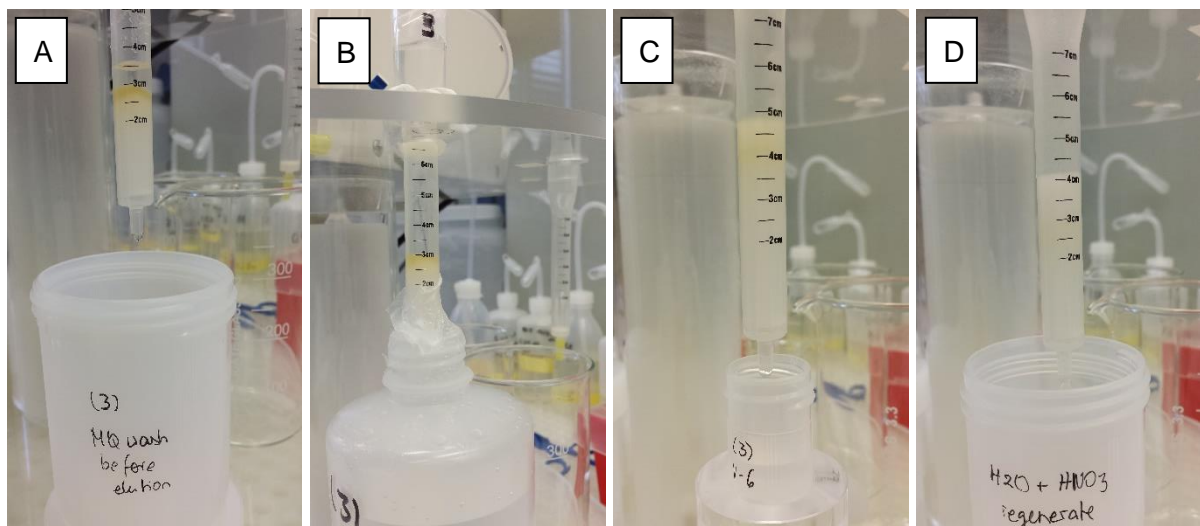
Figure 7: Separation of metals from synthetic seawater according to method (3). In A: the sample is dropping onto the resin and the metals are indicated by the yellowish coloring of the resin. In B: the resin is washed with MQ before elution. In C: the last ml of V fraction is eluted; the metals are still on the resin as indicated by its yellowish color. In D: the resin is regenerated, and the yellowish color has almost vanished.

4.2 Elution curves and yield for Chelex-100 separation of synthetic seawater according to methods (1), (2), and (3)

Elution curves (yields calculated relative to theoretical content from weighed starting amount of respective metal) for V, Cr, Ti, and Fe for all three tested methods are shown in figures 8, 9, and 10. Within method (1) most V, Cr, Ti, and Fe was found in the fraction V-2 which describes the second 2 ml of 2 M HNO_3/0.5 M HCl (total elution volume 10 ml, figure 8). In contrast to the other elements, Fe was not retained on the resin as good because roughly 20 % was found in the seawater after the separation (Table 11). This is due to the different sorption behavior of elemental species in different media with the Chelex-100 resin (Abbasse et al., 2002).
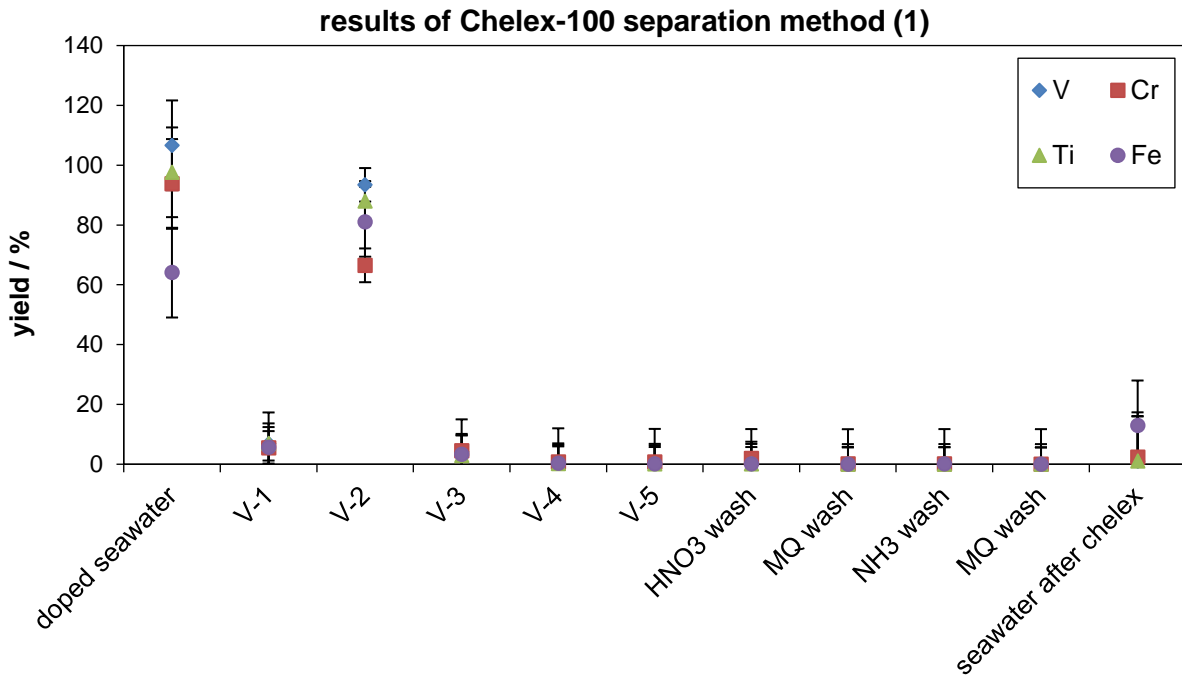
Figure 8: Elution curve (yields versus theoretical amount of respective metal) for Chelex-100 separation according to method (1). HNO_3 wash, MQ wash, and NH_3 wash describe the resin regeneration. V-1 to V-5 describe the metal elution with 5 x 2 ml of 2 M HNO_3/0.5 M HCl.
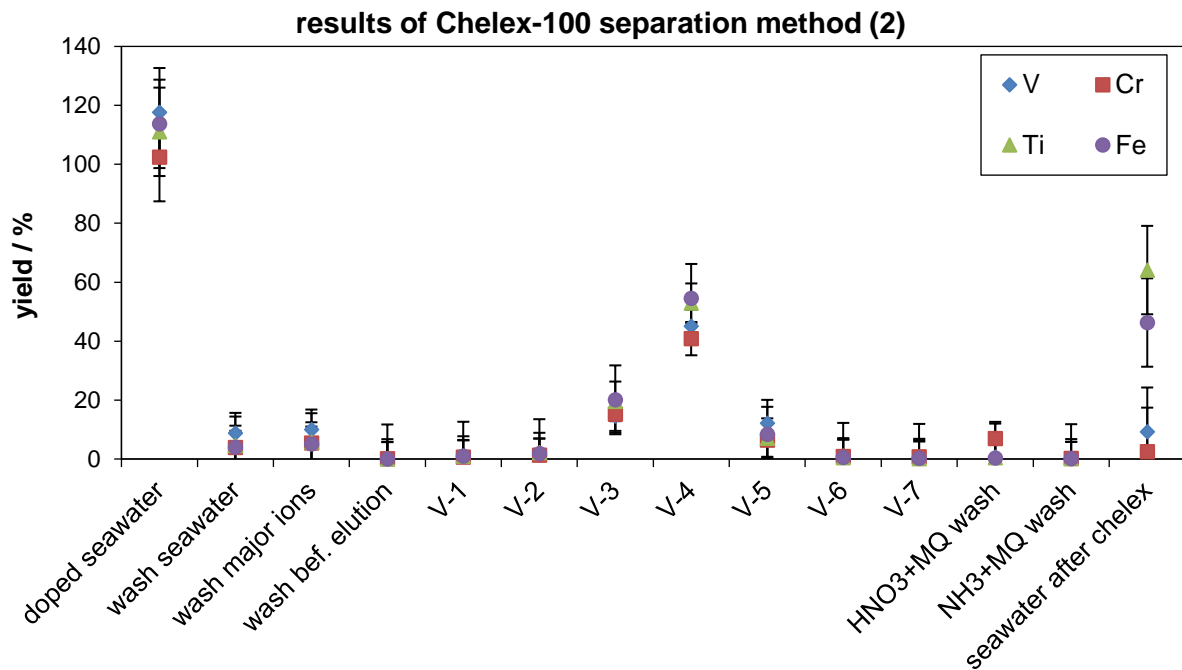
Figure 9: Elution curve (yields versus theoretical amount of respective metal) for Chelex-100 separation according to method (2). HNO_3+MQ wash and NH_3+MQ wash describe the resin regeneration. V-1 to V-7 describe the metal elution with 7 x 1 ml 2 M HNO_3.

Method (2) employs most steps compared to (1) and (3) such as seawater and matrix wash before elution. The elution curve (Figure 9) highlights that all four elements are eluted at step V-4 which describes the fourth ml of elution (total elution of 7 ml). Thus, the elution timing is similar to method (1). In contrast to (1), the separation is performed with pH buffer at a pH of 6.5 (pH = 5 in method (1) and (3)) which is slightly higher and may be responsible for the loss of V during the first washes before elution due to incomplete partitioning onto the resin. Obviously, V is not bound firmly on the resin and can be easily removed. The pH is likely also be the reason why some V (and other metals) are not retained on the resin so well and are found in the seawater after the separation because vanadate speciation highly depends on the pH (Gustafsson, 2019). Some Fe and Ti are also found in the seawater after the Chelex-100 separation, which could be targeted to separate V from these in a first step. Some Cr is eluted further in the resin regeneration which employs the same acid as elution. This indicates that Cr would need more elution acid compared to the used 7 ml.
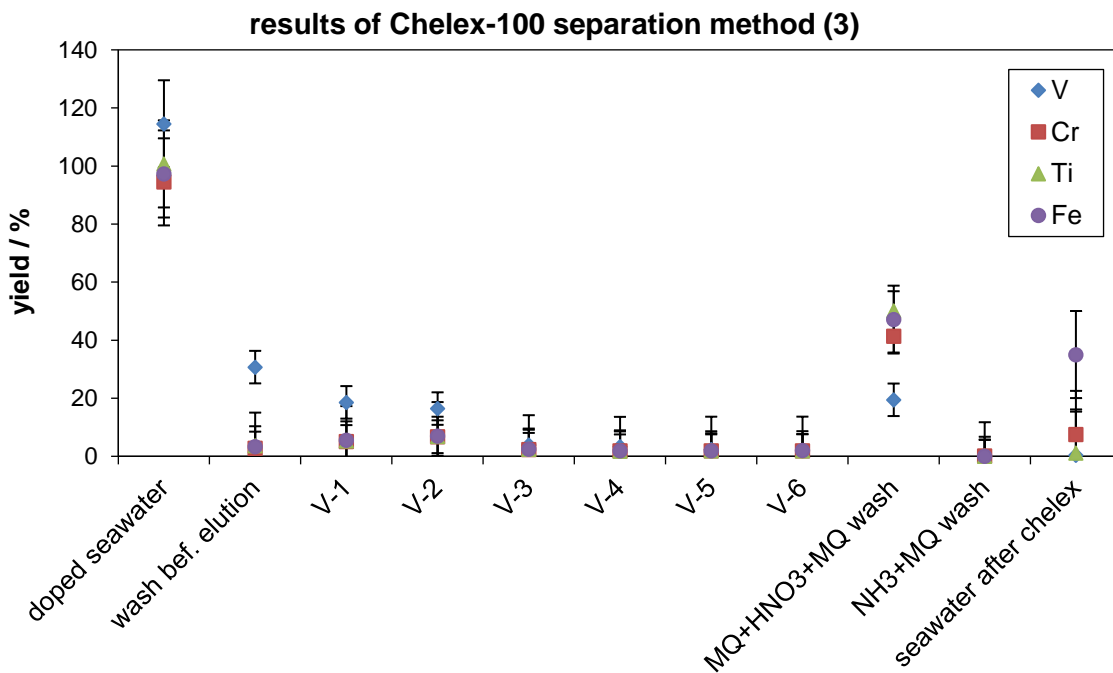
Figure 10: Elution curve (yields versus theoretical amount of respective metal) for Chelex-100 separation according to method (3). MQ+HNO$_3$+MQ wash and NH$_3$+MQ wash describe the resin regeneration. V-1 to V-6 describe the metal elution with 6 x 4 ml 1 M NH$_3$.

In opposite to the other two methods, method (3) elutes the metals with ammonia solution (total elution volume of 24 ml). Before the elution, the resin is washed with 200 ml of MQ water which resulted in a high V loss, probably due to the vast amount of MQ water. Because of the low ionic activity of MQ water, ions will diffuse into it to compensate this disequilibrium. During the elution, a majority of V is eluted, however, part of it only eluted with acid in the later resin

regeneration step. These observations indicate that V was not bound firmly onto the resin and that nitric acids are better eluting reagents than ammonia. Again, it becomes obvious that the Chelex-100 does not bind Fe in the same way as it does V, Ti, and Cr, because Fe was still found in all seawater fractions after the separation.

Due to high internal uncertainties (rest standard deviation up to 15 %) during Element-XR ICP-MS measurements of salt matrix containing solutions (original seawater, doped seawater, seawater after Chelex-100), the calculation of yields needs to be evaluated carefully (Table 11). This problem becomes obvious when comparing the contents of metals theoretically calculated by the weighed portions of doped solution with the measured concentration in synthetic seawater (columns 1 and 3 in table 11). Here, we already observe that the measured V concentration (exemplarily for (1): 54.05 µg) is higher than the theoretically calculated one (exemplarily for (1): 50.68 µg), this applies to all cases even though no V was present in the water before and all weighing, and thus calculations, was done gravimetrically. Nevertheless, the separation of V was successful for method (1) with a V yield of ~98 %. For method (2) the yield is only ~64 % due to the higher pH (as discussed above). Method (3) only yielded ~40 % of V in the final metal fraction and most V was lost to MQ wash prior to elution and to resin regeneration solution due to incomplete elution with ammonia.

In summary, the comparison of the three methods according to Riley and Taylor (1968), Pai et al. (1990), and Abbasse et al. (2002) showed that a combination of HNO_3/HCl is best used as eluting reagent for eluting V off Chelex-100 resin ((1) was giving the highest total yields). Moreover, a pH of 5 shows better retention of V onto the resin than a higher pH. This can be seen in a resin yield of 81 % being lowest in method (2), compared to (1) with 98 % and (3) with 85 %. Also, method (2) lost ~8 % of V into the seawater after Chelex-100 separation which means at the respective pH of 6.5 it was not bound to the resin. The pH can be best kept steady with a pH buffer, while letting the whole sample drop onto the resin (this takes between 1 and 3 days). A buffered pH in the solution provides for steady conditions during sorption of V onto the resin. A wash of major ions utilizing buffer and MQ water improves the purity of the metal fraction. This can be observed between the final composition of the metal fractions (Table 11) of (1) which qualitatively contains much more Ca, Mg, and Na, compared to (2) and (3). Nevertheless, additional washing before elution may result in V loss as seen in method test (2) and (3), which must be considered equally when preparing a purification protocol.

Table 11: Composition (in μg in the first six columns) and yield (in % in the last three columns) of all three tested methods (1), (2), and (3) for Chelex-100 separation. Numbers in brackets are probably inaccurate due to measurement artefacts. Bold numbers belong to V. The 'theo. conc.' column depicts the calculated theoretical composition based on the preparation and doping of synthetic seawater. The 'seawater after Chelex' describes all elements left in the synthetic seawater and thus not bound to the resin. As a counterpart to this, the 'elements bound to resin' column describes the sum of all fractions bound to the resin that were measured in separate fractions afterwards.

element	theo. conc. / μg	original seawater / μg	doped seawater / μg	seawater after Chelex / μg	elements bound to resin / μg	final metal fraction / μg	loss (in seawater after Chelex) / %	yield (bound to resin) / %	yield (in metal fraction) / %
method (1)									
Na	5385046	2529354	2681139	8158362	(4178)	(4151.6)	304.3	0.2	0.15
Mg	651692	657515	654614	592635	13739	13731.4	90.5	2.1	2.10
Ca	210018	219566	213165	129622	4652	4647.4	60.8	2.2	2.18
Ti	51.38	0.00	50.16	0.57	50.47	50.4	1.1	100.6	100.54
V	**50.68**	**0.10**	**54.05**	**0.49**	**53.27**	**53.2**	**0.9**	**98.6**	**98.36**
Cr	51.28	0.00	48.06	1.21	41.02	39.9	2.5	85.4	83.10
Mn	0	32	32	2	29	28.7	5.4	89.2	89.09
Fe	52.00	0.00	33.31	6.76	47.14	47.0	20.3	141.5	141.21
method (2)									
Na	5387178	9203695	8920399	5945868	(5283)	(46.27)	66.7	0.1	0.0005
Mg	649284	673880	653294	588749	18276	128.48	90.1	2.8	0.020
Ca	211160	150357	143710	130288	6562	509.83	90.7	4.6	0.355
Ti	50.31	1.09	55.85	(32.25)	47.25	41.84	57.7	84.6	74.91
V	**50.78**	**0.31**	**59.75**	**4.70**	**48.34**	**38.25**	**7.9**	**80.9**	**64.02**
Cr	51.56	0.31	52.82	1.25	42.55	34.06	2.4	80.6	64.49
Mn	0	37	35	1.43	34.63	32.69	4.1	98.7	93.16
Fe	51.10	7.31	58.11	(23.67)	49.09	44.21	40.7	84.5	76.08
method (3)									
Na	5386465	6450674	6241429	6146336	(14487)	(303.72)	98.5	0.2	0.005
Mg	653936	670933	647721	632840	7635	2.15	97.7	1.2	0.000
Ca	211615	149839	145077	140613	3058	8.57	96.9	2.1	0.006
Ti	53.61	0.89	54.00	0.61	39.76	10.92	1.1	73.6	20.23
V	**52.14**	**0.05**	**59.71**	**0.20**	**50.56**	**24.37**	**0.3**	**84.7**	**40.80**
Cr	51.53	0.34	48.71	3.89	33.18	10.32	8.0	68.1	21.19
Mn	0	36	35	17	13	0.03	49.8	37.2	0.082
Fe	53.40	4.64	51.94	18.72	38.16	11.18	36.0	73.5	21.52

4.3 Purification of separated Chelex-100 fractions of synthetic seawater (1), (2), and (3)

After measuring the separate V cuts for producing elution curves, the cuts were combined into one V fraction. For samples from (1) all respective elution solutions (V-1 to V-5) were combined as one metal fraction. For samples from (2) all eluted fractions (V-1 to V-7) and all three wash solutions prior to elution were combined. For samples from (3) the wash prior to elution, all elution solutions and all resin regeneration solutions were combined. For all three tests, these choices of combining the solutions were done because V loss into several fractions was high. The three resulting metal fractions were purified with a three-step ion chromatography to eliminate the matrix from the V fraction. Therefore, the cleanup purification method from Brüske (2015) was modified according to figure 11. To check the reproducibility of the cleanup procedure itself (Fe, Ti and main cleanup), several pure V standard solutions are processed as well (Alfa Aesar pure solution, Alfa Aesar dissolved V foil, and NIST-3165 solution). Therefore, 50 µl of the standards (2x Alfa sol., 2x Alfa foil, 2x NIST-3165) was weighed into glass beakers, evaporated and taken up for the first step. Also, a blank sample containing only acids was employed.

The first Neptune ICP-MS screening showed that a significant V loss into the main matrix had occurred (see section results 4.1), probably due to left-over salt matrix in the fractions which caused the resin and sample to interact differently. Precise concentration measurements with the Element XR ICP-MS were then performed to quantify the V loss. Also, all matrix fractions from the purification steps were measured for their elemental compositions. To check whether the loss of V was due to the use of synthetic seawater, the Maldive Islands seawater was purified with Chelex-100 and the V and main matrix fractions of (1), (2) and (3) were further processed with Maldive Islands (section 4.4 and 4.5).
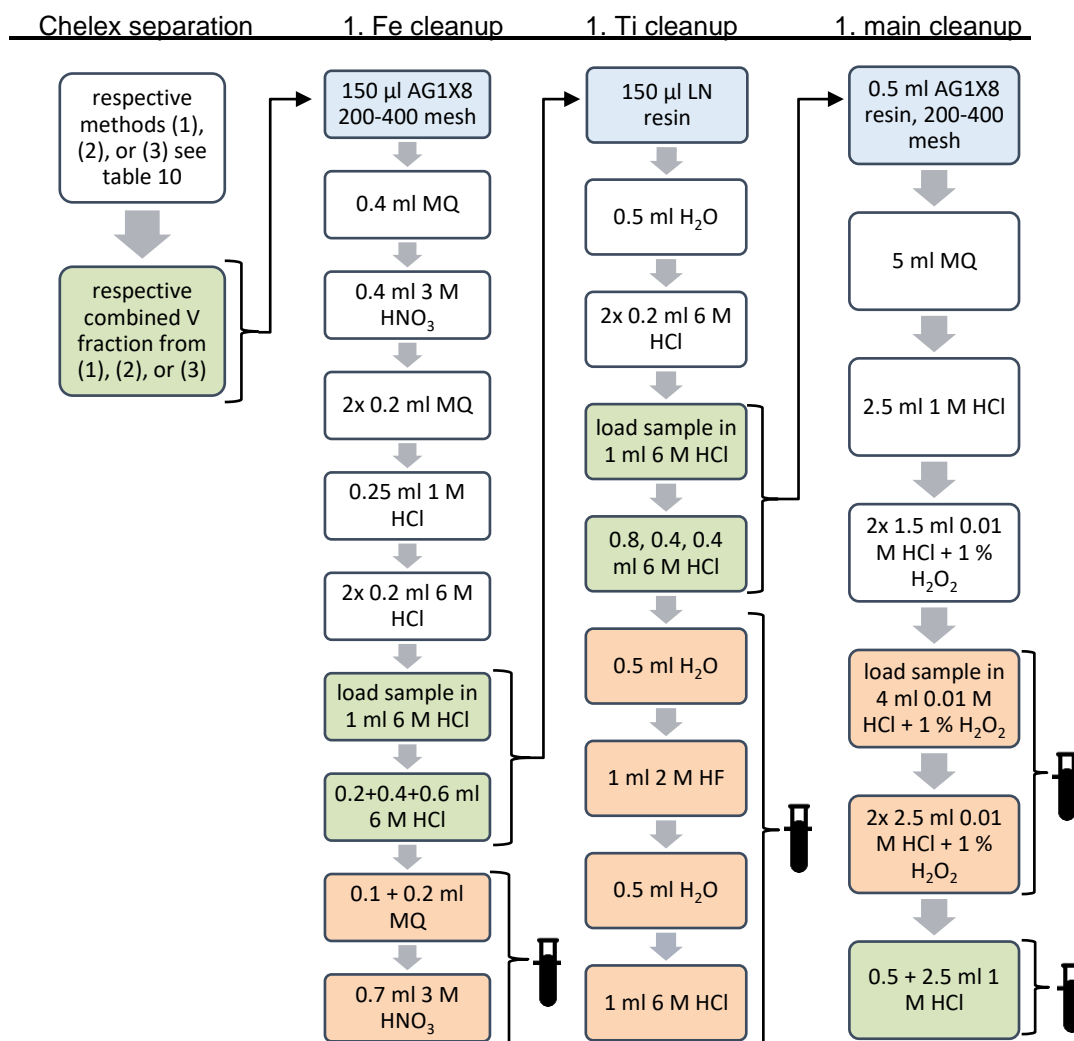
Figure 11: Scheme showing the different purification steps of V from synthetic seawater by ion-chromatography after the respective Chelex-100 separations of (1), (2), and (3). Used resins are highlighted in blue, colorless squares depict resin cleaning prior to sample load, V elution is highlighted in green, and matrix elution in orange. Arrows indicate which fractions were cleaned in the next steps, whereby small test tubes indicate that a fraction is taken out for ICP-MS measurements. Modified from Brüske (2015) and Schuth et al. (2017).

4.4 Application of published method (1) to Maldive Islands sample

The Chelex-100 separation method of (1) (Abbasse et al., 2002) was applied to seawater from the Maldive Islands (2 l) because (1) showed the best V yield in the test with synthetic seawater. The only difference to the described protocol of (1) in table 10, section 4.1 is that the total eluting volume was increased to 17 ml instead of 10 ml. Instead of the two-channel pump that was used before, now a four-channel peristaltic pump (Cole-Parmer four-channel Masterflex L/S pump, model no. 7519-05) was used. After the Chelex-100 separation, the metal fraction was further purified with a Fe, Ti, and main cleanup (Figure 12).
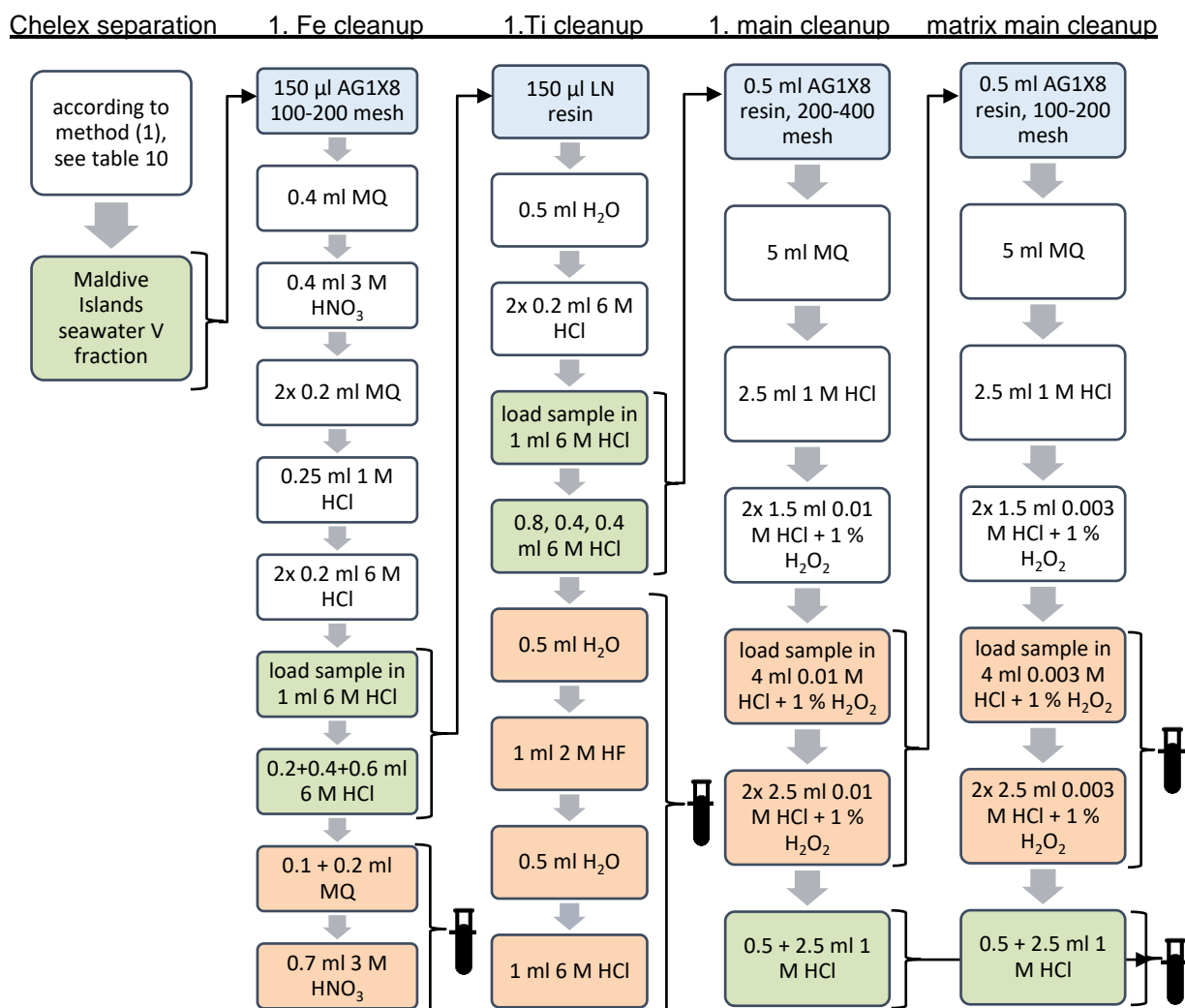
Figure 12: Scheme showing the different purification steps of V from Maldive Islands seawater by ion-chromatography after the Chelex-100 separations according to (1). Used resins are highlighted in blue, colorless squares depict resin cleaning prior to sample load, V elution is highlighted in green, and matrix elution in orange. Arrows indicate which fractions were cleaned in the next steps, whereby small test tubes indicate that a fraction is taken out for ICP-MS measurements. Modified from Brüske (2015) and Schuth et al. (2017).

During the cleanups, an Alfa solution, an Alfa foil, and a NIST-3165 reference standard sample (20 µl from 1000 µg g^{-1} stock) were processed as well. They were volumetrically taken out of their stock solutions, dried down and taken up into 6 M HCl for the Fe cleanup. The cleanup procedure resulted in a Fe, Ti, and main matrix as well as a V fraction, respectively. Concentration measurements with Element XR ICP-MS showed that V loss into the main matrix was high and that the V fractions were not pure enough for isotope ratio measurements. The matrix was purified in a second main cleanup which resulted in another V fraction of the matrix and a matrix of the matrix. Here, another Alfa solution reference standard was processed (20 µl from 1000 µg g^{-1} stock). The resulting V fractions were combined and as one fraction and again qualitatively screened with the Neptune ICP-MS. Again, it showed significant

V loss as well as Ti and Cr contamination. A very unstable signal hinted at residual seawater matrix in the solution, which should be eliminated in a second Chelex-100 cleanup.

4.5 Final Chelex-100 and further cleanup steps of Maldive Islands and synthetic (1), (2), and (3) seawater samples

A combined cleanup method was created (Figure 13) that adopted the advantages of the different tested methods (Riley and Taylor, 1968; Pai et al., 1990; Abbasse et al., 2002).
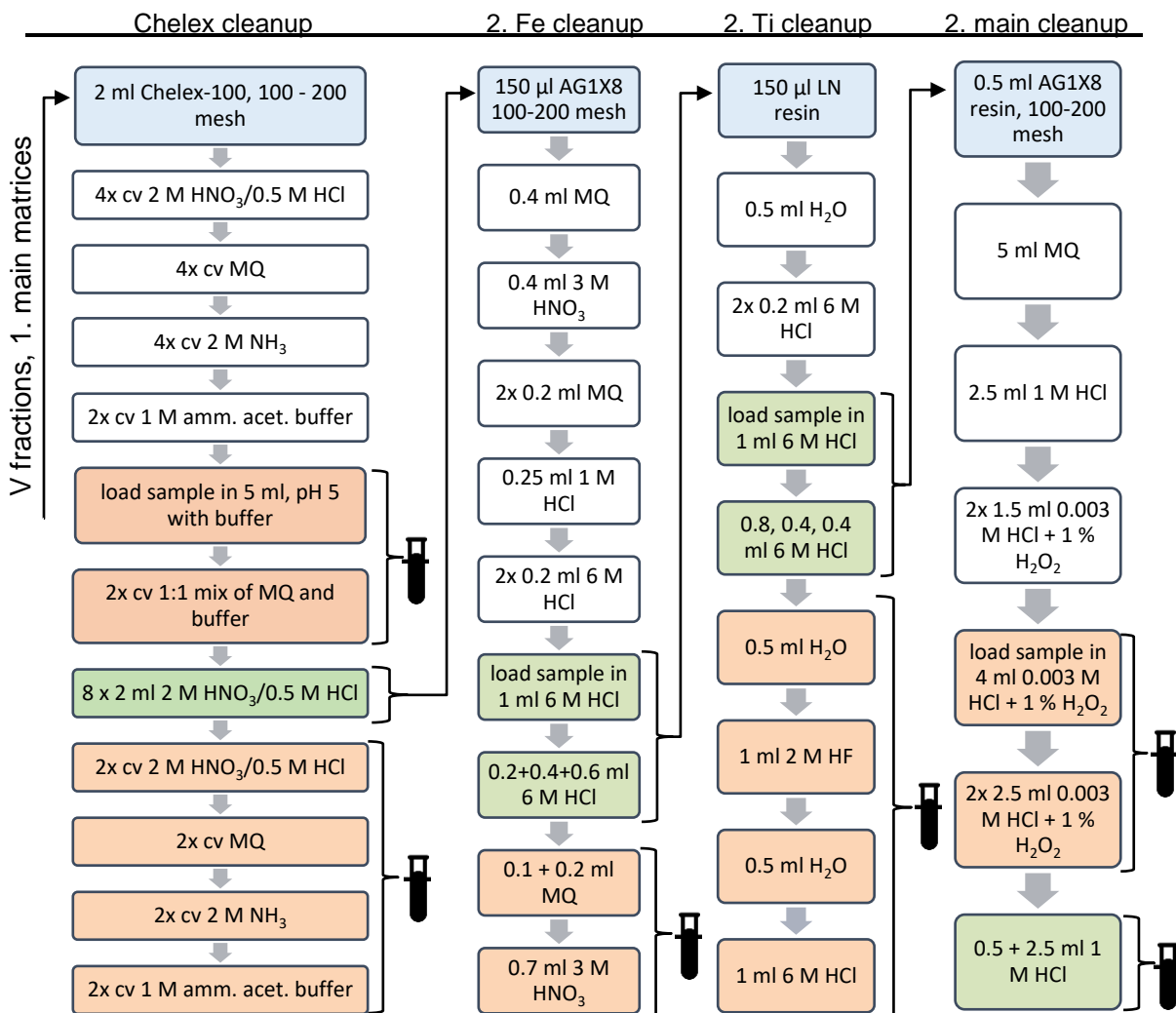
Figure 13: Scheme showing the different purification steps of V fractions and 1. main matrices (scheme follows figs. 6 and 9) from Maldive Islands seawater and synthetic samples according to (1), (2), and (3) with Chelex-100 cleanup and following ion-chromatography (second cleanup round). Used resins are highlighted in blue, colorless squares depict resin cleaning prior to sample load, V elution is highlighted in green, and matrix elution in orange. Arrows indicate which fractions were cleaned in the next steps, whereby small test tubes indicate that a fraction is taken out for ICP-MS measurements. Modified from Brüske (2015) and Schuth et al. (2017).

This cleanup protocol was applied to the V and main matrix fractions of (1), (2), and (3) and Maldive Islands, as well as one Alfa solution reference material (50 µg from 1000 µg g^{-1} stock, dried down and taken up in MQ for the Chelex-100 cleanup). In addition, a blank, containing only MQ water, was processed in the same manner within the Chelex-100 cleanup and all following steps. Finally, all Chelex-100 cleaned fractions of Maldive and synthetic seawater (1), (2), and (3) were again purified with a Fe, Ti and main cleanup (according to figure 13). All fractions were measured again concerning their elemental concentrations.

4.6 Results and discussion of the applied methods of synthetic seawater (1), (2), and (3) and processed reference materials

4.6.1 Vanadium yield for synthetic seawater (1), (2), and (3)

The general distribution of V yields between all fractions from Chelex-100 cleanup and following ion-exchange of all three samples are very similar which indicates that the procedure itself is quite reproducible (Figure 14). All three tests showed that Fe is quantitatively separated during the first Fe cleanup and all other fractions are devoid of Fe after this step (supplementary table S 8). Plus, no V was lost in this step. Strikingly, all samples (first V fractions and first main matrices) showed slight V loss within the second Fe cleanups of (supplementary table S 8). This shows that a second Fe cleanup may be a disadvantage, because no Fe was left to be separated and the V loss could have been prevented. Also, the Ti cleanup successfully separated all Ti from all three first V fractions. This also indicates that the second Ti cleanups of V fraction and main matrix may not have been necessary, however, did also not cause V loss. All first main matrices separated Cr to a high portion (supplementary table S 8), however, all matrices also did not separate V successful and showed high V loss into the matrix fraction which either resulted from remaining seawater matrix ions (alkali and earth alkali) or pH variability. The high V loss resulted in very low yields of 15 % for (1), 11 % for (2), and 18 % for (3) in the first V fractions (Figure 14). Due to this, an additional separation of V from the first main matrix was necessary. As a consequence, in the second main cleanup the acid mixture of 0.003 M HCl + 1 % H$_2$O$_2$ was used.

The first V fraction of (1) shows a total V yield into the second V fraction of 48 % (Figure 14) and the only fraction that resulted in significant V loss of 24 % was the alkali matrix, which describes the alkali wash and sample solution after loading the sample. This shows that the Chelex-100 cleanup bears a risk of losing V. On the other hand, the cleanup of the first V fraction of (2) and (3) was successful. This indicates that the Chelex-100 cleanup, like the Chelex-100 separation, highly depends on the individual sample matrix and may cause high V loss.
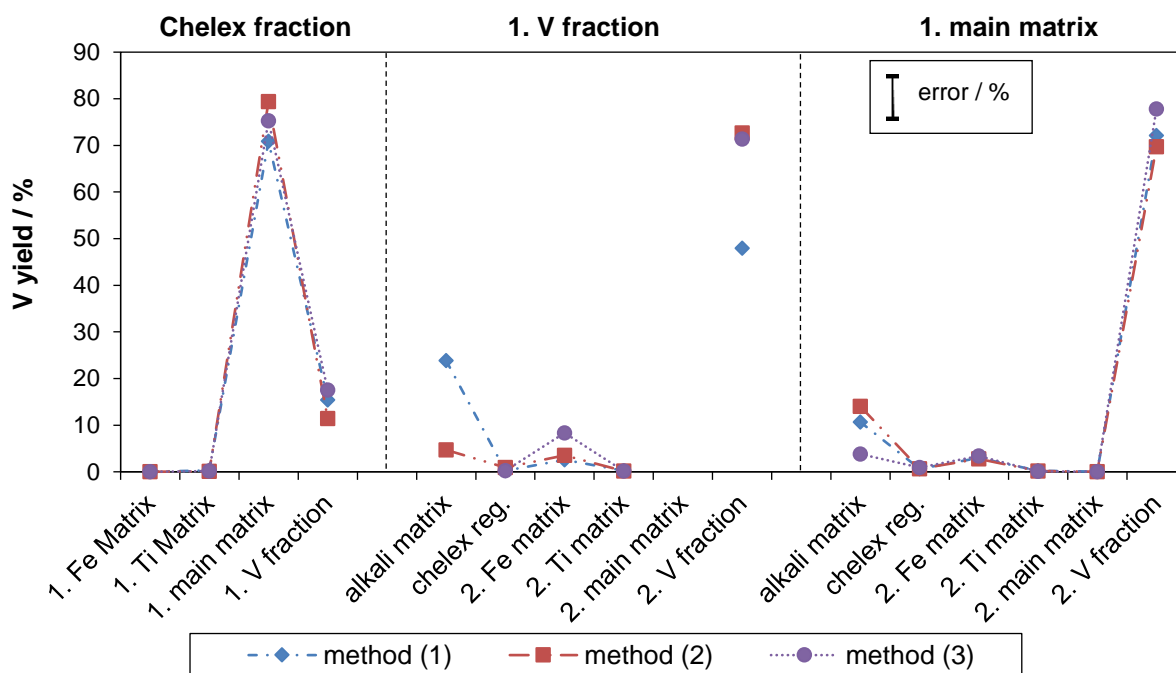
Figure 14: Vanadium yield for all fractions during purification of Chelex-100 fractions (left-hand side), and following cleanup of the first V fraction (middle section) and first main matrix (right-hand section) of synthetic seawater according to methods (1) (diamonds), (2) (squares), and (3) (circles).

It also attracts attention that the sums of all yields for V during the cleanup of the first V fraction does not match 100 %. This can either be explained by high errors of ~20 % on the concentration data or by missing V that was retained on one of the used resins and was discarded after the cleanup. However, both explanations are rather unlikely, first because pure solutions were measured with relatively low errors were measured and secondly because the Chelex-100 resin, for example, was washed after using and the resin regeneration fractions only showed minor V signals (column 'chelex reg.' in left-hand section in supplementary table S 8). The second cleanup of the first main matrix was successful in regard of V and Cr separation in all three tests. Only minor Cr was found in the second V fraction and the main Cr portion was found in the main matrix of all three tests. Very similar to the cleanup procedure of the first V fraction the wash with a buffer/MQ mixture after loading the samples (alkali matrix) was mainly responsible for a V loss. In summary, the Chelex-100 separation tests have shown that they can be well applied for the separation of V from a seawater matrix. From all three tested methods, the advantages were adopted into a new method that was tested with natural seawater in the next step because a natural matrix will likely behave different compared to a synthetic one.

4.6.2 Results of processed reference materials

The pure reference materials Alfa solution, Alfa foil, and a NIST-3165 solution (named I and II, respectively, each ~50 µl of a 100 µg g^{-1} stock) were purified in the first Fe, Ti, and main cleanup along with the Chelex-100 fractions of (1), (2), and (3). All six standards showed a successful procedure with V yields of 96 % to 97 % with respect to the total sum of found V (Figure 15).

Figure 15: Vanadium distribution in Fe, Ti, and main matrix and V fraction for reference materials Alfa solution, Alfa foil, and Nist solution processed together with synthetic seawater samples (1), (2), and (3).

The only other fraction, that caused a significant V loss, was the Fe matrix, which contained the missing 3 – 4 % of V. In all diluted fractions, no Cr could be measured. The only measured Ti was found in the Ti matrix, main matrix and V fraction. The resulting blank from the Ti matrix showed increased values for Fe indicative of a resin contamination of the used LN resin. Hence, any very low contamination of Fe, Cr or Ti in the V fraction may also be the result of a blank, which in total is still very low and does not interfere with V isotope measurements of the V fractions (as seen in very high ^{51}V/^{53}Cr and ^{51}V/^{49}Ti ratios in table 12).

The processed reference materials were measured with the Neptune ICP-MS and the results showed that a few single measurements were not successful likely due to high internal drift. Nevertheless, enough measurements were successful and the δ^{51}V values agree well with previously published and measured ones (Table 12). During the sequence an unprocessed, pure Nist solution and a previously processed XJT-6 were measured as well (see section 2.6). None of the tested reference materials was isotopically fractionated during the cleanup procedures.

Table 12: Results of V isotope measurements of reference materials Nist I, II, Alfa sol. I, II, and Alfa foil I, II., n = number of replicate measurements.

	$^{51}V/^{53}Cr$	$^{51}V/^{49}Ti$	$\delta^{51}V_{Alfa}$ / ‰	$\delta^{51}V$ 2 s.d. / ‰	n
Nist-3165	4710628	84465	0.47	0.31	4
XJT-6	6528815	6559161	-0.52	0.08	3
Nist I	345280	517731	0.52	0.04	2
Nist II	488444	334216	0.50	0.21	2
Alfa sol. I	593443	705425	0.00	0.06	2
Alfa sol. II	520416	480091	-0.02	0.06	3
Alfa foil I	924236	649499	1.39	0.25	2
Alfa foil II	589438	195739	1.16	0.08	3

4.7 Results and discussion of the applied methods of Maldive Islands seawater and of processed reference materials

4.7.1 Vanadium yield during the separation from Maldive Islands seawater

To begin with, Maldive Islands seawater was measured with the Element XR ICP-MS to analyze its starting composition, especially V content and only V contents and yield in all different processed fractions of Maldive Islands will be discussed in this section. During the different sessions (two days with four different replicate measurements the original seawater was measured with 1.86 ng g^{-1} (n = 4) which is in the range of V contents in open-ocean seawater (Jeandel et al., 1987; Holland et al., 2004; Poehle et al., 2015). Still, internal standard deviations of ^{51}V during the four measurements (as well as seawater after Chelex) were up 15 %, indicating that total errors on these values should not be neglected (additional uncertainties from pipette or balance use).

Relative to the measured V contents in Maldive seawater the V yield in the final V fraction is ~36 % (Figure 16). This is similar to the portion of V which was not successfully bound to the Chelex-100 resin (~41 %) and thus stayed in the seawater after the separation, indicating non-quantitative removal from the seawater. The rest of the V is distributed between all matrix fractions, with the V fraction of the main matrix comprising the biggest portion (~29 %). All other matrix fractions only contain minor V, indicating the first Chelex-100 separation and the first main cleanup caused the highest V loss (Figure 16). Interestingly, percentage distributions of yields almost never meet 100 %, but rather vary between ~80 % and ~120 %, maybe indicative of high measurement uncertainties or non-quantitative removal of V from the resin. Both the first Fe and Ti cleanup were successful. However, the first main cleanup caused a very high V loss with only 24 % of V in the first V fraction. The additional main cleanup of the first main matrix again showed only a partly successful separation with the main part of V being found in the main matrix (52 %) and only minor in the V fraction (30 %).
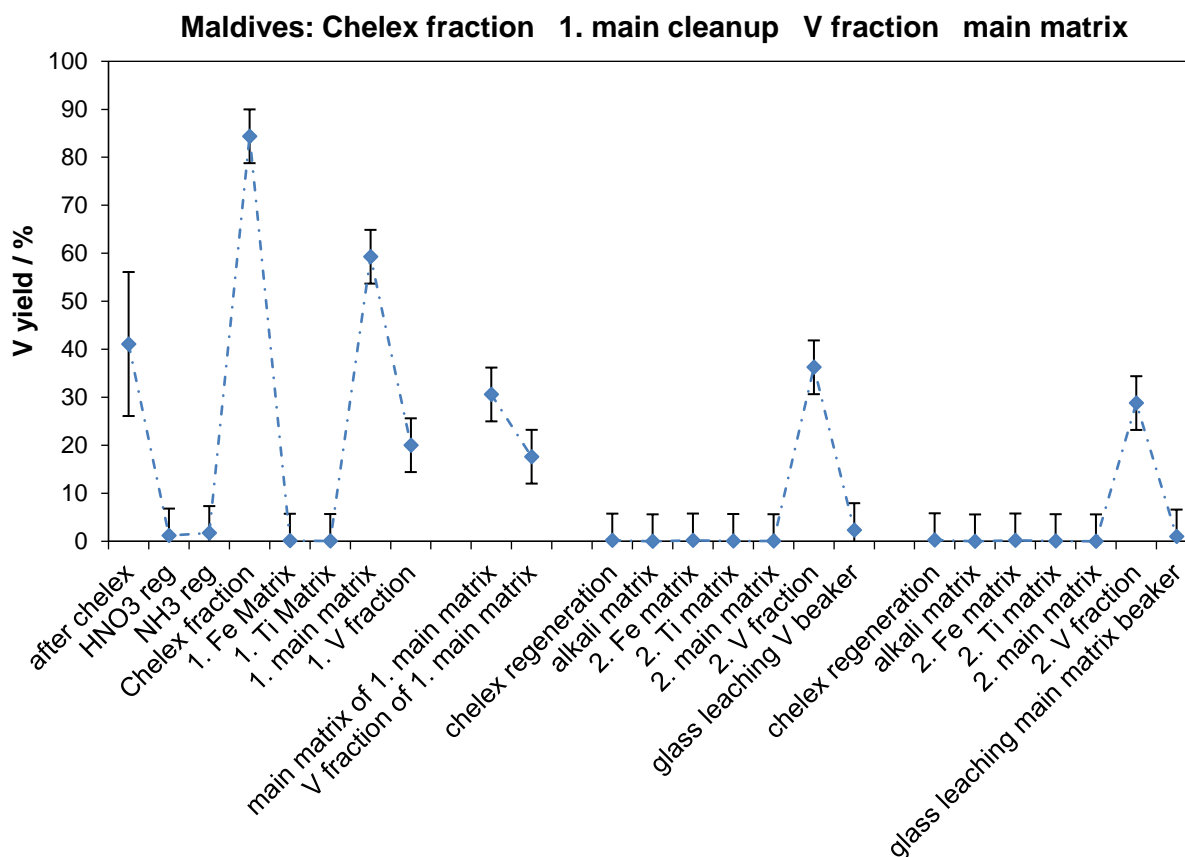
Figure 16: Vanadium yield (calculated relative to starting composition) of Maldive Islands seawater into all different fractions during Chelex-100 separation and cleanup (left-hand side), second main cleanup (second part from left hand-side), Chelex-100 cleanup and other cleanups of the first V fraction (second from right-hand side), and Chelex-100 cleanup and other cleanups of the first main matrix (right-hand side).

During the Chelex-100 fraction cleanup and main cleanup of the first main matrix, a procedure blank was processed as well that accumulated V from all fractions in the same manner as a sample would. This blank accounted for a total V content of 0.41 ng (from both procedures together) which is negligible compared to the amount of V in the combined V fraction (1402 ng). Also, the blank is low enough compared to the first V fraction (746 ng) and V in the V fraction of the first main matrix (656 ng). Another procedure blank was processed during the Chelex-100, Fe, Ti, and main cleanup of the combined V fraction and main matrix cleanup. Compared to the first blank, this blank also included any possible contamination from the Chelex-100 resin, and in total accumulated 0.46 ng. Compared to the V amount in the second V fraction (1350 ng) and V from the main matrix (1072 ng) the blank V content is only minor. To conclude, blank contamination from resins or acids can be neglected in the procedure of V separation from Maldive Islands seawater.

In general, the Chelex-100, Fe, Ti, and main cleanup of the combined V fraction and the main matrix were successful with a V yield in those fractions of 96 % and 94 %, respectively. Slight

V amounts (< 1 %) were found in the Chelex-100 regeneration acids and the second Fe matrices, very similar for both procedures. It strikes that the main cleanups both were successful and did not cause V loss. In this step, the BioRad anion AG1X8 resin in size 200 – 400 mesh was used in combination with the 0.003 M HCl/1 % H_2O_2 mixture and in combination with the already extensively cleaned fraction are responsible for the successful separation. This indicates that the main separation in general works very well.

Finally, it was found that using glass beakers has a big disadvantage as quantitative removal of a solution from them is complicated. Due to surface tension of the glass, some liquid sample will always be left in the beaker if it is not rinsed with a following solution. For the 2. V fractions during Maldive Islands cleanups, both glass beakers were left to be leached with 4 ml of 3 M HNO_3 overnight, thus covering the whole beaker bottom. These solutions were measured for their elemental compositions and showed 6 % V for the second V fraction of the combined V fraction and 3 % of V in the second V fraction of the main matrix. These numbers are significantly higher than blank compositions and a V loss into glass beakers, when not rinsing them repeatedly, must be always considered.

Due to the low V amount in the final fraction, to low V/Cr and V/Ti ratios and high V loss into several fractions, the Maldive Islands seawater was not successfully measured for its V isotope composition with the Neptune ICP-MS. Hence, for evaluating systematic methodical errors and the possible application of the method for V isotope measurements, a sample batch from the North Sea was processed repeatedly.

4.7.2 Processing reference materials with natural seawater of Maldive Islands and synthetic samples (1), (2), and (3)

During the procedure of Maldive Islands seawater, an Alfa solution (a), an Alfa foil, and a Nist-3165 solution reference material were processed in the first Fe, Ti, and main cleanup after the Chelex-100 separation. Also, during the second cleanup of the first main matrix, another Alfa solution (b) standard was processed. The results of these reference materials are shown in figure 17. During all steps, V was recovered successfully in the V fraction with yields of 93 %, 93 %, 92 %, and 100 % for Nist, Alfa sol. a, Alfa foil and Alfa sol. b, respectively. Any V loss within Nist, Alfa sol. a, and Alfa foil was caused by the Fe cleanup, that contained the remaining 7 – 8 % of V (see supplementary table S 12 for raw data). The measured absolute amounts of Cr, Ti, and Fe were all below the blank levels and thus are neglected. During a Neptune Plus session, this Alfa sol. b was measured and yielded a $\delta^{51}V_{Alfa}$ = -0.02 ± 0.00 ‰ (n = 2) versus a pure Alfa-Aesar standard solution, hence, indicating no isotope fractionation during this main cleanup.
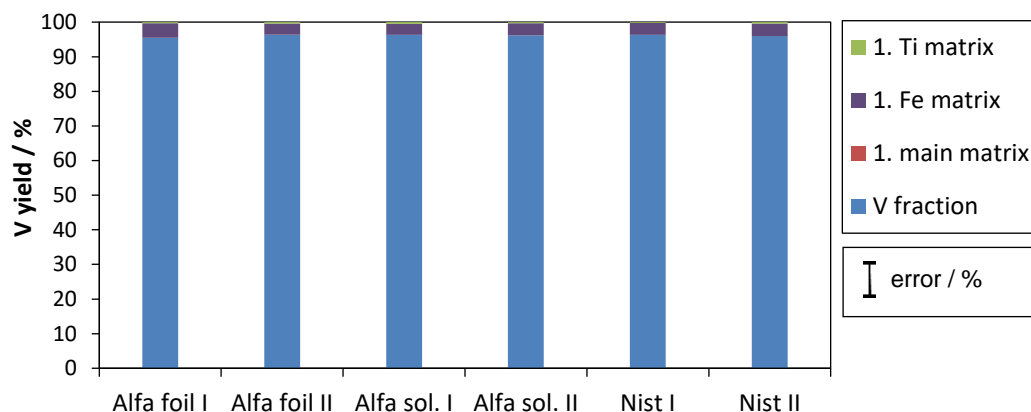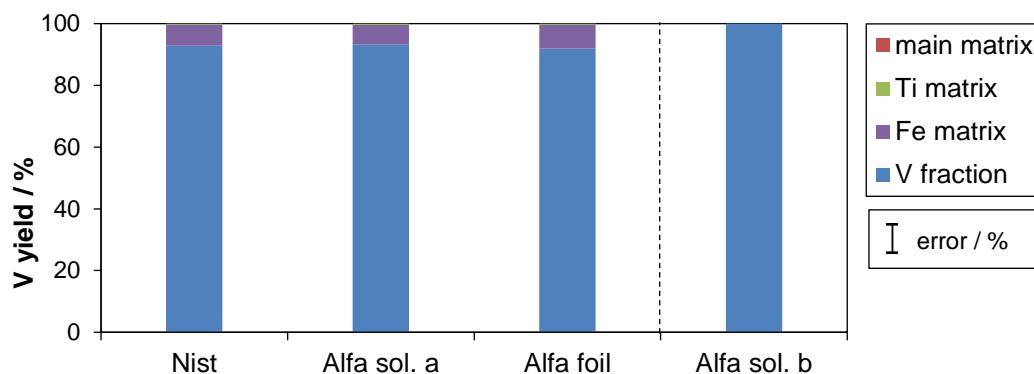
Figure 17: Vanadium yield in Fe, Ti, and main matrix and V fraction for reference materials Alfa solution a, Alfa foil, and Nist solution processed together with Maldive Islands (left-hand side of plot). Vanadium distribution between V fraction and main matrix of reference material Alfa solution b processed in second main cleanup of Maldive Islands seawater (right hand side of plot).

During the Chelex-100, Fe, Ti and main cleanup steps of synthetic seawater (1), (2), and (3), and natural Maldive Islands seawater, an Alfa solution reference material (50 µg from a 100 µg g^{-1} stock) was processed as well. Figure 18 shows the distribution of V between the different resulting fractions. The Alfa solution was gravimetrically prepared from a certified stock solution and in comparison, to this value, the sum of all found V yields 100 %. Relative to the weighed amount of V, the V fraction only contained 71 %, and most of lost V was found in the alkali matrix (sample loading and MQ/buffer wash solutions) and Fe matrix with 20 % and 8 %, respectively (Supplementary table S 13). Elution was quantitative as no V was found in the resin regeneration solutions. The alkali matrix describes the fraction of V that was not bound firmly onto the resin, even though pH was kept steady with a buffer and no matrix was around to disturb the resin-V partitioning equilibrium. This indicates that the conditions for V sorption onto the resin are not optimal and e.g. pH, acid strength or resin volume may be optimized.

Similar to the previous tests of synthetic seawater (1), (2), and (3) (Figure 14), the Fe matrix contained a significant amount of V, when almost no Fe was around (e.g. in the second Fe cleanup) whereas in the first Fe cleanup of (1), (2), and (3) (Figure 14) almost no V was lost into the Fe matrix, while almost all Fe was separated successfully. The reason for this behavior may lay in the Fe/V ratio during the Fe cleanup separation with BioRad AG1X8 anion resin (all these cleanups used the resin in size 100 – 200 mesh). A high Fe/V ratio may result in a successful Fe cleanup whereas a low Fe/V ratio may result in V loss. This may be due to the fact that without Fe in the solution to predominantly interact with the resin, more functional surface groups of the resin are available to interact with V. In contrast, no V was lost into the Fe matrix in the case of natural Maldive Islands seawater (Figure 15) which also indicates that the other remaining matrix elements may play a significant role in V-resin interaction.
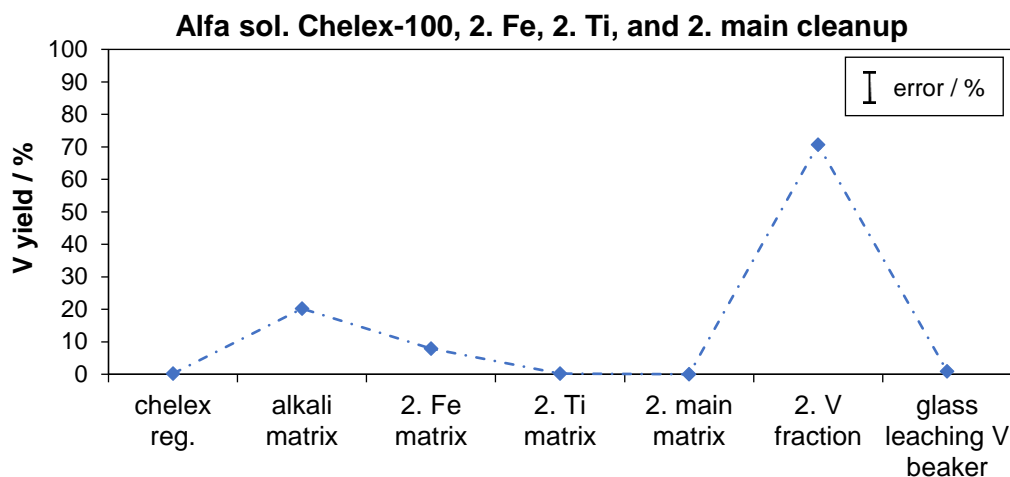
Figure 18: Distribution of V of Alfa sol. reference material into all different fractions during Chelex-100, 2. Fe, 2. Ti, and 2. main cleanup (together with synthetic (1), (2), and (3) and natural Maldive seawater).

Finally, the glass beaker was leached in the same manner as described in section 4.7.1. This showed that only 1 % of V was left in the beaker. Compared to the loss of 3 – 6 % from the beakers of the final V fractions of Maldive Islands seawater, this is negligible, however, also highlights that it is crucial to pipette samples out of glass beakers as careful and complete as possible. The high variability shows that V can be easily lost and rinsing beakers out with another solution should be always done.

5. Separation of V from North Sea seawater with the new Chelex-100 method

5.1 Final Chelex-100 separation protocol and its application

A new Chelex-100 separation protocol was set up and further evaluated by applying it to North Sea seawater (Figure 19) of which a stock of 20 l was subsampled into 2 l portions and processed in 5 different runs named North Sea test 1 – 5 (Table 13). Due to the limitation of the four-channel peristaltic pump (Cole-Parmer 4-channel Masterflex L/S pump, model no. 7519-05), either three samples and a blank or four samples were processed at the same time (Figure 20 for set-up). The blank always contained 2 l of MQ water which was acidified and processed in the same manner as samples. After separating metals from seawater, four seawater matrices were gravimetrically doped with an Alfa Aesar pure V standard solution (II, IV, V, VI) to yield ~5 ng g^{-1} V. The seawater matrix from II was cleaned with Chelex-100 twice (in North Sea tests 1 and 2) because after the first separation there was still V left in the matrix which needed to be separated before doping the matrix. Another three seawater matrices were doped with the pure Nist-3165 (VI, VII, VIII) to yield ~5 ng g^{-1} V. The seawater matrix from VI was doped once with Alfa Aesar, then purified with the Chelex-100 separation and then once doped with a NIST-3165 standard solution to check cross-contamination. The doped samples were processed through the whole procedure as well to test robustness and reliability of the method and their weighed amounts were used as starting compositions to calculate yields.

Table 13: Overview of North Sea tests seawater samples and respective applied methods.

Sample set name	Sample names	Chelex separation	Chelex cleanup	Fe + Ti + main cleanup	Ti + main cleanup
North Sea test 1	North Sea natural I, II, III, blank	X	X	X	X
North Sea test 2	North Sea II after chelex, natural IV + V, blank	X		X	X
North Sea test 3	North Sea doped matrix of II + V, natural VI, blank	X		X	X
North Sea test 4	North Sea doped matrix of IV + VI, natural VII + VIII	X		X	X
North Sea test 5	North Sea doped matrix of VI, VII + VIII, natural IX	X			XX

Chelex-100 resin was taken up into 1 M ammonium acetate buffer with a pH = 5 and put into polypropylene columns thus yielding a resin bed of 5 ml Chelex-100 resin in ammonium-form. The buffer solution was always cleaned on Chelex-100 resin as described in section 4.1.

Seawater samples (each 2 l) were prepared to have a pH = 5 by adding 35 – 50 ml 1 M ammonium acetate buffer solution and/or concentrated NH$_3$ and concentrated HNO$_3$. The sample matrix (called 'seawater after Chelex') is collected in 2 l PP-bottles and is acidified to pH = 1 with concentrated HCl afterwards (except North Sea test 1 was not acidified). The 'alkali matrix' and 'Chelex fractions' (containing any eluted metals) are collected into glass beakers of 50 ml or 100 ml volume, respectively. All 'resin regeneration' fractions are collected into 90 ml Savillex teflon beakers. All fractions are measured concerning their V contents to check for remaining sample V and to assure a clean resin to be re-used.
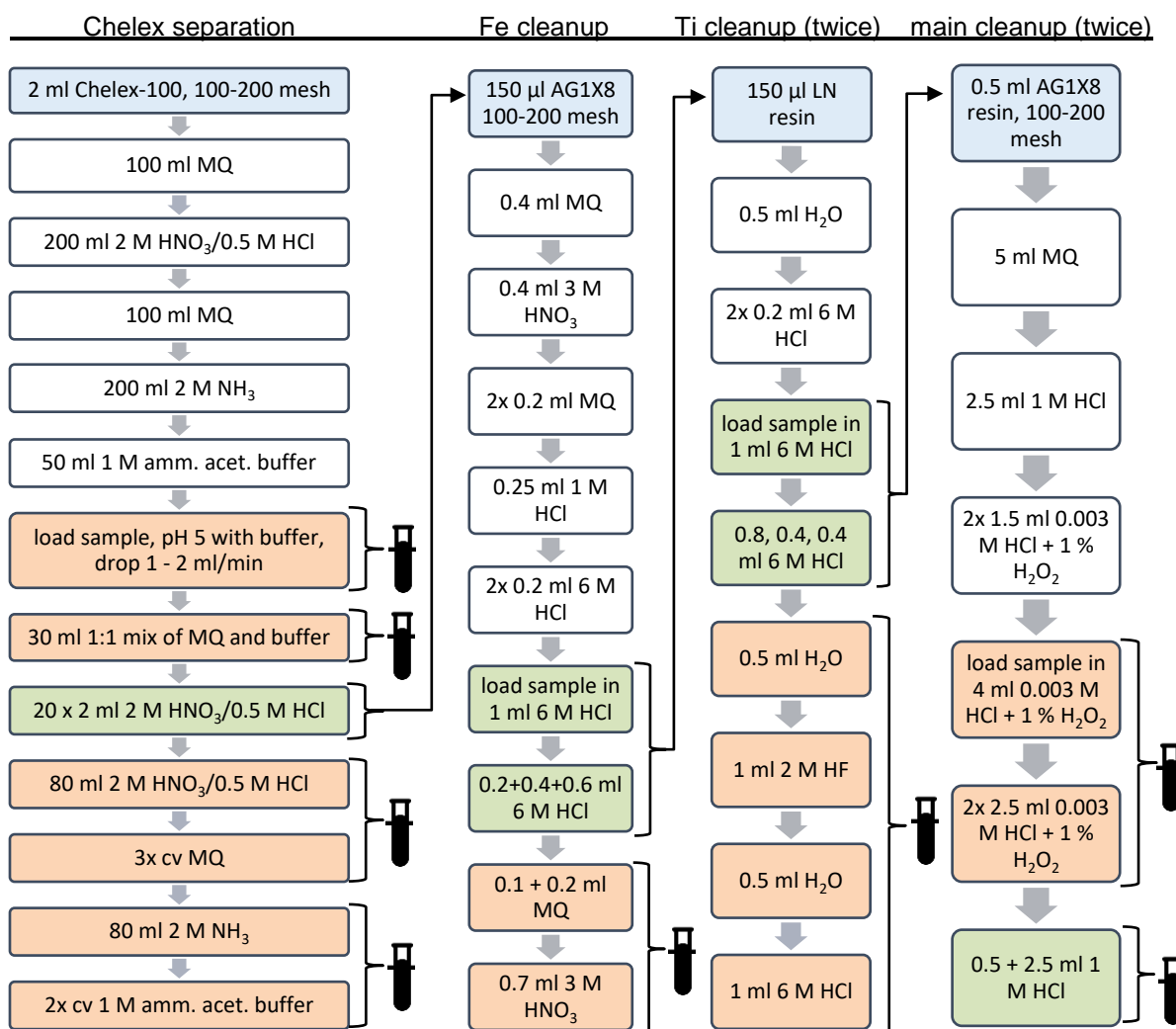
Figure 19: Scheme showing the Chelex-100 separation and following cleanup steps for North Sea samples (check table 13 for detailed information about applied steps in respective test runs). Used resins are highlighted in blue, colorless squares depict resin cleaning prior to sample load, V elution is highlighted in green, and matrix elution in orange. Arrows indicate which fractions were cleaned in the next steps, whereby small test tubes indicate that a fraction is taken out for ICP-MS measurements. Modified from Brüske (2015) and Schuth et al. (2017).
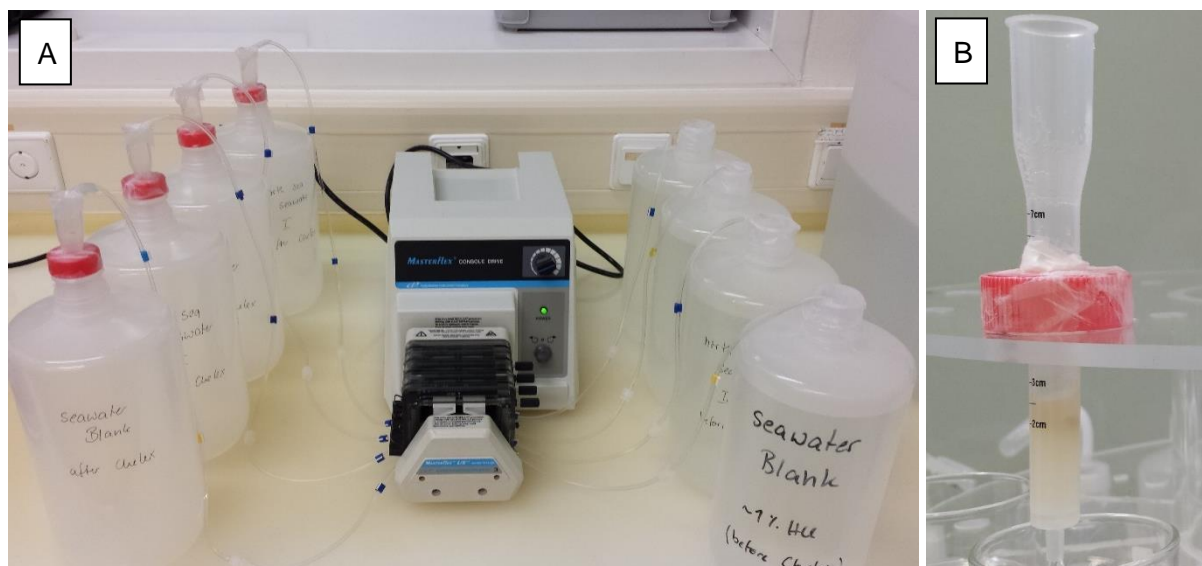
Figure 20: In A: the salt matrix is separated from seawater samples. Right-hand side bottles contain the sample which is pumped through tygon tubing into the columns that sit on top of the cleaned bottles on the left-hand side. In B: a zoom-in of a column is shown, the darker coloring of upper part of the resin is caused by the constrained metals from the seawater sample.
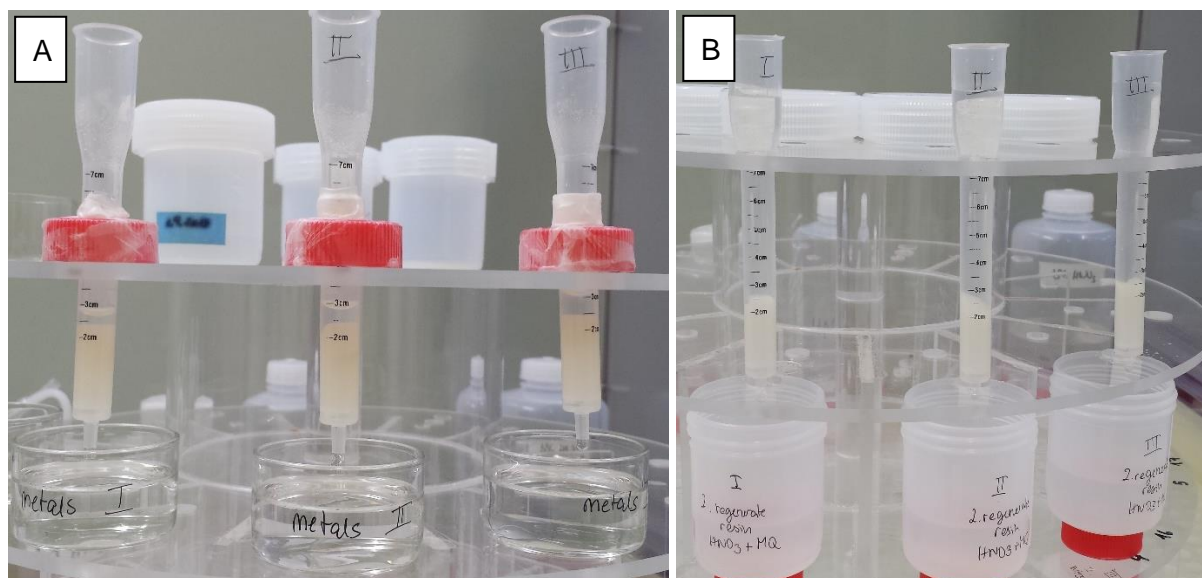
Figure 21: North Sea test 1 exemplarily showing the Chelex-100 salt separation. In A: the metals are eluted from the resin, in B: the resin is washed and regenerated, and the light color indicates its original condition.

After separation of V from North Sea seawater, only North Sea test 1 samples (I, II, III) were purified with a second Chelex-100 cleanup similar to Maldive Islands (protocol in figure 13). The applied respective Fe, Ti, and main cleanup protocols are shown in figure 19 and table 13, and shown as photographs in figure 22. In North Sea test 1, the used resin for the main cleanup was 200 – 400 mesh size, however, since Norths Sea test 2 the resin size 100 – 200

mesh was used (as shown in figure 19). The tests during the Neptune session eventually resulted in the decision for a second cleanup round of all samples that were processed so far.

Several samples from North Sea tests 1 – 4 were checked with the Neptune ICP-MS for purity and were found to need another cleanup of Ti and Cr. For this, all samples were refilled and evaporated which was likely not quantitative due to sorption to glass beakers. Plus, any additional evaporation step may cause spilling and thus loss of solution. Samples and doped fractions from North Sea test 1 – 4 (II, III, IV, V, VI, VII, VIII, doped IV, doped V, doped VI) were purified with a Ti and main cleanup, again. Samples from North Sea tests 5 were purified directly twice with the main and Ti cleanups (Table 13) because Fe was found to be only around in traces. Not doing the Fe cleanup saves another step and thus avoids further V loss. Hence, the main cleanup was processed first to get rid of most major ions. Finally, all natural and doped North Sea samples were measured for their V isotope composition.
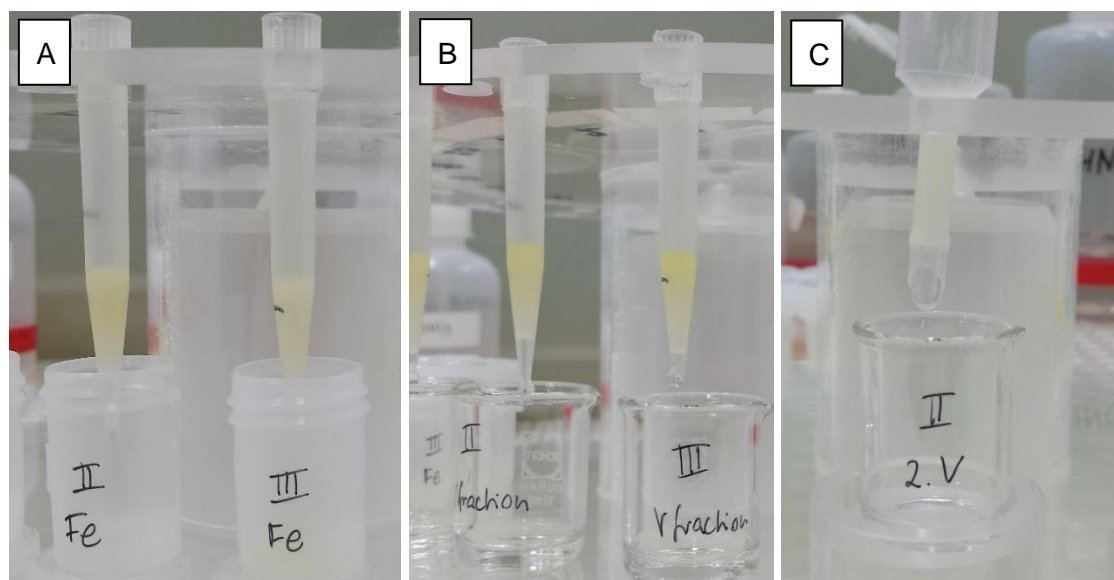
Figure 22: In A: the Fe cleanup (showing collection of the Fe matrix), in B: the Ti cleanup (showing collection of the V fraction), and in C: the main cleanup (showing collection of the V fraction) is pictured (exemplarily shown with seawater samples from North Sea test 1).

5.2 Results and column yield during Chelex-100 purification and clean-up of natural North Sea seawater and doped seawater matrix samples

To have a starting composition of our original seawater of the North Sea, it was measured 10 times with the Element XR ICP-MS, however, only one of those measurements gave realistic results. Mainly, this was due to the high salt matrix compared to very low V concentration in seawater which causes several problems during the measurements (see section 7.1). The only successful measurement of V in North Sea seawater was done with Jet Ni sampler, Ni H

skimmer, a cyclonic spraychamber and a glass nebulizer. Also, during this session the V background was fairly low (< 250 cps in medium resolution). The measured V concentration of North Sea seawater was 2 µg l^{-1} which translates into 39 nmol kg^{-1}. This value is in the range for open ocean seawater concentrations of V (Jeandel et al., 1987; Holland et al., 2004) and previously measured V in the North Sea close by the island Spiekeroog (Kowalski et al., 2009). They determined the V concentrations in November to be 32 nmol kg^{-1} ± 4 nmol kg^{-1} which is only slightly lower than our determined value (our seawater was sampled in december). Hence, our values may be slightly overestimating the V concentration in the North Sea seawater samples. In addition, the absolute amount of the samples was not weighed precisely and thus, back-calculation to total absolute amounts of elements in ~2 l samples can only be estimated. Nevertheless, for each 2 l of North Sea seawater the measured V concentration can be calculated to a total V amount of ~4000 ng which is now used as a starting V composition for the following Chelex-100 tests. The estimated error for this value should not be less than 15 % (± 600 ng or 6 nmol kg^{-1}) to account for differences to published values, weighing and dilution uncertainties, internal errors and deviation from reference materials during ICP-MS concentration measurements.

The results for North Sea test 1 are shown in figure 23. Sample North Sea I was used up in the first Neptune session and thus, did not participate in the second cleanup round. Within the Chelex-100 separation V was mainly separated into the respective Chelex fractions with ~70 %, ~75 %, and ~73 % V yield. However, some V was also left in the seawater after the separation. No V was found in the alkali wash, nor during the resin regeneration, indicative of quantitative elution of adsorbed V. In the second Chelex-100 cleanup, another portion of V was lost and V yield, relative to the starting amount, was only ~46 %, ~48 %, and ~48 % for I, II, and III, respectively. Again, only minor (< 1 %) of V was found in the second alkali wash and resin regeneration solutions (Figure 23). The lost V can be either explained by high measurement errors or V loss due to left-over V in glass beakers, adsorbed onto the starting plastic bottle or due to volumetric dilution and back-calculation uncertainties. The first clean-up round (Fe, Ti, and main cleanup) of samples I, II, and III was successful and no further V was lost. For some reason, the yields in the second final V fraction for samples II and III was only 28 % and 39 %, without any V to be found in the matrix fractions. This difference can be mainly ascribed to dilution uncertainties and several samples transfers, that were most probable not quantitative. Also, some sample solution may be evaporated so that an accurate gravimetric dilution was not possible anymore (samples waited some months before being further processed and measured).
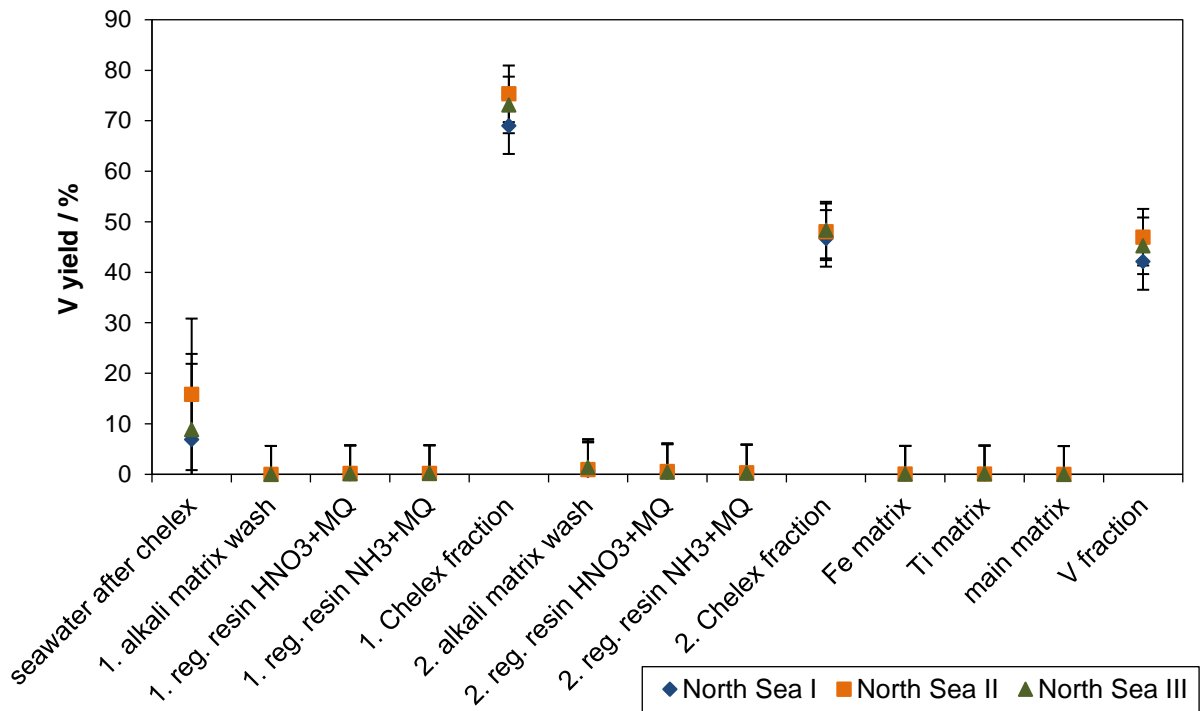
Figure 23: Vanadium yield (relative to starting composition) of all fractions of North Sea test 1 which consists of natural samples North Sea I (diamonds), II (squares), and III (triangles).
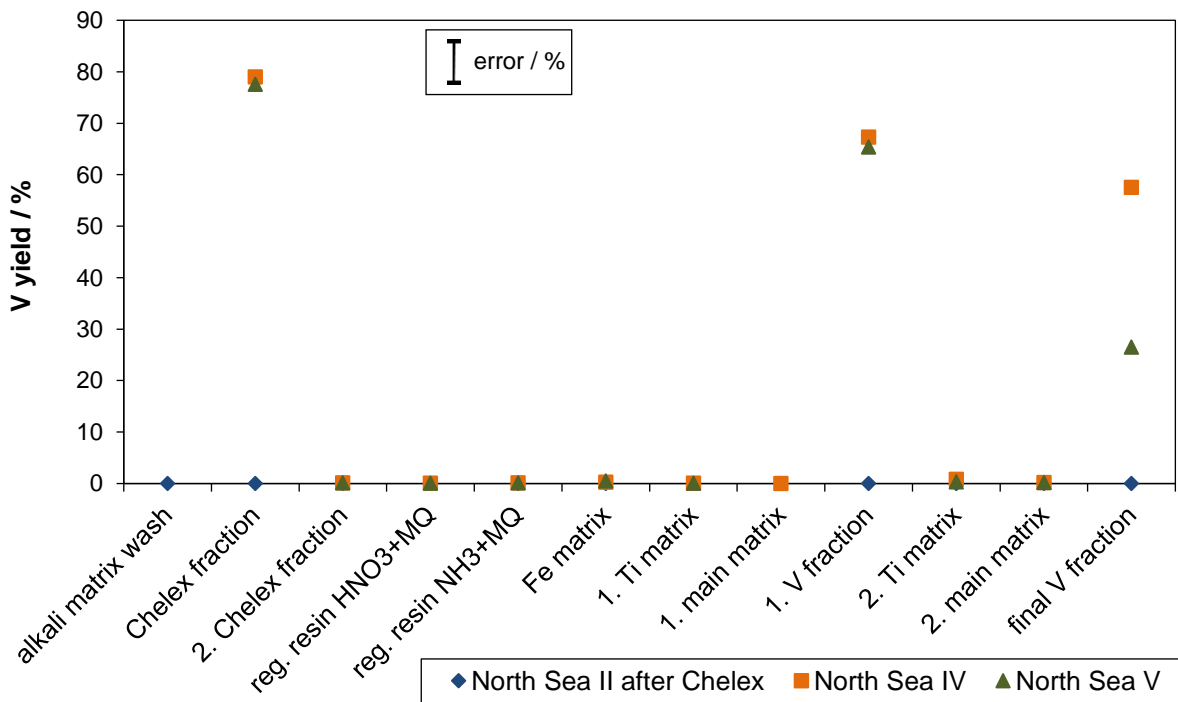
Figure 24: Vanadium yield (relative to starting composition) of all fractions of North Sea test 2 which consists of natural samples North Sea IV (squares) and V (triangles) as well as seawater after Chelex of North Sea seawater II (diamonds).

During North Sea test 2, the natural samples North Sea IV and V as well as the seawater after Chelex of II (from North Sea test 1) were processed (Figure 24). Here, an additional elution step was processed because the resin still looked yellowish, however, no further V was eluted. The Chelex-100 separation was successful and showed V yields of ~79 % and ~78 % for samples IV and V, respectively. The seawater after Chelex fractions could not be measured successfully for V contents even in several different sessions and under different set-ups. After the second cleanup, both samples showed significantly lower V yields. For sample V, this observation can be explained with a take-out of roughly ~50 % solution for a Neptune session prior to the second cleanup. Thus, an accurate V yield determination is simply not possible. For sample IV, the 10 % drop between the first and second V fractions may be explained by V loss during dilution or remaining V in glass beakers.

In the third North Sea test (Figure 25), natural North Sea seawater VI and the doped matrices of natural seawater II and V were processed. The separation of doped V from seawater matrix II was not successful and showed a high V amount in the seawater after Chelex fraction. A speculative reason for a failed separation may be inadequate pH adjustment which caused V not to be retained on the resin which may be due to not acidifying the matrix after the separation of the natural V fraction (e.g. after North Sea test 1). All following fractions showed negligible V contents. The doped sample V, on the other hand, showed a successful V separation with ~97 % V yield in the Chelex-100 fraction. The following cleanup chemistry was also successful and only minor V was lost due to the use of glass beakers and a small and non-quantifiable (roughly ~20 %) sample take-out for a failed Neptune ICP-MS measurement session. The Chelex-100 separation of natural North Sea seawater VI was successful and the Chelex fraction contained ~75 % of V. Minor V was found in all matrix fractions; however, the second V fraction contained less V than expected, likely due to non-quantitative dilution and samples transfers.

Within North Sea test 4 (Figure 26), the Alfa doped matrices of seawater samples IV and VI as well as natural seawater samples VII and VIII were processed. Again, for the doped samples the starting V amount was calculated from the weighing of the stock standard solution. All four samples show a successful separation throughout all steps and no significant V amount in any matrix fraction. Note, however, that the seawater after Chelex was not measured successfully for any of those samples. Noticeably, the second V fraction suffered a significant and unaccountable V loss and the final V yield is only 75 %, 60 %, 55 %, and 62 % for doped IV and VI, and natural VII and VIII, respectively. Again, due to a small and non-quantifiable sample take-out prior to the second cleanups (roughly 5 %) of doped IV and VI during a failed Neptune ICP-MS measurement session (due to high remaining Cr and Ti contents), these final V yields are not representative anymore.
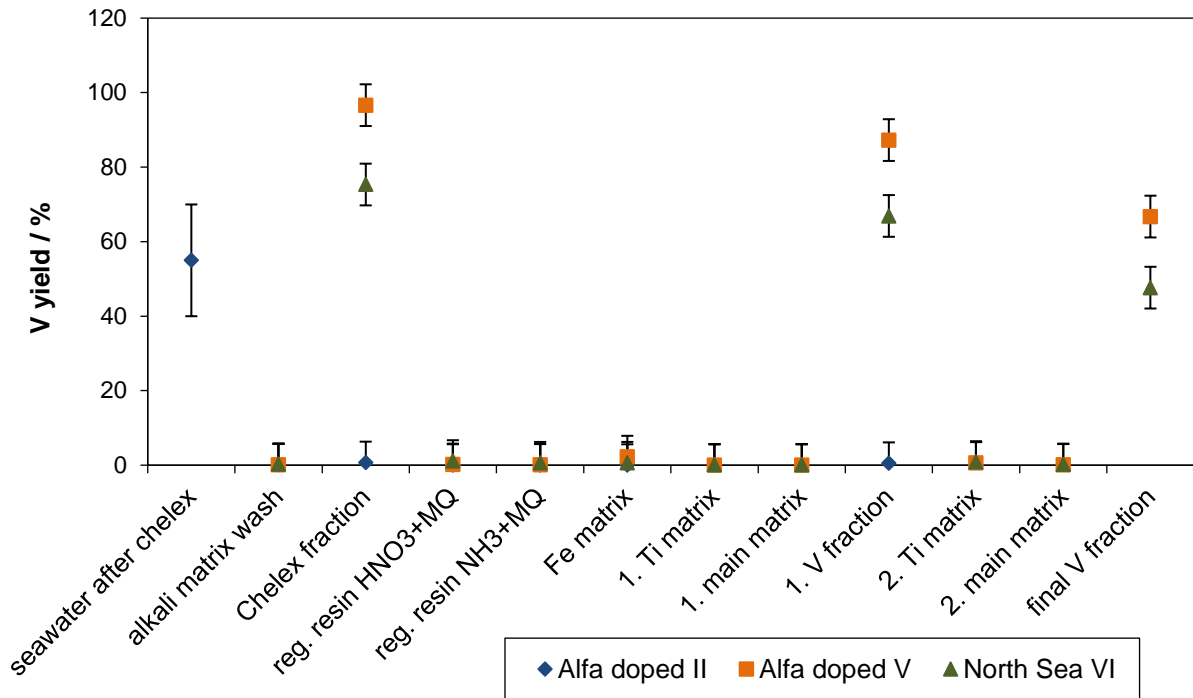
Figure 25: Vanadium yield (relative to starting composition) of all fractions of North Sea test 3 which consists of natural sample North Sea VI (triangles) and Alfa doped matrices of II (diamonds) and V (squares).
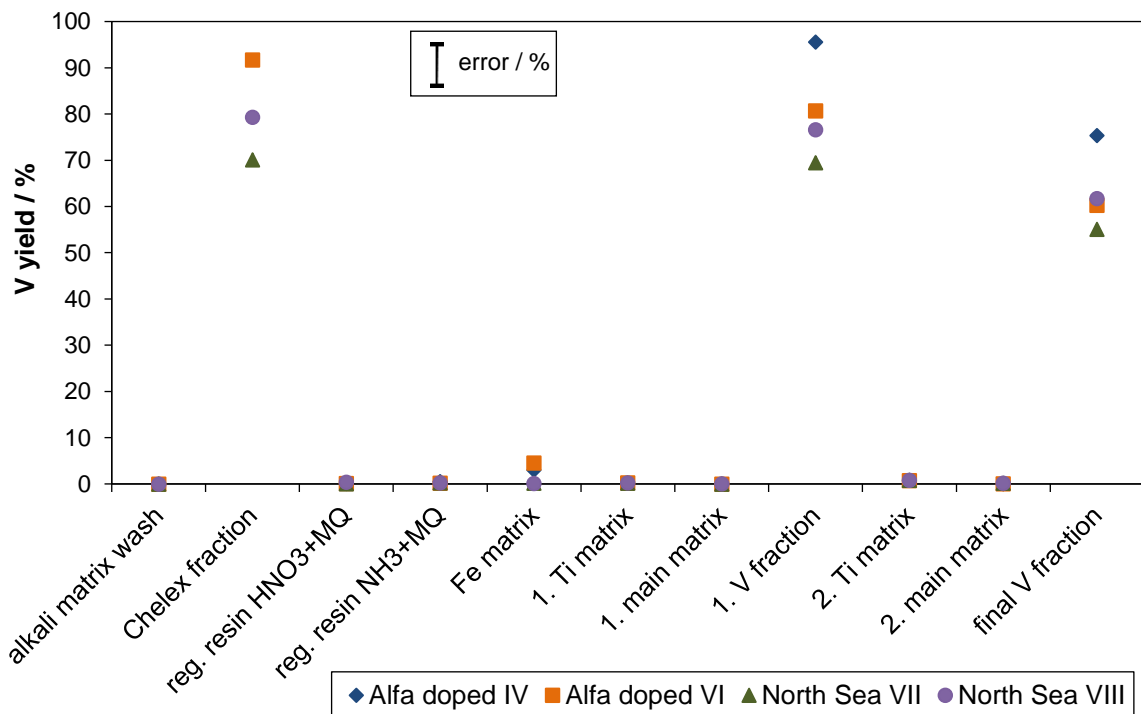
Figure 26: Vanadium yield (relative to starting composition) of all of North Sea test 4 which consists of natural samples North Sea VII (triangles) and VIII (circles), as well as Alfa doped matrices of IV (diamonds) and VI (squares).

North Sea test 5 differs from the previous methods, as it misses the Fe cleanup and already contained a double main and Ti cleanup following right after each other (Figure 27). No V fraction was diluted in between these steps. Also, both Ti matrices were combined into one beaker. All samples showed a successful Chelex-100 separation and alkali wash, resin regeneration, main and Ti matrices showed only minor V amounts which in total accounts for maximal ~2 % V loss. Compared to the previous tests, the final V fractions have higher V yields which highlights that the Chelex-100 separation is responsible for the main V loss and processing samples in a cleanup right away prevents from untraceable V loss.
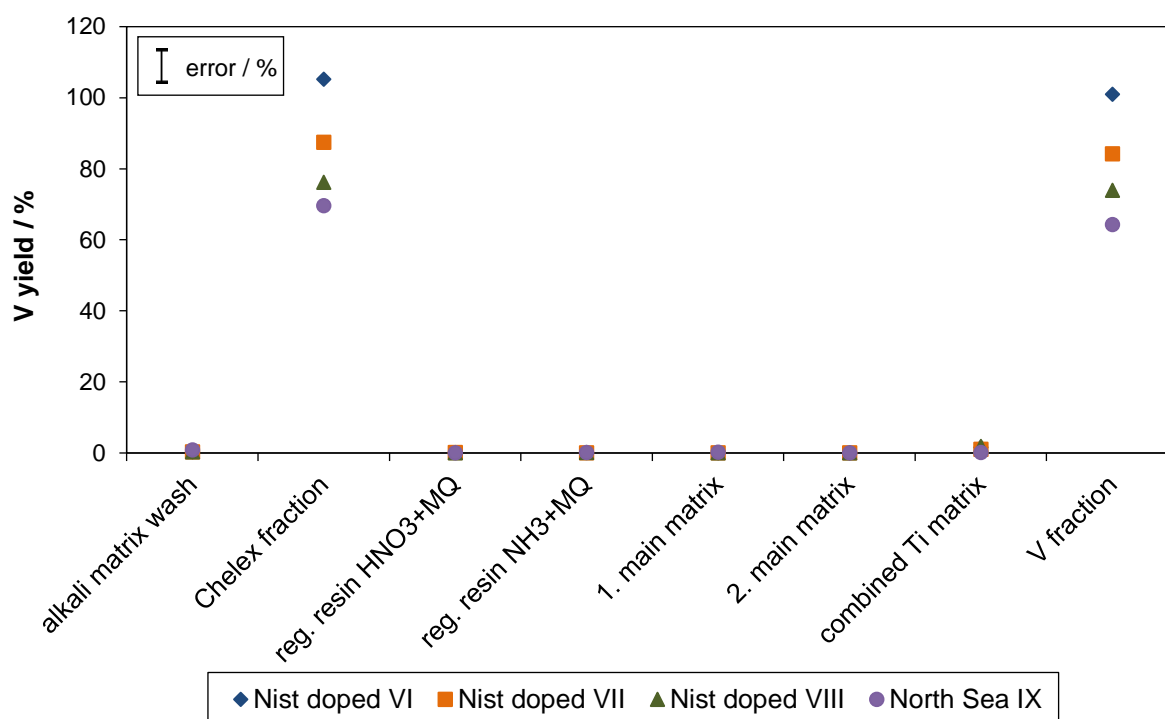
Figure 27: Vanadium yield (relative to starting composition) of all fractions of North Sea test 5 which consists of natural sample North Sea IX (circles) and Nist doped matrices of VI (diamonds), VII (squares) and VIII (triangles).

In summary, all natural North Sea seawater and most doped seawater matrix samples were processed successfully during the Chelex-100 separation and following cleanup steps. Most V loss can be ascribed to non-quantitative sorption of V onto the Chelex-100 resin and sample loss during many different handling steps, like additional evaporation, re-filling, dilution or left-overs in glass beakers. The yield for the doped samples is significantly higher (Average 93 %) than for the natural ones (Average 74 %), even though their matrix is supposed to be very similar. However, the V content is much higher in the doped samples and this together with the previous observation indicates that the V sorption to the resin does not depend on the V content and that enough resin is used. Hence, even small differences between the composition

of the matrices or a different V starting speciation in the samples may cause the different partitioning onto the resin. These observations agree with the reported ones by Wu et al. (2019) who studied the V yield also after various treatments of samples to destroy remaining organic seawater compounds. Yet, these tests did not show an increase in V yields and the true reason for V loss during the application of chelating resins remains to be found. Hence, the new Chelex-100 separation method may be still optimized for the V separation. Additional sample loss from handling can only be prevented by working very careful and processing as few different steps as possible, thus planning any analytical work extensively. Nevertheless, precise isotope measurements are needed to quantify whether the loss of V during the process did also cause isotope fractionation or not.

5.3 Procedure blanks and possible contamination

In addition to samples during North Sea tests 1 – 3 seawater procedure blanks were processed as well that describe the background V content during the Chelex-100 separation (corresponds to the 'Chelex fractions'). Plus, during the first and second cleanup procedure, two additional blanks were determined. Total procedure blanks for the different tests are named p-blank-1, p-blank-2, and p-blank-3 and contain Chelex-100 and cleanup resin contaminations as well as buffer background contents (See supplementary table S 19). The cleaned buffer solution was measured for its purity (contained 0.011 ng g^{-1} V) so that the use of roughly 20 – 30 ml of cleaned buffer translates into a possible V contamination of ~0.35 ng for each sample.

In North Sea test 1, the p-blank-1 accounted for 10.36 ng V which is rather high but still low enough compared to the starting amount of ~4000 ng V in North Sea seawater (1:386). Compared to the doped samples (~10 000 ng V) this has even less significance (1:965). North Sea test 2 contained only one Chelex-100 separation compared to North Sea test 1, and the procedure blank p-blank-2 was processed until the end of the first cleanup round without measuring an aliquot after the Chelex-100 separation. Thus, p-blank-2 (corresponds to Chelex separation, Fe, 2x Ti, and 2x main cleanup) accounts for 1.53 ng V. Compared to North Sea test 1, this is significantly lower and may be explained by the double usage of resin in North Sea test 1 and the usage of extensively cleaned resin in North Sea test 2. In North Sea test 3, pre-cleaned Chelex-100 resin from the same batch as in North Sea test 2 was used. Both methods contained the same steps and thus the corresponding p-blank-3 accounted for 0.73 ng V which again is much lower than in North Sea test 2. This difference may be ascribed to more careful handling of acids and samples and extensive additional cleaning of buffer and tygon tubing in between the different methods and highlights that careful handling and cleaning of used materials can prevent V contamination.

During North Sea tests 4, only a cleanup blank (Fe, 2x Ti, and 2x main cleanup) was accumulated and accounted for 0.14 ng V. In North Sea test 5, a blank contamination could arise from the double processing of Ti and main cleanup and this blank accounted for 1.64 ng V. To sum up, most blank contamination may be added during the Chelex-100 separation from the resin and buffer. Thus, both should be cleaned and checked precisely before usage. The blank contamination during cleanup steps can vary between 0.1 - 2 ng which is not significant compared to processed sample V.

5.4 Processing reference materials along with North Sea seawater

During North Sea test 1 – 4, each an aliquot of the Alfa solution reference material was processed in the first Fe, Ti, and main cleanup as well to check yield of V in pure solutions. In the second Ti and main cleanup, additional new reference materials were processed (Alfa sol., Alfa foil and Nist sol.). Compared to the starting amount of V (weighed or volumetric dilution) all runs were successful (Figure 28) and any V loss was caused during the Fe cleanup, thus, the Fe matrix contained the missing V.
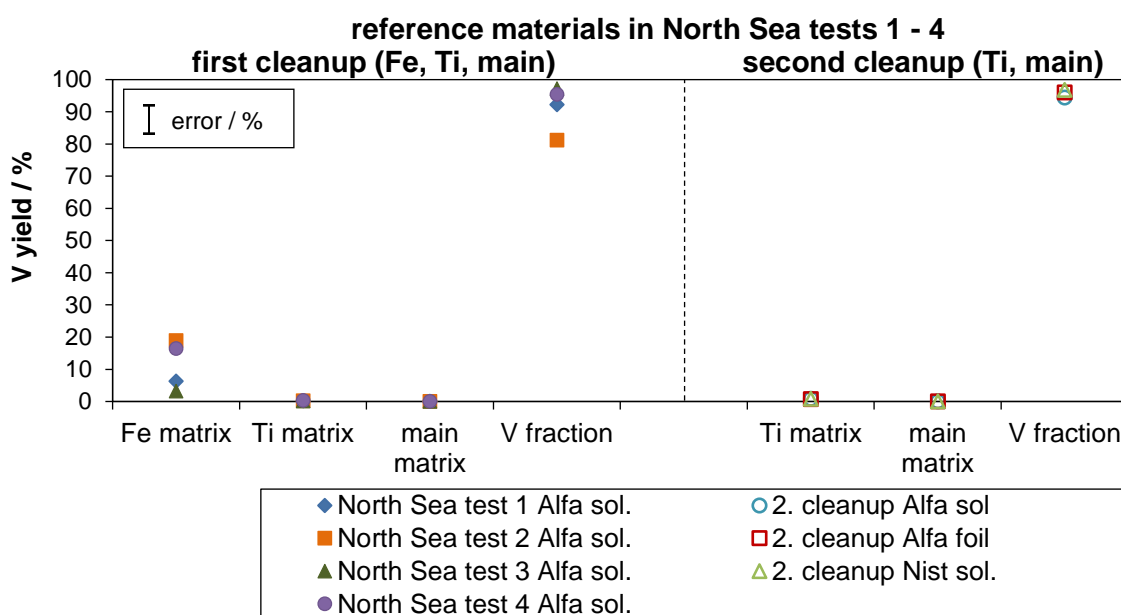
Figure 28: Results of processing an aliquot of the reference materials Alfa sol. in the first cleanups and aliquots of Alfa sol., Alfa foil, and Nist sol. during the second cleanup of North Sea tests 1 – 4.

Those seven reference materials from the first and seconds cleanups of North Sea tests 1 – 4 were measured with the Neptune Plus ICP-MS during the same session. As most samples were Alfa-Aesar standards, they were measured versus an Alfa Aesar ('new') bracketing

solution. The Alfa-Aesar solutions were bracketed against each other and gave a $\delta^{51}V$ = -0.01 ‰ ± 0.20 ‰ (n = 29, 2 s.d.) and the double standard deviation indicates a rather high drift during the session. The drift is also responsible for unsuccessful single measurements and thus, some samples were only measured twice (Table 14). A pure Nist-3164 solution was measured at the beginning and end of the sequence and showed an average $\delta^{51}V$ values of +1.65 ‰ ± 0.12 ‰ (2 s.d., n = 11) which is within the previously measured and published range. Thus, the data may be re-calculated to Nist-3165 as reference standard. The 'old pure Alfa' standard was measured as a second reference to check reproducibility and was within the previously measured range (see section 2.6 for compilation of reference standards).

Table 14: Vanadium isotope results for reference materials during North Sea tests 1 – 4 cleanups, $\delta^{51}V_{reference}$ indicates targeted values (from table 6 in section 2.6). $^{51}V/^{52}Cr$ and $^{51}V/^{49}Ti$ are rounded values.

	V yield / %	$\delta^{51}V_{reference}$ / ‰	$^{51}V/^{49}Ti$	$^{51}V/^{52}Cr$	$\delta^{51}V_{Alfa-new}$ / ‰	$\delta^{51}V$ 2 s.d. / ‰	n
pure Nist-3165		1.66	70,000	90,000	1.65	0.12	11
old pure Alfa-Aesar sol.		1.10	7,000,000	170,000	1.13	0.13	3
Alfa sol. North Sea test 1	92.3	0.00	260,000	120,000	-0.28	0.12	2
Alfa sol. North Sea test 2	81.2	0.00	44,000	88,000	-0.55	0.20	3
Alfa sol. North Sea test 3	97.1	0.00	200,000	78,000	-0.44	0.18	2
Alfa sol. North Sea test 4	95.4	0.00	230,000	75,000	-0.47	0.06	3
2. cleanup Alfa sol.	94.4	0.00	860,000	85,000	-0.09	0.14	2
2. cleanup Alfa foil	95.9	2.38	1,600,000	200,000	2.31	0.08	3
2. cleanup Nist sol.	96.8	1.66	1,000,000	130,000	1.54	0.12	3

Surprisingly, all Alfa standards from the first cleanups of North Sea tests 1 – 4 show fractionated $\delta^{51}V$ values away from their starting composition. Also, their $^{51}V/^{52}Cr$ and $^{51}V/^{49}Ti$ ratios are highly variable and some are lower than the pure starting composition which is indicative of possible Cr and/or Ti contaminations from resins. A loss of V was caused by the Fe cleanup and this may also be the reason for a V isotope fractionation even though a V loss was not indicative of V isotope fractionation in previous analyses (Brüske, 2015). During the second round, no Fe cleanup was performed and all three reference materials from the Ti and main cleanup show unfractionated $\delta^{51}V$ values compared to their starting compositions (Table 14). This highlights that the first Fe cleanup was likely causing the V isotope fractionation in the first place.

In North Sea test 5, two aliquots of the reference material Nist sol. were processed during the Chelex-100 separation. One of those (Nist 2) was processed throughout the whole following

cleanup (2x main, 2x Ti) and one was to be measured on the Neptune ICP-MS after only processing the Chelex-100 separation (Nist-1). Additionally, an Alfa sol., an Alfa foil, and a Nist sol. (Nist-3) reference material were processed in the cleanup (2x main, 2x Ti) as well. All standards showed a successful separation and minor V loss (Figure 29). Within the Chelex-100 separation, Nist-1 showed 98 % and Nist-2 95 % V yield. In the following cleanup, Nist-2 showed a final V yield of 82 % compared to the starting V amount. The Alfa sol., Alfa foil, and Nist-3 standards showed also only 83 %, 85 %, and 83 % V yield and all matrix fractions were devoid of V (< 2 %). Thus, these numbers may be explained by a systematic error in the cleanup of North Sea test 5, like dilution or measurement uncertainties.
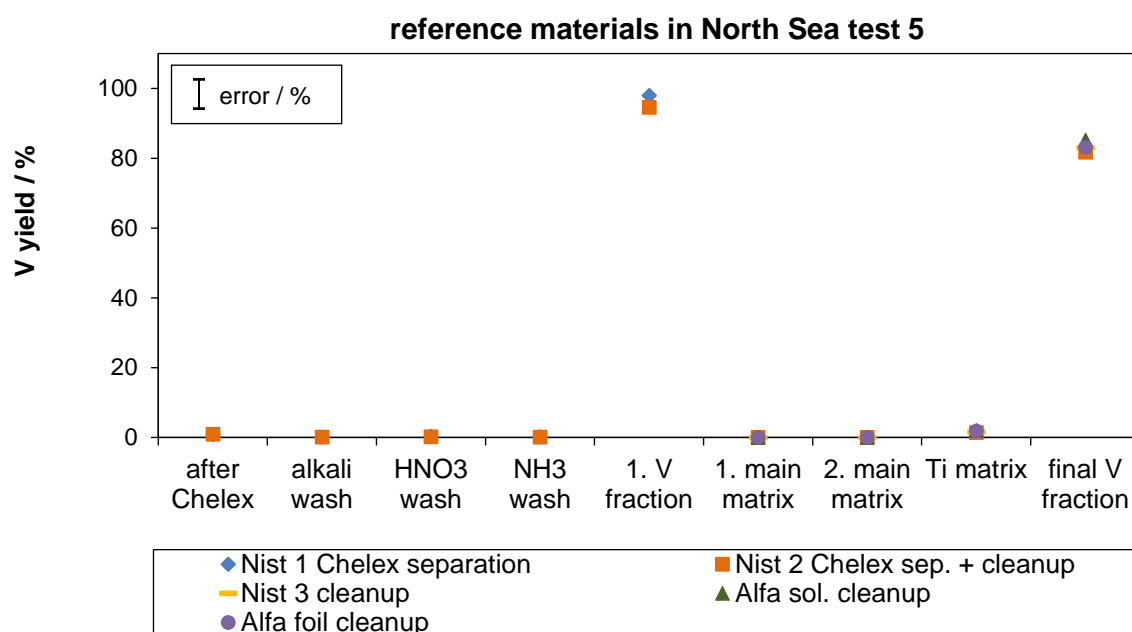
Figure 29: Results of processing reference materials Nist sol. 1, Nist sol. 2, Alfa sol. and Alfa foil together with North Sea test 5 samples.

All reference materials were measured for their V isotope composition with the Neptune Plus ICP-MS against a pure Nist-3165 bracketing standard that gave a $^{51}V/^{50}V_{IC-MB}$ = 401.01 ± 0.33 (1 s.d., n = 28, $^{51}V/^{52}Cr$ ≈ 100,000 and $^{51}V/^{49}Ti$ ≈ 84,000) throughout the whole session. This rather high variability explains also the higher 2 s.d. values for the sample measurements (Table 15). As a pure reference for session reproducibility, a pure Alfa-Aesar solution was measured repeatedly and agrees with previously measured and published values. The Nist-1 standard (only Chelex-100 separation) shows a highly fractionated δ^{51}V value and very low $^{51}V/^{52}Cr$ and $^{51}V/^{49}Ti$ which are responsible for the fractionated δ^{51}V value due to isobaric interferences on the low abundant ^{50}V. These results highlight that a strong Cr and Ti contamination results from the procedure that may arise from resin, acids, buffer, or any

beakers or containers and a Chelex-100 separation always needs a following cleanup for V isotope measurements. On the other hand, the Nist-2 (Chelex-100 and cleanup procedure) agrees with the V isotope composition of the pure Nist-3165 solution (Table 15). Plus, its $^{51}V/^{52}Cr$ and $^{51}V/^{49}Ti$ are increased compared to Nist-1, although the ^{52}Cr content is still higher than in the pure solution, however the ^{49}Ti content is already highly depleted. Nevertheless, this proofs that the cleanup sufficiently removed both Ti and Cr contamination from the previous Chelex-100 separation. All three reference materials from the cleanup steps (2x main and 2x Ti cleanup) show unfractionated $\delta^{51}V$ values and proof that even with the fairly low V yields (between 83 % and 85 %) during these steps, the V isotope signature is preserved.

Table 15: Vanadium isotope results for reference materials during North Sea test 5. $\delta^{51}V_{ref.}$ indicates targeted values (from table 6 in section 2.6). $^{51}V/^{52}Cr$ and $^{51}V/^{49}Ti$ are rounded values.

	V yield / %	$\delta^{51}V_{ref.}$ / ‰	$^{51}V/^{49}Ti$	$^{51}V/^{52}Cr$	$\delta^{51}V_{Nist-3165}$ / ‰	$\delta^{51}V$ 2 s.d. / ‰	n
pure Alfa Aesar sol.		-1.65	1,600,000	58,000	-1.66	0.26	11
Nist 1 Chelex separation	98.0	0.00	7,800	500	-0.59	0.15	2
Nist 2 Chelex sep. + cleanup	81.7	0.00	320,000	16,000	0.06	0.13	3
Nist 3 cleanup	82.8	0.00	570,000	52,000	-0.02	0.11	5
Alfa sol. cleanup	85.2	-1.65	600,000	39,000	-1.84	0.27	3
Alfa foil cleanup	83.0	0.80	2,000,000	55,000	0.69	0.34	3

5.5 Natural North Sea and doped matrix samples V isotope compositions

The natural and doped matrix samples of North Sea seawater were measured within several sessions on the Neptune Plus ICP-MS. With regard to the doped reference material, Alfa doped matrices were measured relative to a pure Alfa-Aesar bracketing solution. All other samples were measured versus a pure Nist-3165 solution. Hence, both bracketing standards were also used as external samples to check their reproducibility within the sessions, which they proofed to be (Table 16). Natural North Sea seawater I was used up in one of the first Neptune sessions which did not give reproducible results, and which led to the application of further cleanups of other North Sea samples. Only North Sea seawater samples III and VII could not be measured successfully for their V isotope compositions, whereas all other samples (II, IV, V, VI, VIII and IX) were measured successful.

Table 16: Vanadium isotope results for natural North Sea samples and doped seawater matrices. Asterisks indicate measurements relative to a pure Alfa-Aesar solution. Sample names in bold indicate successful analyses with respect to the whole procedure and measurements. $\delta^{51}V_{reference}$ indicates targeted values (from table 6 in section 2.6). $^{51}V/^{52}Cr$ and $^{51}V/^{49}Ti$ are rounded values. V yield in the respective final fraction, see section 5.2 for details.

	V yield / %	$\delta^{51}V_{reference}$ / ‰	$^{51}V/^{52}Cr$	$^{51}V/^{49}Ti$	$\delta^{51}V_{Nist-3165}$ / ‰	$\delta^{51}V$ 2 s.d. / ‰	n
pure Alfa Aesar		-1.65	51,000	1,680,000	-1.62	0.19	43
pure Nist-3165		1.66	79,500	72,000	1.65 *	0.12	16
North Sea seawater							
natural I	42.1						
natural II	28.3		8,200	43,000	-0.47	0.02	3
natural III	39.1		5,500	44,000	-1.04	1.80	3
natural IV	57.5		10,000	65,000	-0.67	0.19	3
natural V	26.5		4,700	25,000	-0.57	0.02	2
natural VI	47.7		1,100	83,000	-0.50	0.02	2
natural VII	55.1		5,000	69,000	-1.28	0.19	6
natural VIII	61.7		10,000	70,000	-0.73	0.22	4
natural IX	64.3		5,900	93,000	-0.70	0.20	3
all North Sea seawater (II, IV, V, VI, VIII, IX)					-0.62	0.25	17
doped seawater matrices							
Alfa doped II	0.52						
Alfa doped IV	75.4	0.00	50,000	207,000	-0.27 *	0.15	4
Alfa doped V	66.7	0.00	31,400	162,000	-0.17 *	0.23	10
Alfa doped VI	60.3	0.00	32,000	146,600	-0.19 *	0.10	5
Nist doped VI (2nd time)	100.9	0.00	17,300	452,000	-0.43	0.30	5
Nist doped VII	84.2	0.00	14,900	266,000	-0.16	0.17	5
Nist doped VIII	73.9	0.00	13,600	313,000	-0.08	0.17	6
all doped Alfa		0.00			-0.20	0.19	19
all doped Nist		0.00			-0.11	0.18	11

The analyses of North Sea III and VII both show very low $\delta^{51}V_{Nist-3165}$ signatures which may indicate interfering molecules of $^{36}Ar^{14}N^+$ on the ^{50}V isotope. This molecular interference may be a problem when its intensity increases or the center mass drifts, resulting in peak overlap. As their $^{51}V/^{52}Cr$ and $^{51}V/^{49}Ti$ ratios are comparably high, indicating a sufficient separation, isobaric interfering Cr or Ti seems unlikely the cause of the low $\delta^{51}V$ values. Both samples were processed with Alfa-Aesar solution reference materials within the cleanups (Fe, Ti, and main cleanup) of North Sea tests 1 and 4 that showed fractionated reference materials likely from the Fe cleanup (Table 14 in section 5.4). Hence, those samples may be also already fractionated in the Fe cleanup and carried a "false" signature. On the other hand, all other samples from North Sea test 1 – 4 were successfully and reproducibly measured, also

compared to North Sea test 5 sample IX (without Fe cleanup and with successful reference materials), which may indicate that these samples were not affected by this problem.

The doped matrix of seawater sample II was not separated successfully in the Chelex-100 separation and hence, was not measured for V isotope ratios. All other Alfa doped matrices were measured within their V isotope compositions of starting materials within the general analytical uncertainty (~0.2 ‰). Notably, Alfa doped IV was slightly out of range, however, also adding those data into the average of all Alfa doped samples, did not shift the average out of the starting composition range. The Nist doped matrix of VI (after separating the Alfa standard and doping with Nist for a new Chelex-100 separation) did not show a successful V isotope measurement and instead a very high variability (and thus high 2 s.d.) and a low $\delta^{51}V_{Nist-3165}$ value. This may result from left-over traces of the first Alfa doping as the Alfa Asear solution is isotopically lower than the Nist solution. With regard of the high variability, however, a high matrix component in the measured solution seems more likely and may have caused an unsteady signal.

These results highlight that the Chelex-100 separation method of V from a natural seawater matrix can be applied successfully for high precision V isotope measurements of natural and doped samples. The natural samples gave a final V isotope composition of North Sea seawater of $\delta^{51}V_{Nist-3165}$ = -0.62 ‰ ± 0.25 ‰ from 17 single analyses from 6 different and separately processed samples aliquots. Further discussion and comparisons of this value with published data can be found in section 7.3.

6. Separation of V from further seawater samples with the new Chelex-100 method

6.1 Application of the new Chelex-100 method to natural seawater samples

The new Chelex-100 separation method was applied to natural samples from the Arctic, Southern, Indian, and Pacific Ocean, as well as another North Sea aliquot from a different locality as described in figure 30. Due to the limitation of the four-channel pump, no procedure blank was processed (two runs with each four samples occupied the pump).

Chelex separation   **Ti cleanup (3x)**   **main cleanup (3x)**

Chelex separation	Ti cleanup (3x)	main cleanup (3x)
2 ml Chelex-100, 100-200 mesh	150 µl LN resin	0.5 ml AG1X8 resin, 100-200 mesh
100 ml MQ	0.5 ml H_2O	5 ml MQ
200 ml 2 M HNO_3/0.5 M HCl	2x 0.2 ml 6 M HCl	2.5 ml 1 M HCl
100 ml MQ	load sample in 1 ml 6 M HCl	2x 1.5 ml 0.003 M HCl + 1 % H_2O_2
200 ml 2 M NH_3	0.8, 0.4, 0.4 ml 6 M HCl	load sample in 4 ml 0.003 M HCl + 1 % H_2O_2
50 ml 1 M amm. acet. buffer	0.5 ml H_2O	2x 2.5 ml 0.003 M HCl + 1 % H_2O_2
load sample, pH 5 with buffer, drop 1 - 2 ml/min	1 ml 2 M HF	0.5 + 2.5 ml 1 M HCl
30 ml 1:1 mix of MQ and buffer	0.5 ml H_2O	
20 x 2 ml 2 M HNO_3/0.5 M HCl	1 ml 6 M HCl	
80 ml 2 M HNO_3/0.5 M HCl		
3x cv MQ		
80 ml 2 M NH_3		
2x cv 1 M amm. acet. buffer		

Figure 30: Scheme showing the Chelex-100 separation and following cleanup steps for seawater samples. Used resins are highlighted in blue, colorless squares depict resin cleaning prior to sample load, V elution is highlighted in green, and matrix elution in orange. Arrows indicate which fractions were cleaned in the next steps, whereby small test tubes indicate that a fraction is taken out for ICP-MS measurements. Modified from Brüske (2015) and Schuth et al. (2017).

The first purification was performed with a main, a Ti and a second main cleanup whereby a pure reference solution of Nist-3165 was processed as well. Neptune ICP-MS screenings showed that all V fractions were not clean enough for isotope measurements so that a second Ti cleanup was performed (this matrix was not collected). Again, the solutions were checked on the Neptune Plus ICP-MS and only Antarctic seawater and the processed Nist standard were measured successfully. All other samples needed another main and Ti cleanup. Now, the main and Ti matrix were collected into the same beaker. All matrix and V fractions were measured with Element XR ICP-MS to check purity. However, due to remaining matrix and a highly unstable machine setup, no further successful V isotope measurements could be performed.

6.2 Column yield during the Chelex-100 separation and following cleanup steps

The seawater samples from this procedure were all not measured successful for their respective starting compositions. Hence, yields can only be calculated between Chelex-100 and following fractions and distribution patterns for the different fractions are produced with absolute V amounts (back-calculated to total sample volume).

Samples Jub 14, Jub 16 A + B, and Mauritius seawater all showed a successful Chelex-100 separation and very similar V contents in the Chelex fraction (Figure 31). No significant V was found in the Chelex matrix fractions, and hence, V elution was considered quantitative. Between the Chelex and the first cleaned V fraction a V loss occurred which can be either explained by untraceable V loss into beakers or remaining V on the resin. Also, it may be explained by high measurement errors on the values from the Chelex fractions as these fractions still contain a high salt matrix portion. No V was found in the first Ti and main matrix fractions, nor in the third combined matrix fraction. The final V fractions contained only a portion of V as a part of the samples was taken out, diluted and checked on the Neptune Plus ICP-MS. Hence, the final V yield calculation is not representative.

For samples from the Arctic, Antarctic, and Helgoland A + B, the results look very similar to the previously described ones (Figure 32). In Arctic seawater the Chelex fraction contained only very low amounts of V, either because its V content is ab initio this low, or the separation was not successful. Helgoland A and B show very similar results indicative of a successful and reproducible separation; however, their V content is much lower than previously tested North Sea seawater from Spiekeroog. Either the Helgoland samples both have a low and still comparable V yield, or the original V content differed between Helgoland and Spiekeroog seawater. This may be the case as both samples were sampled rather nearshore and here, the particulate load may influence the V content as well as previously observed seasonal variability in coastal areas (Kowalski et al., 2009; Wang and Sañudo Wilhelmy, 2009). Antarctic

seawater shows a much higher V content in the Chelex fraction which may be due to specific V concentrations and behavior in the Southern Ocean (discussed in detail in section 7.3).
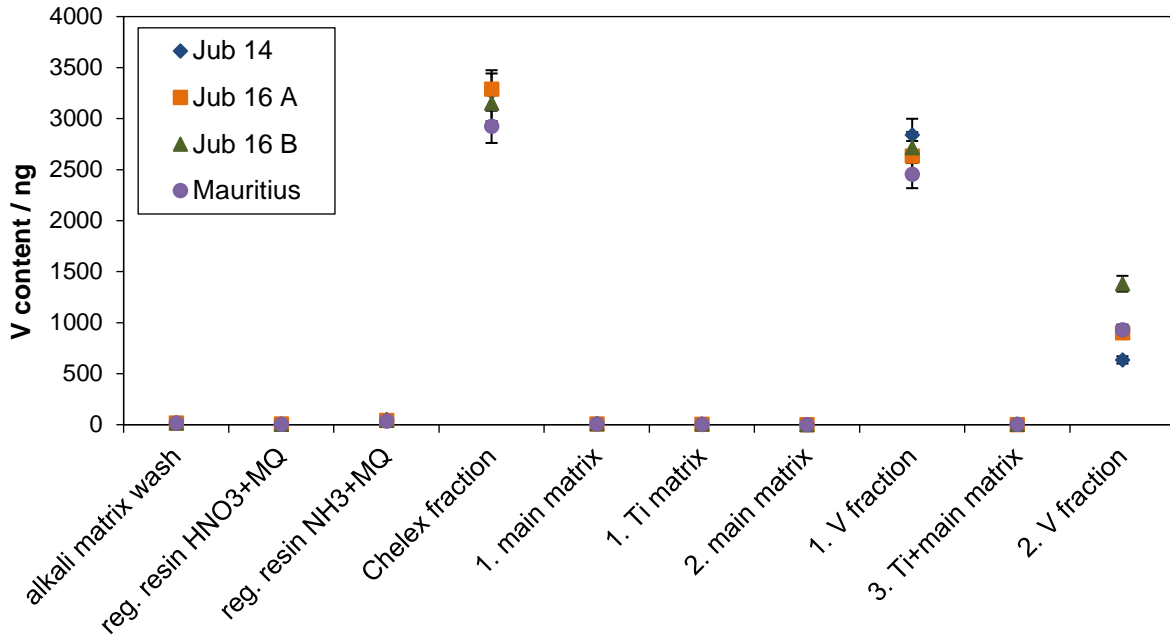
Figure 31: Vanadium distribution between the different fractions from Chelex-100 separation and following cleanups for natural seawater samples Jub 14, Jub 16 A + B, and Mauritius.
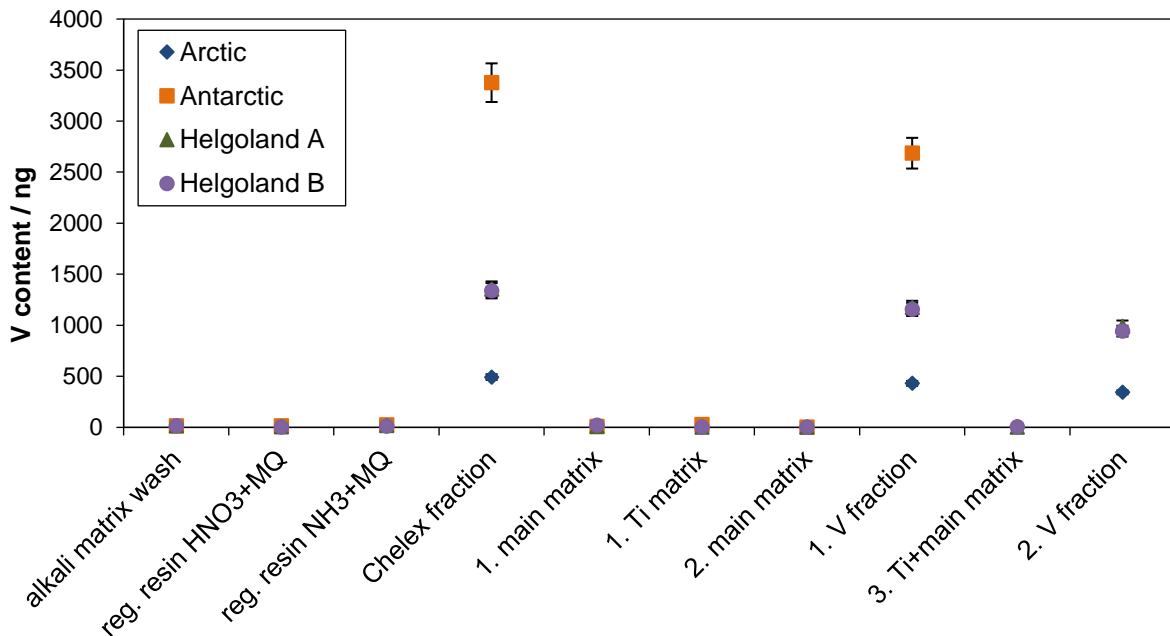
Figure 32: Vanadium distribution between the different fractions from Chelex-100 separation and following cleanups for natural seawater samples Arctic, Antarctic, and Helgoland A + B.

Compared to the Chelex fractions, the V yield in the first V fraction is indicative of V loss with values of 88 %, 80 %, 87 %, and 87 % for Arctic, Antarctic, Helgoland A, and Helgoland B seawater. As those samples were measured during the same session with Jub 14, Jub 16 A+B and Mauritius seawater, the same reasons for this offset apply here as well. All matrix fractions from the Chelex separation and all following cleanups contained only negligible V amounts.

During the first Ti and first and second main cleanups a pure Nist-3165 reference standard was processed as well (Figure 33). Its starting V amount was back-calculated to the weighed sample amount and the V yield in the first V fraction was 90 %. The main matrices contained only minor V, whereas ~1 % was found in the Ti matrix and the glass beaker of the V fraction after re-filling for measurements (supplementary table S 25).
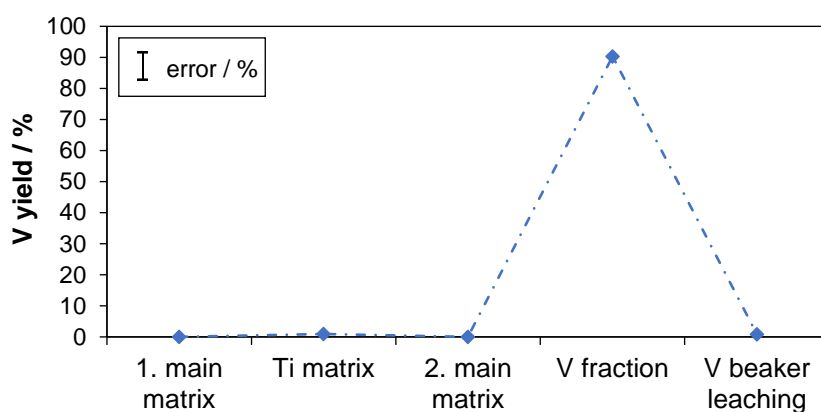
Figure 33: Vanadium distribution of a pure Nist-3165 standard processed in the first main, Ti, and second main cleanup together with seawater samples.

6.3 Vanadium isotope measurements of seawater samples and reference materials

The second V fraction of the samples was depleted in V because some sample material was used up in a qualitative screening with the Neptune Plus ICP-MS. During this first screening, an aliquot of all samples was diluted 1:10 and checked in a short run of 5 cycles each 4 s integration time (Table 17). The check was performed without mass-bias monitor and thus only raw ratios were measured ($^{51}V_{raw}/^{50}V_{raw}$, $^{51}V_{raw}/^{52}Cr_{raw}$, and $^{51}V_{raw}/^{49}Ti_{raw}$). However, these are good indicators whether a fraction is pure enough for precise V isotope ratio measurements. Only Antarctic seawater showed high enough ratios and was diluted again to be measured quantitatively versus a pure Nist-3165 solution. The successful measurement gave a $\delta^{51}V_{Nist-3165} = -2.53$ ‰ ± 0.21 ‰ (n = 5). Hence, the sample was used up and no third Ti and main cleanup were applied. During this Neptune session a pure Alfa-Aesar solution was measured and gave a $\delta^{51}V_{Nist-3165} = -1.71$ ‰ ± 0.14 ‰ (n = 5) which agrees with previously measured and published values. Also, the processed Nist-3165 standard solution still yielded

values of -0.16 ‰ ±0.18 ‰ (2 s.d., n = 3), i.e. within analytical uncertainty for the pure NIST-3165 reference material. After the first screening, all samples except for Antarctic, were cleaned in another Ti and main cleanup. Again, these fractions were diluted 1:10 and checked in a short run of 5 cycles each 4 s integration time (Table 17). A comparison between the raw ratios revealed that none of the samples were sufficiently purified in the third cleanups and some ratios even decreased, indicative of potential contamination in the lab (which is discussed in the next section).

Table 17: Vanadium isotope results for seawater samples, upper area describes successful measurements of processed Nist-3165 and Antarctic seawater. Lower area shows the tested aliquots of all samples after twice processing the cleanup (left-hand side) and after the third cleanup (right hand-side). $\delta^{51}V_{reference}$ indicates targeted values (from table 6 in section 2.6). $^{51}V/^{52}Cr$ and $^{51}V/^{49}Ti$ are rounded values.

	$\delta^{51}V_{reference}$ / ‰	$^{51}V/^{49}Ti$	$^{51}V/^{52}Cr$	$\delta^{51}V_{Nist\text{-}3165}$ / ‰	$\delta^{51}V$ 2 s.d. / ‰	n
pure Alfa-Aesar	-1.65	770,000	39,000	-1.71	0.14	5
Antarctic		51,000	3,500	-2.53	0.21	5
processed Nist	0.00	145,000	55,000	-0.16	0.18	3
	after 2x Ti and 2x main cleanup			*after 3x Ti and 3x main cleanup*		
10-fold dilution, only 5 cycles	$^{51}V_{raw}/^{50}V_{raw}$	$^{51}V_{raw}/^{49}Ti_{raw}$	$^{51}V_{raw}/^{52}Cr_{raw}$	$^{51}V_{raw}/^{50}V_{raw}$	$^{51}V_{raw}/^{49}Ti_{raw}$	$^{51}V_{raw}/^{52}Cr_{raw}$
Jub 14	369.8	5,700	3,100	394.5	13,900	4,300
Jub 16 A	397.6	12,500	2,400	394	12,900	5,500
Jub 16 B	405.7	18,300	5,100	389.4	8,700	8,700
Mauritius	406	23,300	5,300	401	23,000	5,900
Arctic	282.3	1,300	430	263.9	980	897
Antarctic	411.5	55,700	2,500			
Helgoland A	399.6	13,500	2,400	391.8	12,000	2,400
Helgoland B	387.7	12,800	460	398.4	16,800	3,800

6.4 Blank values and discussion of V isotope measurements of seawater

During the Element XR ICP-MS sessions all blank fractions from the cleanup steps were quantified as well. The first V blank (first main, Ti, and second main) contained 0.37 ng V which is sufficiently low compared to V contents in the first V fraction. The second cleanup blank contained 0.07 ng V and hence also the accumulated total V blank of 0.45 ng does not interfere with natural V in the second V fraction. However, no Chelex-100 blank was processed during the separations because the four-channel pump was occupied twice with each four samples. Considering the Chelex-100 separation procedure blanks from the North Sea tests (section 5.3), the whole procedure blanks (including the Chelex-separation and several cleanups)

varied between 0.73 ng V and 10.36 ng V. This high variability may also translate into a high Chelex-100 blank for the seawater samples separation in this section, even though, here again, the resin and buffer solution, which were responsible for the highest blank contribution, were cleaned excessively prior to the separation. Considering the high p-blank-1 from North Sea test 1 for the seawater samples second V fractions, the V_{sample}/V_{blank} ratio of the seawater samples would be too low (< 1:100) and hence, the V blank contamination may interfere with V isotope measurements.

Additionally, the Ti, Cr and Fe content of the blanks also plays a significant role as it contributes to the natural background content. As samples are usually doped with a Fe standard solution for mass-bias control, the Fe blank contamination by this amount is negligible and hence should be also be negligible in the samples. Purification of the final V fractions can only be achieved until blank levels are reached which are 0.45 ng Ti and 0.015 ng Cr for the corresponding last V fraction (supplementary table S 26). The boundaries for $^{51}V/^{52}Cr$ = 2,853 and $^{51}V/^{49}Ti$ = 25,000 (Wu et al., 2016) translate into V/Cr = 2,381 and V/Ti = 1,356. From concentration measurements, the seawater samples have V/Cr between 23,000 and 95,000 and V/Ti between 770 and 3000. Hence, Cr and Ti contribution from the lab blanks plays a significant role and does inhibit successful V isotope measurement due to high remaining Ti.

The only sample that showed a successful measurement was Antarctic seawater, which was also one of those with the highest total V amount and comparably high $^{51}V/^{52}Cr$ = 3,500 and $^{51}V/^{49}Ti$ = 51,000. Regarding the first screening of the sample, a $^{51}V/^{52}Cr$ = 2,500 (Table 17) was determined indicating that the errors on these raw ratios are high due to the short data collection time of only ~20 s. Taking all these problems into consideration, a high V, Cr, and/or Ti lab blank together with low V concentrations inhibits a successful V isotope measurement of natural seawater. Thus, only cleaning any solutions and labware extensively and using as few steps as possible to separate V from a matrix may result in a successful measurement at the end. For our samples, applying a third Ti and main cleanup only resulted in V loss (even taking a sample aliquot for a Neptune check-up into consideration) and this compensated the potential cleaning of Cr and Ti and hence, the final $^{51}V/^{52}Cr$ and $^{51}V/^{49}Ti$ ratios stayed in a similar range. These low ratios may still be successfully corrected with the applied mass bias and interference correction methods only if the $^{50}Cr/^{52}Cr$ (or $^{50}Cr/^{53}Cr$) and $^{50}Ti/^{49}Ti$ ratios in the samples do not deviate highly from the applied natural correction ratios (section 2.6) as observed by Schuth et al. (2017) for natural samples. Our samples, on the other hand, are likely highly fractionated during the different cleanup columns and hence, the application of natural $^{50}Cr/^{52}Cr$ (or $^{50}Cr/^{53}Cr$) and $^{50}Ti/^{49}Ti$ ratios for interference correction is not possible.

7. Final implications and conclusions from this study

7.1 General problems during the procession of seawater

During the different methodical tests that were performed in this study, several issues regarding analytical work were encountered. A general problem during the purification of a V fraction from a matrix is V loss due to failed ion-exchange processes. During the main cleanup, this may happen due to its pH sensitivity during partitioning onto the resin and the instability of the V-peroxide complexes. Hence, solutions must be carefully completely dried down before re-fluxing with low molar chloric acid and then immediately adding the peroxide. During the different runs, it was observed that using only 0.003 M HCl the pH is kept steady around 2.5 and not lower. Wu et al. (2019) even observed a better separation of V and Ti with 2 % H_2O_2 which was not tested in this study. During the Fe cleanup steps, V was found to be lost without a systematic reason, however, matrices with a high Fe/V ratio may result in a successful Fe cleanup whereas a low Fe/V ratio may result in V loss (section 4.7.2). Additionally, a natural sample matrix may influence the ion-exchange process as well and disturb V partitioning onto the resin.

During the process of V separation from seawater and for the calculation of true V yields, it is necessary to measure the composition of seawater. Because of the high salt matrix load of seawater, these measurements are not trivial. At the beginning of this study, the ICP-OES was used which has the disadvantage that the very low V concentrations may be below the detection limit because of too high dilution factors applied to unknown samples. Due to a continuum spectral background in the ICP-OES, the detection limits are easily three orders of magnitude higher than in ICP-MS (Olesik, 1991) which was used additionally. In both machines, the sample introductory system (capillaries and nebulizer) can be obstructed by a high matrix load so that the sample uptake becomes unstable or even stops. Further, the high matrix load can disturb the ionization process in the plasma in both machines and may also increase detection limits due to spectral or isobaric interferences (Olesik, 1991).

In the mass spectrometer, an unsteady plasma can cause higher space-charge effects which occur in the plasma due to the different masses of the ions and result in discrimination of light isotopes over heavy ones (Montaser, 1998). Usually, during combined internal and external calibration these effects are neglected, but in a high salt matrix, the standards and samples do behave different. A solution to this problem would be the use of matrix-matched standards, however, the high salt matrix of seawater cannot easily be simulated in reference materials. In general, samples are diluted down so far that also the matrix is diluted and thus roughly matches the matrix of pure reference solutions. In the case of seawater, the matrix is simply too high and even matrix-matched standards may not be measured successful. Thus, in this study, different introductory and interface setups for the Element XR ICP-MS were tested to

minimize matrix effects. Also, the V background should be kept low (< 250 cps in medium resolution). The V background was found to vary highly during most sessions with values up to 8000 cps. A high V background in the machine, likely resulting from cones, capillaries, nebulizer or injector, results in high limits of detection. This can also affect the quality of the external calibration curve as low standards might then also be below the LOD. All these problems must be considered when measuring seawater samples with the Element XR ICP-MS and increase the external errors on measured concentrations. Hence, specified approaches, such as a seaFAST-introductory system may solve these issues (Hathorne et al., 2012; Poehle et al., 2015) and give precise and accurate elemental compositions of seawater.

Apart from the machine caused problems, handling of samples can also induce uncertainties on the calculations of yields. For example, matrix fractions are diluted volumetric to save time during the preparation and of course, this increases uncertainties on the final calculated compositions. All of the above discussed problems apply to measurements of 'original or doped seawater' and 'after Chelex seawater' that may still contain alkali and earth alkali elements in the mg-range. Thus, a precise interpretation of yields within the Chelex separation cannot be performed and these data is carefully reviewed (indicated by '~' before V yield). In the final cleaned V fractions, on the other hand, yields can be calculated accurately.

During this study, it was found that V readily adsorbs into PFA beakers when a pure V solution is evaporated. Hence, glass beakers were chosen to be used for eluting V fractions and preparing them to be measured. This, however, results unpredictable V loss due to non-quantitative transfer of sample solutions from one glass beaker onto columns or into tubes for measurements. This problem was quantified with different samples during this study and showed V loss between 1 % and 6 % in the final V beaker (supplementary tables S 10, S 13, and S 25). In detail, the final V fraction is re-dissolved in low molar nitric acid gravimetrically in the glass beaker. This solution is re-filled into tubes or eppis and cannot be rinsed through the beaker with additional acid, or it would be again diluted. For all other steps, such as loading the columns or non-gravimetric transfers, the solution was rinsed through the beaker by adding new acid and re-filling this into the foreseen new column or container. Here, additional dilution is not problematic.

7.2 Comparison of the applied method with those from other labs

In October 2018, Wu et al. (2019) published the first V isotope results of seawater. Their method applies Nobias chelating resin and several following ion-exchange columns for cleanup and in general is very similar to the here tested final method. We applied Chelex-100 resin which consists of styrene divinylbenzene copolymers that operate with iminodiacetate functional groups. In addition, Nobias resin has the ethylenediaminetriacetic and iminodiacetic

acid functional groups (Sohrin et al., 2008). Thus, both resins work similarly and have the potential to be used for pre-concentrating V and of course, their application differs in the individual resin optimization. The following cleanup of the pre-concentrated metals fraction differs as well. Wu et al. (2019) also test two slightly different approaches (WHOI and FSU methods) that were modified and optimized from previously published methods from Nielsen et al. (2011) and Wu et al. (2016) whereas our cleanup method was modified from Brüske (2015) and Schuth et al. (2017).

In total, the WHOI and FSU methods apply three cleanup steps to sufficiently remove especially Cr and Ti whereas here, we used either three (North Sea test 5 and Antarctic) or five columns (North Sea tests 1 – 4) for the successfully processed samples. However, the methods with three cleanup columns (North Sea test 5 and Antarctic) showed better V yield and will be finally compared to WHOI and FSU. Both WHOI and FSU methods apply an anion AG1X8 (200 – 400 mesh resin) column right after the Nobias separation where V is retained with 0.01 M HCl and 1 or 2 % H_2O_2. Our approach is very similar, only uses the resin in size 100 – 200 mesh and only 0.003 M HCl. Remaining Cr and Ti are further removed with the same, only down-scaled column additionally twice in the FSU method and once in the WHOI method. We used our main cleanup a second time as well, however, the third cleanup (Ti cleanup) differs from both the third of the WHOI. The WHOI method utilizes another additional anion resin column where V is retained on the resin in low-molar HF to separate Ti quantitatively. We adopted a LN resin column for the V-Ti separation. Between all these different ion-exchange resin, major difference may lay in the blank contributions from the resins and acids. The exact blank contributions are not published in Wu et al. (2019) and hence, cannot be directly compared to our approach. Also, measured $^{51}V/^{52}Cr$ and $^{51}V/^{49}Ti$ ratios of the samples are not published and unfortunately not discussed in the paper. Nevertheless, the WHOI and FSU methods were extensively tested for reasons of V loss in natural and spiked seawater samples.

Very similar to our results, it was found that natural seawater samples experienced a general V loss of ~30 % in the first Nobias column, which we observed for many North Sea samples as well (Table 16). In comparison, the doped matrix samples showed higher V recovery in our experiments as well as the doped samples (matrices and seawater with V standard-addition) in Wu et al. (2019). Hence, this V loss is likely a sample phenomenon and does not result from the used chelating resin, as already pointed out by Wu et al. (2019). Further test, on how to prepare and pre-treat samples to gain control on further sample components, such as organics, may help to optimize the V yield. However, our results and Wu et al. (2019) showed that V isotopes are usually not fractionated during the seawater separation even though V loss occurs. It should be noted, however, that Wu et al. (2019) did not measure their real starting compositions of seawater due to lack of a precise method. They back-calculated their starting

compositions from the comparison of ion beam intensities of samples and standards and used the measured-to-certified V contents for this calculation. Nevertheless, precise measurements are recommended for the true calculation of V yields, as yields vary during both methods. Here, we encountered many problems during the concentration measurements of pure seawater as well (section 7.1) and using a specified approach may solve this problem and increase precision of the method by accurate calculation of V yields.

7.3 Discussion of measured V isotopic signatures of seawater

The mass-spectrometric protocols that were used in this work and in Wu et al. (2019) differ to some extent. We use Fe as a mass bias monitor for any mass discrimination in the ICP-source, whereas Wu et al. (2019) apply the standard-sample bracketing and correct mass discrimination of Cr and Ti with previous measurements of respective pure Cr and Ti solutions. Moreover, Wu et al. (2019) use a Jet sampler cone, which in our study cannot be used due to too high molecular interferences on the ^{54}Fe. The Jet sampler, however, gives the big advantage of possible measurements of much lower V contents and hence, reduces the needed seawater amount (0.5 l in Wu et al. (2019) compared to 2 l in our approach). The use of X skimmer cones in further seawater analyses is recommended to be tested as we only used standard H skimmer and sampler cones. However, a lower V sample amount is also more sensitive to blank contaminations and hence, blanks should be extensively controlled. In opposite to Wu et al. (2019), we use a SEM and 10^{13} Ω resistor for the very low signals of ^{52}Cr and ^{49}Ti. These detectors enable higher precision on the low abundant interferences, however, also require exact calibration. Wu et al. (2019) use 10^{11} Ω resistors for both, however, due to their whole setup, measure with higher V intensities. This in turn, also increases precision and may compensate the poorer detectors/amplifiers.

Apart from these differences, however, the use of the same reference materials proofs inter-lab comparability of measured δ^{51}V values. Our data is given relative to the Nist-3165 solution, whereas Wu et al. (2019) present the data relative to the Alfa-Aesar solution provided by Julie Prytulak, Imperial College, UK. We also got an aliquot of this standard as well as the BDH solution from Imperial College. These two were measured during our sessions and BDH resulted in δ^{51}V$_{Alfa-JP}$ = -1.27 ‰ ± 0.20 ‰ (n = 19) which is in agreement with previously reported values (Nielsen et al., 2011; Prytulak et al., 2011; Wu et al., 2016; Schuth et al., 2017; Wu et al., 2019). Hence, our data and that of Wu et al. (2019) are comparable by re-calculating their values into the Nist-3165 nomenclature. For this, we use the reported values from Schuth et al. (2017) for Nist-3165 relative to Alfa-Aesar from Julie Prytulak of δ^{51}V$_{Alfa-JP}$ = +0.67 ‰ ± 0.07 ‰ (n = 4). This translates the measured seawater value from Wu

et al. (2019) of $\delta^{51}V_{\text{Alfa-JP}}$ = +0.20 ‰ ± 0.15 ‰ into a calculated average seawater V isotope composition of $\delta^{51}V_{\text{Nist-3165, calc}}$ = -0.47 ‰ ± 0.15 ‰.

Our North Sea seawater samples gave an average $\delta^{51}V_{\text{Nist-3165}}$ = -0.62 ‰ ± 0.25 ‰ (n = 17), which agrees with the reported value from Wu et al. (2019) within both analytical uncertainties. A more precise analysis maybe resolves slight differences between the two values, which may result from the nearshore origin of our North Sea sample and indicate individual characters of tidal-influenced basins, such as the North Sea. However, the similarity of both the seawater values from Wu et al. (2019) and our data may also indicate that the North Sea shows the same homogenous V isotope composition as the open-ocean. No information is available about the sampling depth of the North Sea water and the distance to the coast; hence, these parameters cannot be discussed in view of the final V isotope composition.

For the Antarctic seawater sample, a V isotope signature of $\delta^{51}V_{\text{Nist-3165}}$ = -2.53 ‰ ± 0.21 ‰ (n = 5) was measured. This value is significantly lower than North Sea and open-ocean (Wu et al., 2019) and needs thorough analyses of possible explanations. The measured V isotope value may be falsified by high Cr and Ti contents as indicated by the low $^{51}V/^{52}Cr$ and $^{51}V/^{49}Ti$ ratios or other molecular interferences. On the other hand, such a low V isotope signature in the Antarctic ocean may be real and indicative of different conditions, e.g. salt, pH, or temperature, and non-conservative behavior of V compared to the other oceans due to the different properties of the Southern Ocean. Here, the influence from continental run-off, the circumpolar current (less mixing with other oceans), less seasonal variations, less input of organic matter and less anthropogenic influence should be considered. However, a systematic study about these parameters and their influence on V contents and isotope compositions is missing and hence, any conclusions remain hypothetic and elusive. Very low and variable $\delta^{51}V$ signatures have been previously measured in two manganese nodules (Nod-A from the Atlantic Ocean and Nod-P from the Pacific Ocean) by Wu et al. (2016). The re-calculated $\delta^{51}V_{\text{Nist-3165\_Nod-A}}$ = -1.66 ‰ ± 0.1 ‰ and $\delta^{51}V_{\text{Nist-3165\_Nod-P}}$ = -2.32 ‰ ± 0.06 ‰ indicate that V isotopes are significantly fractionated towards low isotope values during low-temperature marine processes. Potential future studies will reveal these characteristic processes and V isotopes may be potentially used to track environmental cycling in low temperature regimes.

7.4 Concluding remarks

The comparison of the Fe co-precipitation method in opposite to the Chelex-100 chelating resin ion-exchange method revealed that both methods may be applied for the separation of V from seawater, however, both methods have their limits. The main problem during analyses of V isotopes in seawater are the comparatively similar amounts of Cr and Ti. Their quantitative separation revealed to be the main issue during all tests. This is increased by the fact that V

was lost during several steps in both methods and hence, compensated also the separated Cr and Ti. Consequently, the V/Cr and V/Ti ratios in most final V fractions were not high enough for precise and accurate V isotope measurements. For the natural samples, the measurements of starting compositions proved to be a major problem and resulted in high uncertainties. These are responsible for highly variable yields and hence, these numbers cannot be quantitatively interpreted.

The Fe co-precipitation approach included the addition of a high portion of Fe into the samples which may cause a failure of the following main cleanup ion-chromatography. Hence, Fe must be quantitatively separated with additional Fe cleanup steps, however, additional steps always bear the risks of additional V loss. In total, the Fe co-precipitation needed more cleanups steps than a successful separation with ion-exchange resin Chelex-100. Less steps decrease the risk of V loss and time consumption. Further tests to optimize the Fe co-precipitating conditions, such as pH, ageing of the precipitate and optimal amount of added Fe are needed to successfully apply this method for V isotope measurements.

The separation of V with ion-exchange resin Chelex-100 showed highly variable results for different seawater samples (natural, synthetic, and doped), indicative of a high dependence of the partitioning of V onto the resin on seawater matrices or V speciation. The replicate analyses of North Sea samples revealed an average yield of 74 % of V onto Chelex-100 resin, which may be optimized in further methodical development by varying pH (and buffer), resin volume or sample preparation, especially to destroy organic compounds as already tested for some approaches by Wu et al. (2019). This non-quantitative V sorption revealed to be the major cause of V loss during the procedure. Nevertheless, the replicate North Sea seawater samples were successfully analyzed for their V isotope composition and revealed a signature of $\delta^{51}V_{Nist-3165}$ = -0.62 ‰ ± 0.25 ‰ (n = 17 single analyses from 6 different and separately processed samples aliquots). Some natural seawater matrices were doped with synthetic V and these analyses showed a much more quantitative separation and reproducible V isotope analyses. This proofs that the method of V separation with ion-exchange resin Chelex-100 can be well applied for V isotope analyses. Even though the application of the method failed for other seawater samples, it may be optimized to yield quantitative V sorption, less V loss during sample cleanup steps as well as sample handling, and quantitative separation of Cr and Ti.

Acknowledgements

References (Chapters I + II, including supplementary)

Abbasse G., Ouddane B. and Fischer J. C. (2002) Determination of trace levels of dissolved vanadium in seawater by use of synthetic complexing agents and inductively coupled plasma-atomic emission spectroscopy (ICP-AES). *Anal. Bioanal. Chem.* **374**, 873–878.

Algeo T. J. and Tribovillard N. (2009) Environmental analysis of paleoceanographic systems based on molybdenum–uranium covariation. *Chem. Geol.* **268**, 211–225. Available at: http://linkinghub.elsevier.com/retrieve/pii/S0009254109003805.

Anbar A. D. and Rouxel O. (2007) Metal Stable Isotopes in Paleoceanography. *Annu. Rev. Earth Planet. Sci.* **35**, 717–746. Available at: http://www.annualreviews.org/doi/10.1146/annurev.earth.34.031405.125029.

Andersen M. B., Romaniello S., Vance D., Little S. H., Herdman R. and Lyons T. W. (2014) A modern framework for the interpretation of 238U/235U in studies of ancient ocean redox. *Earth Planet. Sci. Lett.* **400**, 184–194. Available at: http://dx.doi.org/10.1016/j.epsl.2014.05.051.

Andersen M. B., Stirling C. H., Potter E. K. and Halliday A. N. (2004) Toward epsilon levels of measurement precision on 234U/ 238U by using MC-ICPMS. *Int. J. Mass Spectrom.* **237**, 107–118.

Andersen M. B., Stirling C. H. and Weyer S. (2017) Uranium Isotope Fractionation. *Rev. Mineral. Geochemistry* **82**, 799–850. Available at: http://rimg.geoscienceworld.org/lookup/doi/10.2138/rmg.2017.82.19.

Andersen M. B., Vance D., Morford J. L., Bura-Nakić E., Breitenbach S. F. M. and Och L. (2016) Closing in on the marine 238U/235U budget. *Chem. Geol.* **420**, 11–22. Available at: http://linkinghub.elsevier.com/retrieve/pii/S0009254115300887.

Archer C. and Vance D. (2008) The isotopic signature of the global riverine molybdenum flux and anoxia in the ancient oceans. *Nat. Geosci.* **1**, 597–600.

Arnold G. L., Anbar A. D., Barling J. and Lyons T. W. (2004) Molybdenum Isotope Evidence for Widespread Anoxia in Mid-Proterozoic Oceans. *Science (80-.).*

Barling J., Arnold G. L. and Anbar A. . (2001) Natural mass-dependent variations in the isotopic composition of molybdenum. *Earth Planet. Sci. Lett.* **193**, 447–457. Available at: http://linkinghub.elsevier.com/retrieve/pii/S0012821X01005143.

Beck M., Dellwig O., Fischer S., Schnetger B. and Brumsack H. J. (2012) Trace metal geochemistry of organic carbon-rich watercourses draining the NW German coast. *Estuar. Coast. Shelf Sci.* **104**–**105**, 66–79. Available at: http://dx.doi.org/10.1016/j.ecss.2012.03.025.

Bekker A., Holland H. D., Wang P. L., Rumble D., Stein H. J., Hannah J. L., Coetzee L. L. and Beukes N. J. (2004) Dating the rise of atmospheric oxygen. *Nature* **427**, 117–120.

Berglund M. and Wieser M. E. (2011) Isotopic compositions of the elements 2009 (IUPAC Technical Report). *Pure Appl. Chem.* **83**, 397–410. Available at: http://www.degruyter.com/view/j/pac.2011.83.issue-2/pac-rep-10-06-02/pac-rep-10-06-02.xml.

Bigeleisen J. (1996) Nuclear Size and Shape Effects in Chemical Reactions. Isotope Chemistry of the Heavy Elements. *J. Am. Chem. Soc.* **118**, 3676–3680. Available at: https://doi.org/10.1021/ja954076k.

Bittner F. and Mendel R. R. (2010) Cell biology of molybdenum. *Plant Cell Monogr.* **17**, 119–143.

Brennecka G. A., Herrmann A. D., Algeo T. J. and Anbar A. D. (2011) Rapid expansion of oceanic anoxia immediately before the end-Permian mass extinction. *Proc. Natl. Acad. Sci.* **108**, 17631–17634. Available at: http://www.pnas.org/cgi/doi/10.1073/pnas.1106039108.

Brüske A. (2015) Vanadium isotopes – a potential new proxy for paleo-oceanography. .

Chen X., Romaniello S. J. and Anbar A. D. (2017) Uranium isotope fractionation induced by aqueous speciation: Implications for U isotopes in marine CaCO3 as a paleoredox proxy. *Geochim. Cosmochim. Acta* **215**, 162–172. Available at: http://dx.doi.org/10.1016/j.gca.2017.08.006.

Cheng H., Edwards R. L., Hoff J., Gallup C. D., Richards D. A. and Asmerom Y. (2000) The half-lives of uranium-234 and thorium-230. *Chem. Geol.*, 17–33.

Cheng H., Lawrence Edwards R., Shen C. C., Polyak V. J., Asmerom Y., Woodhead J., Hellstrom J., Wang Y., Kong X., Spötl C., Wang X. and Calvin Alexander E. (2013) Improvements in 230Th dating, 230Th and 234U half-life values, and U-Th isotopic measurements by multi-collector inductively coupled plasma mass spectrometry. *Earth Planet. Sci. Lett.* **371**–**372**, 82–91. Available at: http://dx.doi.org/10.1016/j.epsl.2013.04.006.

Chou C. L. and Moffatt J. D. (2000) A simple co-precipitation inductively coupled plasma mass spectrometric method for the determination of uranium in seawater. *Fresenius. J. Anal. Chem.* **368**, 59–61.

Collier R. W. (1985) Molybdenum in the Northeast Pacific Ocean. *Limnol. Oceanogr.* **30**, 1351–1354.

Dahl T. W., Anbar A. D., Gordon G. W., Rosing M. T., Frei R. and Canfield D. E. (2010) The behavior of molybdenum and its isotopes across the chemocline and in the sediments of sulfidic Lake Cadagno, Switzerland. *Geochim. Cosmochim. Acta* **74**, 144–163.

Deutsches Institut für Normung e. V. (2008) DIN 32 645:2008-11, Beuth Verlag, Berlin.

Dellwig O., Leipe T., März C., Glockzin M., Pollehne F., Schnetger B., Yakushev E. V., Böttcher M. E. and Brumsack H. J. (2010) A new particulate Mn-Fe-P-shuttle at the redoxcline of anoxic basins. *Geochim. Cosmochim. Acta* **74**, 7100–7115.

Dunk R. M., Mills R. A. and Jenkins W. J. (2002) A reevaluation of the oceanic uranium budget for the Holocene. *Chem. Geol.* **190**, 45–67.

Emerson S. R. and Huested S. S. (1991) Ocean anoxia and the concentrations of molybdenum and vanadium in seawater. *Mar. Chem.* **34**, 177–196.

Erickson B. E. and Helz G. R. (2000) Molybdenum(VI) speciation in sulfidic waters: Stability and lability of thiomolybdates. *Geochim. Cosmochim. Acta* **64**, 1149–1158.

Gao Y., Casey J. F., Bernardo L. M., Yang W. and Bissada K. K. (Adry) (2017) Vanadium

isotope composition of crude oil: effects of source, maturation and biodegradation. *Geol. Soc. London, Spec. Publ.*, SP468.2. Available at: http://sp.lyellcollection.org/lookup/doi/10.1144/SP468.2.

Goldberg T., Archer C., Vance D. and Poulton S. W. (2009) Mo isotope fractionation during adsorption to Fe (oxyhydr)oxides. *Geochim. Cosmochim. Acta* **73**, 6502–6516.

Gordon G. W., Lyons T. W., Arnold G. L., Roe J., Sageman B. B. and Anbar A. D. (2009) When do black shales tell molybdenum isotope tales? *Geology* **37**, 535–538.

Goto K. T., Anbar A. D., Gordon G. W., Romaniello S. J., Shimoda G., Takaya Y., Tokumaru A., Nozaki T., Suzuki K., Machida S., Hanyu T. and Usui A. (2014) Uranium isotope systematics of ferromanganese crusts in the Pacific Ocean: Implications for the marine 238U/235U isotope system. *Geochim. Cosmochim. Acta* **146**, 43–58. Available at: http://dx.doi.org/10.1016/j.gca.2014.10.003.

Greaney A. T., Rudnick R. L., Gaschnig R. M., Whalen J. B., Luais B. and Clemens J. D. (2018) Geochemistry of molybdenum in the continental crust. *Geochim. Cosmochim. Acta* **238**, 36–54.

Gumsley A. P., Chamberlain K. R., Bleeker W., Söderlund U., de Kock M. O., Larsson E. R. and Bekker A. (2017) Timing and tempo of the Great Oxidation Event. *Proc. Natl. Acad. Sci.* **114**, 1811–1816. Available at: http://www.pnas.org/lookup/doi/10.1073/pnas.1608824114.

Gustafsson J. P. (2019) Vanadium geochemistry in the biogeosphere –speciation, solid-solution interactions, and ecotoxicity. *Appl. Geochemistry* **102**, 1–25. Available at: https://linkinghub.elsevier.com/retrieve/pii/S0883292718303883.

Hathorne E. C., Haley B., Stichel T., Grasse P., Zieringer M. and Frank M. (2012) Online preconcentration ICP-MS analysis of rare earth elements in seawater. *Geochemistry, Geophys. Geosystems* **13**, 1–12.

Helz G. R., Miller C. V., Charnock J. M., Mosselmans J. F. W., Pattrick R. A. D., Garner C. D. and Vaughan D. J. (1996) Mechanism of molybdenum removal from the sea and its concentration in black shales: EXAFS evidence. *Geochim. Cosmochim. Acta* **60**, 3631–3642.

Ho P., Lee J.-M., Heller M. I., Lam P. J. and Shiller A. M. (2018) The distribution of dissolved and particulate Mo and V along the U.S. GEOTRACES East Pacific Zonal Transect (GP16): The roles of oxides and biogenic particles in their distributions in the oxygen deficient zone and the hydrothermal plume. *Mar. Chem.* **201**, 242–255. Available at: https://www.sciencedirect.com/science/article/pii/S0304420317303079?via%3Dihub [Accessed February 25, 2019].

Holland H. D., Turekian K. K., Elderfield H., Craig H., Edmond John and Emiliani C. (2004) *Treatise on geochemistry. Vol. 6, The oceans and marine geochemistry.*, Elsevier, Amsterdam.

Huang J. H., Huang F., Evans L. and Glasauer S. (2015) Vanadium: Global (bio)geochemistry. *Chem. Geol.* **417**, 68–89. Available at: http://dx.doi.org/10.1016/j.chemgeo.2015.09.019.

Inagaki K., Zhu Y., Miura T. and Chiba K. (2009) Coprecipitation in Trace Element Analysis. *Encycl. Anal. Chem.* Available at: http://doi.wiley.com/10.1002/9780470027318.a9065.

IRMM (2008) *Isotopic Reference Materials Catalogue*.

Jeandel C., Caisso M. and Minster J. F. (1987) Vanadium behaviour in the global ocean and in the Mediterranean sea. *Mar. Chem.* **21**, 51–74.

Kendall B., Dahl T. W. and Anbar A. D. (2017) THE STABLE ISOTOPE GEOCHEMISTRY OF MOLYBDENUM. *Rev. Mineral. Geochemistry* **82**, 683–732. Available at: http://rimg.geoscienceworld.org/lookup/doi/10.2138/rmg.2017.82.16.

Kendall B., Komiya T., Lyons T. W., Bates S. M., Gordon G. W., Romaniello S. J., Jiang G., Creaser R. A., Xiao S., McFadden K., Sawaki Y., Tahata M., Shu D., Han J., Li Y., Chu X. and Anbar A. D. (2015) Uranium and molybdenum isotope evidence for an episode of widespread ocean oxygenation during the late ediacaran period. *Geochim. Cosmochim. Acta* **156**, 173–193. Available at: http://dx.doi.org/10.1016/j.gca.2015.02.025.

Kester D. R., Duedall I. W., Connors D. N. and Pytkowicz R. M. (1976) Preparation of artificial seawater. , 176–179.

Kowalski N., Dellwig O., Beck M., Fischer S., Brumsack H.-J., Piepho M., Freund H., Böttcher

M. E., Grunwald M. and Riedel T. (2009) Trace metal dynamics in the water column and pore waters in a temperate tidal system: response to the fate of algae-derived organic matter. *Ocean Dyn.* **59**, 333–350.

Ku T., Knauss K. G. and Mathieu G. G. (1977) Uranium in open ocean: concentration and isotopic composition. *Deep Sea Res.* **24**, 1005–1017.

Laboratories Bio-Rad (2016) *Certificate chelex-100*.

Laboratories Bio-Rad *Manual Chelex 100 and Chelex 200*.

Lau K. V., Macdonald F. A., Maher K. and Payne J. L. (2017) Uranium isotope evidence for temporary ocean oxygenation in the aftermath of the Sturtian Snowball Earth. *Earth Planet. Sci. Lett.* **458**, 282–292.

Leya I., Schönbächler M., Wiechert U., Krähenbühl U. and Halliday A. N. (2007) High precision titanium isotope measurements on geological samples by high resolution MC-ICPMS. *Int. J. Mass Spectrom.* **262**, 247–255.

Luo G., Ono S., Beukes N. J., Wang D. T., Xie S. and Summons R. E. (2016) Rapid oxygenation of Earth ' s atmosphere 2 . 33 billion years ago. *Sci. Adv.* **2**, e1600134.

Miller C. A., Peucker-Ehrenbrink B., Walker B. D. and Marcantonio F. (2011) Re-assessing the surface cycling of molybdenum and rhenium. *Geochim. Cosmochim. Acta* **75**, 7146–7179.

Montaser A. (1998) *Inductively coupled plasma mass spectrometry.*, John Wiley & Sons.

Morford J. L. and Emerson S. (1999) The geochemistry of redox sensitive trace metals in sediments. *Geochim. Cosmochim. Acta* **63**, 1735–1750.

Morford J. L., Emerson S. R., Breckel E. J. and Kim S. H. (2005) Diagenesis of oxyanions (V, U, Re, and Mo) in pore waters and sediments from a continental margin. *Geochim. Cosmochim. Acta* **69**, 5021–5032.

Moynier F., Fujii T., Brennecka G. A. and Nielsen S. G. (2013) Nuclear field shift in natural environments. *Comptes Rendus - Geosci.* **345**, 150–159.

Münker C., Weyer S., Scherer E. and Mezger K. (2001) Separation of high field strength elements (Nb, Ta, Zr, Hf) and Lu from rock samples for MC-ICPMS measurements. *Geochemistry, Geophys. Geosystems* **2**.

Nägler T., Neubert N., Böttcher M. E., Dellwig O. and Schnetger B. (2011) Molybdenum isotope fractionation in pelagic euxinia: Evidence from the modern Black and Baltic Seas. *Chem. Geol.* **289**, 1–11.

Nägler T., Siebert C., Lüschen H. and Böttcher M. E. (2005) Sedimentary Mo isotope record across the Holocene fresh-brackish water transition of the Black Sea. *Chem. Geol.* **219**, 283–295.

Nakagawa Y., Takano S., Firdaus M. L., Norisuye K., Hirata T., Vance D. and Sohrin Y. (2012) The molybdenum isotopic composition of the modern ocean. *Geochem. J.* **46**, 131–141.

Neubert N., Nägler T. F. and Böttcher M. E. (2008) Sulfidity controls molybdenum isotope fractionation into euxinic sediments: Evidence from the modern Black Sea. *Geology* **36**, 775–778.

Nielsen S. G., Owens J. D. and Horner T. J. (2016) Analysis of high-precision vanadium isotope ratios by medium resolution MC-ICP-MS. *J. Anal. At. Spectrom.* **31**, 531–536. Available at: http://xlink.rsc.org/?DOI=C5JA00397K.

Nielsen S. G., Prytulak J. and Halliday A. N. (2011) Determination of Precise and Accurate 51V/50V Isotope Ratios by MC-ICP-MS, Part 1: Chemical Separation of Vanadium and Mass Spectrometric Protocols. *Geostand. Geoanalytical Res.* **35**, 293–306.

Nielsen S. G., Prytulak J., Wood B. J. and Halliday A. N. (2014) Vanadium isotopic difference between the silicate Earth and meteorites. *Earth Planet. Sci. Lett.* **389**, 167–175. Available at: http://dx.doi.org/10.1016/j.epsl.2013.12.030.

Noordmann J., Weyer S., Georg R. B., Jöns S. and Sharma M. (2016) 238U/235U isotope ratios of crustal material, rivers and products of hydrothermal alteration: new insights on the oceanic U isotope mass balance. *Isotopes Environ. Health Stud.* **52**, 141–163.

Olesik J. W. (1991) Elemental Analysis Using ICP-OES and ICP/MS. *Anal. Chem.* **63**.

Pai S.-C., Fang T.-H., Chen C.-T. A. and Jeng K.-L. (1990) A low contamination chelex-100 technique for shipboard pre-concentration of heavy metals in seawater. *Mar. Pet. Geol.* **29**, 295–306.

Pai S. C., Whung P. Y. and Lai R. L. (1988) Pre-concentration efficiency of chelex-100 resin

for heavy metals in seawater. Part 1. Effects of pH and Salts on the Distribution Ratios of Heavy Metals. *Anal. Chim. Acta* **211**, 257–270.

Peacock C. L. and Sherman D. M. (2004) Vanadium(V) adsorption onto goethite (α-FeOOH) at pH 1.5 to 12: A surface complexation model based on ab initio molecular geometries and EXAFS spectroscopy. *Geochim. Cosmochim. Acta* **68**, 1723–1733.

Poehle S., Schmidt K. and Koschinsky A. (2015) Determination of Ti, Zr, Nb, V, W and Mo in seawater by a new online-preconcentration method and subsequent ICP-MS analysis. *Deep. Res. Part I Oceanogr. Res. Pap.* **98**, 83–93. Available at: http://dx.doi.org/10.1016/j.dsr.2014.11.014.

Poulson Brucker R. L., McManus J., Severmann S. and Berelson W. M. (2009) Molybdenum behavior during early diagenesis: Insights from Mo isotopes. *Geochemistry, Geophys. Geosystems* **10**.

Proemse B. C., Grasby S. E., Wieser M. E., Mayer B. and Beauchamp B. (2013) Molybdenum isotopic evidence for oxic marine conditions during the latest Permian extinction. *Geology* **41**, 967–970. Available at: https://pubs.geoscienceworld.org/geology/article/41/9/967-970/131345.

Prytulak J., Nielsen S. G. and Halliday A. N. (2011) Determination of Precise and Accurate 51V/50V Isotope Ratios by Multi-Collector ICP-MS, Part 2: Isotopic Composition of Six Reference Materials plus the Allende Chondrite and Verification Tests. *Geostand. Geoanalytical Res.* **35**, 307–318.

Prytulak J., Nielsen S. G., Ionov D. A., Halliday A. N., Harvey J., Kelley K. A., Niu Y. L., Peate D. W., Shimizu K. and Sims K. W. W. (2013) The stable vanadium isotope composition of the mantle and mafic lavas. *Earth Planet. Sci. Lett.* **365**, 177–189. Available at: http://dx.doi.org/10.1016/j.epsl.2013.01.010.

Prytulak J., Sossi P. A., Halliday A. N., Plank T., Savage P. S. and Woodhead J. D. (2017) Stable vanadium isotopes as a redox proxy in magmatic systems? *Geochemical Perspect. Lett.*, 75–84. Available at: http://www.geochemicalperspectivesletters.org/article1708.

Renshaw J. C., Butchins L. J. C., Livens F. R., May I., Charnock J. M. and Lloyd J. R. (2005) Bioreduction of uranium: Environmental implications of a pentavalent intermediate. *Environ. Sci. Technol.* **39**, 5657–5660.

Riley J. P. and Taylor D. (1968) The use of chelating ion exchange in the determination of molybdenumand vanadium in seawater. *Anal. Chim. Acta* **41**, 175–178.

Rolison J. M., Stirling C. H., Middag R. and Rijkenberg M. J. A. (2017) Uranium stable isotope fractionation in the Black Sea: Modern calibration of the 238 U/ 235 U paleo-redox proxy. *Geochim. Cosmochim. Acta* **203**, 69–88. Available at: http://linkinghub.elsevier.com/retrieve/pii/S0016703716307116.

Romaniello S. J., Herrmann A. D. and Anbar A. D. (2013) Uranium concentrations and238U/235U isotope ratios in modern carbonates from the Bahamas: Assessing a novel paleoredox proxy. *Chem. Geol.* **362**, 305–316.

Rudnick R. L. and Gao S. (2003) The composition of the continental crust. In *Treatise on Geochemistry* pp. 1–64.

Schlesinger W. H., Klein E. M. and Vengosh A. (2017) Global biogeochemical cycle of vanadium. *Proc. Natl. Acad. Sci.* **114**, E11092–E11100.

Schuth S., Horn I., Brüske A., Wolff P. E. and Weyer S. (2017) First vanadium isotope analyses of V-rich minerals by femtosecond laser ablation and solution-nebulization MC-ICP-MS. *Ore Geol. Rev.* **81**, 1271–1286. Available at: http://dx.doi.org/10.1016/j.oregeorev.2016.09.028.

Severmann S. and Anbar A. D. (2009) Reconstructing paleoredox conditions through a multitracer approach: The key to the past is the present. *Elements* **5**, 359–364.

Sherrell R. M. and Boyle E. A. (1988) Zinc, chromium, vanadium and iron in the Mediterranean Sea. *Deep Sea Res. Part A, Oceanogr. Res. Pap.* **35**, 1319–1334.

Siebert C., McManus J., Bice A., Poulson R. and Berelson W. M. (2006) Molybdenum isotope signatures in continental margin marine sediments. *Earth Planet. Sci. Lett.* **241**, 723–733.

Siebert C., Nägler T. F., von Blanckenburg F. and Kramers J. D. (2003) Molybdenum isotope records as a potential new proxy for paleoceanography. *Earth Planet. Sci. Lett.* **211**, 159–

171.

Van der Sloot H. A., Hoede D. and Wijkstra J. (1989) Trace oxyanions and their behaviour in the rivers Porong and Solo, the Java Sea and the adjacent Indian Ocean. *Netherlands J. Sea Res.* **23**, 379–386.

Sohrin Y., Nakatsuka Y., Minami T., Umetani K. N. S., Urushihara S., Nakatsuka S., Kono T., Higo E., Norisuye K. and Umetani S. (2008) Multielemental determination of GEOTRACES key trace metals in seawater by ICPMS after preconcentration using an ethylenediaminetriacetic acid chelating resin. *Anal. Chem.* **80**, 16.

Stirling C. H., Andersen M. B., Potter E. K. and Halliday A. N. (2007) Low-temperature isotopic fractionation of uranium. *Earth Planet. Sci. Lett.* **264**, 208–225.

Takeno N. (2005) Atlas of Eh-pH diagrams Intercomparison of thermodynamic databases. *Natl. Inst. Adv. Ind. Sci. Technol. Tokyo*, 285. Available at: http://scholar.google.com/scholar?hl=en&btnG=Search&q=intitle:Atlas+of+Eh-pH+diagrams+Intercomparison+of+thermodynamic+databases#0.

Teng F.-Z., Dauphas N. and Watkins J. M. (2017) Non-Traditional Stable Isotopes: Retrospective and Prospective. *Rev. Mineral. Geochemistry* **82**, 1–26.

Terada K. (2000) ELEMENTS BY COPRECIPITATION : Extraction. *J. Chromatogr. A*, 4394–4402.

Tissot F. L. H. and Dauphas N. (2015) Uranium isotopic compositions of the crust and ocean: Age corrections, U budget and global extent of modern anoxia. *Geochim. Cosmochim. Acta* **167**, 113–143.

Ventura G. T., Gall L., Siebert C., Prytulak J., Szatmari P., H??rlimann M. and Halliday A. N. (2015) The stable isotope composition of vanadium, nickel, and molybdenum in crude oils. *Appl. Geochemistry* **59**, 104–117. Available at: http://dx.doi.org/10.1016/j.apgeochem.2015.04.009.

Verbruggen A., Alonso A., Eykens R., Kehoe F., Kühn H., Richter S. and Aregbe Y. (2008) Preparation and Certification of IRMM-3636 , IRMM-3636a and IRMM-3636b.

Voegelin A. R., Pettke T., Greber N. D., von Niederhäusern B. and Nägler T. F. (2014) Magma differentiation fractionates Mo isotope ratios: Evidence from the Kos Plateau Tuff (Aegean Arc). *Lithos* **190**–**191**, 440–448.

Wang D. and Sañudo Wilhelmy S. A. (2009) Vanadium speciation and cycling in coastal waters. *Mar. Chem.* **117**, 52–58. Available at: http://dx.doi.org/10.1016/j.marchem.2009.06.001.

Wehrli B. and Stumm W. (1989) Vanadyl in natural waters: Adsorption and hydrolysis promote oxygenation. *Geochim. Cosmochim. Acta* **53**, 69–77.

Weisel C. P., Duce R. A. and Fasching J. L. (1984) Determination of Aluminum, Lead, and Vanadium in North Atlantic Seawater after Coprecipitation with Ferric Hydroxide. *Anal. Chem.* **56**, 1050–1052.

Weyer S., Anbar A. D., Gerdes A., Gordon G. W., Algeo T. J. and Boyle E. A. (2008) Natural fractionation of 238U/235U. *Geochim. Cosmochim. Acta* **72**, 345–359.

Weyrauch M., Oeser M., Brüske A. and Weyer S. (2017) In situ high-precision Ni isotope analysis of metals with femtosecond LA-MC-ICP-MS. *J. Anal. At. Spectrom.*, 1312–1319. Available at: http://pubs.rsc.org/en/Content/ArticleLanding/2017/JA/C7JA00147A.

Wiederhold J. G. (2015) Metal stable isotope signatures as tracers in environmental geochemistry. *Environ. Sci. Technol.* **49**, 2606–2624.

Wu F., Owens J. D., Huang T., Sarafian A., Huang K. F., Sen I. S., Horner T. J., Blusztajn J., Morton P. and Nielsen S. G. (2019) Vanadium isotope composition of seawater. *Geochim. Cosmochim. Acta* **244**, 403–415. Available at: https://doi.org/10.1016/j.gca.2018.10.010.

Wu F., Qi Y., Yu H., Tian S., Hou Z. and Huang F. (2016) Vanadium isotope measurement by MC-ICP-MS. *Chem. Geol.* **421**, 17–25. Available at: http://dx.doi.org/10.1016/j.chemgeo.2015.11.027.

Wu F., Qin T., Li X., Liu Y., Huang J. H., Wu Z. and Huang F. (2015) First-principles investigation of vanadium isotope fractionation in solution and during adsorption. *Earth Planet. Sci. Lett.* **426**, 216–224. Available at: http://dx.doi.org/10.1016/j.epsl.2015.06.048.

Supplementary

S 1. Fe co-precipitation with synthetic and natural seawater

Table S 1: Preparation of synthetic seawater A and B and doping with metals for Fe co-precipitation test.

synthetic A+B			*synthetic seawater A*		*Synthetic seawater B*	
Weight / g	2100		1100		1000	
compound	weighed portion / g	element	conc. / mg kg-1	absolute amount / µg	conc. / mg kg-1	absolute amount / µg
NaCl	56.825	Na	11189.5	12308499	10172.3	11189545
MgSO4 * 7 H2O	14.428	Mg	1412.0	1553240	1283.7	1412037
MgCl2 * 6 H2O	11.736	Ca	427.9	470688	389.0	427898
CaCl2	2.384	K	414.3	455750	376.7	414318
KCl	1.578	Cl	19031.6	20934736	17301.4	19031578
		SO4	2812.0	3093200	2556.4	2812000
U	19.983	U	9.52	10.47	9.52	9.52
V	19.997	V	9.52	10.47	9.52	9.52
Mo	20.029	Mo	9.54	10.49	9.54	9.54
Re	20.0188	Re	9.53	10.49	9.53	9.53

Table S 2: Compositions of all fractions of synthetic seawater A and B. Only the '1. V fraction' was measured with ICP-OES and is marked with an asterisk. All other data was generated with Element ICP-MS.

Element	Fe matrix / µg	1. main matrix / µg	* 1. V fraction / µg	2. main matrix / µg	Ti cleanup matrix / µg	final V fraction / µg	V fraction out of 1. main matrix / µg	2. main matrix out of 1. main matrix/ µg	Ti cleanup matrix out of 1. main matrix/ µg
				synthetic seawater A (total vol. 1.1 l)					
Na	1441	106458	65.90	17.69	0.970	1.572	18.20	236818	3.58
Mg	2.47	52913	61.30	7.91	0.014	0.210	20.39	129864	0.09
Ca		5771	11.12	1.03	0.199	0.408	2.65	5511	0.91
Ti	0.02	0.87		0.001	0.0001	0.001	0.0006	0.95	0.001
V	0.13	1562	6686	0.07	0.5323	135.7	373.1	2448	0.84
Cr	0.08	26.19	0.11	0.01	0.0009	0.003	0.05	27.32	0.001
Fe	62181	0.03		0.03	0.0011	0.022	0.01	0.12	0.004
				synthetic seawater B (total vol. 1 l)					
Na	1364	278770	44.585	9.233	1.106	1.96	8.80	205176	0.97
Mg	6.56	213822	54.07	2.953	0.076	0.30	16.36	161716	0.05
Ca	159.9	14647	8.60	19.827	0.413	0.86	1.46	4317	0.20
Ti	0.475	2.85	0.04	0.012	0.002	0.01	0.0004	0.93	0.001
V	0.07	1302	6233	0.0253	0.2753	128.8	175.2	916.4	0.66
Cr	0.09	89.74	0.11	0.0069	0.0026	0.00	0.04	28.35	0.001
Fe	57056	0.48	0.00	0.0319	0.0038	0.01	0.0021	0.15	0.001

Table S 3: Compositions of all fractions of natural seawater from Elba, Corfu and Madeira. Only the 'original seawater' was measured with ICP-OES and is marked with an asterisk. All other data was generated with Element ICP-MS. All values are back-calculated into µg relative to total samples amount (Elba 3000 g, Corfu and Madeira each 2000 g).

Element	* original seawater / µg	in seawater after precip. / µg	Fe matrix / µg	1. main matrix / µg	1. V fraction / µg	2. main matrix / µg	Ti cleanup matrix / µg	final V fraction conc / µg	V fraction out of 1. main matrix / µg	2. main matrix out of 1. main matrix / µg	Ti cleanup matrix out of 1. main matrix / µg
				Elba seawater							
Na	171489	262480661	7332	254363	102.7	51.40	0.314	0.532	63.70	249928	1.13
Mg	115737	14751099	27.91	532477	154.8	129.9	0.015	9.048	152.0	542602	0.52
Ca	296112	4284516	31.18	13628	4.32	3.612	0.117	0.410	3.22	4828	0.18
Ti		10.65	0.235	0.24	0.01	0.005	0.022	0.018	0.001	0.10	0.001
V	9.78	3.9	0.36	8.09	1.08	0.058	0.0014	0.832	0.25	2.91	0.002
Cr	1.08	2.1	0.2	0.89	0.01	0.012	0.001	0.002	0.002	0.35	0.001
Fe	1.32	7043.85	207550	2.17	0.12	0.091	0.0039	0.004	0.002	1.41	0.01
				Corfu seawater							
Na	114086	108104586	2278	39041	56.0	17.18	0.434	0.819	7.59	85316.89	1.40
Mg	77124	6448076	5.98	91458	49.69	44.48	0.007	5.449	26.22	230308	0.23
Ca	198969	1769682	8.51	4150	2.58	3.641	0.043	0.446	1.41	3793.20	0.35
Ti		1	0.05	0.01	0.01	0.011	0.001	0.0004	0.0005	0.04	0.001
V	6.42	1.6	0.07	1.77	1.54	0.106	0.0019	1.351	0.40	1.49	0.003
Cr	1.00	1.6	0.09	0.28	0.02	0.021	0.0009	0.003	0.003	0.31	0.001
Fe	0.00	1865.6	142066	2.85	1.61	1.206	0.0032	0.001	0.002	2.88	0.004
				Madeira seawater							
Na	114237	102816192	1835	11490	42.2	45.30	1.016	1.794	2.23	22899	0.75
Mg	78336	6364544	82.62	5308	8.10	26.82	0.025	1.146	4.16	5211	0.02
Ca	189657	1663392	84.38	4939	12.18	11.93	0.318	2.260	6.29	3960	0.14
Ti		1.9	0.18		1.13	0.755	0.006	0.001	0.001	0.004	0.0005
V	6.22	1.2	0.77	0.20	3.50	0.282	0.0046	3.123	0.30	0.004	0.003
Cr	1.94	3.2	0.1	0.12	0.15	0.124	0.0015	0.006	0.005	0.13	0.001
Fe	2.42	852.7	125066	0.00	3.39	1.991	0.0034	0.006	0.003	0.04	0.002

S 2. Reproduction of Chelex-100 ion-chromatography methods from the literature

Table S 4: Preparation of synthetic seawater and doping with metals for V separation tests (1), (2), and (3).

	compound	weighed portion / g	element	conc. / mg kg^{-1}	absolute amount / µg
Method (1)	NaCl	13.615	Na	10336.0	5385046
	MgSO$_4$ * 7 H$_2$O	3.489	Mg	1250.8	651692
	MgCl$_2$ * 6 H$_2$O	2.573	Ca	403.1	210018
	CaCl$_2$ * 2 H$_2$O	0.770	K	376.4	196093
	KCl	0.374	Cl	18628.3	9705340
	NaHCO$_3$	0.106	SO$_4$	2610.1	1359872
			HCO$_3$	148.4	77308
	Fe	0.00520	Fe	0.100	52.00
	V	0.05068	V	0.097	50.68
	Cr	0.05128	Cr	0.098	51.28
	Ti	0.05138	Ti	0.099	51.38
	Seawater weight / g	0.5210			
Method (2)	NaCl	13.620	Na	10338.1	5387178
	MgSO$_4$ * 7 H$_2$O	3.487	Mg	1246.0	649284
	MgCl$_2$ * 6 H$_2$O	2.555	Ca	405.2	211160
	CaCl$_2$ * 2 H$_2$O	0.775	K	374.9	195348
	KCl	0.372	Cl	18622.2	9704013
	NaHCO$_3$	0.106	SO$_4$	2607.5	1358784
			HCO$_3$	147.5	76858
	Fe	0.00511	Fe	0.098	51.10
	V	0.05078	V	0.097	50.78
	Cr	0.05156	Cr	0.099	51.56
	Ti	0.05031	Ti	0.097	50.31
	Seawater weight / g	0.5211			
Method (3)	NaCl	13.621	Na	10336.7	5386465
	MgSO$_4$ * 7 H$_2$O	3.495	Mg	1254.9	653936
	MgCl$_2$ * 6 H$_2$O	2.587	Ca	406.1	211615
	CaCl$_2$ * 2 H$_2$O	0.776	K	383.5	199822
	KCl	0.381	Cl	18654.0	9720605
	NaHCO$_3$	0.102	SO$_4$	2613.8	1362074
			HCO$_3$	141.9	73953
	Fe	0.00534	Fe	0.102	53.40
	V	0.05214	V	0.100	52.14
	Cr	0.05153	Cr	0.099	51.53
	Ti	0.05361	Ti	0.103	53.61
	Seawater weight / g	0.5211			

Table S 5: Absolute amounts of elements from measurements with the Element XR ICP-MS for Chelex-100 separation of synthetic sample (1), all values calculated to µg.

element	original seawater	doped seawater	V-1	V-2	V-3	V-4	V-5	HNO$_3$ wash	MQ wash	NH$_3$ wash	MQ wash	seawater after Chelex
Na	2529353.56	2681139.03	26.7	3885.3	136.9	52.9	49.9	20.7	2.1	2.5	1.3	8158361.993
Mg	657515.31	654614.10	3583.8	10009.2	100.5	22.7	15.2	6.7	0.1	0.3	0.2	592634.9204
Ca	219565.85	213164.92	938.6	3642.6	50.3	10.2	5.7	3.0	0.2	1.1	0.7	129622.364
Ti	0.00	50.16	3.56	45.19	1.50	0.13	0.05	0.03	0.00	0.01	0.00	0.57
V	0.10	54.05	3.459	47.354	2.089	0.184	0.079	0.074	0.002	0.031	0.000	0.493
Cr	0.00	48.06	2.781	34.107	2.300	0.400	0.353	0.963	0.067	0.047	0.003	1.208
Mn	32.48	32.19	1.208	26.751	0.580	0.089	0.051	0.023	0.000	0.001	0.001	1.726
Fe	0.00	33.31	2.926	42.159	1.724	0.167	0.066	0.034	0.011	0.032	0.021	6.757
Mo	0.05	0.07	0.56	0.01	0.00	0.00	0.00	0.00	0.00	0.00	0.00	0.05

Table S 6: Absolute amounts of elements from measurements with the Element XR ICP-MS for Chelex-100 separation of synthetic sample (2), all values calculated to µg.

element	original seawater	doped seawater	wash seawater	wash major ions	wash bef. elution	V-1	V-2	V-3	V-4	V-5	V-6	V-7	HNO$_3$+MQ wash	NH$_3$+MQ wash	seawater after Chelex
Na	9203695	8920399	18.34	5205.86	5.16	9.49	5.49	9.00	7.09	4.62	4.76	5.81	5.00	2.34	5945868
Mg	673880	653294	1850.10	16234.67	60.69	1.23	5.55	41.47	70.20	7.78	1.99	0.27	1.55	0.22	588749
Ca	150357	143710	442.96	5442.23	161.37	3.50	17.66	144.78	302.80	33.47	6.51	1.10	1.84	3.65	130288
Ti	1.09	55.85	2.31	2.89	0.01	0.50	1.09	9.84	26.59	3.56	0.18	0.07	0.19	0.02	32.25
V	0.31	59.75	4.47	5.04	0.11	0.44	0.66	7.37	22.89	6.15	0.56	0.17	0.35	0.11	4.70
Cr	0.31	52.82	2.02	2.76	0.04	0.34	0.69	7.83	21.06	3.30	0.46	0.38	3.59	0.08	1.25
Mn	36.60	35.09	1.81	0.04	0.01	0.00	0.01	10.03	20.63	1.98	0.04	0.01	0.08	0.00	1.43
Fe	7.31	58.11	2.03	2.60	0.01	0.49	0.93	10.26	27.85	4.28	0.29	0.11	0.17	0.07	23.67
Mo	0.62	0.25	0.53	0.00	0.00	0.00	0.00	0.00	0.00	0.00	0.00	0.00	0.00	0.00	0.13

Table S 7: Absolute amounts of elements from measurements with the Element XR ICP-MS for Chelex-100 separation of synthetic sample (3), all values calculated to µg.

element	original seawater	doped seawater	wash bef. elution	V-1	V-2	V-3	V-4	V-5	V-6	MQ+HNO$_3$+MQ wash	NH$_3$+MQ wash	seawater after Chelex
Na	6450674	6241429	8969.01	27.24	51.28	54.43	53.84	56.53	60.40	5212.49	2.07	6146335.60
Mg	670933	647721	1643.01	0.71	0.19	0.60	0.19	0.33	0.13	5989.64	0.13	632839.56
Ca	149839	145077	384.73	2.90	0.47	2.74	0.72	1.30	0.44	2664.13	0.15	140613.03
Ti	0.89	54.00	1.95	2.85	3.71	1.31	1.00	1.02	1.04	26.88	0.01	0.61
V	0.05	59.71	16.02	9.69	8.57	2.06	1.75	1.22	1.07	10.15	0.03	0.20
Cr	0.34	48.71	1.47	2.63	3.48	1.24	0.97	0.99	1.01	21.33	0.06	3.89
Mn	35.91	34.61	0.51	0.01	0.01	0.00	0.00	0.00	0.00	12.33	0.00	17.24
Fe	4.64	51.94	1.80	2.99	3.74	1.32	1.02	1.05	1.06	25.15	0.03	18.72
Mo	0.10	0.08	0.18	0.01	0.00	0.00	0.00	0.00	0.00	0.00	0.00	0.10

Table S 8: Absolute amounts of elements from measurements with Element XR ICP-MS for all fractions from Chelex-100, Fe, Ti, and main cleanup of Chelex-100 separation fractions and first V and main matrix fractions from synthetic seawater samples (1), (2), and (3), all values calculated to µg. The column 'Chelex fraction' describes the sum of combined fractions of the three tests (see section 4.3 for explanation).

element	Chelex fraction	1. Fe Matrix	1. Ti Matrix	1. main matrix	1. V fraction	alkali matrix	chelex reg.	2. Fe matrix	2. Ti matrix	2. main matrix	2. V fraction	1. main matrix	alkali matrix	chelex reg.	2. Fe matrix	2. Ti matrix	2. main matrix	2. V fraction
						method (1) 1. V fraction								*method (1) 1. main matrix*				
Na		27.60	62.81	35750	51.00	42.26		0.080	1.68	0.953	0.731	35750	18374	1.44	0.037	0.107	43.32	0.489
Mg	13731	11.86	55.02	19981	42.75	0.978	0.029	0.041	0.863	19.41	0.213	19981	8207	10.42	0.248	1.759	652	4.37
Ca	4647							0.691	13.23				5856	9.92	0.410	4.66	1750	8.33
Ti	50.43	0.011	38.92	0.084	0.016	0.004			0.004	0.007	0.002	0.084	0.0022			0.0001	0.0007	0.0010
V	53.16	0.024	0.159	37.69	8.19	1.95	0.019	0.212	0.019	0	3.926	37.69	4.03	0.236	1.13	0.084	0.013	27.18
Cr	39.94	0.015	0.089	33.45	0.100	0.043	0.005	0.000	0.001	0.022	0.002	33.45	2.95	1.31	0.048	0.015	18.92	0.399
Mn	28.68	0.012	0.069	24.20	0.056		0.0002	0.0003	0.001	0.050	0.001	24.20	0.7886	0.1250	0.020	0.062	22.81	0.162
Fe	47.04	45.99	0.025			0.001		0.031	0.003						0.057	0.001	0.007	0.010
Mo	0.575	0.017	0.005	0.0005	0.002	0.0001	0.0002	0.0002	0.004	0.0001	0.0002	0.0005	0.0005	0.0002	0.0003	0.0001	0.0006	0.0001
		method (2) Chelex fraction				*method (2) 1. V fraction*						*method (2) 1. main matrix*						
Na		11.01	27.22	*40629*	27.40	22.37		0.076	0.005	0.852	0.470	40629	20110	24.9	0.007	0.005	24.9	0.138
Mg	18274	1.688	27.02	*27279*	27.45	0.265	0.091	0.027	0.028	11.34	0.508	27279	11250	32.2	0.439	0.95	627	0.200
Ca	6556	3.459							0.059	7.99			10095	36.2	1.06	2.67	2044	0.000
Ti	47.05	0.002	39.061	0.095	0.013	0.001	0.001		0.001	0.001	0.001	0.095	0.011	0.003	0.0001	0.001	0.0005	0.002
V	47.88	0.003	0.061	37.99	5.45	0.257	0.049	0.192	0.008	0	3.962	37.99	5.33	0.247	1.05	0.062	0.015	26.50
Cr	38.88		0.030	35.08	0.053	0.024	0.005	0.000	0.0001	0.013	0.001	35.08	3.33	1.17	0.038	0.009	20.55	0.327
Mn	34.55	0.001	0.026	25.86	0.027		0.0003	0.0001	0.0001	0.022	0.001	25.86	1.81	0.148	0.030	0.035	23.27	0.011
Fe	48.85	46.75	0.021	0.022		0.0003	0.001	0.02	0.001	0.001	0.001	0.022	0.004		0.067		0.004	0.023
Mo	0.543	0.013	0.005	0.001	0.0002	0.00005	0.001	0.000	0.0001		0.0001	0.0006	0.0005	0.0003	0.0004	0.00004	0.0003	0.0001
		method (3) Chelex fraction				*method (3) 1. V fraction*						*method (3) 1. main matrix*						
Na		6.60	25.00	*36571*	2.49	2.75	0.00	0.04	0.03	0.25	0.53	36571	19069	8.84	0.092	0.120	47.19	0.106
Mg	7635	0.056	17.80	*17632*	1.38	0.032	0.000	0.016	0.030	0.803	0.020	17632	7139	17.92	0.846	0.230	911	1.06
Ca	3058	5.57			3.39								4486	17.84	1.97	0.453	2338	
Ti	39.76	0.003	33.664	0.037	0.008				0.001	0.001	0.0002	0.037	0.005			0.003	0.002	0.001
V	50.56	0.001	0.074	38.06	8.86	0	0.020	0.735	0.016	0	6.321	38.06	1.43	0.348	1.28	0.030	0.020	29.61
Cr	33.18	0.0003	0.028	32.90	0.064	0.014	0.006	0.001	0.0001	0.022	0.002	32.90	2.13	1.88	0.047	0.004	20.73	0.166
Mn	12.87		0.014	14.16	0.002			0.0001	0.0001	0.002	0.001	14.16	0.104	0.098	0.017	0.003	14.77	0.019
Fe	38.16	43.22	0.061	0.131	0.055		0.009	0.094	0.006		0.003	0.131	0.0001	0.004	0.190	0.001	0.001	0.002
Mo	0.194	0.018	0.003	0.0002	0.0002		0.0007	0.0003	0.0001		0.0001	0.0002	0.0003	0.0001	0.0004		0.0003	0.0000

Note: The first section header row reads *method (1) Chelex fraction*, *method (1) 1. V fraction*, *method (1) 1. main matrix*.

S 3. Maldive Islands seawater

Table S 9: Absolute composition of Maldive Islands seawater (2000 ml), all fractions from Chelex-100 separation and first cleanups (n = number of repeated analyses). All values calculated to µg or ng.

| element | Original seawater | Chelex-100 separation | | | | Chelex fraction cleanup | | | | 2. main cleanup | | blank |
		Seawater after chelex	Chelex fraction	HNO$_3$ reg.	NH$_3$ reg.	Fe matrix	Ti matrix	1. main matrix	1. V fraction	main matrix of 1. main matrix	V fraction of 1. main matrix	
Na / µg	14339927	14318088	41846	365	0.542	129	159	39824	248	32025	100	1.068
Mg / µg	2512190	2372059	23170	52.4		21.1	13.0	21899	59.6	18259	79.7	0.033
Ca / µg	794221	774737	15141	27.5		6.86	6.91	14232	30.0	11087	64.4	1.441
Ti / ng	14374	15419	60.57	12.98	0.411	1.92	13.87	11.50		26		1.737
V / ng	3724	1531	3142	45.29	64.80	5.04	3.13	2208	746	1139	656	0.408
Cr / ng												1.101
Mn / ng			72.1					69		55		0.327
Fe / ng												27.10
Mo / ng	20423	1438	17767	195	22.30	16737	42.99	6.20	1.50	4.75	0.817	0.088
n	4	2	2	2	2	2	2	2	2	2	2	2

Table S 10: Absolute composition of Maldive Islands fractions from cleanups of combined V fraction and main matrix. All values calculated to µg or ng.

| element | V fraction cleanup | | | | | | glass leaching | main matrix cleanup | | | | | | glass leaching | blank |
	chelex reg.	alkali matrix	2. Fe matrix	2. Ti matrix	2. main matrix	2. V fraction	glass leaching V beaker	chelex reg.	alkali matrix	2. Fe matrix	2. Ti matrix	2. main matrix	2. V fraction	glass leach. matrix beaker	
Na / µg		201.29	0.55	8.29	3.40	1.44	0.23	5.39	36710	0.13	0.03	70.76	0.82	0.15	0.36
Mg / µg	0.46	3.08	0.09	3.65	112.95	1.66	0.09	7.00	13102	0.24	0.38	606.90	1.05	0.02	0.02
Ca / µg				3.12	116.16	6.07	0.89	3.61	10327	0.09	0.28	899.10	0.05		0.37
Ti / ng		0.15		2.54	3.29	3.78	0.97		6.00		1.98	2.54	2.08	0.47	1.75
V / ng	6.06	0.79	6.78	3.25	1.56	1350	87.35	8.83		7.24	1.86	0.41	1072.45	37.64	0.46
Cr / ng	3.38	7.65	0.23	0.22	5.68	0.72	0.34	3.91	8.64	0.09	0.08	16.92	1.57	0.14	1.51
Mn / ng		0.20	0.07	0.73	2.66	0.77	0.15		30.12	0.04	0.07	23.13	0.05	0.02	0.14
Fe / ng	13.32	13.94	2764	10.90		8.51	3.89			177.81	1.10	18.22	52.55	2.04	11.12
Mo / ng	0.10	0.44	0.70	4.01	0.05	0.31	0.02	0.25	2.28	0.46	0.06	0.03	0.13	0.02	0.02

S 4. Reference materials along with (1), (2), and (3) and Maldive Islands

Table S 11: Vanadium, Ti, Cr, and Fe contents in reference materials during Fe, Ti, and main cleanup (processed with first cleanup round of (1), (2), and (3)). All values in µg, except for the blank (in ng).

Unit	µg	µg	µg	µg	µg	µg	ng
samples	Alfa foil I	Alfa foil II	Alfa sol. I	Alfa sol. II	Nist I	Nist II	blank
V fraction							
V	54.79	53.87	58.59	53.94	62.74	58.34	
Ti		0.006		0.361			
Cr							
Fe							
Fe matrix							
V	2.42	1.75	1.92	1.93	2.25	2.16	0.019
Ti							0.01
Cr							
Fe							
Ti matrix							
V	0.166	0.218	0.318	0.201	0.153	0.267	0.184
Ti	0.011	0.008	0.008	0.011	0.029	0.024	4.127
Cr							0.558
Fe	0.060	0.069	0.056	0.056	0.355	0.057	110.6
main matrix							
V	0.0004	0.0002	0.0002		0.0003	0.0005	0.586
Ti	0.001	0.002	0.0005		0.001		0.406
Cr				0.003			0.584
Fe							2.463

Table S 12: Vanadium, Ti, Cr, and Fe contents in reference materials during Chelex cleanup and second main cleanup (processed with Maldive Islands). All values in µg, except for the blank (in ng).

	µg	µg	µg	ng	µg
	Chelex cleanup				**main cleanup**
	Nist	Alfa sol.	Alfa foil	blank	Alfa sol.
V fraction					
V	20.24	18.08	18.30		19.17
Ti					
Cr					
Fe					
Fe matrix					
V	1.51	1.25	1.54	0.218	
Ti				0.034	
Cr				0.028	
Fe				0.953	
Ti matrix					
V	0.057	0.070	0.065	0.919	
Ti				0.336	
Cr				0.014	
Fe				1.243	
main matrix					
V				0.045	0.0001
Ti				1.107	
Cr	0.00035	0	0.00015	0.196	
Fe				1.519	

Table S 13: Absolute amounts of V, Cr, Ti, and Fe in all Chelex-100, Fe, Ti, and main cleanup matrices as well as respective blanks for reference material Alfa solution (processed together with synthetic (1), (2), (3), and Maldive Islands). Matrix compositions are blank corrected.

	weighed V amount	chelex reg.	alkali matrix	Fe matrix	Ti matrix	main matrix	V fraction	glass leaching V beaker
Chelex-100, Fe, Ti, and main cleanup								
V / ng	51540	114.0	10399	4076	93.12		36417	475.0
Ti / ng			0.170		0.742	2.811		
Cr / ng		0.497	0.453		0.204	2.684		
Fe / ng		0.301	4.485	5.704	2.486	5.445		
blanks								
		Acid	Chelex resin+acid	anion resin + acid	LN resin + acid	anion resin + acid	accum. Resins + acids	
V / ng		0.167	0.056	0.023	0.373	0.006	0.459	
Ti / ng		0.229	1.050	0.095	0.536	1.282	1.753	
Cr / ng		1.431	0.249	0.192	0.010	2.184	1.507	
Fe / ng		4.050	4.741	21.157	0.760	5.042	11.117	

S 5. North Sea test 1 – 5, natural and doped samples

Table S 14: Absolute composition of North Sea test 1 samples (natural North Sea I, II, and III) in all fractions from Chelex-100 separation and following cleanups. All values calculated to µg or ng. Each sample is 2000 g.

	seawater after chelex	1. alkali wash	1. reg. resin HNO3+MQ	1. reg. resin NH3+MQ	1. Chelex fraction	2. alkali matrix wash	2. reg. resin HNO3+MQ	2. reg. resin NH3+MQ	2. Chelex fraction	Fe matrix	1. Ti matrix	1. main matrix	1. V fraction	2. Ti matrix	2. main matrix	final V fraction
						North Sea I										
Na / µg	8084319	6808	12.98	1.79	36.65	35.68	1.64	1.88	3.14			2.06	0.63			
Mg / µg	2051506	3753	11.17	0.07	1689	168.66	1.56	0.04	1383			1020	0.57			
Ca / µg	912845	2725	6.93	0.00	2585	38.35	1.25		2360			2063				
Ti / ng	13351	7.04	0.48	5.21	296	3.78	0.63	0.22	163.2	2.09	13.37	16.01	2.87			
V / ng	275.80	0.87	3.90	6.98	2768	29.07	13.77	10.24	1873	0.67	2.59	0.15	1690			
Cr / ng					8.95							2.34				
Mn / ng		19.89			172.5				158.1			144.5				
Fe / ng			3.41	272.90	32267	234.2	71.67	3.66	19653	20457						
Mo / ng	1491	3.56	24.94	17.98	16360	76.75	138.39	58.12	13382	11948	0.99	0.90	0.55			
						North Sea II										
Na / µg	8119305	6290	2.70	1.89	16.39	16.20	1.69	1.95	2.88	0.09	0.08	2.03	0.64	0.01	0.73	0.14
Mg / µg	2020336	3848	0.66	0.07	1552	147.12	2.49	0.04	1282	0.63	0.36	1009	3.45	0.02	2.72	0.23
Ca / µg	904890	2791			2762	30.56	3.90		2519	0.96	0.28	2266	7.64		2.44	0.12
Ti / ng		0.57	0.82	6.94	399.1	7.51	1.84	7.84	206.5	1.80	14.19	18.51	1.98	2.41	6.19	12.95
V / ng	635.0	0.55	6.80	6.66	3021	38.49	22.59	12.83	1925	1.26	3.21	0.05	1883	19.42	7.69	1136
Cr / ng					8.77							0.48		0.34	7.43	13.81
Mn / ng		26.21		0.25	248.1				232.1	0.31	0.21	212.4	0.63	0.41	6.36	17.14
Fe / ng			34.24	311.26	46083	393.92	223.34	38.00	30455	26481				5.31	5.19	6.70
Mo / ng	631.12	2.99	45.08	19.14	16750	126.63	120.58	103.3	13639	10354	1.25	0.66	0.57	0.06	2.32	6.85
						North Sea III										
Na / µg	7874619	8198	1.55	1.67	29.18	27.79	1.97	2.90	2.85	0.09	0.09	2.54	0.52	0.01	0.65	0.17
Mg / µg	2063793	5177	2.70	0.07	1801	124.3	4.61	0.19	1563	0.88	1.86	1192	5.82	0.02	5.17	0.39
Ca / µg	911221	4027	1.07		3009	23.63	8.88		2792	1.57	3.59	2753	6.48		4.08	0.45
Ti / ng		8.73	0.17	6.04	474.1	9.89	1.29	0.23	281.0	2.00	14.22	34.88	1.16	2.69	5.78	12.84
V / ng	355	0.72	5.91	5.97	2932	55.45	17.68	10.78	1939	1.31	5.24		1814	19.9	7.72	1568
Cr / ng					6.42		2.33					2.60		0.35	7.88	14.12
Mn / ng		41.11			246.3				238.9	0.38	0.52	234.50	0.61	0.41	6.48	17.56
Fe / ng			25.60	197.06	51440	801.48	140.35		34393	29765					5.63	1.48	6.68
Mo / ng	657.23	3.20	37.79	20.46	16291	195.35	138.61	57.41	13349	11433	0.66	0.44	0.50	0.06	2.36	6.98

Table S 15: Absolute composition of North Sea test 2 samples (natural North Sea IV and V, and seawater matrix after Chelex of sample II) in all fractions from Chelex-100 separation and following cleanups. All values calculated to µg or ng. Each sample is 2000 g.

	after chelex	alkali matrix wash	Chelex fraction	2. Chelex fraction	reg. resin HNO$_3$+MQ	reg. resin NH$_3$+MQ	Fe matrix	1. Ti matrix	1. main matrix	1. V fraction	2. Ti matrix	2. main matrix	final V fraction
North Sea II after Chelex													
Na / µg	117904502	229637	47.3	3.255	65.57	0.217	0.052	0.458	5.32	0.364			
Mg / µg	944857	5964	1649	0.216	0.652	0.019	1.73	0.514	1429	1.217			
Ca / µg	200227	1651	1691	0.475	0.502	0.125	1.70	0.685	1417	1.926			
Ti / ng	1545		215.1	2.231	0.953	0.121		27.66		31.9			
V / ng			0.521	0.251	0.315	0.020							
Cr / ng			22.31	47.15	15.44	1.48			18.02	2.45			
Mn / ng			333.0				0.039		374.6				
Fe / ng			3934		5.65		3541	3.71	3.49				
Mo / ng	3864	15.4	3.86	0.332	0.226	0.181	3.907	0.363	0.742	0.408			
North Sea IV													
Na / µg	122659944	239077	209.9	5.63	100.8	0.08	0.12	0.57	16.8	0.37	0.010	0.64	0.16
Mg / µg	979376	6253	1326	0.05	1.00	0.03	2.99	0.59	1119	0.73	0.013	0.71	0.25
Ca / µg	205702	1735	1566	1.04	0.53	0.20	3.35	0.85	1278	1.53		1.53	0.02
Ti / ng		0.62	622.7	3.94	1.97	6.44	3.43	18.34	5.12	1.34	5.19	5.94	12.70
V / ng			3167	3.96	1.60	5.46	10.8	1.98	0.26	2698	31.6	7.5	2306
Cr / ng			1611	51.6	17.0	4.6	5.7	0.9	23.9	1348	16.0	7.9	1161
Mn / ng			218.8				0.8		288.1		0.41	6.04	17.7
Fe / ng			63821	17.0	21.5	237.2	55169				3.96	1.50	7.63
Mo / ng		21.83	18555	7.04	1.40	4.02	13662	0.25	0.64	0.77	0.09	2.28	6.91
North Sea V													
Na / µg	123596826	246447	23.05	7.58	73.53		0.105	0.270	3.72	0.45	0.011	0.494	0.256
Mg / µg	990745	6197	1453	0.201	0.753	0.033	8.44	0.32	1259	5.84	0.012	2.56	0.317
Ca / µg	211545	1682	1621	0.701	0.371	0.308	8.73	0.50	1351	7.09		2.69	0.020
Ti / ng			477.49	4.07	0.92	5.79	4.44	22.55	11.46	6.66	5.61	7.54	12.68
V / ng			3109	5.41	1.46	6.38	21.20	2.18		2620	13.35	7.54	1062
Cr / ng		0.92	54.68	84.12	22.61	3.87	0.07		48.28		0.383	8.31	14.06
Mn / ng			71.80				1.49		189.1		0.421	6.57	17.28
Fe / ng			48280	12.63	22.93	246.20	40267				2.49	3.77	8.08
Mo / ng	87294	95.93	9354	5.14	1.05	2.35	6597	0.236	4.39	0.666	0.038	3.46	6.60

Table S 16: Absolute composition of North Sea test 3 samples (Alfa doped II and V, natural North Sea VI) in all fractions from Chelex-100 separation and cleanups. All values calculated to µg or ng. Each sample is 2000 g.

	seawater after chelex	alkali matrix wash	Chelex fraction	reg. resin HNO$_3$+MQ	reg. resin NH$_3$+MQ	Fe matrix	1. Ti matrix	1. main matrix	1. V fraction	2. Ti matrix	2. main matrix	final V fraction
						Alfa doped II						
Na / µg	19487756	990	7.868	5.072	9.601	0.234	0.158	8.07	0.598			
Mg / µg	1497229	2721	756.8	0.709	1.06	5.94	0.204	661.9	0.418			
Ca / µg	272572	840	965.6	0.277	0.219	7.916	0.327	879.8	0.691			
Ti / ng	9033	13.05	85.44	1.469	2.298	1.294	5.493	3.903	9.31			
V / ng	5498	11.22	71.17	1.763	5.36	0.856	0.247	1.186	52.16			
Cr / ng	4222	10.82	57.80	10.18	3.44	1.20	0.173	37.52	2.09			
Mn / ng		38.91	307.5	1.554	1.097	3.69	0.414	255.3	0.498			
Fe / ng	13059	18.12	1912	16.70	53.51	1877	8.91		1.443			
Mo / ng		7.89	8.24	0.921	1.077	2.199	1.484	1.14	0.199			
						Alfa doped V						
Na / µg	19015167	2141	73	3.635	0.884	0.882	0.183	70.40	1.041	0.005	1.093	0.107
Mg / µg	1473684	2531	900	1.594	0.124	5.794	0.122	830.15	5.29	0.023	3.870	0.411
Ca / µg	278566	794	892	0.694	0.174	5.815	0.239	830.96	5.56	0.007	5.575	0.123
Ti / ng	9928.59	14.61	314.9	1.98	10.55	3.08	26.75	3.23	13.57	8.16	7.16	13.14
V / ng		11.3	9664	18.28	13.46	228.3	3.20	1.484	8727	58.66	6.66	6673
Cr / ng	4766	14.9	65.1	49.26	6.97	0.784	0.203	48.61	1.82	1.24	8.15	14.22
Mn / ng		40.3	291.8	1.487	3.82	3.116	0.128	260.2	2.03	0.739	11.58	18.86
Fe / ng	23928	13.9	14983	28.45	442.5	15071	0.969	0.159	1.52	8.58	7.24	10.30
Mo / ng		6.53	145.09	0.817	13.31	129.2	1.176	0.556	0.051	0.304	3.61	7.01
						North Sea VI						
Na / µg	24276942	1014	35.07	138.9	0.168	0.446	0.172	33.36	0.472	0.008	0.693	0.114
Mg / µg	1883983	2878	702.7	32.56	0.063	4.76	0.545	630	0.344	0.016	0.325	0.247
Ca / µg	337424	1010	1028	8.84	0.839	7.16	0.896	947.5	0.725		0.946	
Ti / ng	9879	52.64	718.2	10.15	2.20	7.16	31.56	8.77	6.87	4.14	5.52	12.60
V / ng		10.19	3021	44.27	25.59	25.89	2.52	3.78	2682	33.6	7.38	1911
Cr / ng	6125	11.21	111.8	80.44	4.00	2.20	0.203	92.26	1.705	0.752	7.38	13.88
Mn / ng		68.08	531.3	2.37	1.32	5.416	0.484	464.3	0.602	0.677	5.90	17.66
Fe / ng	10175	23.80	59982	661.8	72.88	70888	3.023	4.43		5.19	1.63	6.58
Mo / ng	197187	26.09	24.32	4.31	1.82	1.16	1.11	15.14	10.73	0.702	5.24	7.65

Table S 17: Absolute composition of North Sea test 4 samples (Alfa doped IV and VI, natural North Sea VII and VIII) in all fractions from Chelex-100 separation and following cleanups. All values calculated to µg or ng. Each sample is 2000 g.

	seawater after Chelex	alkali matrix wash	Chelex fraction	reg. resin HNO₃+MQ	reg. resin NH₃+MQ	Fe matrix	1. Ti matrix	1. main matrix	1. V fraction	2. Ti matrix	2. main matrix	final V fraction
						Alfa doped IV						
Na / µg	24832491	1234	5.07	0.115		0.096	0.060	4.471		0.004	0.691	0.098
Mg / µg	1896769	1164	481.3	0.030		0.425	0.266	350.35	1.97	0.014	1.77	0.278
Ca / µg	340860	576	566.3	0.216	0.048	0.699	0.362	428.91	2.834		2.70	0.009
Ti / ng	8753		122.0	1.96	2.31	1.81	6.87	9.54	22.11	7.34	7.07	12.37
V / ng			10821	15.60	58.97	320.0	23.00		10078	83.70	6.77	7947
Cr / ng	5232		1.285	13.66	7.46	1.69		17.42	13.18	0.691	7.66	14.15
Mn / ng		14.06	247.7	1.65	1.58	2.06		205.1	14.51	0.696	10.18	17.31
Fe / ng	4930		3969	11.87	39.08	3509		3.75	6.96	12.73	13.69	9.27
Mo / ng		1.09	65.10	0.345	0.185	59.64	0.097	2.14	0.049	0.273	3.66	6.87
						Alfa doped VI						
Na / µg	22701330	951.595	6.822	0.211	0.029	0.048	0.046	6.72		0.001	0.575	0.320
Mg / µg	1768766	1371.072	290.814	0.300	0.000	0.410	0.146	240.9	0.328	0.012	0.471	0.246
Ca / µg	314277	769.635	544.321	0.414	0.131	0.955	0.287	465.0	1.66		1.50	0.405
Ti / ng	7995		61.700	1.791	2.208	1.679	18.56	7.956	77.24	38.03	7.02	14.88
V / ng			9560	10.573	20.761	476.69	26.81		8412	74.37	6.80	6278
Cr / ng	4997		10.57	13.00	2.66	2.09		28.54	13.49	0.692	7.58	13.97
Mn / ng		19.086	253.0	1.765	1.472	2.23		232.5	13.59	0.674	9.46	17.31
Fe / ng			923.6	13.55	24.34	892.7		0.610	2.74	1.30	4.93	8.20
Mo / ng			52.79	0.182	0.100	44.69	0.104	0.737		0.299	3.47	6.83
						North Sea VII						
Na / µg	21955561	945.8	4.827	0.586	0.078	0.034	0.064	5.602		0.015	0.650	0.088
Mg / µg	1698851	1321	284.8	0.190	0.015	0.430	0.154	249.7	0.397	0.016	0.559	0.252
Ca / µg	305044	730.1	527.5	0.279	0.048	0.897	0.354	487.3	1.36		1.24	0.333
Ti / ng	10631		394.0	2.32	13.72	3.55	16.87	14.65	32.61	14.14	6.07	12.49
V / ng			2810	2.81	9.64	8.41	8.50	0.456	2785	31.41	7.36	2209
Cr / ng	5616		71.02	32.73	5.88	2.10		84.64	16.21	0.714	9.27	14.23
Mn / ng		39.73	403.8	1.86	3.85	2.40		389.0	13.64	0.701	6.14	17.64
Fe / ng	28984	34.64	41204	50.47	412.9	38069		0.936	1.74	5.35	3.25	8.21
Mo / ng		0.099	16265	7.22	8.10	14289	0.308	0.405		0.288	2.31	6.88
						North Sea VIII						
Na / µg	23152364	1022	5.41	0.626	11.07		0.050	6.421		0.006	0.862	0.117
Mg / µg	1810742	1517	293.0	0.353	1.299	0.353	0.612	273.0	0.353	0.016	0.590	0.278
Ca / µg	328665	791.0	516.3	0.378	0.117	0.808	1.09	501.4	1.25		1.492	0.166
Ti / ng	9097		566.2	4.36	31.76	0.614	13.20	29.44	54.81	24.82	6.43	13.12
V / ng			3180	15.72	9.43	4.85	11.17	1.72	3071	32.53	7.53	2475
Cr / ng	6267		80.69	32.67	11.11			96.18	16.16	0.731	9.48	14.19

	seawater after Chelex	alkali matrix wash	Chelex fraction	reg. resin HNO$_3$+MQ	reg. resin NH$_3$+MQ	Fe matrix	1. Ti matrix	1. main matrix	1. V fraction	2. Ti matrix	2. main matrix	final V fraction
						North Sea VIII						
Mn / ng		52.83	460.629	2.322	10.833		0.239	469.9	13.92	0.684	7.003	20.22
Fe / ng	12938	26.76	64769	120.513	1459	76926		3.07	1.41	4.323	3.005	7.91
Mo / ng		0.099	16265	7.22	8.10	14289	0.308	0.405		0.288	2.310	6.88

Table S 18: Absolute composition of North Sea test 5 samples (Nist doped VI, VII, and VIII, natural North Sea IX) in all fractions from Chelex-100 separation and cleanups. All values calculated to µg or ng. Each sample is 2000 g.

	seawater after Chelex	alkali matrix wash	Chelex fraction	reg. resin HNO$_3$+MQ	reg. resin NH$_3$+MQ	1. main matrix	2. main matrix	combined Ti matrix	V fraction
					Nist doped VI				
Na / µg		1396	48.71	3.08	0.087	38.26	0.350		
Mg / µg		1477	470.5	0.539	0.026	357.4	1.001	0.007	0.053
Ca / µg		285.9	260.4	0.080	0.045	207.7	0.805	0.013	0.483
Ti / ng		23.91	62.39	2.97	1.46	3.64	44.61	5.38	7.38
V / ng		32.63	10831	9.43	11.97	7.12	2.75	159.9	10391
Cr / ng		22.35	45.98	6.86	3.36	15.45	3.48	0.686	10.32
Mn / ng		40.32	254.4	0.303	0.244	192.5	1.15	0.254	1.99
Fe / ng		18.89	405.6	7.19	8.02	28.40	333.5	37.81	5.63
Mo / ng		11.01	15.69	0.635	0.523		0.599		3.41
					Nist doped VII				
Na / µg		528.6	70.91	7.65		58.99	0.459		
Mg / µg		1523	335.2	1.08		274.5	1.44	0.015	0.038
Ca / µg		288.63	263.0	0.105	0.037	228.4	1.56	0.013	0.360
Ti / ng		24.11	279.2	1.34	0.78	209.4	20.33	3.17	7.37
V / ng		32.93	9078	16.542	5.11	7.57	2.69	110.1	8747
Cr / ng		22.08	57.91	9.457	2.01	24.42	4.38	0.713	10.38
Mn / ng		36.22	215.1	0.275		178.1	1.48	0.270	3.10
Fe / ng		21.26	16095	29.18	12.83	13256	839.3	57.22	6.35
Mo / ng		11.09	81.05	0.707			0.582		3.40
					Nist doped VIII				
Na / µg		706.1	52.34	15.82	0.124	42.74	0.196		1.10
Mg / µg		1291	283.5	2.35	0.066	228.3	0.860	0.008	
Ca / µg		278.1	222.7	0.179	0.081	189.4	1.32	0.012	1.45
Ti / ng		25.03	215.8	1.30	3.05	164.5	24.41	2.38	1.66
V / ng		34.21	7915	3.02	9.00	6.854	2.68	191.1	7682
Cr / ng		22.97	56.97	9.69	4.23	25.20	4.81	0.696	2.06
Mn / ng		46.95	290.7	0.487	0.460	247.5	1.60	0.235	
Fe / ng		21.12	6427	36.48	41.00	5285	566.1	43.03	21.04
Mo / ng		11.34	62.85	1.005	0.726		0.589		

	seawater after Chelex	alkali matrix wash	Chelex fraction	reg. resin HNO$_3$+MQ	reg. resin NH$_3$+MQ	1. main matrix	2. main matrix	combined Ti matrix	V fraction
					North Sea IX				
Na / µg		911.2	74.72	0.793	0.037	60.44	0.641		
Mg / µg		1990	405.9	0.136	0.037	325.4	0.724	0.005	0.032
Ca / µg		344.7	279.3	0.046	0.052	233.6	0.699	0.013	0.541
Ti / ng		24.54	467.42	2.49	14.95	360.7	19.56	2.58	7.33
V / ng		32.86	2790	2.66	5.14	9.85	2.65	4.55	2578
Cr / ng		23.05	70.87	13.34	7.47	48.15	3.91	0.869	10.062
Mn / ng		46.59	275.1	0.415	1.81	227.5	1.21	0.242	1.954
Fe / ng		67.45	45982	30.49	584.38	37653	1560	99.57	4.005
Mo / ng		11.85	16761	3.82	15.06	39.47	0.597	0.768	3.712

Table S 19: Absolute amounts of V, Cr, Ti, and Fe in V fractions of blank. All values in ng.

all values in ng	V	Cr	Ti	Fe
North Sea test 1				
Chelex-100 separation	9.07	6.47	5.99	66.84
buffer	0.35		0.34	
1. cleanup	0.84	0.23	1.65	7.97
2. cleanup	0.11	0.23	0.60	1.88
only cleanups	0.94	0.45	2.25	9.85
p-blank-1	10.36	6.92	8.58	76.69
North Sea test 2				
Chelex-100 + 1. cleanup	1.07	2.85	2.60	4.23
buffer	0.35		0.34	
2. cleanup	0.11	0.23	0.60	1.88
p-blank-2	1.53	3.07	3.54	6.11
North Sea test 3				
Chelex-100 + 1. cleanup	0.27	2.92	5.52	5.58
buffer	0.35		0.34	
2. cleanup	0.11	0.23	0.60	1.88
p-blank-3	0.73	3.15	6.46	7.46
North Sea test 4				
1. cleanup	0.03	0.14	0.91	1.76
2. cleanup	0.11	0.23	0.60	1.88
only cleanups	0.14	0.37	1.50	3.64
North Sea test 5				
only cleanups	1.64	0.36	0.41	1.94

Table S 20: Absolute amounts of V, Cr, Ti, and Fe in Fe, Ti, and main cleanup matrices and V fraction as well as respective blanks for reference material Alfa solution, each processed in the first cleanups in North Sea test 1 – 4. Matrix compositions are blank corrected. All values in ng.

in ng	starting V amount	Fe matrix	Ti matrix	main matrix	V fraction	Fe matrix blank	Ti matrix blank	main matrix blank	procedure blank
					Alfa sol. in North Sea test 1				
V	50000	3132	92.08	0.049	46125	0.007	0.164	0.012	0.835
Ti				6.05		0.009	2.68	3.68	1.65
Cr				1.34				1.15	0.23
Fe				14.61		12.30		5.80	7.97
					Alfa sol. in North Sea test 2				
V	20930	3961	42.28	0.00	16992	0.035	0.039		1.072
Ti			16.94	21.71		0.109		0.907	2.604
Cr						0.16		9.48	2.85
Fe			0.97			67.27		2.23	4.23
					Alfa sol. in North Sea test 3				
V	20720	651.6	21.54	0.16	20128	0.103			0.267
Ti		0.02	5.01	6.93	1.42	0.251	1.56	0.787	5.52
Cr						0.63	0.13	20.77	2.92
Fe			0.56	2.30		101.5	0.37	2.73	5.58
					Alfa sol. in North Sea test 4				
V	20870	3435	53.55	0.02	19899				0.032
Ti			2.03		29.95		1.21	3.01	0.909
Cr					31.44			0.42	0.14
Fe		3.72		1.28		0.92	0.43	1.85	1.76

Table S 21: Absolute amounts of V, Cr, Ti, and Fe in Ti and main cleanup matrices and V fraction as well as respective blank for reference materials Alfa sol., Alfa foil, and Nist sol., that were processed in the second cleanup of North Sea tests 1 – 4. Matrix compositions are blank corrected. All values in ng.

in ng	starting V amount	Ti matrix	main matrix	V fraction
		Alfa sol.		
V	20710	166.0	0.282	19540
Ti		0.711	0.247	107.3
Cr			0.680	126.9
Fe				42.22
		Alfa foil		
V	51300	372.9	0.476	49226
Ti		0.30	0.803	109.3
Cr			0.643	127.7
Fe		0.88		37.91
		Nist sol.		
V	60100	455.2	0.503	58191
Ti		5.09	0.604	115.3
Cr			1.26	134.6
Fe		3.66	1.39	43.90
		blank		
V		0.072	0.568	0.109
Ti		0.557	0.761	0.595
Cr		1.28	0.452	0.228
Fe		5.73	2.27	1.88

Table S 22: Absolute amounts of V, Cr, Ti, and Fe in Chelex-100 separation and cleanups fractions and cleanup blanks for reference materials Alfa sol., Alfa foil, and Nist sol., that were processed with North Sea test 5. Matrix compositions are blank corrected. All values in ng.

in ng	starting V amount	after chelex	alkali matrix	reg. resin HNO$_3$	reg. resin NH$_3$	Chelex fraction	1. main matrix	2. main matrix	Ti matrix	V fraction
Nist-1 Chelex separation										
V	10561	84.44	6.41	25.81	13.90	10347				
Ti		3.79	1.92	0.19	0.57	77.35				
Cr		1.93	1.74	2.24	0.93	86.34				
Fe		5.82	14.24	4.11	8.68	49.65				
Nist-2 Chelex separation + cleanup										
V	10930	98.43	8.67	20.89	8.67	10332	2.51	1.20	148.7	8927
Ti		2.91	2.34	0.31	0.39	50.88	7.47	4.74	1.33	60.97
Cr		1.73	1.49	2.46	1.21	50.15	16.94	1.74	0.47	88.87
Fe		7.37	4.25	3.67	5.44	72.93	40.16	18.39		68.88
Nist 3 cleanup										
V	20496						2.47	1.22	309.6	16987
Ti							3.95	1.27	3.82	61.51
Cr							1.26	0.15	0.50	89.88
Fe							5.49			40.78
Alfa foil cleanup										
V	59600						2.49	1.21	1084	49502
Ti							1.44	0.88	0.66	62.34
Cr							1.05	0.22	0.50	90.91
Fe							8.39	0.40		71.27
Alfa sol. cleanup										
V	20850						2.51	1.22	408.7	17760
Ti							1.64	0.84	5.78	62.48
Cr							1.23	0.19	0.44	91.33
Fe							0.69	0.22		47.51
blank cleanup										
V							0.22	0.16	0.20	1.64
Ti							0.90	0.72	1.50	0.41
Cr							0.42	0.79	0.32	0.36
Fe							2.59	4.76	27.87	1.94

S 6. Further natural seawater samples

Table S 23: Absolute composition of natural seawater samples Jub 14 (2000 g), Jub 16 A + B (each 2000 g), and Mauritius (2000 g) in all fractions from Chelex-100 separation and following cleanups. All values calculated to µg or ng.

	alkali matrix wash	reg. resin HNO$_3$+MQ	reg. resin NH$_3$+MQ	Chelex fraction	1. main matrix	1. Ti matrix	2. main matrix	1. V fraction	3. Ti+main matrix	2. V fraction
					Jub 14					
Na / µg	23430	1.02	1.98	476.6	434.7	0.016	0.630		0.39	0.17
Mg / µg	8885	0.470	0.163	1229	1062	0.013	1.56	0.218	0.04	-0.02
Ca / µg	1341	0.190	0.209	882.1	778.5	0.010	2.70	0.213	0.37	0.69
Ti / ng	4.33	1.56	1.04	32.76	21.20	3.27	8.52	9.62	2.67	24.58
V / ng	16.13	6.10	52.00	3260	8.78	2.73	1.02	2840	2.86	634.93
Cr / ng	9.28	16.83	3.54	58.32	44.99	0.55	1.80	12.66	1.22	22.42
Mn / ng	9.91	1.62	0.94	17.96	15.48	0.58	1.09	13.44	1.31	21.36
Fe / ng	70.20	31.20	6.86	357.3	312.04	267.4	65.39	22.77	2.96	18.09
Mo / ng	11.01	4.52	14.25	18652	0.380	0.508		0.196	1.350	14.817
					Jub 16 A					
Na / µg	19859	7.23	0.574	738	659	0.019	1.01	0.000	0.734	0.147
Mg / µg	7227	1.25	0.032	1292	1117	0.010	1.47	0.200	0.116	-0.035
Ca / µg	1090	0.312	0.011	899	808	0.008	1.56	0.267	2.738	-0.025
Ti / ng	4.107	21.13	5.688	71.95	31.76	8.875	10.36	16.81	2.287	25.671
V / ng	15.85	6.057	40.96	3290	8.72	4.496	1.042	2634	2.345	902.780
Cr / ng	8.30	15.98	3.81	64.12	49.30	0.52	1.97	12.82	1.38	21.84
Mn / ng	7.219	1.712	1.283	14.88	12.30	0.587	0.893	14.29	1.744	20.724
Fe / ng	15.06	36.90	43.81	194.5	141.4	235.9	39.92	25.04	2.68	19.60
Mo / ng	11.28	4.450	13.55	19359	0.286	0.276			1.854	16.056
					Jub 16 B					
Na / µg	23947	23.23	1.186	220	235	0.013	0.359	0.000	0.442	0.206
Mg / µg	8197	3.737	0.337	1607	1566	0.010	1.318	0.197	0.080	-0.005
Ca / µg	1267	2.177	0.131	1014	923	0.012	1.386	0.104	0.608	0.955
Ti / ng	4.66	4.46	1.58	57.88	10.43	15.20	6.96	12.53	4.65	25.99
V / ng	16.88	5.81	46.43	3150	9.19	8.14	1.08	2716	3.88	1381.71
Cr / ng	8.57	15.27	3.74	60.89	48.76	0.53	9.98	12.63	1.31	23.10
Mn / ng	7.56	2.01	0.93	16.05	14.19	0.58	1.21	13.51	1.51	21.97
Fe / ng	24.95	34.51	6.72	205.6	198.7	287.0	67.88	23.94	16.08	19.17
Mo / ng	11.34	7.44	14.07	18079	0.45	0.33			1.98	23.54
					Mauritius					
Na / µg	19127	88.63	1.92	399.3	367.9	0.013	0.753	0.000	0.490	0.114
Mg / µg	6488	9.38	0.337	1370	1169	0.006	2.133	0.230	0.096	

	Mauritius									
	alkali matrix wash	reg. resin HNO_3+MQ	reg. resin NH_3+MQ	Chelex fraction	1. main matrix	1. Ti matrix	2. main matrix	1. V fraction	3. Ti+main matrix	2. V fraction
Ca / µg	989.5	1.66	0.096	868.3	778.5	0.0	2.4	0.3	1.4	0.3
Ti / ng	2.78	1.03	1.01	44.20	19.93	9.68	2.87	6.27	2.08	24.26
V / ng	15.87	4.88	34.76	2925	8.96	3.82	1.02	2456	5.22	929.4
Cr / ng	8.39	9.99	2.57	39.42	31.49	0.52	1.79	12.63	1.20	21.47
Mn / ng	7.561	1.753	0.901	22.68	19.57	0.577	1.068	13.41	1.459	20.59
Fe / ng	18.24	32.42	5.310	482.6	347.5	219.4	28.18	21.39	3.088	17.67
Mo / ng	11.34	7.44	14.07	18079	0.45	0.33			1.98	23.54

Table S 24: Absolute composition of natural seawater samples Arctic, Antarctic, Helgoland A and B in all fractions from Chelex-100 separation and following cleanups.

	alkali matrix wash	reg. resin HNO_3+MQ	reg. resin NH_3+MQ	Chelex fraction	1. main matrix	1. Ti matrix	2. main matrix	1. V fraction	3. Ti+main matrix	2. V fraction
	Arctic									
Na / µg	20872	135.37	0.80	423.5	398.1	0.000	1.412		0.45	0.17
Mg / µg	7720	14.380	0.075	1139	1024	0.006	3.56	0.377	0.28	-0.02
Ca / µg	1250	2.075	0.031	845.5	783.1	0.006	4.06	0.501	1.09	0.03
Ti / ng	3.58	1.42	1.00	26.85	19.24	7.17	1.28	6.82	1.54	22.42
V / ng	16.10	4.81	15.64	493	8.77	1.48	1.02	432	4.03	343.90
Cr / ng	8.90	11.55	3.43	33.55	27.84	0.69	1.35	12.70	1.43	18.97
Mn / ng	7.58	1.04	0.99	17.11	15.09	0.84	1.42	13.63	1.56	18.15
Fe / ng	21.52	5.90	5.49	266.4	206.92	36.3	4.19	18.52	2.16	16.20
Mo / ng	10.65	13.13	10.63	19066	0.771	0.126			1.353	14.814
	Antarctic									
Na / µg	19002	4.87	1.408	126	118	0.000	0.56	0.000		
Mg / µg	6932	0.72	0.033	985	818	0.003	1.09	0.166		
Ca / µg	1156	0.235	0.016	797	686	0.000	1.40	0.160		
Ti / ng	3.614	1.44	0.973	36.51	26.08	13.149	6.72	5.62		
V / ng	16.53	16.101	23.65	3377	8.61	27.808	1.216	2686		
Cr / ng	8.76	35.20	5.52	55.50	41.89	0.71	1.18	12.96		
Mn / ng	6.812	1.460	0.873	13.75	11.32	0.841	0.927	13.70		
Fe / ng	18.28	25.24	2.82	346.1	269.0	33.2	3.77	25.34		
Mo / ng	10.09	28.567	8.18	20147	0.143	0.156				
	Helgoland A									
Na / µg	16887	34.18	2.201	457	406	0.001	0.464	0.000	0.807	0.208
Mg / µg	5872	4.041	0.260	1189	1023	0.006	0.999	0.118	0.116	-0.021
Ca / µg	976	0.683	0.104	871	773	0.020	1.473	0.067	1.894	0.075
Ti / ng	6.60	1.61	0.90	31.14	21.95	7.37	4.60	6.10	2.05	21.23

	Helgoland A									
	alkali matrix wash	reg. resin HNO$_3$+MQ	reg. resin NH$_3$+MQ	Chelex fraction	1. main matrix	1. Ti matrix	2. main matrix	1. V fraction	3. Ti+main matrix	2. V fraction
V / ng	16.06	5.75	18.24	1354	9.39	3.04	1.02	1174	3.28	991.25
Cr / ng	9.42	29.63	14.48	71.54	57.73	0.70	1.92	12.84	1.24	18.79
Mn / ng	6.98	1.09	0.97	14.61	12.82	0.86	0.96	13.58	1.65	17.79
Fe / ng	16.73	6.16	26.03	688.4	518.2	72.7	6.31	17.42	1.87	16.76
Mo / ng	15.35	16.55	14.04	20094	8.82	3.26			1.32	15.04
	Helgoland B									
Na / µg	16663	5.07	0.53	609.5	583.0	0.006	0.579		0.485	0.175
Mg / µg	5899	0.68	0.118	1169	1099	0.007	0.864	0.111	0.081	
Ca / µg	994.1	0.32	0.066	844.3	807.8	0.0	1.1	0.0	0.8	0.2
Ti / ng	3.40	1.20	1.14	44.33	26.97	13.58	2.15	7.19	1.47	21.05
V / ng	15.85	4.00	10.99	1339	20.90	3.06	1.02	1156	4.13	942.8
Cr / ng	9.10	18.61	5.58	180.30	149.29	0.72	8.31	13.23	1.25	18.50
Mn / ng	7.716	1.015	0.910	23.34	21.81	0.837	0.998	13.58	1.778	17.74
Fe / ng	26.00	17.85	48.860	37577.4	27091.2	4456.8	251.22	44.45	2.650	15.40
Mo / ng	15.35	16.55	14.04	20094	8.82	3.26			1.32	15.04

Table S 25: Absolute amounts of V, Cr, Ti, and Fe in cleanups fractions for processed reference material Nist-3165 along with further seawater samples.

	starting V amount	1. main matrix	Ti matrix	2. main matrix	V fraction	V beaker leaching
V / ng	20384	1.78	187.55	0.92	18415.21	169.62
Ti / ng				5.18	22.58	2.36
Cr / ng		0.97	0.42	0.60	88.71	0.14
Fe / ng		6.07	191.61	39.44	149.50	0.62

Table S 26: Absolute amounts of V, Cr, Ti, and Fe in blank fractions during cleanups of further seawater samples

	Blank 1. Cr matrix	Blank Ti matrix	Blank 2. Cr matrix	Blank 1. V fraction	Blank Cr+Ti matrix	Blank 2. V fraction
Na / ng	119.0	0.87	323.5	60.67	162.5	186.2
Mg / ng	46.44	2.64	7.65	3.16	8.89	3.95
Ca / ng	903.5	20.64	176.4	88.34	197.7	74.94
Ti / ng	8.18	3.14	1.43	0.83	0.28	0.45
V / ng	0.16	0.23	0.10	0.37	0.053	0.071
Cr / ng	0.45	0.12	0.28	0.23	0.022	0.015
Mn / ng	0.25	0.23	0.17	0.11	0.046	0.049
Fe / ng	4.48	7.13	1.63	1.70	0.77	1.13
Mo / ng	0.043	0.038			1.02	2.23

Chapter III:

Correlated molybdenum and uranium isotope signatures in modern anoxic sediments

A. Brüske[a*], S. Weyer[a], M.-Y. Zhao[b], N. J. Planavsky[b], A. Wegwerth[c], N. Neubert[a], O. Dellwig[c], K. V. Lau[d], T. W. Lyons[d]

[a] Leibniz University of Hannover, Institute of Mineralogy, Germany

[b] Yale University, Department of Geology and Geophysics, USA

[c] Leibniz Institute for Baltic Sea Research (IOW), Marine Geology, Germany

[d] UC-Riverside, Department of Earth Sciences, USA

*submitted under birth name

Abstract

Redox-sensitive trace metals and their isotopes have emerged as important tools that can be used to reconstruct the redox-evolution of the ocean-atmosphere system. However, reliability of such reconstructions ultimately depends on a solid understanding of the proxies in the present-day oceanic system and their behavior at near-surface processes. To this end, this study is designed to compare isotope fractionation of molybdenum (Mo) and uranium (U) during their removal from seawater and deposition into sediments by investigating sediments along the slopes and at various depths of the two largest restricted anoxic oceanic basins present today: The Black Sea and the Cariaco Basin. In support of previous investigations, our data indicate that Mo scavenging, and isotope fractionation is mainly controlled by water column sulfide levels. However, other factors, such as a particulate shuttle, may also play an additional nonnegligible role. In contrast to Mo, U reduction and immobilization appears to occur mainly at the sediment-water interface and within the uppermost few cm of the sediment pile in both basins. Water column δ^{238}U values appear to be the main factor controlling the sediment δ^{238}U values in the Black Sea. However, the efficiency of U reduction within the sediment pile also effects the U isotope fractionation, in particular in the Cariaco Basin. Despite the different mechanisms for Mo and U removal and associated isotope fractionations, a similar inverse correlation between U and Mo isotope ratios is observed in sediments deeper than ~5 cm (Black Sea) or 15 cm (Cariaco Basin), although there is an offset towards lower Mo and U isotope ratios in the Cariaco Basin. The correlation of δ^{98}Mo and δ^{238}U indicates a similar response of isotope fractionation to the efficiency of Mo and U removal that is mainly controlled by sulfate reduction rates and resulting dissolved sulfide concentrations. High dissolved sulfide concentrations are responsible for very effective Mo and U removal and corresponding minor Mo and U isotope fractionation. This results in high δ^{98}Mo and low δ^{238}U in sediments under strong euxinic conditions. Although both basins experience very different characteristic correlations and multiple factors may be involved in shaping and driving our observed δ^{98}Mo and δ^{238}U trends, we are able to reproduce this relationship in a simple coupled water column and sediment reactive transport model. Different slopes in δ^{98}Mo and δ^{238}U trends can be linked to varying degree of basin restriction, sulfate reduction rates, and isotope compositions of the respective water columns. The results of this study will help build the foundation used to interpret sedimentary Mo and U isotope values, while showing that coupling of δ^{98}Mo and δ^{238}U in sedimentary archives may be useful for paleo-reconstruction work.

1. Introduction

1.1 Geochemical behavior of Molybdenum and Uranium

Molybdenum (Mo) and uranium (U) are transition metals that belong to the group of redox-sensitive metals — along with, for example Fe, Cr, and Se — and their isotopic ratios (^{98}Mo/^{95}Mo and ^{238}U/^{235}U, reported in delta notation) are increasingly used to investigate metal fluxes, environmental processes and to reconstruct paleoceanographic conditions (recently reviewed by Andersen et al., 2017, and Kendall et al., 2017, and references therein). Their present-day oceanic cycles are reasonably well understood and isotope fractionation into the various oceanic sinks is well characterized; however, the processes remain to be understood in detail. Accordingly, the signatures of sedimentary archives combined with mass balance calculations are frequently used to reconstruct changes in the past oceanic cycling of Mo and U as driven, for example, by redox changes (Arnold et al., 2004; Wille et al., 2007; Wille et al., 2008; Kendall et al., 2009; Montoya-Pino et al., 2010; Brennecka et al., 2011; Kendall et al., 2013; Eroglu et al., 2015; Lau et al., 2016; Elrick et al., 2017). Commonly, Mo and U isotopes have been used separately, either to explore the controlling mechanisms of these elements during oceanic cycling and related isotope fractionation, or estimate the extents of anoxia In the ancient ocean as well (Barling et al., 2001; Siebert et al., 2003; Arnold et al., 2004; Barling and Anbar, 2004; Siebert et al., 2006; Neubert et al., 2008; Nägler et al., 2011; Goldberg et al., 2012; Noordmann et al., 2015; Kendall et al., 2017).

In order to gain more reliable information on past conditions, the two elements have also been coupled with other proxies or used together based on their redox-sensitivities. For example, combined U and Mo isotopes data were used by Asael et al. (2013), Kendall et al. (2013), Lu et al. (2017), and Bura-Nakić et al. (2018). Nevertheless, their interrelationships in modern marine systems are still poorly understood, as there are only limited data for Mo and U isotope compositions analyzed on the same samples, which is essential for comparing responses to the same depositional conditions. To date, only Noordmann et al. (2015) and recently Bura-Nakić et al. (2018) analyzed Mo and U isotope compositions in the water column and sediments of a small fjord (Kyllaren Fjord, Norway), the Baltic Sea, and a small euxinic (H_2S > 11 µmol l^{-1}, O_2 = 0 mol l^{-1}, Noordmann et al., 2015) marine lake (Rogoznica, Croatia). They observed a complex relationship of Mo and U isotope fractionation as a function of a variety of different parameters.

In this study, we investigated Mo and U isotope compositions of sediments from the type modern localities for restricted marine basins with euxinic deep water columns — the Black Sea and the Cariaco Basin — in order to fully exploit the potential of using the two systems combined. Sediments from drill cores as well as core top surface sediments from different water depths were analyzed for their Mo and U isotope compositions to investigate isotope

fractionation under highly (sulfidic) euxinic conditions (central Black Sea), moderately euxinic (Cariaco Basin), and suboxic to only weakly euxinic (such as along the slopes of Black Sea and Cariaco Basin). We addressed the influence of ocean and pore-water chemistry by analyzing samples from different burial depths along the slope and deep portions of both basins. Finally, we analyzed deeper drill cores through various sediment units, which helps us refine the historical evolution of sedimentation in the Black Sea and Cariaco Basin.

Both Mo and U are mobile and non-reactive in their oxidized hexavalent states (molybdate MoO_4^2 and uranyl UO_2^{2-}) and thus are conservative and well mixed in present-day oceans. The two elements have long oceanic residence times of 250 - 500 thousand years (ky) and 440 ky for U and Mo, respectively (Ku et al., 1977; Emerson and Huested, 1991; Miller et al., 2011). However, under anoxic or euxinic environments, both elements are readily reduced and enriched in the sediment. During this process, they undergo characteristic isotope fractionations that can be preserved in sediment archives.

Apart from this similarity, both elements show distinct differences in their removal pathways and affinities towards chemical reactants — for example, H_2S in the water column or organic matter in the sediment. Molybdenum removal is controlled by its tendency to react with H_2S to form particle-reactive oxythiomolybdates ($MoO_{4-x}S_x^{2-}$) and thiomolybdate (MoS_4^{2-}) above H_2S_{aq} concentrations of ~11 µmol l^{-1} ("action point of switch" APS) (Helz et al., 1996; Erickson and Helz, 2000). Sulfide-driven Mo transformation and subsequent removal results in minor net isotope fractionation and thus euxinic sediments come close to capturing the isotope signature of coeval seawater, which has a uniform $\delta^{98}Mo$ across oxygenated water columns of +2.3 ‰ (Neubert et al., 2008; Nägler et al., 2011). However, at lower or only intermittently high H_2S concentrations, $\delta^{98}Mo$ values vary between -0.6 and 1.8 ‰ because of slow or incomplete reaction to thiomolybdates (Arnold et al., 2004; Dahl et al., 2010; Nägler et al., 2011; Nägler et al., 2005). Apart from sulfide driven removal of Mo, the operation of a metal oxy hydroxide particulate shuttle can further enhance the authigenic enrichment of Mo in sediments (Algeo and Tribovillard, 2009). Due to this contrasting behavior — from conservative under oxic conditions to particle-reactive in euxinic environments — Mo is ideal for studying euxinic systems.

In contrast to Mo, U behaves conservatively even under strongly euxinic seawater conditions and is thought to be removed predominantly within the sediment pore water, where uranyl (U^{VI}) is reduced to U^{IV}-species U^{IV}-species that are sparingly soluble. The U(IV) subsequently forms authigenic minerals such as uraninite (UO_2) or is bound to organic matter (Cumberland et al., 2016). In marine settings, the reduction process appears to be catalyzed by enzymes from iron or sulfate reducing bacteria (Lovley et al., 1991), a process that is thought to occur on particle surfaces within the pore water rather than in the water column (Anderson et al., 1989; Klinkhammer and Palmer, 1991; Algeo and Tribovillard, 2009). A nuclear volume effect

appears to drive the observed $^{238}U/^{235}U$ isotope fractionation. Because the redox-transition for U involves f-electrons, the nuclear field shift is in the opposite direction of the mass-dependent effect (Bigeleisen, 1996; Moynier et al., 2013). Consequently, the resulting net isotope fractionation during redox reactions is opposite to that observed for other metal isotopes and the heavy isotope ^{238}U is enriched in reduced U species rather than in the oxidized form. Such effects are observed from authigenic U reduction in organic-rich black shales deposited under reducing conditions.

1.2 Study Area

The Black Sea and the Cariaco Basin are, respectively, the first and second largest anoxic basins in the world today. Therefore, they represent the dominant anoxic sinks in the modern budgets of redox-sensitive trace elements such as Mo and U. The Black Sea is located north of Turkey and covers an area of 423,000 m^2 (Murray and İzdar, 1989). Its maximum depths exceed 2000 m, and it has a highly restricted marine input derived entirely from the Mediterranean Sea via the Bosporus Strait across a shallow sill (30 - 35 m deep). It is a hyposaline basin with salinities ranging from 18 - 22 g kg^{-1}, including the denser higher salinity deep waters. With additional contributions from the thermocline, a strong pycnocline leads to permanent water column stratification and limited vertical mixing (Kempe et al., 1991; Murray et al., 1991; Yakushev et al., 2007). The deep water renewal time is between 500 and 2000 years (Östlund, 1974; Dyrssen, 1999; Algeo and Lyons, 2006). A chemocline is established between 120 and 180 m depth at the center of the basin and at the margins, respectively, with surface waters that are well oxygenated and anoxic/euxinic deep waters (Meyer and Kump, 2008). The H$_2$S concentrations increase to 400 to 600 µmol l^{-1} in the deep basin and are maintained by the strong stratification and low rates of dissolved O$_2$ penetration (Murray et al., 1989; Murray et al., 1991). At present, depositional conditions in the central Black Sea are highly euxinic; however, a major change in water column conditions likely occurred between the deposition of unit II (before ~ 3000 y) and unit I sediments (Degens and Ross, 1972; Lamy et al., 2006).

The Cariaco Basin is located on the northern part of the Venezuelan shelf and covers an area of ~7000 km^2. It consists of two deep basins (~1400 m) that are separated by a 900 m deep saddle. It is bordered toward the Caribbean Sea by two sills (with depths of 120 m and 146 m to the north and west, respectively). Surface water exchanges with the open Caribbean Sea (Zhang and Millero, 1993). Salinity values range between 36.2 g kg^{-1} and 37 g kg^{-1} (McConnell et al., 2009). A chemocline maintained by the thermocline occurs at about 200 m depth (Zhang and Millero, 1993; Scranton et al., 2001; Algeo and Tribovillard, 2009), and the deep water renewal time is roughly 50 - 100 years (Deuser, 1973; Piper and Dean, 2002; Algeo and Lyons,

2006). Oxygen concentrations decrease sharply at the chemocline, and H_2S increases to values between 30 - 80 µmol l^{-1} at the sediment-water interface. However, the chemocline varies over short time intervals depending on the density of the water and flux of organic matter (Scranton et al., 2001). Deepwater anoxia is maintained by high primary productivity, and resulting sinking and oxidation of organic matter that increases O_2 demand during remineralization.

2. Samples & analytical Methods

2.1 Samples

We analyzed organic-rich sediments from the Black Sea and the Cariaco Basin. Among them, we analyzed core top surface sediments from 16 stations in the Black Sea (from 0 - 1 cm and 1 - 2 cm below the seafloor = bsf) at varying water depths (214 m to 2083 m below the sea level = bsl, see figure 1A). The sediments were collected by a multicorer device during cruise MSM33 in 2013 at stations 22, 29, 30, 31, 32, 42, 43, 44, 45, 46, 47, 49, 51, 54, 55, and 59 (Arz et al., 2014). Furthermore, we analyzed twelve samples from a short core from site 32 (0 cm to 43 cm bsf) collected during the same cruise at a water depth of 2030 m.
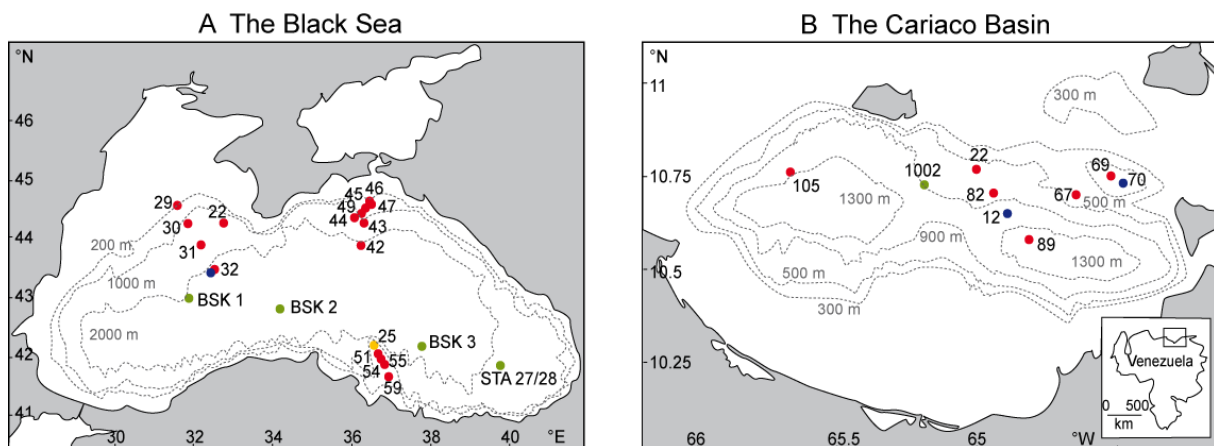
Figure 1: Maps of A: The Black Sea and B: The Cariaco Basin showing sampling sites during the different cruises modified from Arz et al. (2014), Gueguen et al. (2016), and Lyons et al. (2003). In A and B: red circles show core top surface sediments and blue circles show deep cores during the same cruises MSM33 and PLUME07 for the Black Sea and the Cariaco Basin, respectively. In A: yellow circle shows sampling site from cruise M72/5 and green circles show sampling sites from cruise R/V Knorr. In B: green circle shows sampling site from ODP cruise. For details about sampling sites, see text and supplementary table S1.

Additional data from the site 25 (core 25GC, taken during cruise M72-5 in 2007), BSK1, BSK2, BSK3, and STA27/28 (cores BC21, BC25, BC43, and BC55, taken during cruise R/V Knorr 134-8, leg 1 in 1988) are from Barling et al. (2001), Weyer et al. (2008), Montoya-Pino et al.

(2010), Montoya-Pino (2011), Arnold et al. (2012), and Ravizza et al. (1991), from which both Mo and U isotope data of the same samples are available, are used as a complement to our data (see figure 1A and tables S1, S12 for details).

From the Cariaco Basin, we analyzed six core top surface samples (0 - 1 cm bsf), which were collected during cruise PLUME-07 in June 1990 on the R/V Thomas Washington at water depths from 400 m to 1342 m at stations 22, 67, 69, 82, 89, and 105 (Lin et al., 1997; Gueguen et al., 2016). From this cruise, two additional gravity cores from stations 12 (1039 m bsl) and 70 (547 m bsl) from the Cariaco Basin were analyzed (Figure 1B and supplementary table S1). They yielded 17 and 18 samples, respectively, and both cores extended 50 cm into the sediments. Additional samples were obtained from ODP leg 165core 1002B, which was drilled in 1996 at a water depth of 900 m. We analyzed 15 samples spanning down to ~14.5 ky (5.9 m depth) — the bottom of the most recent euxinic interval (Lyons et al., 2003).

2.2 Sample preparation

Black Sea samples were freeze dried and powdered with an agate ball mill at the Leibniz Institute of Baltic Research, Warnemünde (IOW). For major and trace metal determination at IOW, around 50 mg of the dried material were then dissolved in closed Teflon vessels at 180°C for 12 h by acid digestion using a HNO_3-HF-$HClO_4$ mixture. After evaporation of the acids at 180 °C, the digestions were fumed off 3-times with 2 ml 6 M HCl and finally dissolved in 2 vol % HNO_3 to a final dilution factor of ~1000 (Wegwerth et al., 2018). Wet core samples from Cariaco Basin cores 12GGC and 70GGC were dried at 100 °C before powdering with an agate mortar at the Leibniz University of Hannover (LUH). For total digestion at LUH for trace element and isotope analyses, all dried bulk sample powders were weighed into ceramic crucibles and ashed at 500 °C for ~10 hours to volatilize any organics. Between 50 and 200 mg of ashed solid powder was weighed in Savillex® teflon screw top beakers for dissolution. Dissolution involved a multi-acid approach beginning with 6 M HCl for 24 h at 140 °C. After evaporation, 6 ml of a 1:1 mixture of HNO_3 (65 %) and HF (40 %) were added and heated at 140 °C for 5 to 6 days. After evaporating this solution — again, 6 ml of a 3:1 mixture of HCl (37 %) and HNO_3 (65 %) — were added and heated at 140 °C for 24 h. This solution was again evaporated, and 5 g HNO_3 (3 N) were added gravimetrically. After heating this solution to 120 °C for a few hours, all samples were completely dissolved. Aliquots were taken for Mo and U concentration and isotope measurements.

2.3 Major and trace element analyses, TOC determination

The chemical composition of all Black Sea sediments was measured at IOW with ICP-OES (Al, Fe, Mn; iCAP 7400 Duo, Thermo Fisher Scientific) and ICP-MS (Mo, U; iCAP Q, Thermo

Fisher Scientific). External calibration was used for both systems and Sc (ICP-OES) as well as Rh and Ir (ICP-MS) served as internal standards. ICP-MS analyses were carried out in KED mode using He as collision gas. Precision and accuracy were determined with the international reference material SGR-1b (USGS) and were better than 2.7 % and -4.3 % for Al, Fe, and Mn and 2.0 % and 1.8 % for Mo and U, respectively. Additional complementary ICP-MS measurements were performed at LUH.

The chemical composition of Cariaco core top sediments was published by Gueguen et al. (2016). Major and trace element data for samples from core 1002B were published by Lyons et al. (2003), and additional trace element ICP-MS measurements were carried out at our laboratory in Hannover. Also, trace element data on cores 12GGC and 70GGC were analyzed at LUH. All concentration measurements in Hannover were performed with a Thermo Fisher Scientific Element XR single-collector mass spectrometer (SC-ICP-MS) (Noordmann et al., 2015) using Rhodium as the internal standard and applying a five-point external calibration curve diluted from pure standard solutions in the range from 1 - 100 ng g^{-1} for Mo, U, and Th (low resolution) and Al, Fe, Ti, and Mn (medium resolution) (supplementary table S7). Samples were diluted with 3 vol % HNO_3. The certified black shale reference material SDO-1 and the river water standard TMDA-51.3 were processed in several batches, whereby SDO-1 was prepared in the aforementioned manner and TMDA-51.4 was purchased as solution and then diluted and doped with internal standard. The results were within 11.4 % to 15.1 % and 5.8 % to 7.7 % of the certified values for SDO-1 (n_{total} = 9) and TMDA-51.3 (n_{total} = 13), respectively.

Total organic carbon (TOC) of the Black Sea surface sediment samples was calculated from the difference between total carbon (TC) and total inorganic carbon (TIC) determined at IOW by elemental analyzer and infrared detection after acidification, respectively. TOC of Black Sea core samples (32MUC24) and Cariaco core samples (12GGC, 70GGC) were measured in Hannover according to the procedure described in Harris et al. (2001). TOC of Cariaco surface samples was determined at the Stable Isotope Center at Yale University using a Thermo Delta Plus IRMS. Uncertainties are less than 5 % based on duplicate analysis of samples and a BBOT carbon standard.

2.4 Mo isotope analyses

Molybdenum isotope analyses were performed according to Barling et al. (2001) and Noordmann et al. (2015) in the lab in Hannover. For each sample, aliquots of a maximum 2000 ng of Mo were taken. The matrix was then separated from Mo using two ion chromatographic columns (Dowex anion resin 1x8, 100 - 200 mesh, and Dowex cation resin 50Wx8, 200 - 400 mesh). Next, remaining organic particles were broken down by adding 300 µl HCl (37 %) and 100 µl HNO_3 (65 %) and heating this solution to 120 °C. After

evaporating this solution again, samples were doped with a Zr reference solution (Lot #700193E) to serve as a mass bias monitor during measurements. Samples were diluted to 3 vol % HNO_3, yielding final Mo and Zr concentrations of 200 ng ml^{-1} and 100 ng ml^{-1}, respectively. Measurements were performed with a Thermo Fisher Scientific Neptune equipped with a small glass spraychamber (double pass Scott design) and 100 µl capillaries. A nickel H sampler cone and a X skimmer cone were used. The electronic baseline was measured once at the beginning of each sequence.

Briefly, ^{90}Zr, ^{91}Zr, ^{92}Mo, ^{95}Mo, ^{96}Mo, ^{97}Mo, ^{98}Mo, and ^{100}Mo were measured on Faraday cups equipped with $10^{11}\,\Omega$ resistor amplifiers, whereas the very small ^{99}Ru ion beam was measured using an $10^{13}\,\Omega$ resistor. Signals of ^{98}Ru overlapping with ^{98}Mo were corrected using ^{99}Ru and a $^{99}Ru/^{98}Ru$ ratio of 6.82350. $^{90}Zr/^{91}Zr$ ratios of 4.58421 were used to correct for instrumental mass discrimination by applying the exponential law. All measurements were performed using a standard sample-bracketing method relative to a NIST-3134 standard solution prepared to match the Mo and Zr concentrations of our samples within 10 %. The ratio of the two most abundant Mo isotopes ($^{98}Mo/^{95}Mo$) is reported in delta notation relative to NIST-3134 with a value of +0.25 ‰ (Nägler et al., 2014), as calculated with equation 1:

$$\delta^{98}Mo = \left[\left(\left(^{98}Mo/^{95}Mo\right)_{sample}/\left(^{98}Mo/^{95}Mo\right)_{NIST-SRM-3134}\right) - 1\right] * 1000 + 0.25 \; [‰] \qquad \text{Eqn. 1}$$

In addition to SDO-1, the reference materials Mo2Ro (Johnson Matthey Specpure® Mo plasma standard Lot #802309E) and Grav95 (Grav Rochester Mo 2) were frequently measured to check instrument performance. Over an 18-month time period, SDO-1 produced $\delta^{98}Mo$ values of 1.04 ± 0.09 ‰ (n = 41), Mo2Ro yielded values of -0.08 ± 0.10 ‰ (n = 91), and Grav95 yielded -1.06 ± 0.08 ‰ (n = 64). Our measurements agree with previously reported values (Barling et al., 2001; Wasylenki et al., 2008; Kendall et al., 2009; Goldberg et al., 2013; Nägler et al., 2014).

The $\delta^{98}Mo$ ratios for detrital contributions were calculated according to equations 2 and 3. The isotope composition of the detritus was assumed to be equivalent to that of the average continental crust with a $\delta^{98}Mo$ value of 0.3 ‰ (Voegelin et al., 2014). If Al contents were available, the $[Mo]_{upper\ crust}/[Al]_{upper\ crust}$ of 0.1350 µg g^{-1} wt%$^{-1}$ was used (Eqn. 2.1+3). Because we did not have Al contents for six Cariaco surface samples, we used the $[Mo]_{upper\ crust}/[Ti]_{upper\ crust}$ of 2.8677 µg g^{-1} wt%$^{-1}$ (Rudnick and Gao, 2003) (Eqn. 2.2+3). Aluminium and titanium are both considered to be mainly derived from detritus, and crustal average values can be used to estimate the detrital contribution in sediments (Cole et al., 2017). Nevertheless, the detrital Mo components are small, and the correction resulted in only minor changes in the analyzed isotopic composition of the sediments (see supplementary table S8). To compare the differences between Al and Ti corrected detrital Mo isotope ratios, the

calculations were performed with both elements with the data from Cariaco cores 12GGC and 70GGC (supplementary table S9). These calculations show that both elements are adequate detrital monitors, as their respective corrected Mo isotope ratios agree.

$$[Mo]_{detr.} = \frac{[Mo]_{upper\ crust}}{[Al]_{upper\ crust}} * [Al]_{sample} \text{ or } [Mo]_{detr.} = \frac{[Mo]_{upper\ crust}}{[Ti]_{upper\ crust}} * [Ti]_{sample} \qquad \text{Eqn. 2.1; 2.2}$$

$$\text{with } [Mo]_{bulk} = [Mo]_{detr.} + [Mo]_{auth.}$$

$$\delta^{98}Mo_{auth.} = \frac{(\delta^{98}Mo_{bulk} * [Mo]_{bulk} - \delta^{98}Mo_{detr.} * [Mo]_{detr.})}{[Mo]_{auth.}} \qquad \text{Eqn. 3}$$

2.5 U isotope analyses

Uranium isotope analyses followed the protocol of Noordmann et al. (2015) and Weyer et al. (2008). From all dissolved samples, an aliquot with ~500 ng U was subsampled and equilibrated with the IRMM-3636a $^{233}U/^{236}U$ double spike (Richter et al., 2008) prior to separating U from the remaining matrix by using Eichrom UTEVA resin (Weyer et al., 2008). The purified U fraction was treated with a 1:1 solution of hydrogen peroxide (30 %) and HNO_3 (65 %) and was then diluted to ~70 ng g^{-1} U with 3 vol % HNO_3. All measurements were performed with the Thermo Fisher Scientific Neptune in Hannover at dry plasma conditions using a Cetac Aridus 2. A nickel H sampler cone and a X skimmer cone were used. The ion beams of ^{233}U, ^{235}U, and ^{236}U were measured on Faraday detectors attached to 10^{11} ohm resistors and ^{238}U with a 10^{10} ohm resistor. Tailing of larger ^{238}U peaks on smaller ^{236}U peaks (abundance sensitivity) was monitored throughout all sessions but was always < 1 µg g^{-1} and thus negligible. An electronic baseline was measured each day and subtracted from all data. Isotope data were integrated each 4 s in 80 cycles, resulting in a total data collection time of 5.33 minutes. An acid blank was measured every 20 samples, and those values were subtracted automatically during any sequence. Instrumental mass bias was corrected using a mass discrimination factor, β, which was calculated from the deviation of measured $^{233}U/^{236}U$ from the certified IRMM-3636a value using the exponential law. All sequences were performed using a standard sample-bracketing method relative to a CRM-112A standard solution prepared to match the U concentration of our samples within 10 %. The $^{238}U/^{235}U$ results are expressed using the delta notation and reported relative to CRM-112A (Eqn. 4) assuming a $^{238}U/^{235}U$ ratio of 137.837 ± 0.015 (Richter et al., 2010).

$$\delta^{238}U = \left[\left(\left(^{238}U/^{235}U \right)_{sample} / \left(^{238}U/^{235}U \right)_{CRM-112A} \right) - 1 \right] * 1000 \; [\text{‰}] \qquad \text{Eqn. 4}$$

In addition to SDO-1, the reference materials IRMM-184 and Reimep-18a were measured repeatedly during all sequences in order to check instrument performance. Over an 18-month

duration, SDO-1 yielded a $\delta^{238}U$ value of -0.07 ± 0.05 ‰ (n = 49), while the values for IRMM-184 and Reimep-18a were -1.17 ± 0.04 ‰ (n = 75) and -0.14 ± 0.06 ‰ (n = 37), respectively. These results are in agreement with those previously reported for these reference materials (Weyer et al., 2008; Asael et al., 2013; Goldmann et al., 2015; Andersen et al., 2017; Lu et al., 2017). All samples were measured in triplicate. The reported uncertainties are two standard deviations of replicate measurements (2 s.d.), which generally fall between ±0.01 ‰ and ±0.07 ‰. Isotope measurements were also used to calculate U concentrations by isotope dilution. The results agree with those measured by previously described SC-ICP-MS within 15 % in most cases; however, the isotope dilution data are generally used because they are more precise and accurate (s.d. < 5 %). Total procedure blanks (including digestion and column chromatography steps) for U varied between 0.01 - 5 ng. They were considered as negligible compared to the sample concentrations, and so a procedure blank correction was not applied.

For all analyzed samples, authigenic U concentrations and isotope compositions were calculated by using equations 5 and 6, assuming an average continental crust composition ($\delta^{238}U_{detritus}$) of -0.3 ‰ (Tissot and Dauphas, 2015; Noordmann et al., 2016). As shown by Cole et al. (2017), the U detrital flux is commonly constant regardless of the lithology of the weathered bedrock. Those authors suggested using the $[U]_{topsoil}/[Th]_{topsoil}$ ratio of 0.282 µg g^{-1} / µg g^{-1}, with a confidence interval of ± 0.102 (2 s.d.). For samples from the Cariaco Basin, Th was used as detrital monitor, and the topsoil ratio was used to estimate detrital compounds (Eqn. 5.1+6). However, no Th contents are available for samples from the Black Sea, and thus the $[U]_{crust}/[Al]_{crust}$ = 0.000018 µg g^{-1} / µg g^{-1} (Andersen et al., 2014) was used instead, which was determined from detrital sediments of the Cariaco Basin (Eqn. 5.2+6). To evaluate the potential use of Al and Th as detrital monitors in our dataset, the calculations were performed with the data from Cariaco cores 12GGC and 70GGC and the above-cited ratios because in this case, both Al and Th contents are available. These comparisons reveal that both elements are sufficient and only deviate within average analytical error (supplementary table S1). Detrital corrected and bulk U isotope data can be found in supplementary table S10.

$$[U]_{detr.} = \frac{[U]_{Top\,soil}}{[Th]_{Top\,soil}} * [Th]_{sample} \text{ or } [U]_{detr.} = \frac{[U]_{crust}}{[Al]_{crust}} * [Al]_{sample} \qquad \text{Eqn.5.1;} \quad 5.2$$

$$\text{with } [U]_{bulk} = [U]_{detr.} + [U]_{auth.}$$

$$\delta^{238}U_{auth.} = \frac{(\delta^{238}U_{bulk}*[U]_{bulk} - \delta^{238}U_{detr.}*[U]_{detr.})}{[U]_{auth.}} \qquad \text{Eqn. 6}$$

2.6 A uranium and molybdenum isotope reactive transport model

To understand the factors that control the final composition of U and Mo isotopes in marine sediments, we built a 1D reactive transport model that includes a water column and sediment

diagenesis. For simplicity, and consistent with observations in the Black Sea and Cariaco Basin, we assume that the conversion and removal of Mo occurs only in the water column and the reduction and removal of U occurs only in sediments. Although some Mo sequestration occurs within the sediment pile, in euxinic systems it is likely that the majority of Mo flux comes from the water column. The organic flux and sulfate concentration are fully coupled between water column and sediments. The U isotope composition of bottom seawater is assumed to be related to the degree of local basin restriction. Only sulfate reduction is included as the pathway for organic matter decomposition in the water column, but Fe, Mn, and sulfate reduction, as well as methanogenesis, are included within the sediments. For the water column, the mass balance functions for solutes (index l) and solids (index s) are:

$$\frac{\partial C_l}{\partial t} = \frac{\partial}{\partial x}\left(\mathbf{D}_e \frac{\partial C_l}{\partial x}\right) + \sum R_l \quad \text{and} \qquad\qquad \text{Eqn. 7}$$

$$\frac{\partial C_s}{\partial t} = -\frac{\partial}{\partial x}\left(\mathbf{v_{sink}}C_s\right) + \sum R_s, \qquad\qquad \text{Eqn. 8}$$

where C_l is the solute concentration per volume of water, C_s is the solid concentration per volume of water, D_e is the eddy diffusion term, v_{sink} is the sinking rate of particles, and $\sum R_s$ and $\sum R_l$ are the total solid and solute reaction rates, respectively. For sediments, the mass balance function for solutes and solids are (Berner, 1980; Boudreau, 1997):

$$\frac{\partial C_l}{\partial t} = \frac{1}{\phi}\frac{\partial}{\partial x}\left(\phi D \frac{\partial C_l}{\partial x}\right) - \frac{1}{\phi}\frac{\partial}{\partial x}\left(\phi v C_l\right) + \sum R_l \quad \text{and} \qquad \text{Eqn. 9}$$

$$\frac{\partial C_s}{\partial t} = -\frac{1}{1-\phi}\frac{\partial}{\partial x}\left((1-\phi)\omega C_s\right) + \sum R_s, \qquad\qquad \text{Eqn. 10}$$

where ϕ is porosity, D is the molecule diffusion, v is the solute advection rate, ω is the solid advection rate, and $\sum R_s$ and $\sum R_l$ are the total solid and solute reaction rates, respectively. $D = D_m/(1 - 2\ln\phi)$, in which D_m is the molecule diffusion coefficient. Compaction is included to describe the change of v and ω with depth.

Organic matter decomposition

We have used a continuum-type model (Boudreau and Ruddick, 1991) to describe the decomposition of organic matter:

$$\frac{dG}{dt} = \frac{v}{a} \cdot \frac{G^{\frac{v+1}{v}}}{G_0^{\frac{1}{v}}}, \qquad\qquad \text{Eqn. 11}$$

where G is the concentration of organic matter, G_0 is the initial content of organic matter at the chemical line of water column or the sediment-water interface, *a* is a term describing the average life-time for the more reactive organic matter, and *v* is a parameter describing the shape of organic matter distribution. A Monod scheme is used to describe the reaction rate law of sulfate reduction and methanogenesis (Table S3). The chemical components, boundary

conditions, chemical reactions, reaction rate laws, and model parameters are shown in supplementary tables S3 to S6 and the annotated code (in R) is included as a supplementary file.

Mo reduction in water column

The rate of reduction and removal of MoO_4^{2-} from water column is assumed to be related to the H_2S concentration of seawater:

$$R_{Mo} = k_{Mo}[H_2S]([Mo] - [Mo]_f) ,$$
<div align="right">Eqn. 12</div>

where k_{Mo} is the rate constant for Mo removal in water column, $[H_2S]$ is the concentration of Mo in seawater, $[Mo]_f$ is the limiting concentration for Mo reduction.

Diagenetic removal of U

The reduction and removal of U from pore water is coupled with the sulfate reduction rate (Barnes and Cochran, 1993). Michaelis-Menten kinetics is used to describe the reduction of U from pore-water because the reduction of U in pore water is likely to be predominantly microbially mediated (Lovley et al., 1991). A term f_U is applied to describe the ratio of rate between U reduction and sulfate reduction. Thus, the U reduction rate is described as:

$$k_{U238} = f_U \frac{dG}{dt} \left(\frac{KMnO_2}{KMnO_2 + [MnO_2]}\right)\left(\frac{KFe(OH)_3}{KFe(OH)_3 + [Fe(OH)_3]}\right)\left(\frac{[U^{238}]}{KU + [U^{238}]}\right) ,$$
<div align="right">Eqn. 13</div>

where terms $\frac{KMnO_2}{KMnO_2 + [MnO_2]}$ and $\frac{KFe(OH)_3}{KFe(OH)_3 + [Fe(OH)_3]}$ describe the effect of inhibition on U reduction by Mn reduction and Fe reduction.

3. Results

In order to investigate the relationship between Mo and U in anoxic water columns and accumulation in the sediments, only the authigenic components are considered. Therefore, only authigenic Mo and U concentrations and respective isotope compositions, calculated as described above, are plotted in figure 2 to figure 13. Further details about the detrital correction and a full data table, including corrected and uncorrected Mo and U concentrations and isotope compositions, can be found in the supplementary tables S8 and S10. In most cases, the estimated authigenic Mo concentrations and isotope compositions are no more than ~5 % and 0.1 ‰ different from the bulk value, respectively. Relative to bulk values, authigenic U concentrations are up to ~40 % less, and authigenic U isotope compositions are more positive by up to 0.2 ‰. We evaluate correlations between geochemical data using R^2. Further details are discussed in supplementary section S4.

3.1 Black Sea core top surface sediments

In sediments deposited in shallower environments (< 430 m water depth), Mo and U contents increase in the surface sediment samples from the Black Sea, coupled with increasing TOC and H_2S, reaching a maximum of 64 µg g^{-1} and 7 µg g^{-1}, respectively (Figure 2B). Uranium contents (in the deep water column also Mo) of sediments at 1.5 cm bsf are generally enriched compared to those of sediments at 0.5 cm bsf. δ^{98}Mo values increase from -0.55 ‰ to 1.47 ‰ with increasing depth within the first 430 m and then show only small variation, with most samples ranging between 1.5 ‰ and 2 ‰. These observations confirm previous findings by Neubert et al. (2008). Uranium isotope compositions in our sediment samples range between 0.18 ‰ and 0.43 ‰ above 430 m water depth and then generally decrease to values between -0.02 ‰ and 0.17 ‰ at greater water depth. These data compare well with previously reported values (Weyer et al., 2008; Andersen et al., 2014). Notably, most samples above 430 m bsl show lower δ^{238}U in top surface samples (0.5 cm bsf), relative to those at 1.5 cm bsf. At deeper water levels, no offset in δ^{238}U can be resolved between samples from 0.5 cm and 1.5 cm bsf.
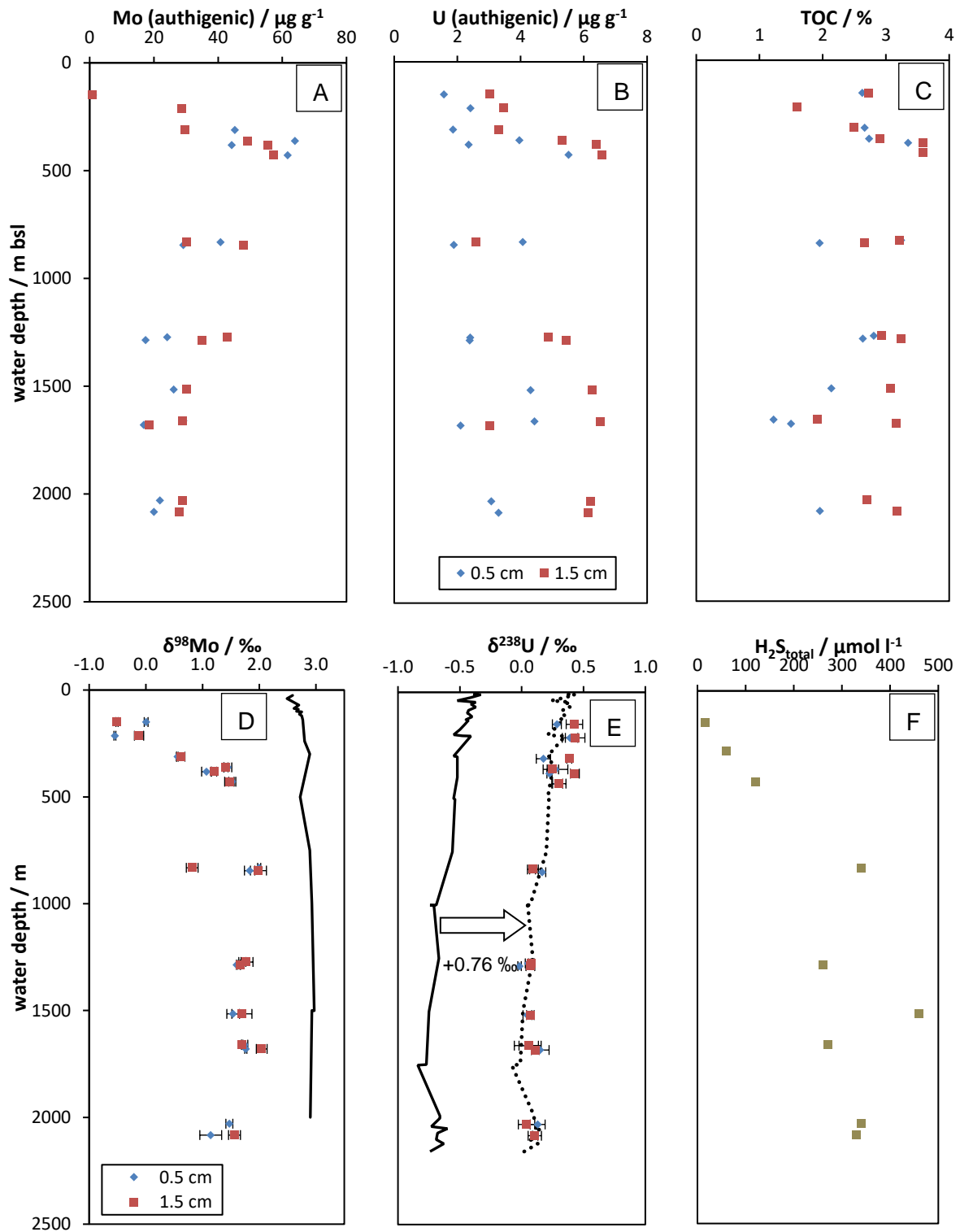
Figure 2: Black Sea sediment data from samples with depths of 0.5 cm (diamonds) and 1.5 cm (squares), A: Mo content, B: U content, C: total organic carbon (TOC), D: δ⁹⁸Mo (NIST-3134+0.25 ‰), and E: δ²³⁸U (CRM112A). In F: H₂S$_{total}$ in bottom water taken from above the sediment at the same stations as the analyzed sediments (Arz et al., 2014). In D: solid line describes the Black Sea water profile from average of both profiles from Nägler et al. (2011). In E: solid line describes the Black Sea water profile from average of all profiles from Rolison et al. (2017), dotted line describes this profile plus additional +0.76 ‰, which is the observed difference between seawater and sediments (see section 4.1 for explanation). Error bars depict 2 s.d. values calculated from triplicate isotope measurements.

Total organic carbon (TOC) contents in the sediments increase with increasing water depth from values of 1.6 % to ~4 % within the uppermost 430 m of water depth. They then vary between 3.5 % and 6.6 % with no systematic difference between samples from sediments depths of 0.5 cm and 1.5 cm. Furthermore, samples from both depositional depths show a weak, but statistically significant, negative correlation between $\delta^{238}U$ and $\delta^{98}Mo$ (Figure 3A), whereas only samples from 0.5 cm bsf show a weak positive correlation between Mo and U contents (Figure 3B).
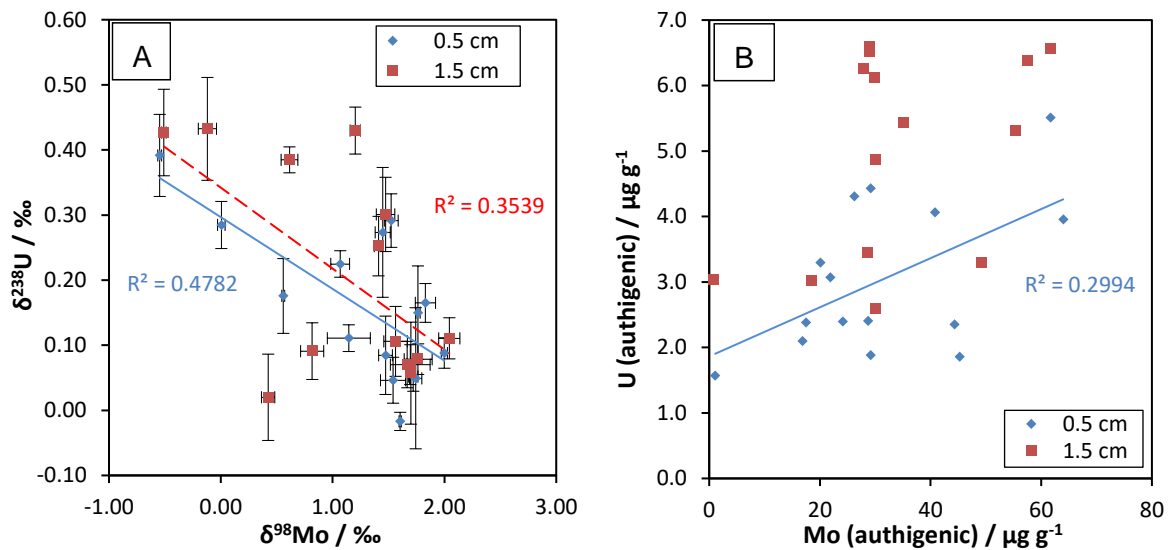
Figure 3: Crossplots of A: $\delta^{98}Mo$ (NIST-3134+0.25 ‰) vs. $\delta^{238}U$ (CRM112A), and B: Mo vs. U contents for sediment samples along the slope of the Black Sea from depths of 0.5 cm bsf (diamonds) and 1.5 cm bsf (squares). Error bars depict 2 s.d. calculated from triplicate isotope measurements.

3.2 Black Sea core 32MUC24

Core 32MUC24 yielded twelve samples from Black Sea unit I (0 cm to 24.5 cm bsf), one sample from a turbidite layer (34.5 cm bsf), and one sample from unit II (42.5 cm bsf). Uranium contents increase regularly from 3 µg g^{-1} at the top of the core to 15 µg g^{-1} at 10.5 cm bsf (Figure 4B). Below this depth, they remain relatively constant with a spike to lower values at 34.5 cm bsf. Molybdenum contents vary between 17 µg g^{-1} and 35 µg g^{-1} within unit I but increase dramatically to 92 µg g^{-1} in the unit II sample. The $\delta^{238}U$ values vary between -0.25 ‰ and 0.08 ‰ within unit I, showing a general decrease with depth, whereas the unit II sample is distinctly more positive with a value of 0.55 ‰. In contrast, $\delta^{98}Mo$ values increase slightly within the first 25 cm of the core from values of 1.47 ‰ to 2.40 ‰, and they drop sharply to 1.23 ‰ in the unit II sample.
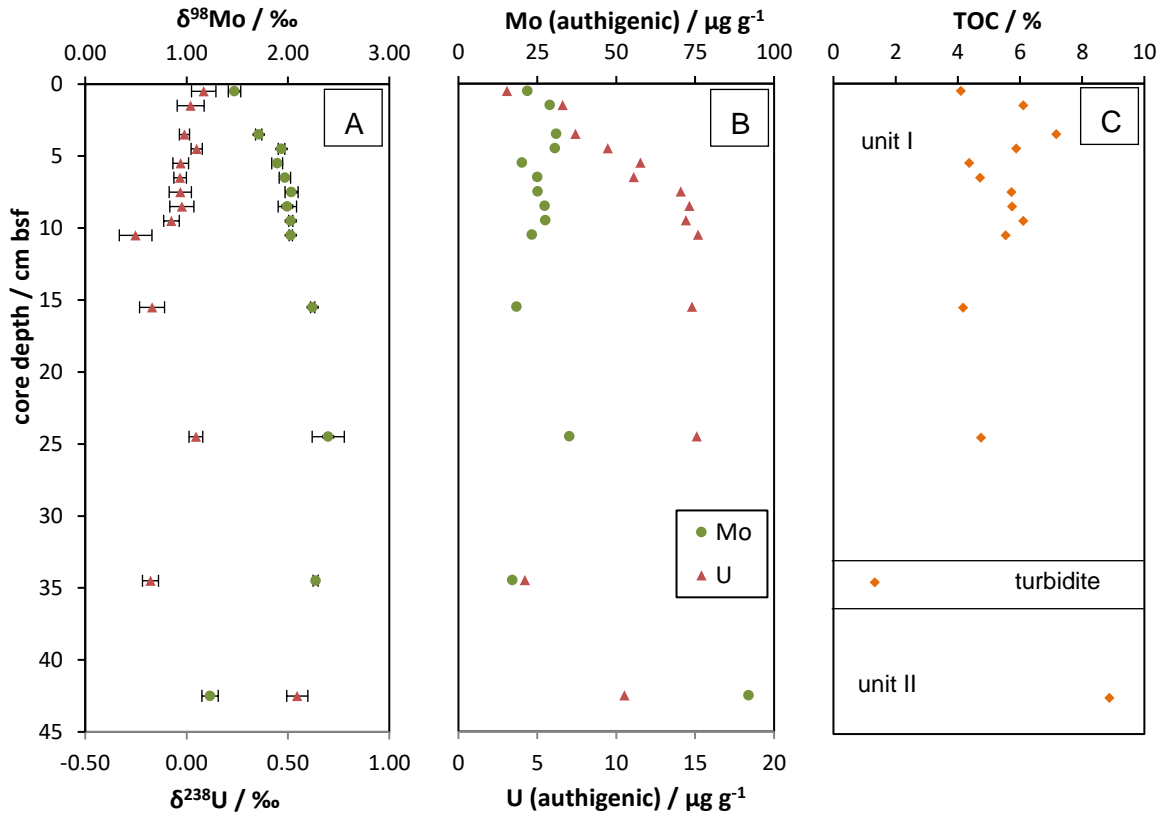
Figure 4: Depth profiles for core 32MUC24 from the Black Sea, A: δ⁹⁸Mo (NIST-3134+0.25 ‰) vs. δ²³⁸U (CRM112A), B: Mo and U contents, C: TOC contents. Triangles: U values, circles: Mo values, diamonds: TOC values. Error bars are 2 s.d. calculated from triplicate isotope measurements.

Figure 5: Crossplots of A: δ⁹⁸Mo (NIST-3134+0.25 ‰) vs. δ²³⁸U (CRM112A) and B: Mo vs. U contents in core 32MUC24 from the Black Sea. Error bars depict 2 s.d. calculated from triplicate isotope measurements.

Total organic carbon contents show no systematic variation with depth and vary between 4 % and 7.1 % within unit I, followed by an increase to 8.9 % at 42.5 cm bsf (unit II, figure 4C). This transition suggests a significant environmental change from unit II to unit I deposition. The

contrasting geochemical properties of the two units, (e.g., δ^{98}Mo, δ^{238}U, and TOC), have also been reported in many previous studies (e.g. Barling et al., 2001; Nägler et al., 2005; Algeo and Lyons, 2006; Neubert et al., 2008; Weyer et al., 2008; Montoya-Pino et al., 2010; Arnold et al., 2012; Wegwerth et al., 2018). The opposite isotope behavior for Mo and U with depth manifests as a negative correlation between δ^{238}U and δ^{98}Mo values from units I and II (Figure 5A).

3.3 Cariaco Basin core top surface sediments

All Cariaco Basin sediment surface samples were previously analyzed for trace elements by Gueguen et al. (2016). The authigenic Mo contents vary between 28 µg g^{-1} and 88 µg g^{-1}, with sediments deposited in deeper settings being generally lower in Mo contents (Figure 6B). The U contents vary between 2.9 µg g^{-1} and 7 µg g^{-1} and show the same depletion with depth. Both Mo and U show one strongly depleted sample at 656 m bsl. This similar behavior for Mo and U is expressed in a pronounced positive correlation between Mo and U contents (Figure 7B). Both Mo and U show no correlation with TOC (Figure S5B) but a weak negative correlation with bottom-water H_2S concentrations (Zhang & Millero, 1993), which increase with water depth from values of 20 µmol l^{-1} to 58 µmol l^{-1} (Figure 6). The δ^{98}Mo values vary only slightly between 1.2 ‰ and 2.0 ‰, except for the sample at 656 m bsl, which shows a very heavy δ^{98}Mo signature of 2.8 ‰. The δ^{238}U values vary between 0.09 ‰ and 0.27 ‰ with no correlation with depth or with δ^{98}Mo (Figures 6A and 7A). Furthermore, levels of H_2S do appear to have a major influence for variations in δ^{98}Mo or δ^{238}U (Figure S4A).
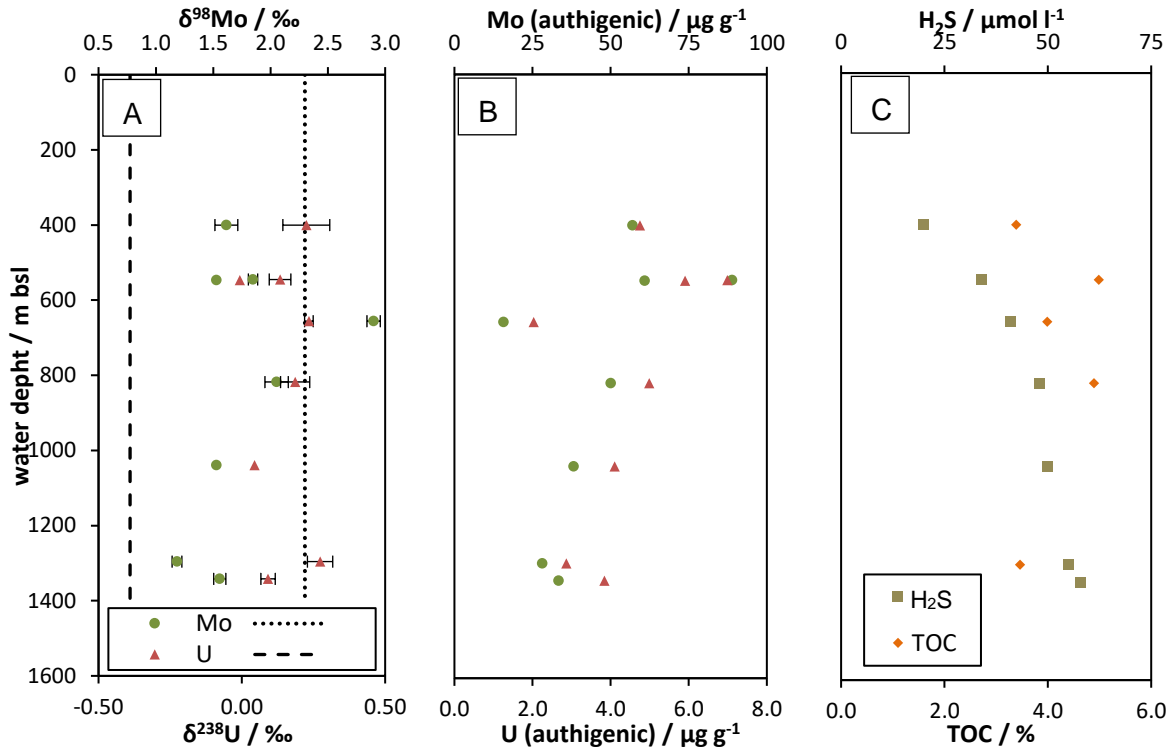
Figure 6: Cariaco Basin sediment data from core top surface samples (upper cm of sediment), A: δ98Mo (NIST-3134+0.25 ‰) vs. δ238U (CRM112A), B: Mo and U contents, C: TOC contents in the sediments and H2S concentration in the bottom water analyzed at respective depth bsl at all stations during cruise PLUME-07, H2S data were taken from Zhang and Millero (1993). In A: dashed and dotted lines represent open ocean seawater values for U and Mo, respectively, according to Siebert et al., 2003; Stirling et al., 2007; Weyer et al., 2008; Nakagawa et al., 2012 and Tissot and Dauphas, 2015. Triangles: U values, circles: Mo values, squares: H2S values, diamonds: TOC values. Error bars show 2 s.d. calculated from triplicate isotope measurements.
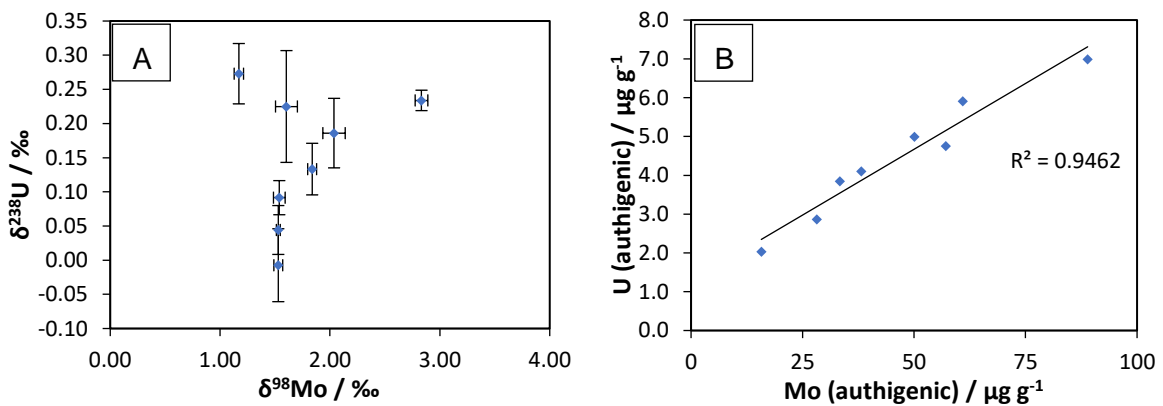
Figure 7: Crossplots of A: δ98Mo (NIST-3134+0.25 ‰) vs. δ238U (CRM112A) and B: Mo vs. U contents in surface sediments from the Cariaco Basin. Error bars depict 2 s.d. calculated from triplicate isotope measurements.

3.4 Cariaco Basin cores 12GGC and 70GGC

In the uppermost 10 cm of gravity core 12GGC (taken at 1039 m water depth), both authigenic Mo and U contents show only limited variations from 37 µg g^{-1} to 54 µg g^{-1} and 4.1 µg g^{-1} and 5.3 µg g^{-1}, respectively. At 15 cm, both Mo and U increase sharply to 108 µg g^{-1} and 9.5 µg g^{-1}, respectively (Figure 8B). In the deeper part of the core, Mo and U contents are more scattered and show a distinct positive correlation (Figure 9B). A similar depth distribution is also observed for δ^{98}Mo and δ^{238}U (Figure 8A). Within the first 10 cm of the core, the δ^{98}Mo and δ^{238}U data show little variations (1.32 ‰ to 1.56 ‰ and 0.11 ‰ and 0.18 ‰, respectively), while at greater depths, δ^{98}Mo and δ^{238}U show a distinct negative correlation (0.96 ‰ to 1.59 ‰ and 0.11 ‰ to -0.18 ‰, respectively; figures 8A and 9A). Total organic carbon values show little variation between 4.0 % and 5.9 % (Figure 8C). Molybdenum and U contents show a weak correlation with TOC, while no correlation is observed for δ^{98}Mo and δ^{238}U (Fig. S6).
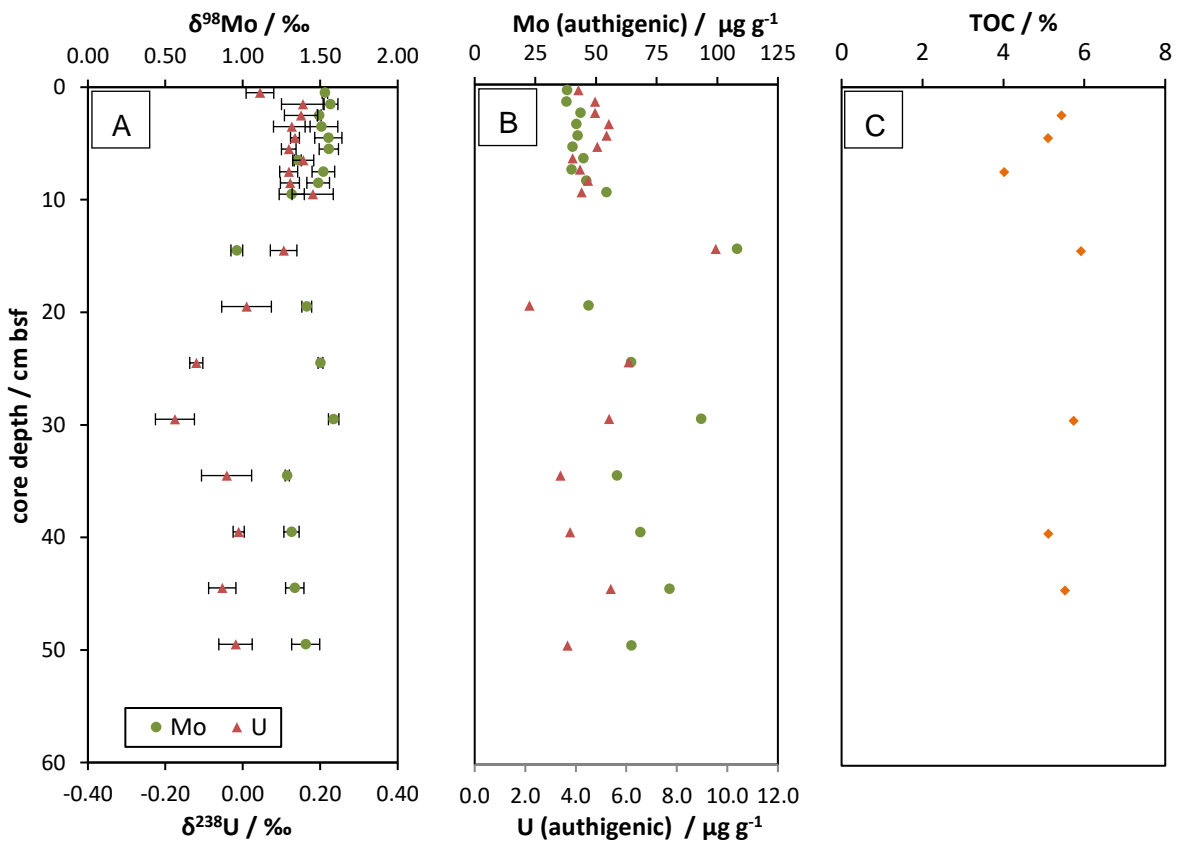
Figure 8: Depth profiles of A: δ^{98}Mo (NIST-3134+0.25 ‰) vs. δ^{238}U (CRM112A), B: Mo and U contents and C: TOC content in sediments from Cariaco basin core 12GGC. Triangles: U values, circles: Mo values, diamonds: TOC values. Error bars show 2 s.d. calculated from triplicate isotope measurements.
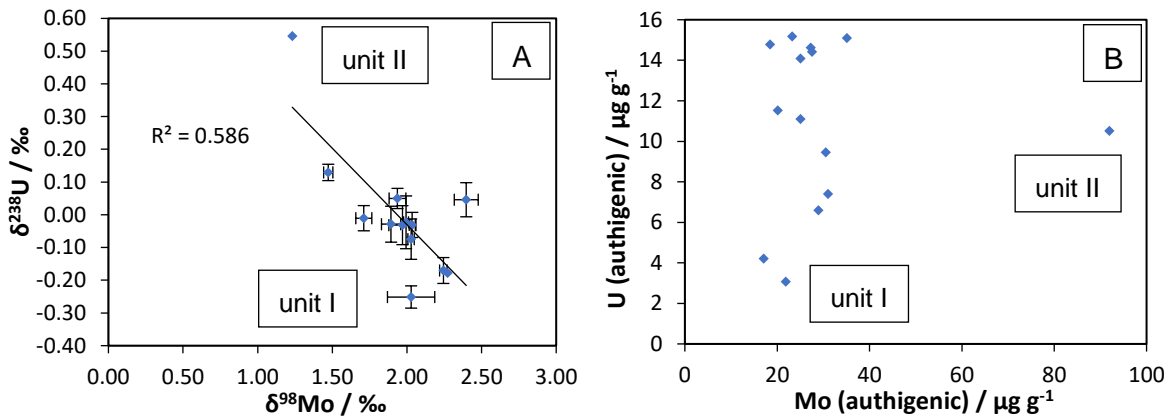
Figure 9: Crossplots of A: δ⁹⁸Mo (NIST-3134+0.25 ‰) vs. δ²³⁸U (CRM112A) and B: Mo vs. U contents in sediments from the 12GGC core from the Cariaco Basin. In A and B: squares depict samples from 0 cm to 10 cm bsf and diamonds are samples from 15 cm to 50 cm bsf. Error bars depict 2 s.d. calculated from triplicate isotope measurements.

In core 70GGC (taken at 547 m water depth), U and Mo contents vary between 56.2 µg g⁻¹ and 160.7 µg g⁻¹ and 5.9 µg g⁻¹ to 18.9 µg g⁻¹ for Mo and U, respectively (Figure 10B), and show a significant correlation (Figure 11B). Similarly, δ²³⁸U (-0.09 ‰ to 0.25 ‰) and δ⁹⁸Mo (1.04 ‰ to 1.81 ‰) appear to be randomly distributed with depth; however, samples deposited below 15 cm bsf show a distinct correlation between δ²³⁸U and δ⁹⁸Mo. In contrast to core 12GGC, however, there is no systematic offset in the δ²³⁸U versus δ⁹⁸Mo relationship at 15 cm bsf. Over the total depth of the core, TOC values vary between 4.7 % and 5.9 %, and no correlation between TOC and Mo or U contents or isotope compositions is observed (Fig. S7).
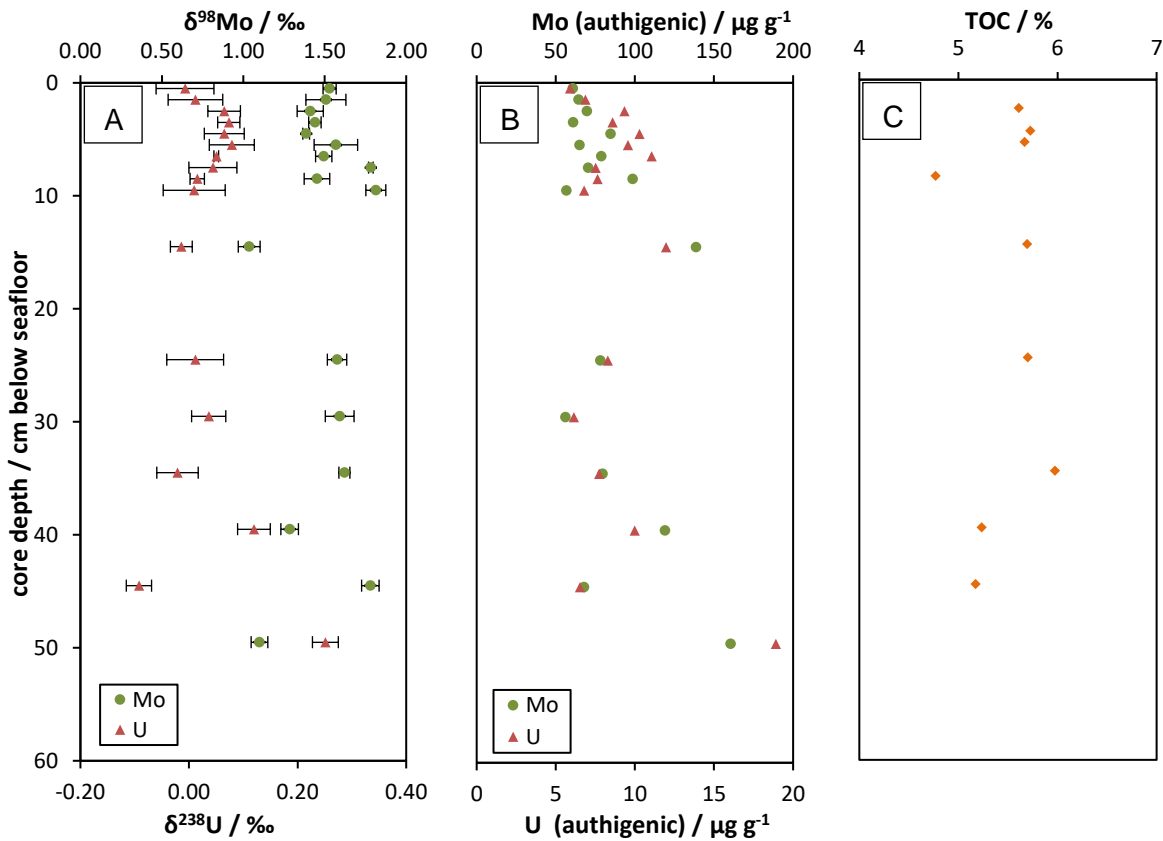
Figure 10: Depth profiles of A: δ⁹⁸Mo (NIST-3134+0.25 ‰) vs. δ²³⁸U (CRM112A), B: Mo and U contents and C: TOC content in sediments from Cariaco Basin core 70GGC. Triangles: U values, circles: Mo values, diamonds: TOC values. Error bars depict 2 s.d. calculated from triplicate isotope measurements.
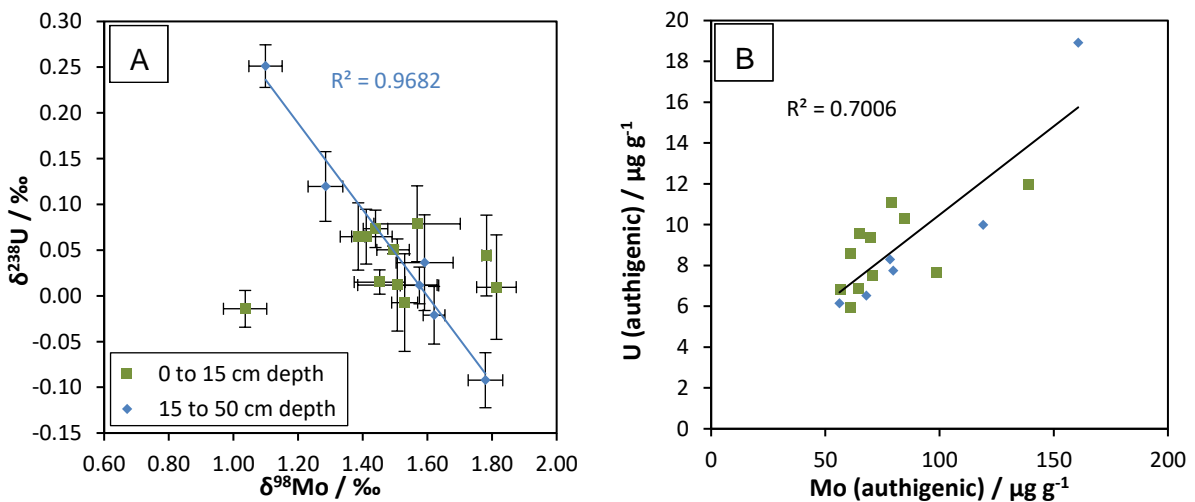
Figure 11: Crossplots of A: δ⁹⁸Mo (NIST-3134+0.25 ‰) vs. δ²³⁸U (CRM112A) and B: Mo vs. U contents in sediments from core 70GGC from the Cariaco Basin (trend line is for all samples). In A and B: squares depict samples from 0 cm to 10 cm bsf and diamonds to samples from 15 cm to 50 cm bsf. Error bars depict 2 s.d. values for triplicate isotope measurements.

3.5 Cariaco Basin core 1002B (ODP site 165)

In sediment samples from this core, Mo contents vary between 65 µg g^{-1} and 177.9 µg g^{-1} and U contents between 4.8 µg g^{-1} and 18.7 µg g^{-1} (Figure 12B). Over the whole length of the core, Mo and U show parallel concentration profiles, resulting in a well-defined positive correlation between Mo and U (Figure 13B).
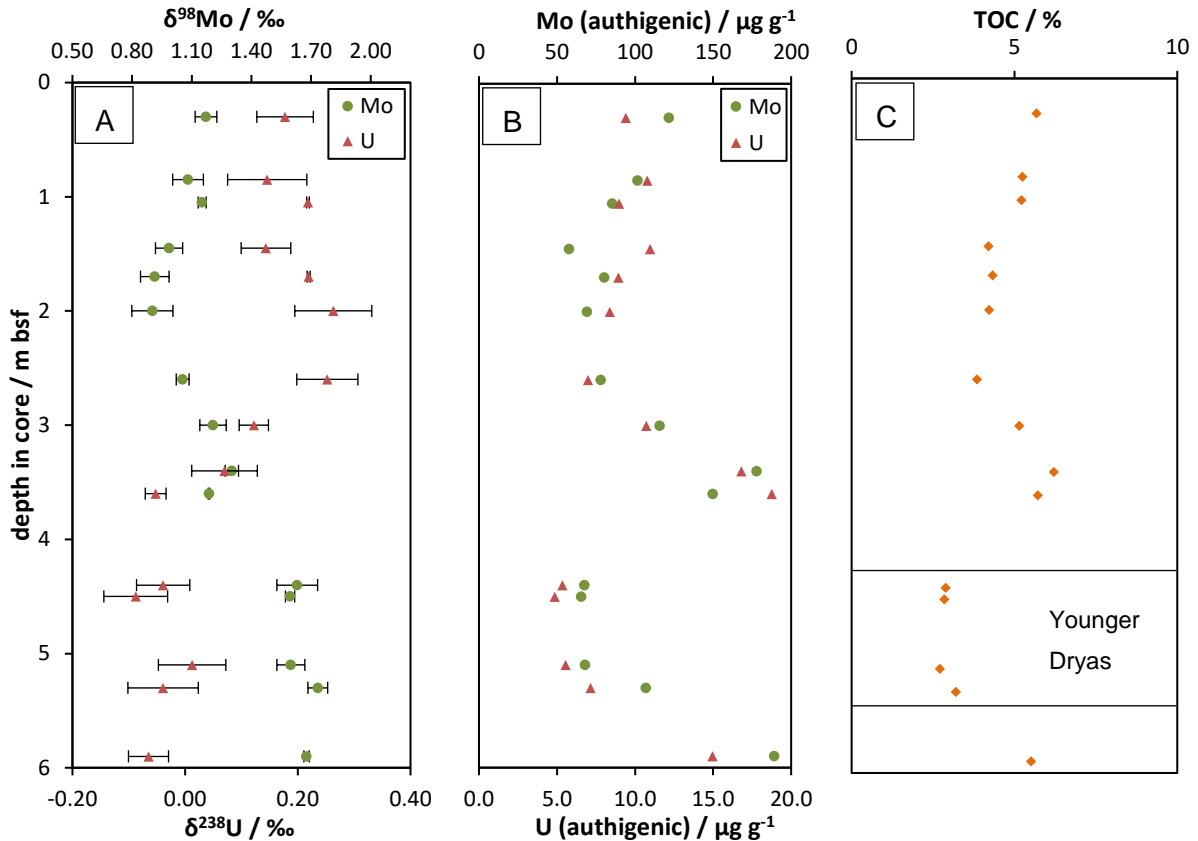
Figure 12: Depth profiles of A: δ^{98}Mo (NIST-3134+0.25 ‰) vs. δ^{238}U (CRM112A), B: Mo and U contents and C: TOC content in sediments from Cariaco Basin core 1002B (leg 165, Lyons et al., 2003). Triangles: U values, circles: Mo values, diamonds: TOC values. Error bars show 2 s.d. calculated from triplicate isotope measurements.

The δ^{98}Mo and δ^{238}U depth profiles show opposed trends over the entire core (Figure 12A), resulting in a negative correlation between δ^{98}Mo and δ^{238}U (Figure 13A). Furthermore, Mo and U contents display pronounced positive and negative correlations with δ^{98}Mo and δ^{238}U, respectively (Fig. S9). Samples between 4.2 m to 5.6 m bsf were deposited during the Younger Dryas, a cold period with high primary productivity beginning at 13.0 ka BP and lasting until 11.6 ka (Werne et al., 2000). These samples show lower Mo and U contents, as well as TOC contents (Lyons et al., 2003; Algeo and Lyons, 2006; Reinhard et al., 2014) and relatively high δ^{98}Mo (1.59 ‰ to 1.73 ‰), as well as relatively low δ^{238}U (-0.09 ‰ to 0.01 ‰) compared to

those deposited before and after (Figure 12). Furthermore, this difference between Younger Dryas samples and those deposited below and above can also be interpreted as an offset from the correlation between Mo and δ^{98}Mo as well as between U and δ^{238}U (Fig. S9).

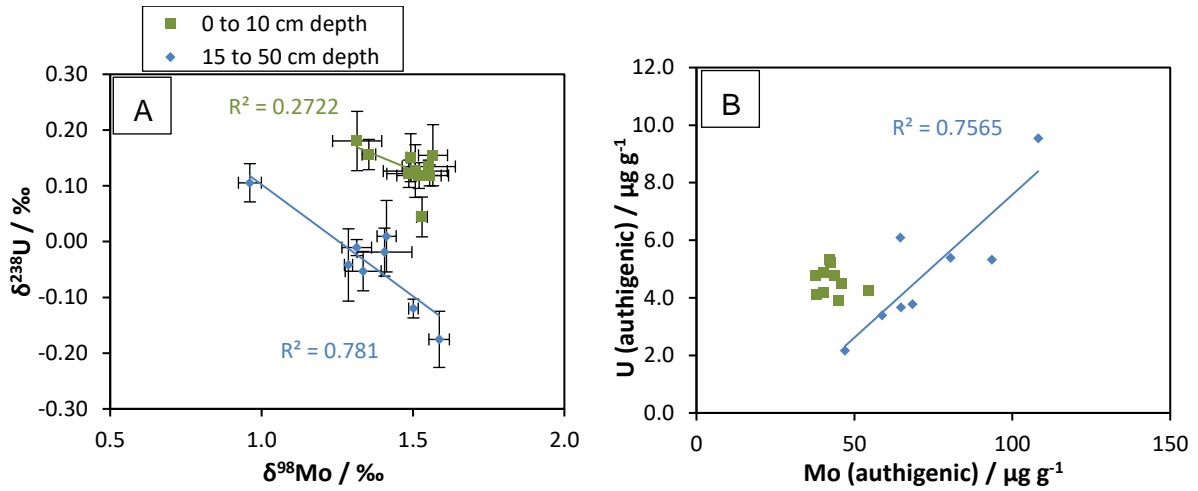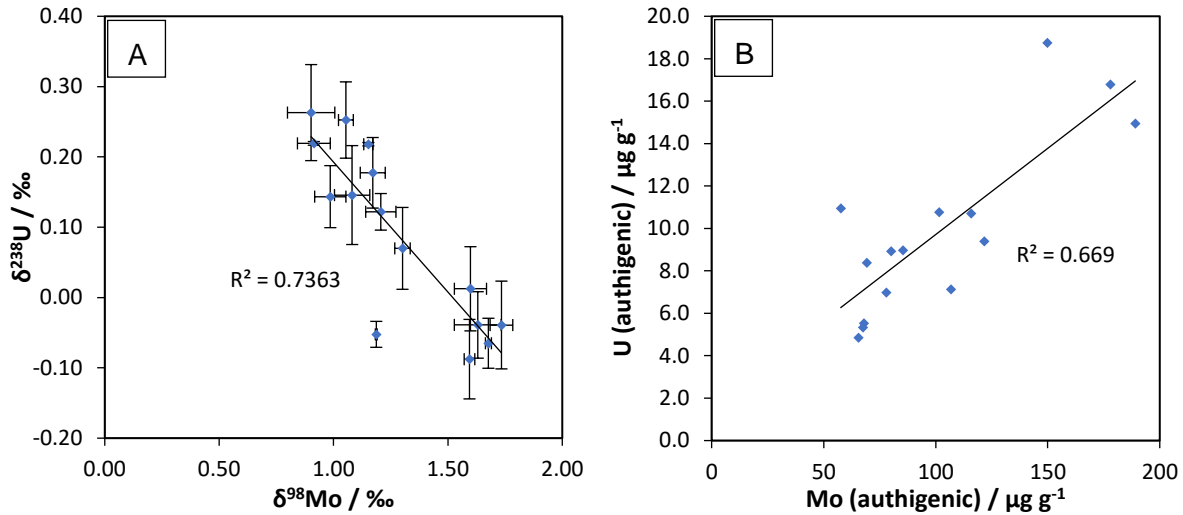**Figure 13: Crossplots of A: δ^{98}Mo (NIST-3134+0.25 ‰) vs. δ^{238}U (CRM112A) and B: Mo vs. U contents in sediments from core 1002B (leg 165) from the Cariaco Basin. Error bars depict 2 s.d. values for triplicate isotope measurements.**

4. Discussion

4.1 Metal removal and isotope fractionation in the Black Sea

Sediments in the Black Sea show increasing Mo contents with depth (until water depths of ~430 m), correlating with increasing bottom-water H_2S concentrations, which results in the formation of thiomolybdates and enhanced Mo particle reactivity and scavenging. The strong basin restriction of the Black Sea and related long deep water renewal times result in very low dissolved Mo concentrations in the deep water column (Neubert et al., 2008; Nägler et al., 2011). Consequently, Mo contents in Black Sea sediments deposited at depths below 430 m — well below the chemocline — are lower than in sediments deposited above 430 m (Figure 2B). Furthermore, bulk Mo contents are diluted by $CaCO_3$ contributions, which average ~50 % in the deep basin (Lyons, 1991; Algeo and Lyons, 2006). Because of the occurrence of H_2S in the water column and a positive correlation between H_2S and δ^{98}Mo (Figure S2A), Mo isotope fractionation in the Black Sea can be attributed to the formation of particle-reactive thiomolybdates. Our data confirm the previously reported correlation between δ^{98}Mo in top surface sediments and water column H_2S_{aq} values (Figure S2A) (Neubert et al., 2008). An alternative model is based on the formation of a Fe(II)-Mo(VI)-sulfide mineral, which depends on pH and sulfide concentrations, as the main Mo removal phase in euxinic basins (Helz et al.,

2011). However, to date no systematic study has been performed that couples this model with Mo isotope fractionation. Nevertheless, both models rely on Mo removal that is strongly coupled with sulfide concentrations.

Because H_2S_{aq} in the upper water of the Black Sea column concentrations are below the APS of 11 µmol l^{-1} (which equals ~100 µmol l^{-1} H_2S_{total} and characterizes the active point of switch, Helz et al., 1996; Neubert et al., 2008), Mo transformation to thiomolybdates is incomplete and Mo is thus not quantitatively removed from the water column, resulting in variable isotope fractionation (Neubert et al., 2008). Sediments that were deposited below 430 m show constant heavy, almost seawater-like signatures (Figure 14A). Only minor offsets in Mo enrichment and isotope values are observed between samples from 0.5 cm and 1.5 cm in Black Sea surface sediments, suggesting that Mo isotope fractionation likely occurs within the water column (Figure 2B, E) and is not affected by interactions between the pore water and sediments. Likely, Mo concentrations in pore water are negligible because of quantitative removal in the water column or directly at the water-sediment interface.

Bura-Nakić et al. (2018) showed that Mo concentrations in sediment pore waters of a small euxinic lake are significantly depleted compared to the overlying oxic water column. However, Mo and δ^{98}Mo in Black Sea pore water are not constrained and warrant further investigation. Furthermore, no significant increase is observed in Mo contents between samples from 0 to 10 cm in core 32MUC24 from the deep central Black Sea (Figure 4B), also suggesting Mo removal in the water column (Little et al., 2015). Still, even at a water depth of 2030 m, Mo isotopes in the uppermost centimeters of the core are lower by ~0.6 ‰ than the expected seawater value, which may be explained by incomplete conversion of MoO_4^{2-} to MoS_4^{2-} and associated Mo isotope fractionation (Tossell, 2005; Nägler et al., 2011). Likely, progressive quantitative capture of these partially converted thiomolybdates within the first ~ 5 cm of the sediments pore-water, ultimately resulting in essentially seawater-like Mo isotope signatures of ~2 ‰ at 6 cm depth (Figure 4A).

Alternatively, the isotopically lighter Mo of the first few cm of the core may be attributed to the operation of a Fe-Mn oxide particulate shuttle. During adsorption of Mo onto Fe-Mn oxides, light Mo isotopes are preferentially taken up with a total offset of ~1 ‰ to 3 ‰ between adsorbed and dissolved Mo for Fe and Mn oxides, respectively (Barling and Anbar, 2004; Goldberg et al., 2009). The adsorbed light molybdate is released in deeper anoxic waters during re-dissolution, in particular of Mn oxides (Fe oxides are more stable and may carry Mo directly to the sediment: Ho et al., 2004 and Benitez-Nelson et al., 2007). An oxide shuttle would be expected to result in lower δ^{98}Mo values recorded in the sediments compared to the seawater values (Kendall et al., 2015; Kurzweil et al., 2016; Lu et al., 2017; Scholz et al., 2017; Bura-Nakić et al., 2018). In this alternative explanation to our data, Fe-Mn oxides were

remobilized under rising anoxic conditions from the slope of the Black Sea releasing light Mo, which may have locally contributed to the Mo signature of seawater, even in the deep Black Sea sediments (Lyons and Severmann, 2006).

Within the core 32MUC24, Mo isotope signatures increase with depth and reach a modern seawater Mo isotope composition below 15 cm, indicating constant redox conditions and Mo source composition during the deposition of these sediments. On the other hand, samples from unit I from deeper water depths (418 m to 837.7 m) show more variable δ^{98}Mo that can be best explained by a combination of processes. Incomplete conversion of molybdate to tetrathiomolybdate under lower H_2S_{aq} concentrations and an isotopically lighter Mo source due to the Fe-Mn oxide particulate shuttle effects may explain these data. All samples from unit II show a general offset towards lower δ^{98}Mo values; however, this difference is only distinguishable relative to unit I in sediments of the deep Black Sea and not in those from the slope. Lower δ^{98}Mo values of the latter samples compared to those from the deep Black Sea (core 32MUC24) are in agreement with previous interpretations of lower H_2S_{aq} levels during deposition of Black Sea unit II sediments (Arnold et al., 2004; Barling and Anbar, 2004; Nägler et al., 2005; Wegwerth et al., 2018).

Uranium may be removed from the water column via four pathways: (1) active uptake and reduction by sulfate-reducing organisms whose remains are preserved in the sediments; (2) complexation and reduction of U(VI) by particulate organic matter; (3) chemical reduction of soluble U(VI) to insoluble U(IV) (e.g., by H_2S, Barnes and Cochran (1993)), which is scavenged by settling particles; and (4) diffusion from bottom water into the sediment pore water, followed by reduction of U(VI) to U(IV) via mechanisms 1 to 3 and subsequent precipitation within the uppermost sediment layers (Anderson et al., 1989; Barnes and Cochran, 1990; Klinkhammer and Palmer, 1991; Morford et al., 2005). In principle, any process of U reduction is expected to enrich isotopically heavy U in the reduced sediments (Abe et al., 2008; Weyer et al., 2008; Brown et al., 2018), although experiments presented by Stylo et al. (2015) resulted in significant differences in the direction and extent of U isotope fractionation, depending on the mechanism of U reduction.

It has been shown by Romaniello et al. (2009) and Rolison et al. (2017) that the deep water column of the Black Sea is fractionated toward lower δ^{238}U values by 0.28 ‰ compared to open ocean seawater. The strong restriction and slow deep water renewal of the Black Sea results in depletion of U and isotopically heavy U in the deep water column as the ^{238}U is preferentially removed into sediments. Taking the fractionated Black Sea water column from Rolison et al. (2017) into account, the fractionation of U isotopes between the deep water column and our sediment samples is $\Delta^{238}U_{sed-water}$ of 0.76 ‰ ±0.17 ‰, which is similar to that inferred by Montoya-Pino et al. (2010), Brennecka et al. (2011), Andersen et al. (2014), and

Rolison et al. (2017). This isotope fractionation appears to be remarkably constant throughout the water column, as determined by top-surface sediments (0.5 cm bsf) taken at variable water depth along the slope below the chemocline (Figure 2E). Thus, the higher δ^{238}U of sediments of the upper water column compared to those from the central Black Sea can be explained by the fractionated δ^{238}U in the water column. Our diagenetic model results also indicate that δ^{238}U of bottom water is responsible for the variation of δ^{238}U in core-top sediments, while the sedimentation rate and TOC do not have much influence (for detailed model results the reader is referred to section 4.3).

A similar U isotope fractionation between the water column and authigenic U in the sediment was also observed by Noordmann et al. (2015) for a small fjord (Kyllaren Fjord in Norway). The heavy U isotope compositions of top-surface (0.5 cm bsf) sediments may indicate that a significant portion of U reduction and enrichment occurs either in the water column or directly at the water-sediment interface by mechanisms 1 to 3. Assuming a simple Rayleigh model (Wiederhold, 2015) for U reduction and removal from the water column, would indicate an isotope fractionation factor of $\varepsilon = (\alpha - 1) * 1000$ of ~0.6 ‰ (Andersen et al., 2017; Rolison et al., 2017). As this fractionation factor is lower than experimentally determined intrinsic (or instantaneous) fractionations (Basu et al., 2014; Stylo et al., 2015; Brown et al., 2018), Andersen et al. (2014) suggested a model of U removal and isotope fractionation occurring predominantly in the sediment, during diffusive transport and reaction of U from seawater and through pore water, resulting in a muted isotope fractionation (see also Clark and Johnson, 2008 for modelling details). In this Andersen et al. (2014) model, the fractionated U isotope signature of surface sediments may be explained by diffusion driven pore water U cycling within the uppermost few cm of the sediments.

On the other hand, all surface sediment samples from the Black Sea show an enrichment in the U content between 0.5 cm to 1.5 cm (Figure 2A). In samples deposited at water depth from 0 m to 430 m, this enrichment is coupled with an overall increase of δ^{238}U values between 0.5 cm and 1.5 cm. This observation of increasing U content and isotope fractionation with depth may be attributed to ongoing U enrichment as a result of U diffusion from seawater into pore water due to a concentration gradient and subsequent partial U reduction within the sediment. The increase in δ^{238}U with depth may indicate that the degree of U reduction within the sediment (as a result of diffusion within pore water) is small compared to that at the water-sediment interface (or within water column), resulting in more pronounced isotope fractionation implied by the fact that low rates of reduction result in high isotope fractionation (Figure 14A). Likewise, the mechanism of U reduction in the sediment may be different than that at the water-sediment interface, including, for example, a higher portion of biotic versus abiotic reduction (Stylo et al., 2015). In either way, these findings indicate incomplete mixing and reduction of U in the uppermost sediment pile. Rather, the sediments may (at least partially) preserve their

isotopic signal from U reduction at the water-sediment interface, which results from different isotope sources (e.g., seawater and pore water).

Samples deposited below 430 m water depth do not show resolvable differences in U isotope compositions within the first few cm, despite a significant increase in U contents (Figure 2). This finding may indicate that either U mixing by pore water cycling within the uppermost sediment pile is sufficient enough to homogenize U isotope signatures (Figure 14A) or that effectiveness and mechanism of U reduction in sediment pore waters at more sulfidic conditions is similar to that directly at the sediment-water interface. Enhanced effectiveness of U reduction in the deep water sediments compared to that in slope sediments may be related to their higher TOC contents (Lüning and Kolonic, 2003; Campbell et al., 2012). A potential relationship between reduction rate and TOC is supported by a positive correlation of TOC with U contents and a negative correlation with δ^{238}U in surface sediments of the upper 430 m of the Black Sea (Fig. S1A, B). This model may explain variable δ^{238}U within the uppermost few cm of surface sediments as a result of variable efficiencies of U reduction.

Overall, the variable U isotope signatures of Black Sea sediments from different water depths may be best explained by (1) U reduction and removal at the sediment-water interface from an isotopically fractionated water column and (2) additional reduction and scavenging of U from pore water diffusion in the sediment (Figure 14). The latter mechanism appears to be less effective in sediments of the slope of the Black Sea, resulting in increasing δ^{238}U with depth, compared to those in the basin center, which display constant δ^{238}U.
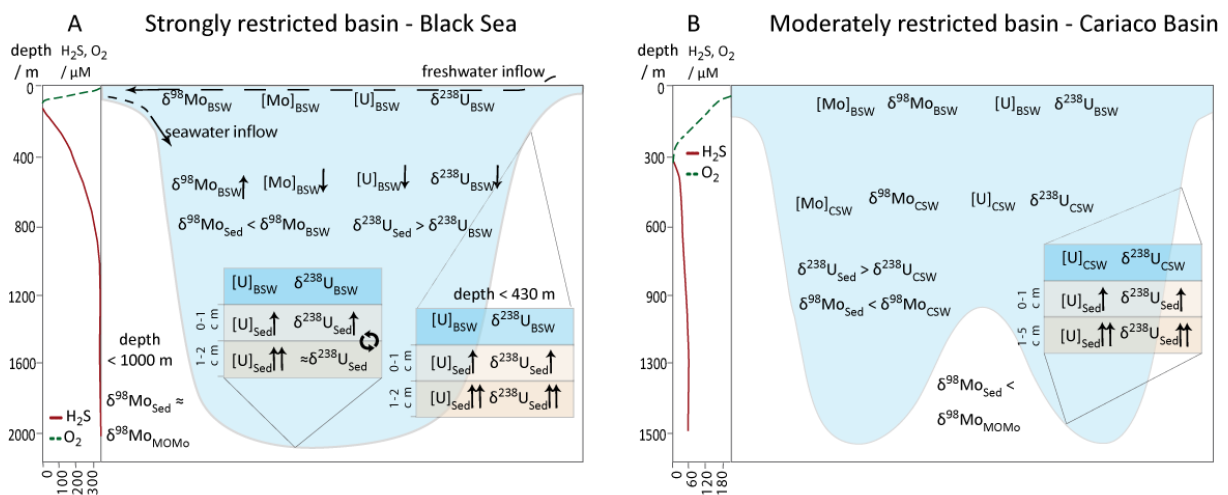
Figure 14: Simplified sketch showing the different U and Mo isotope fractionation behavior in the Black Sea and the Cariaco Basin within the water column and at different sedimentation depth. Circled black arrow indicates complete isotope homogenization in the deep Black Sea sediment pile. Vertical arrows show increase in U isotope compositions or contents, respectively. For a detailed description and discussion of the presented processes the reader is referred to sections 4.1 and 4.2. BSW = Black sea water and CSW = Cariaco Seawater. H₂S and O₂ profiles are from Zhang and Millero (1993), Scranton et al. (2001), Algeo and Tribovillard (2009) and Arz et al. (2014). Size of sketch is not to scale.

4.2 Removal processes and isotope fractionation in the Cariaco Basin

The Cariaco Basin differs from the Black Sea with respect to water column H_2S_{aq} concentrations and deep water renewal times. As a result of lower H_2S_{aq}, which do not exceed the APS of 11 µmol l^{-1} (Helz et al., 1996; Erickson and Helz, 2000), the removal of Mo from the water column of the Cariaco Basin is not quantitative (Figure 14). Furthermore, the Cariaco Basin is less restricted than the Black Sea, resulting at present in a relatively short deep water renewal time, a salinity similar to open-ocean water, and almost constant Mo contents throughout the water column (Algeo and Tribovillard, 2009). Accordingly, the Mo isotope composition of Cariaco basin seawater should be isotopically homogeneous with a Mo isotope composition similar to that of open seawater (+2.3 ‰), although this has not yet been demonstrated. The non-quantitative Mo removal results in strong Mo isotope fractionation in all sediments throughout the basin (Figure 6A) with only one sample showing a high δ^{98}Mo signature (+2.83 ‰). There is a striking positive correlation between Mo and U contents in top surface sediments (Figure 7B), suggesting related removal mechanism at present. Though conversion of molybdate to thio-molybdates is likely to occur in the water column, Mo scavenging may take place mostly along with U scavenging — e.g., at the water-sediment interface. Notably, the coupled mechanisms of Mo and U removal does not result in correlated Mo and U isotope signatures. The two analyzed sediment cores 12GGC and 70GGC, from 1039 m and 547 m bsl, respectively (Figures 8 and 10) show relatively constant Mo contents and isotope compositions, and no or only weak correlation of Mo and U within the first 10 cm of sediment cores. This observation may suggest that a decoupling of Mo and U occurs within the sediment pile, assuming that additional U and no additional Mo scavenging occurs during pore water cycling in the upper few cm of sediment.

In contrast, Mo contents and isotope compositions are more variable in the deeper parts of both cores. While the upper 10 to 15 cm of the sediment are strongly affected by active diffusion-driven metal cycling in pore-water, the lower sediment pile may be considered as an archive for historical changes of the condition of the water column. In such cases, Mo contents are weakly correlated with TOC (core 12GGC), likely because of adsorption of thiomolybdate to organic particles in the deep Cariaco Basin (Fig. S6B). While the formation of particle-reactive thio-molybdates within the water column appears to be the dominant removal mechanism of Mo from the water column, which may explain much of the observed variations in δ^{98}Mo in the sediments, the operation of a Fe-Mn oxide particulate shuttle may also affect the isotope composition of the Mo source of the Cariaco Basin (Arnold et al., 2004; Dellwig et al., 2010; Scholz et al., 2013). Such a mechanism would shift the isotope composition of anoxic waters in the Cariaco basin toward lower δ^{98}Mo values (for explanation see section 4.1). However, it is important to note that this mechanism is speculative given the potential for rapid metal reduction in the presence of sulfide.

The behavior of U in the Cariaco Basin appears to be similar to that observed along the slope in the Black Sea. In general, Cariaco surface sediments do not show a difference between deposition along the slope and within deep basin sediments, in contrast to the Black Sea. Uranium isotope ratios in Cariaco surface sediments show variable values between 0.09 ‰ to 0.27 ‰. There is no correlation between H_2S_{aq} concentrations in the water column and U (Fig. S4B), suggesting a decoupling of these two parameters. The $\delta^{238}U$ values are best explained by reductive removal at the water-sediment interface and within the uppermost few centimeters of the sediment. Core top surface sediments show a negative correlation between $\delta^{238}U$ and TOC (Fig. S5A), which is consistent with more quantitative U reduction at higher TOC, resulting in less pronounced U isotope fractionation and thus lower $\delta^{238}U$ signatures in the sediments. The slight down-core increase in U contents and isotope compositions in cores 12GGC and 70GGC (Figures 8 and 10) within the first few cm are similar to the behavior of U in the Black Sea slope sediments (Figure 2D).

Similar to Black Sea surface sediments, which were deposited along the basin slopes (at relatively low H_2S_{aq}), there is likely ongoing U reduction in the sediment pore waters, resulting in additional U enrichment and isotope fractionation with depth. In the deeper part of the cores 12GGC and 70GGC (below ~ 15 cm), pore water U reduction has no further influence on the U content or $\delta^{238}U$ signatures of the sediments. In core 70GGC, taken above 600 m, a $\delta^{238}U$ increase from 0 cm to 5 cm can be observed, whereas in core 12GGC from 1039 m, at slightly higher H_2S_{aq}, $\delta^{238}U$ only increases within the top 1.5 cm bsf and then remains relatively constant (Figures 8 and 10). This difference may be explained by differences in the depths of the main U reduction horizon during pore water U cycling in the sediment. At shallower water levels and lower H_2S_{aq} (core 70GGC), the U reduction rate may be relatively low in the uppermost 5 cm of the sediment, resulting in additional U isotope fractionation during U removal. In this scenario, U reduction is more intense below 5 cm. In contrast, at greater water depths and higher H_2S_{aq} (core 12GGC), more quantitative U reduction during pore water U cycling may already occur below 1.5 cm bsf, resulting in no additional U isotope fractionation because steady state conditions are reached. Besides potentially H_2S_{aq}–related differences in U reduction rates, the diffusion-driven U supply from seawater into pore water will also control the effective rate of U reduction and thus the sediment $\delta^{238}U$ values. Sediment textures may also play a role in interpreting different U reduction rates as coarse-grained sediments may lead to larger $\Delta^{238}U$ values (Dang et al. 2018).

Core 12GGC (sampled at a water depth of 1039 m) displays a striking offset in $\delta^{98}Mo$ versus $\delta^{238}U$ between core depth of 0 – 10 cm and 15 – 50 cm (Figure 9A). This offset is not observed in core 70GGC, which was sampled at an intermediate water depth of 547 m (Figure 11A). One possible explanation for the offset may be related to a shift from more fractionated deep water in the past (resulting in lower $\delta^{238}U$ of the deeper sediments) toward an essentially

unfractionated water column at present. Alternatively, the Mo input may have changed at this time (e.g., a change in particulate shuttle that affected the sediments of the central Cariaco basin). These distinctly different correlations suggest that the two sites experienced different metal sources or conditions during deposition.

Taking the average value from surface sediments ($\delta^{238}U$ = +0.15 ‰ ± 0.14 ‰) and open ocean seawater value ($\delta^{238}U$ = -0.39 ‰) (note that the $\delta^{238}U$ value of Cariaco seawater is not known), we can infer U isotope fractionation between water and sediment to $\Delta^{238}U_{sed-water}$ = 0.54 ‰ ± 0.14 ‰ for the present Cariaco Basin. This value is similar but slightly lower to the isotopic offset between water column and sediment of 0.76 ‰ that is observed for the Black Sea (Andersen et al., 2014; Rolison et al., 2017; this study). Using a simple Rayleigh model for U removal from the Cariaco Basin water column, similar to that applied above for the Black Sea, and assuming ~10 % U removal at present (Barnes and Cochran, 1990) and the open-ocean seawater values of -0.39 ‰, results in a U isotope fractionation factor of $\varepsilon \approx 0.6$ ‰. The offset observed between deeper sediment from the cores and present day seawater, however, is slightly lower than 0.54 ‰ because the sediments in general have lower $\delta^{238}U$. These differences may be explained by two possible scenarios: (1) the $\delta^{238}U$ of the Cariaco Basin water column of the recent past was lower than the open ocean, similar to the present-day Black Sea, or (2) there was on average a lower U isotope fractionation factor compared to that estimated for the Black Sea (and the present Cariaco Basin).

Scenario #1 — a fractionated water column like that in the Black Sea — was suggested by Andersen et al. (2014). However, the Cariaco Basin is less restricted and deep water renewal was likely always faster in the Cariaco Basin compared to the Black Sea. Instead, we hypothesize that the Cariaco Basin water column was always more weakly stratified with a deeper and less stable chemocline as compared that in the Black Sea (Scranton et al., 2001). Therefore, differences in U isotope fractionation between Black Sea and Cariaco Basin sediments may be related to differences in the effective U isotope fractionation factors in the recent past (scenario #2).

Alternatively, multiple factors could result in contrasting $\Delta^{238}U_{sed-water}$ values in the Black Sea and Cariaco Basin. If abiotic reduction results in lower U isotope fractionation relative to biotic reduction (Basu et al., 2014; Stylo et al., 2015; Brown et al., 2018), the degree of abiotic reduction in the Cariaco Basin may be higher than that of the Black Sea. Alternatively, a higher degree of U reduction or a strongly diffusion-limited U supply to the pore-water (Andersen et al. 2014) may also result in a less effective U isotope fractionation between the water column and sediments of the Cariaco Basin. In this latter scenario, the difference between the two basins may be explained by inhibited U replenishment (e.g., if additional reduction occurred deeper in the sediment and at the sediment-water interface) or more rapid reduction during

pore water cycling, resulting in more quantitative U reduction and suppressed isotope fractionation in sediments of the Cariaco Basin.

4.3 A Mo und U isotope fractionation trend

Even though Mo and U undergo very different removal processes during enrichment in anoxic sediments, the δ^{238}U and δ^{98}Mo signatures are inversely correlated in samples from both the Black Sea and Cariaco Basin (Figure 15). For the Cariaco Basin, we distinguished between samples from the upper 10 cm of the sediment pile with ongoing pore water cycling and those from below. Pore water cycling in this interpretation results from concentration gradients that cause ongoing U diffusion and subsequent reduction in deeper sediments, as well as at the sediment-water interface. Accordingly, in the Cariaco Basin near surface samples include the top-surface samples and the uppermost 10 cm of the cores 12GGC and 70GGC. Deep sediment samples include samples below 10 cm bsf of the cores 12GGC and 70GGC and all samples of the core 1002B. For the Black Sea, we treat all samples taken at 0.5 cm and 1.5 cm along the slope as top surface samples. The deep sediments are represented by samples with sampling depth > 3 cm from the deep basin (cores 32MUC24, BSK 1, BSK 2, BSK 3, Sta 10, Sta 27/28, and 25GC1 including samples from unit I and unit II).

The deep sediments of both basins, whose pore waters are no longer strongly influenced by diffusion from seawater and where authigenic enrichment may be near completion — and which thus record Mo and U isotope fractionation of the historical past — show a negative correlation for δ^{238}U and δ^{98}Mo with similar slopes but different intercepts. As Mo and U isotopes are fractionated in opposite directions during reduction and removal from water into sediments, the negative correlation of δ^{238}U and δ^{98}Mo translates into a positive correlation for the extent of isotope fractionation between water and sediment. The similar correlations in both basins indicate an overall coupling between Mo and U isotope fractionation, with variations of water column conditions and the mechanism of Mo and U removal playing a secondary role. Deep sediments of the Cariaco Basin (in particular from core 1002B) show the most pronounced correlation between Mo and U isotopes, as well as a positive correlation between δ^{98}Mo and Mo contents and an inverse correlation between δ^{238}U and U contents (Fig. S9). If high Mo enrichment and small Mo isotope fractionation indicate higher sulfide levels in the water column, such conditions would then also result in high U enrichment and small U isotope fractionation. In deep sediments of the Black Sea, the inverse relationship between Mo and U isotopes is driven by the high δ^{98}Mo and moderately high δ^{238}U of unit I and the lower δ^{98}Mo and very high δ^{238}U of unit II sediments. As unit II sediments were perhaps deposited under less euxinic conditions (Degens and Ross, 1972; Lamy et al., 2006), a stronger effective Mo

and U isotope fractionation may have resulted, as a result of less effective Mo and U reduction and removal from the water column.

In contrast, near surface sediments of both basins, which are affected by ongoing pore water cycling, show only a weak correlation between $\delta^{238}U$ and $\delta^{98}Mo$ (Figure 15). While those from the Black Sea broadly overlap with the deeper Black Sea sediments, the Cariaco Basin data fall between the deeper Cariaco and deeper Black Sea sediments. The weakly negative $\delta^{238}U$ - $\delta^{98}Mo$ correlation of the near-surface sediments of the Black Sea may be attributed to differences between U and Mo isotopes that are unique to each system. As discussed above, U isotope variations of these sediments reflect (with roughly constant isotope fractionation) a deep water column that has $\delta^{238}U$ values lower than that of average seawater (Rolison et al., 2017). In contrast, Mo isotope variations are related to the lower sulfidic conditions in the upper water column, resulting in stronger Mo isotope fractionation.
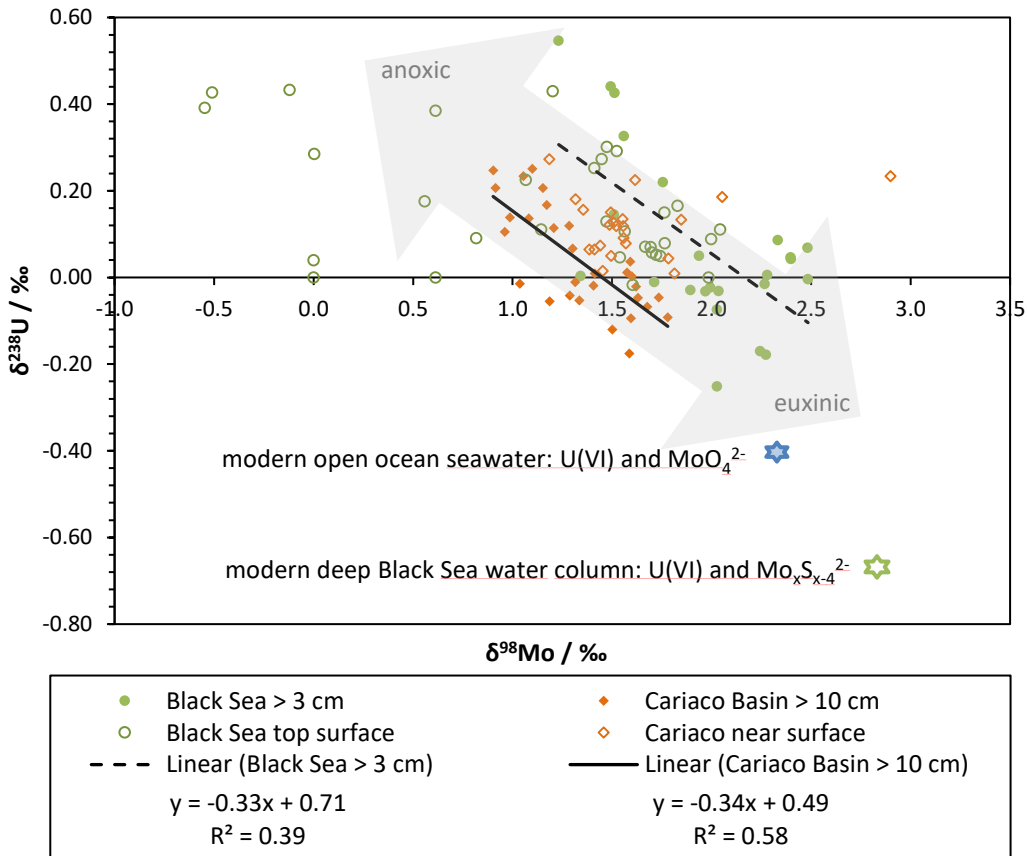
Figure 15: Correlation between $\delta^{98}Mo$ (NIST-3134+0.25 ‰) vs. $\delta^{238}U$ (CRM112A) in Back Sea (open and closed circles) and Cariaco (open and closed diamonds) sediment samples (for details see text). Correlation coefficients (R^2) are calculated for the deep sediment samples and are statistically significant for both basins. Modern Black Sea water column signature according to Romaniello et al., 2009; Nägler et al., 2011 and Rolison et al., 2017 and modern open-ocean seawater according to Siebert et al., 2003; Stirling et al., 2007; Weyer et al., 2008; Nakagawa et al., 2012 and Tissot and Dauphas, 2015.

This correlation between $\delta^{238}U$ and $\delta^{98}Mo$ in the deeper sediments of both basins is striking given that Mo and U are likely removed by fundamentally different mechanisms (Barnes and Cochran, 1990; Erickson and Helz, 2000). However, the $\delta^{238}U$ - $\delta^{98}Mo$ trends for Black Sea and Cariaco Basin show a distinct offset. As Mo isotope fractionation is generally controlled by sulfide concentrations in the water column, the lower $\delta^{98}Mo$ of Cariaco basin sediments may be a result of the overall much lower sulfide concentrations in the water column compared to that of the Black Sea, which is supported by our model results. High dissolved sulfide concentrations are maintained only in a highly restricted basin because of inhibited vertical circulation and correspondingly slow deep water renewal. Thus, a potential offset in $\delta^{238}U$ and $\delta^{98}Mo$ may be a result of different basin geometries. However, a particulate oxide shuttle may also be important in generating locally variable or overall lower $\delta^{98}Mo$. A more pronounced effect of such a particle shuttle may be considered as a possible mechanism to generate an offset in the relationships between $\delta^{238}U$ and $\delta^{98}Mo$ in deep sediments of the Black Sea and Cariaco Basin, although there is no compelling evidence for these processes in modern euxinic water columns.

Another possible explanation for the shift in the $\delta^{98}Mo$ - $\delta^{238}U$ relationships between Black Sea and Cariaco Basin could be that effective U isotope fractionation between the water column and sediment is different between both basins. As argued above, the U isotope signature of deep sediments is likely a combined signal of U reduction and U removal in the water column, or at the sediment-water interface, and further U reduction in the pore water. While the estimated U isotope fractionation factor in surface sediments (only determined by U isotope fractionation above or at the water-sediment interface) is similar for both basins, deeper sediments of the Cariaco Basin likely indicate a lower U isotope fractionation factor compared to fractionation in the deeper sediments of the Black Sea. The deeper sediments (< 1.5 cm bsf) include additional U removal during pore water cycling associated with additional isotope fractionation. For this latter process, the efficiency of U removal will play a major role in controlling $\Delta^{238}U_{sed-water}$ values. At more weakly euxinic conditions in the historical past of the Cariaco Basin, U removal through pore water cycling may have occurred generally deeper in the sediment, and thus was more quantitative as pore water U replenishment is inhibited (Andersen et al., 2015; Andersen et al., 2017). This process is expected to result in more-limited U isotope fractionation. In contrast, in the Black Sea, U removal during pore water cycling seems to be limited to the uppermost 2 – 5 cm of the sediment with sufficient U supply, where partial U reduction and removal results in strong U isotope fractionation. Thus, the rates of U reduction are may be a more important control on the magnitude of the intrinsic U isotope fractionation.

We can also explore the factors driving changes in sediment U and Mo isotope values using a quantitative framework (see above for model description). We are able to reproduce the

general trends in Black Sea and Cariaco Basin sediment δ^{238}U and δ^{98}Mo values with a reactive transport model by only having organic flux coupled between water column and sediments and parameterizing the effects of basin isolation on the water column isotope values (Figure 16). At the most basic level, what the model captures is extensive Mo removal in high sulfide waters (and thus high, seawater-like δ^{98}Mo values) and lower δ^{238}U values, relative to overlying waters, with rapid rates of organic matter remineralization in the sediment pile. However, as stressed above, because of basin restriction, the Black Sea isotope water column isotope values vary, and this variation must also be considered.
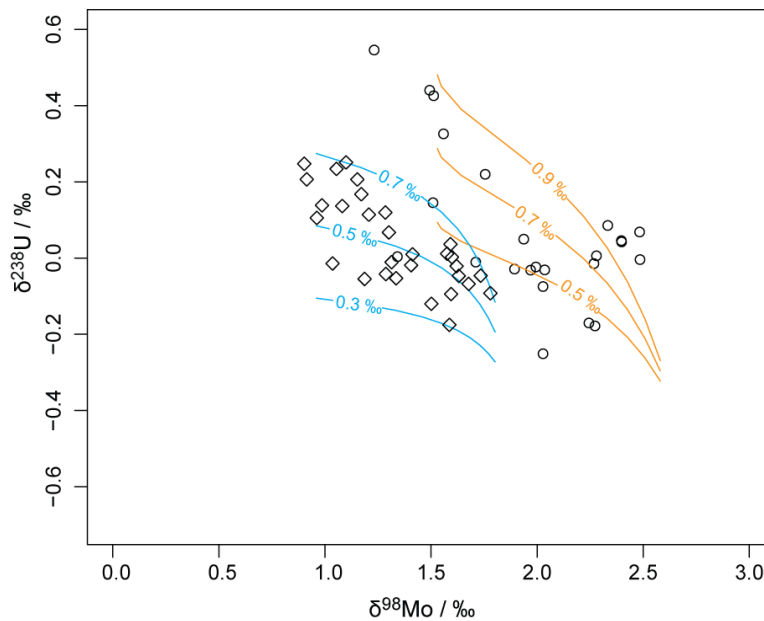
Figure 16: Results from the coupled water column and sediment U and Mo isotope reactive transport model. The lines represent the model outputs with different intrinsic fractionation factors for U isotopes. For the Black Sea (orange lines, open circles), ε = 0.5 ‰, 0.7 ‰, and 0.9 ‰ are used. For Cariaco Basin (blue lines, open diamonds) ε = 0.3 ‰, 0.5 ‰ and 0.7 ‰ are used. The correlation between δ^{238}U and δ^{98}Mo is driven primarily by a coupling between the efficiency of Mo and U removal, in the water column and sediment pile, respectively. With higher water column sulfide levels Mo removal rates increase resulting in heavier δ^{98}Mo isotope values. With higher sediment organic remineralization rates, U removal is closer to quantitative capture, resulting in lower δ^{238}U values. Shifting the degree of isolation, which results in shifts in water column isotope values, can shift the degree of the modeled isotope contours, explaining the difference between in the Black Sea and Cariaco Basin contours.

Our model can cover the deviation from a single δ^{238}U and δ^{98}Mo trend assuming that there is a small difference in the intrinsic isotope fractionation within both the Black Sea and the Cariaco Basin. As mentioned above, some deviation in intrinsic isotope fractionations might be expected with different reduction pathways (e.g., varying efficiency of U reduction in the sediment or varying ratios of sulfide to microbial meditated U reduction). Alternatively, water

column sulfide levels in euxinic basins are not simply the result of the local sulfate reduction rates — sulfide and sulfate advections play a role in controlling dissolved sulfide values — and our 1D model did not accurately represent the complexity of water mass transport in either basin. Translating our reaction scheme into a model with a more complex transport may provide insights into some of the scatter from the general trend in $\delta^{238}U$ and $\delta^{98}Mo$ values in both basins.

That we are able to model the $\delta^{238}U$ and $\delta^{98}Mo$ data and reproduce the offset in these values, of course, does not imply that our model exactly captures the processes driving the isotope fractionations. Our model is, admittedly, based on several simplifying assumptions. For instance, we do not include a particulate Mo shuttle, which has been commonly invoked. However, we would argue that being able to reproduce the data by only invoking a limited number of processes — changing removal efficiencies (or basin residence time) and the intrinsic isotopic fractionation factor of U — bolsters the case that these processes play critical roles in controlling sediment $\delta^{238}U$ and $\delta^{98}Mo$ values and in driving the $\delta^{238}U$ and $\delta^{98}Mo$ co-variation.

4.4 The use of Mo-U correlations to decipher global extent of anoxia now and during times of enhanced ocean anoxia

Previous work suggested that a correlation between Mo and U isotopes may also be used as a redox proxy to characterize former seawater isotope compositions — in addition to using U and Mo coupled enrichments in reducing sediments (Algeo and Tribovillard, 2009; Asael et al., 2013; Kendall et al., 2015; Noordmann et al., 2015; Lu et al., 2017; Bura-Nakić et al., 2018). In particular, $\delta^{98}Mo$ and $\delta^{238}U$ correlations may be used to infer signatures of a paleo-ocean. During past periods of enhanced seafloor anoxia, the seawater isotope composition for U and Mo would have been shifted, which can be preserved in the rock record. Specifically, black shales are a very important reservoir for Mo and U burial and have been used previously to reconstruct ancient seawater isotope signatures (Arnold et al., 2004; Wille et al., 2007; Wille et al., 2008; Kendall et al., 2009; Montoya-Pino et al., 2010; Brennecka et al., 2011; Kendall et al., 2013; Eroglu et al., 2015; Lau et al., 2016; Elrick et al., 2017). To this end, it is very important to understand how different factors like water column chemistry or water renewal times influence each isotope systems differently. The differences between the Cariaco Basin and the Black Sea result from characteristic features of each basin, which may be informative of similar environments in the past. It is likely that these modern settings do not represent environmental end-members, and likely do not cover the wide variety of depositional environments — including more restricted basins or euxinia along continental slopes — that were possible in ancient oceans. Accordingly, independent characterization of the degree of

basin restriction and the extent of sulfide concentrations, as well as quantitative modeling as shown above, will aid in interpreting Mo and U isotope signatures. Our results highlight that a combination of δ^{98}Mo and δ^{238}U values can improve paleo-redox interpretations, although further research is required — in particular to better understand the processes controlling U isotope fractionation between seawater and black shales.

5. Conclusions

In this study we observed inversely correlated Mo and U isotope signatures in sediments of the Black Sea and the Cariaco Basin. This relationship indicates that effective isotope fractionation of Mo and U during reduction and removal from the water column is positively correlated. However, the correlation is only significant in deep sediments (> ~ 15 cm bsf), while no or only a very weak correlation is observed for near-surface sediments with ongoing U supply by pore water cycling.

Our data confirm that Mo isotope fractionation occurs in the water column, mostly as a function of concentrations of H_2S_{aq}, resulting in strongly fractionated Mo isotopes in sediments of the upper Black Sea water column and almost no Mo isotope fractionation (resulting from near-quantitative Mo removal) in sediments of the deep Black Sea, which were deposited under highly sulfidic conditions. The U isotope signature in upper surface sediments indicates that some U removal with associated isotope fractionation likely also occurs in the water column or at the sediment-water interface. Isotope fractionation between the water column and the top-surface sediments is relatively constant throughout the water column of the Black Sea. The weak correlation between Mo and U isotopes in near-surface sediments of the Black Sea is a result of both a fractionated U isotope composition in the water column, which is inherited by the shallow surface sediments, and by a depth relationship with H_2S_{aq}, the driver of Mo isotope fractionation. In the Cariaco Basin, Mo- and U isotope ratios in near-surface sediments are uncorrelated, although Mo and U contents show a striking correlation. This observation indicates that, although Mo and U removal from the water column appears to be driven by similar mechanisms (e.g. adsorption to organics) or is at least controlled by similar conditions in Mo and U isotope correlation need not result.

Accordingly, the correlation between Mo and U isotopes, observed for deep sediments of the Cariaco Basin and the Black Sea must be related to additional U removal and isotope fractionation during pore water U cycling in the sediment. Variations in the extent of sulfate reduction and related variations in concentrations H_2S_{aq} are the most likely driver of the correlated isotope signatures. While strong euxinic conditions in the water column result in more effective Mo removal and less Mo isotope fractionation (high δ^{98}Mo in sediments), the same conditions also appear to result in smaller U isotope fractionation, likely as a result of

more effective U removal in the sediment (resulting in low δ^{238}U). This relationship between Mo and U isotope fractionation can also be quantitatively described using a reactive transport model and may explain the correlated δ^{98}Mo and δ^{238}U observed in deep sediments of both, the Cariaco Basin and Black Sea.

However, there is also a significant offset between the two basins for the reasons that are less clear. Possible factors generating this offset may involve the generally more euxinic conditions in the Black Sea (as a result of its very restricted nature), a potentially isotopically lighter Mo source in the Cariaco Basin (generated by oxide particle shuttle), and a generally lower net U isotope fractionation in the Cariaco Basin, potentially as a result of a more effective (decoupled from the water column) U isotope fractionation in sediments. The general coupling between δ^{238}U and δ^{98}Mo in reducing sediments observed in this study contributes to a better understanding of the isotope fractionations associated with euxinic depositional conditions and thus increases the potential value of these isotope systems for reconstructing Earth's redox evolution.

Acknowledgements

References (including supplementary)

Algeo T. J. and Lyons T. W. (2006) Mo-total organic carbon covariation in modern anoxic marine environments: Implications for analysis of paleoredox and paleohydrographic conditions. *Paleoceanography* **21**.

Algeo T. J. and Tribovillard N. (2009) Environmental analysis of paleoceanographic systems based on molybdenum–uranium covariation. *Chem. Geol.* **268**, 211–225. Available at: http://linkinghub.elsevier.com/retrieve/pii/S0009254109003805.

Andersen M. B., Romaniello S., Vance D., Little S. H., Herdman R. and Lyons T. W. (2014) A modern framework for the interpretation of 238U/235U in studies of ancient ocean redox. *Earth Planet. Sci. Lett.* **400**, 184–194. Available at: http://dx.doi.org/10.1016/j.epsl.2014.05.051.

Andersen M. B., Elliott T., Freymuth H., Sims K. W. W., Niu Y. and Kelley K. A. (2015) The terrestrial uranium isotope cycle. *Nature* **517**, 356–359. Available at: http://www.nature.com/doifinder/10.1038/nature14062.

Andersen M. B., Stirling C. H. and Weyer S. (2017) Uranium Isotope Fractionation. *Rev. Mineral. Geochemistry* **82**, 799–850. Available at: http://rimg.geoscienceworld.org/lookup/doi/10.2138/rmg.2017.82.19.

Anderson R. F., Fleisher M. Q. and LeHuray A. P. (1989) Concentration, oxidation state, and particlwith flux of uranium in the Black Sea. *Geochim. Cosmochim. Acta* **53**, 2215–2224.

Arnold G. L., Anbar A. D., Barling J. and Lyons T. W. (2004) Molybdenum Isotope Evidence for Widespread Anoxia in Mid-Proterozoic Oceans. *Science (80-.).*

Arnold G. L., Lyons T. W., Gordon G. W. and Anbar A. D. (2012) Extreme change in sulfide concentrations in the Black Sea during the Little Ice Age reconstructed using molybdenum isotopes. *Geology* **40**, 595–598.

Arz H. W., Böttcher M. E., Burmeister C., Dellwig O., Fisch K., Hehl U., Jeschek J., Jürgens K., Kaiser D., Konovalov S., Krüger S., Laudan C., Lipka M., Meeske C., Melnikov V., Orekhova N. K. O. N., Orlikowska A., Plewe S., Pollehne F., Proskurnin V., Scholz C., Schuffenhauer I., Schulz-Bull D., Schulz-Vogt H., Shumilovskikh L., Wegwerth A. and Wlost K.-P. (2014) BIOLOGICAL/BIOGEOCHEMICAL PROCESSES AND ELEMENT FLUXES AT THE BLACK SEA PELAGIC REDOXCLINE, SEDIMENTATION PROCESSES AND THE LATE HOLOCENE DEVELOPMENT OF THE SYSTEM - Cruise MSM33 – November 2 – December 6, 2013 – Cádiz (Spain) – Varna (Bulgaria). *MARIA*

S. MERIAN-Berichte MSM33 **DFG**-**Senat**, 55. Available at: doi:10.2312/cr_m91.

Asael D., Tissot F. L. H., Reinhard C. T., Rouxel O., Dauphas N., Lyons T. W., Ponzevera E., Liorzou C. and Chéron S. (2013) Coupled molybdenum, iron and uranium stable isotopes as oceanic paleoredox proxies during the Paleoproterozoic Shunga Event. *Chem. Geol.* **362**, 193–210. Available at: http://dx.doi.org/10.1016/j.chemgeo.2013.08.003.

Barling J., Arnold G. L. and Anbar A. . (2001) Natural mass-dependent variations in the isotopic composition of molybdenum. *Earth Planet. Sci. Lett.* **193**, 447–457. Available at: http://linkinghub.elsevier.com/retrieve/pii/S0012821X01005143.

Barling J. and Anbar A. D. (2004) Molybdenum isotope fractionation during adsorption by manganese oxides. *Earth Planet. Sci. Lett.* **217**, 315–329. Available at: http://linkinghub.elsevier.com/retrieve/pii/S0012821X03006083.

Barnes C. E. and Cochran J. K. (1990) Uranium removal in oceanic sediments and the oceanic U balance. *Earth Planet. Sci. Lett.* **97**, 94–101.

Barnes C. E. and Cochran J. K. (1993) Uranium geochemistry in estuarine sediments: Controls on removal and release processes. *Geochim. Cosmochim. Acta* **57**, 555–569.

Basu A., Sanford R. A., Johnson T. M., Lundstrom C. C. and Löffler F. E. (2014) Uranium isotopic fractionation factors during U(VI) reduction by bacterial isolates. *Geochim. Cosmochim. Acta* **136**, 100–113.

Benitez-Nelson C. R., O'Neill Madden L. P., Styles R. M., Thunell R. C. and Astor Y. (2007) Inorganic and organic sinking particulate phosphorus fluxes across the oxic/anoxic water column of Cariaco Basin, Venezuela. *Mar. Chem.* **105**, 90–100.

Berner R. A. (1980) Early Diagenesis: a Theoretical Approach. *Princet. Univ. Press.*

Bigeleisen J. (1996) Temperature dependence of the isotope chemistry of the heavy elements. *Proc. Natl. Acad. Sci.* **93**, 9393–9396. Available at: http://www.pnas.org/cgi/doi/10.1073/pnas.93.18.9393.

Boudreau B. P. and Ruddick B. R. (1991) On a reactive continuum representation of organic matter diagenesis. *Am. J. Sci.*

Boudreau B. P. (1997) *Diagenetic models and their implementation: modelling transport and reactions in aquatic sediments.*, Available at: http://linkinghub.elsevier.com/retrieve/pii/S0264817298800056.

Brennecka G. A., Herrmann A. D., Algeo T. J. and Anbar A. D. (2011) Rapid expansion of oceanic anoxia immediately before the end-Permian mass extinction. *Proc. Natl. Acad. Sci.* **108**, 17631–17634. Available at: http://www.pnas.org/cgi/doi/10.1073/pnas.1106039108.

Brown S. T., Basu A., Ding X., Christensen J. N. and DePaolo D. J. (2018) Uranium isotope fractionation by abiotic reductive precipitation. *Proc. Natl. Acad. Sci.* **2**, 201805234. Available at: http://www.pnas.org/lookup/doi/10.1073/pnas.1805234115.

Bura-Nakić E., Andersen M. B., Archer C., de Souza G. F., Marguš M. and Vance D. (2018) Coupled Mo-U abundances and isotopes in a small marine euxinic basin: Constraints on processes in euxinic basins. *Geochim. Cosmochim. Acta* **222**, 212–229.

Campbell K. M., Kukkadapu R. K., Qafoku N. P., Peacock A. D., Lesher E., Williams K. H., Bargar J. R., Wilkins M. J., Figueroa L., Ranville J., Davis J. A. and Long P. E. (2012) Geochemical, mineralogical and microbiological characteristics of sediment from a naturally reduced zone in a uranium-contaminated aquifer. *Appl. Geochemistry* **27**, 1499–1511.

Clark S. K. and Johnson T. M. (2008) Effective isotopic fractionation factors for solute removal by reactive sediments: A laboratory microcosm and slurry study. *Environ. Sci. Technol.* **42**, 7850–7855.

Cole D. B., Zhang S. and Planavsky N. J. (2017) A new estimate of detrital redox-sensitive metal concentrations and variability in fluxes to marine sediments. *Geochim. Cosmochim. Acta* **215**, 337–353.

Cumberland S. A., Douglas G., Grice K. and Moreau J. W. (2016) Uranium mobility in organic matter-rich sediments: A review of geological and geochemical processes. *Earth-Science Rev.* **159**, 160–185. Available at: http://dx.doi.org/10.1016/j.earscirev.2016.05.010.

Dahl T. W., Anbar A. D., Gordon G. W., Rosing M. T., Frei R. and Canfield D. E. (2010) The behavior of molybdenum and its isotopes across the chemocline and in the sediments of

sulfidic Lake Cadagno, Switzerland. *Geochim. Cosmochim. Acta* **74**, 144–163.

Dang D. H., Evans R. D., Wang W., Omanović D., El Houssainy A., Lenoble V., Mullot J. U., Mounier S. and Garnier C. (2018) Uranium isotope geochemistry in modern coastal sediments: Insights from Toulon Bay, France. *Chem. Geol.* **481**, 133–145.

Degens E. T. and Ross D. A. (1972) Chronology of the Black Sea over the last 25,000 years. *Chem. Geol.* **10**, 1–16.

Dellwig O., Leipe T., März C., Glockzin M., Pollehne F., Schnetger B., Yakushev E. V., Böttcher M. E. and Brumsack H. J. (2010) A new particulate Mn-Fe-P-shuttle at the redoxcline of anoxic basins. *Geochim. Cosmochim. Acta* **74**, 7100–7115.

Deuser W. G. (1973) Cariaco Trench: Oxidation of Organic Matter and Residence Time of Anoxic Water. *Nature* **242**, 601–603. Available at: http://www.nature.com/nature/journal/v242/n5393/abs/242117a0.html.

Dyrssen D. (1999) The anoxic bottom waters of the Black Sea and Framvaren - similarities and differences. *Aquat. Geochemistry* **5**, 59–73. Available at: http://www.tandfonline.com/doi/abs/10.1080/11035899609546238.

Elrick M., Polyak V., Algeo T. J., Romaniello S., Asmerom Y., Herrmann A. D., Anbar A. D., Zhao L. and Chen Z. Q. (2017) Global-ocean redox variation during the middle-late Permian through Early Triassic based on uranium isotope and Th/U trends of marine carbonates. *Geology* **45**, 163–166.

Emerson S. R. and Huested S. S. (1991) Ocean anoxia and the concentrations of molybdenum and vanadium in seawater. *Mar. Chem.* **34**, 177–196.

Erickson B. E. and Helz G. R. (2000) Molybdenum(VI) speciation in sulfidic waters: Stability and lability of thiomolybdates. *Geochim. Cosmochim. Acta* **64**, 1149–1158.

Eroglu S., Schoenberg R., Wille M., Beukes N. and Taubald H. (2015) Geochemical stratigraphy, sedimentology, and Mo isotope systematics of the ca. 2.58-2.50Ga-old Transvaal Supergroup carbonate platform, South Africa. *Precambrian Res.* **266**, 27–46. Available at: http://dx.doi.org/10.1016/j.precamres.2015.04.014.

Goldberg T., Archer C., Vance D., Thamdrup B., McAnena A. and Poulton S. W. (2012) Controls on Mo isotope fractionations in a Mn-rich anoxic marine sediment, Gullmar Fjord, Sweden. *Chem. Geol.* **296**–**297**, 73–82.

Goldberg T., Gordon G., Izon G., Archer C., Pearce C. R., McManus J., Anbar A. D. and Rehkämper M. (2013) Resolution of inter-laboratory discrepancies in Mo isotope data: an intercalibration. *J. Anal. At. Spectrom.* **28**, 724. Available at: http://xlink.rsc.org/?DOI=c3ja30375f.

Goldmann A., Brennecka G., Noordmann J., Weyer S. and Wadhwa M. (2015) The uranium isotopic composition of the Earth and the Solar System. *Geochim. Cosmochim. Acta* **148**, 145–158. Available at: http://dx.doi.org/10.1016/j.gca.2014.09.008.

Gueguen B., Reinhard C. T., Algeo T. J., Peterson L. C., Nielsen S. G., Wang X., Rowe H. and Planavsky N. J. (2016) The chromium isotope composition of reducing and oxic marine sediments. *Geochim. Cosmochim. Acta* **184**, 1–19. Available at: http://dx.doi.org/10.1016/j.gca.2016.04.004.

Harris D., Horwáth W. R. and van Kessel C. (2001) Acid fumigation of soils to remove carbonates prior to total organic carbon or CARBON-13 isotopic analysis. *Soil Sci. Soc. Am. J.* **65**, 1853.

Helz G. R., Miller C. V., Charnock J. M., Mosselmans J. F. W., Pattrick R. A. D., Garner C. D. and Vaughan D. J. (1996) Mechanism of molybdenum removal from the sea and its concentration in black shales: EXAFS evidence. *Geochim. Cosmochim. Acta* **60**, 3631–3642.

Helz G. R., Bura-Nakić E., Mikac N. and Ciglenečki I. (2011) New model for molybdenum behavior in euxinic waters. *Chem. Geol.* **284**, 323–332.

Ho T.-Y., Taylor G. T., Astor Y., Varela R., Müller-Karger F. and Scranton M. I. (2004) Vertical and temporal variability of redox zonation in the water column of the Cariaco Basin: implications for organic carbon oxidation pathways. *Mar. Chem.* **86**, 89–104. Available at: http://linkinghub.elsevier.com/retrieve/pii/S0304420304000039.

Kempe S., Diercks A.-R., Liebezeit G. and Prange A. (1991) Geochemical and Structural Aspects of the Pycnocline in the Black Sea (R/V KNORR 134-8 LEG 1, 1988). In *Black*

Sea Oceanography (eds. E. \.Izdar and J. W. Murray). Springer Netherlands, Dordrecht. pp. 89–110. Available at: https://doi.org/10.1007/978-94-011-2608-3_6.

Kendall B., Creaser R. A., Gordon G. W. and Anbar A. D. (2009) Re-Os and Mo isotope systematics of black shales from the Middle Proterozoic Velkerri and Wollogorang Formations, McArthur Basin, northern Australia. *Geochim. Cosmochim. Acta* **73**, 2534–2558.

Kendall B., Brennecka G. A., Weyer S. and Anbar A. D. (2013) Uranium isotope fractionation suggests oxidative uranium mobilization at 2.50Ga. *Chem. Geol.* **362**, 105–114. Available at: http://dx.doi.org/10.1016/j.chemgeo.2013.08.010.

Kendall B., Komiya T., Lyons T. W., Bates S. M., Gordon G. W., Romaniello S. J., Jiang G., Creaser R. A., Xiao S., McFadden K., Sawaki Y., Tahata M., Shu D., Han J., Li Y., Chu X. and Anbar A. D. (2015) Uranium and molybdenum isotope evidence for an episode of widespread ocean oxygenation during the late ediacaran period. *Geochim. Cosmochim. Acta* **156**, 173–193. Available at: http://dx.doi.org/10.1016/j.gca.2015.02.025.

Kendall B., Dahl T. W. and Anbar A. D. (2017) the Stable Isotope Geochemistry of Molybdenum. *Rev. Mineral. Geochemistry* **82**, 683–732. Available at: http://dx.doi.org/10.2138/rmg.2017.82.16.

Klinkhammer G. P. and Palmer M. R. (1991) Uranium in the oceans: Where it goes and why. *Geochim. Cosmochim. Acta* **55**, 1799–1806.

Ku T., Knauss K. G. and Mathieu G. G. (1977) Uranium in open ocean: concentration and isotopic composition. *Deep Sea Res.* **24**, 1005–1017.

Kurzweil F., Wille M., Gantert N., Beukes N. J. and Schoenberg R. (2016) Manganese oxide shuttling in pre-GOE oceans ??? evidence from molybdenum and iron isotopes. *Earth Planet. Sci. Lett.* **452**, 69–78. Available at: http://dx.doi.org/10.1016/j.epsl.2016.07.013.

Lamy F., Arz H. W., Bond G. C., Bahr A. and Pätzold J. (2006) Multicentennial-scale hydrological changes in the Black Sea and northern Red Sea during the Holocene and the Arctic/North Atlantic Oscillation. *Paleoceanography* **21**, 1–11.

Lau K. V., Maher K., Altiner D., Kelley B. M., Kump L. R., Lehrmann D. J., Silva-Tamayo J. C., Weaver K. L., Yu M. and Payne J. L. (2016) Marine anoxia and delayed Earth system recovery after the end-Permian extinction. *Proc. Natl. Acad. Sci.* **113**, 2360–2365. Available at: http://www.pnas.org/lookup/doi/10.1073/pnas.1515080113.

Lin H. L., Peterson L. C., Overpeck J. T., Trumbore S. E. and Murray D. W. (1997) Late Quaternary climate change from δ18O records of multiple species of planktonic foraminifera: High-resolution records from the Anoxic Cariaco Basin, Venezuela. *Paleoceanography* **12**, 415–427.

Little S. H., Vance D., Lyons T. W. and McManus J. (2015) Controls on trace metal authigenic enrichment in reducing sediments: Insights from modern oxygen-deficient settings. *Am. J. Sci.* **315**, 77–119.

Lovley D. R., Phillips E. J. P., Gorby Y. A. and Landa E. R. (1991) Microbial Reduction of Uranium. *Nature* **350**, 413–416.

Lu X., Kendall B., Stein H. J., Li C., Hannah J. L., Gordon G. W. and Ebbestad J. O. R. (2017) Marine redox conditions during deposition of Late Ordovician and Early Silurian organic-rich mudrocks in the Siljan ring district, central Sweden. *Chem. Geol.* **457**, 75–94. Available at: http://linkinghub.elsevier.com/retrieve/pii/S0009254117301407.

Lüning S. and Kolonic S. (2003) Uranium spectral gamma-ray response as a proxy for organic richness in black shales: Applicability and limitations. *J. Pet. Geol.* **26**, 153–174.

Lyons T. W. (1991) Upper Holocene Sediments of the Black Sea: Summary of Leg 4 Box Cores (1988 Black Sea Oceanographic Expedition). In *Black Sea Oceanography* (eds. E. \.Izdar and J. W. Murray). Springer Netherlands, Dordrecht. pp. 401–441. Available at: https://doi.org/10.1007/978-94-011-2608-3_25.

Lyons T. W., Werne J. P., Hollander D. J. and Murray R. W. (2003) Contrasting sulfur geochemistry and Fe/Al and Mo/Al ratios across the last oxic-to-anoxic transition in the Cariaco Basin, Venezuela. *Chem. Geol.* **195**, 131–157.

Lyons T. W. and Severmann S. (2006) A critical look at iron paleoredox proxies: New insights from modern euxinic marine basins. *Geochim. Cosmochim. Acta* **70**, 5698–5722. Available at: http://www.sciencedirect.com/science/article/pii/S0016703706020047.

McConnell M. C., Thunell R. C., Lorenzoni L., Astor Y., Wright J. D. and Fairbanks R. (2009) Seasonal variability in the salinity and oxygen isotopic composition of seawater from the Cariaco Basin, Venezuela: Implications for paleosalinity reconstructions. *Geochemistry, Geophys. Geosystems* **10**.

Meyer K. M. and Kump L. R. (2008) Oceanic Euxinia in Earth History: Causes and Consequences. *Annu. Rev. Earth Planet. Sci.* **36**, 251–288. Available at: http://www.annualreviews.org/doi/10.1146/annurev.earth.36.031207.124256.

Miller C. A., Peucker-Ehrenbrink B., Walker B. D. and Marcantonio F. (2011) Re-assessing the surface cycling of molybdenum and rhenium. *Geochim. Cosmochim. Acta* **75**, 7146–7179.

Montoya-Pino C., Weyer S., Anbar A. D., Pross J., Oschmann W., van de Schootbrugge B. and Arz H. W. (2010) Global enhancement of ocean anoxia during oceanic anoxic event 2: A quantitative approach using U isotopes. *Geology* **38**, 315–318.

Montoya-Pino C. (2011) Molybdenum and uranium isotope signatures of Mesozoic black shales : Implications on the spatial dimension of oceanic anoxic events. PhD thesis.

Morford J. L., Emerson S. R., Breckel E. J. and Kim S. H. (2005) Diagenesis of oxyanions (V, U, Re, and Mo) in pore waters and sediments from a continental margin. *Geochim. Cosmochim. Acta* **69**, 5021–5032.

Moynier F., Fujii T., Brennecka G. A. and Nielsen S. G. (2013) Nuclear field shift in natural environments. *Comptes Rendus - Geosci.* **345**, 150–159.

Murray J. W. and İzdar E. (1989) The 1988 Black Sea Oceanographic Expedition: Overview and New Discoveries. *Oceanography* **2**, 15–21.

Murray J. W., Jannasch H. W., Honjo S., Anderson R. F., Reeburgh W. S., Top Z., Friederich G. E., Codispoti L. A. and Izdar E. (1989) Unexpected changes in the oxic/anoxic interface in the Black Sea. *Nature* **338**, 411–413.

Murray J. W., Top Z. and Özsoy E. (1991) Hydrographic properties and ventilation of the Black Sea. *Deep Sea Res. Part A. Oceanogr. Res. Pap.* **38**, S663–S689. Available at: http://linkinghub.elsevier.com/retrieve/pii/S0198014910800032.

Nägler T., Siebert C., Lüschen H. and Böttcher M. E. (2005) Sedimentary Mo isotope record across the Holocene fresh-brackish water transition of the Black Sea. *Chem. Geol.* **219**, 283–295.

Nägler T., Neubert N., Böttcher M. E., Dellwig O. and Schnetger B. (2011) Molybdenum isotope fractionation in pelagic euxinia: Evidence from the modern Black and Baltic Seas. *Chem. Geol.* **289**, 1–11.

Nägler T. F., Anbar A. D., Archer C., Goldberg T., Gordon G. W., Greber N. D., Siebert C., Sohrin Y. and Vance D. (2014) Proposal for an International Molybdenum Isotope Measurement Standard and Data Representation. *Geostand. Geoanalytical Res.* **38**, 149–151.

Nakagawa Y., Takano S., Firdaus M. L., Norisuye K., Hirata T., Vance D. and Sohrin Y. (2012) The molybdenum isotopic composition of the modern ocean. *Geochem. J.* **46**, 131–141.

Neubert N., Nägler T. F. and Böttcher M. E. (2008) Sulfidity controls molybdenum isotope fractionation into euxinic sediments: Evidence from the modern Black Sea. *Geology* **36**, 775–778.

Noordmann J., Weyer S., Montoya-Pino C., Dellwig O., Neubert N., Eckert S., Paetzel M. and Böttcher M. E. (2015) Uranium and molybdenum isotope systematics in modern euxinic basins: Case studies from the central Baltic Sea and the Kyllaren fjord (Norway). *Chem. Geol.* **396**, 182–195. Available at: http://dx.doi.org/10.1016/j.chemgeo.2014.12.012.

Noordmann J., Weyer S., Georg R. B., Jöns S. and Sharma M. (2016) 238U/235U isotope ratios of crustal material, rivers and products of hydrothermal alteration: new insights on the oceanic U isotope mass balance. *Isotopes Environ. Health Stud.* **52**, 141–163.

Östlund H. G. (1974) Expedition'Odysseus 65': Radiocarbon age of Black Sea deep water. In *In: Degens, E.T., Ross, D.A. (Eds.), The Black Sea—Geology, Chemistry, and Biology. American Association of Petroleum Geologists Memoir* pp. 127–132. Available at: http://archives.datapages.com/data/specpubs/sedimen1/data/a145/a145/0001/0100/0127.htm.

Piper D. Z. and Dean W. E. (2002) Trace-element Deposition in the Cariaco Basin, Venezuela Shelf, under sulfate-reducing Conditions - a History of the Local Hydrography and Global

Climate, 20 ka to the Present. *U.S. Geol. Sur. Prof. Pap.* **1670**, 41 pp.

Ravizza G., Turekian K. K. and Hay B. J. (1991) The geochemistry of rhenium and osmium in recent sediments from the Black Sea. *Geochim. Cosmochim. Acta*.

Reinhard C. T., Planavsky N. J., Wang X., Fischer W. W., Johnson T. M. and Lyons T. W. (2014) The isotopic composition of authigenic chromium in anoxic marine sediments: A case study from the Cariaco Basin. *Earth Planet. Sci. Lett.* **407**, 9–18. Available at: http://dx.doi.org/10.1016/j.epsl.2014.09.024.

Richter S., Alonso-Munoz A., Eykens R., Jacobsson U., Kuehn H., Verbruggen A., Aregbe Y., Wellum R. and Keegan E. (2008) The isotopic composition of natural uranium samples-Measurements using the new n(233U)/n(236U) double spike IRMM-3636. *Int. J. Mass Spectrom.* **269**, 145–148.

Richter S., Eykens R., Kühn H., Aregbe Y., Verbruggen A. and Weyer S. (2010) New average values for the n(238U)/n(235U) isotope ratios of natural uranium standards. *Int. J. Mass Spectrom.* **295**, 94–97.

Rolison J. M., Stirling C. H., Middag R. and Rijkenberg M. J. A. (2017) Uranium stable isotope fractionation in the Black Sea: Modern calibration of the 238 U/ 235 U paleo-redox proxy. *Geochim. Cosmochim. Acta* **203**, 69–88. Available at: http://linkinghub.elsevier.com/retrieve/pii/S0016703716307116.

Romaniello S., Brennecka G., Anbar A. and S. Colman A. (2009) Natural Isotopic Fractionation of 238U/235U in the Water Column of the Black Sea. In *AGU Fall Meeting Abstracts* Available at: https://www.researchgate.net/publication/241558437_Natural_Isotopic_Fractionation_of_238U235U_in_the_Water_Column_of_the_Black_Sea.

Rudnick R. L. and Gao S. (2003) The composition of the continental crust. In *Treatise on Geochemistry* pp. 1–64.

Scholz F., McManus J. and Sommer S. (2013) The manganese and iron shuttle in a modern euxinic basin and implications for molybdenum cycling at euxinic ocean margins. *Chem. Geol.* **355**, 56–68.

Scholz F., Siebert C., Dale A. W. and Frank M. (2017) Intense molybdenum accumulation in sediments underneath a nitrogenous water column and implications for the reconstruction of paleo-redox conditions based on molybdenum isotopes. *Geochim. Cosmochim. Acta* **213**, 400–417. Available at: http://linkinghub.elsevier.com/retrieve/pii/S0016703717304076.

Scranton M. I., Astor Y., Bohrer R., Ho T.-Y. and Muller-Karger F. (2001) Controls on temporal variability of the geochemistry of the deep Cariaco Basin. *Deep. Res. Part I Oceanogr. Res. Pap.* **48**, 1605–1625.

Siebert C., Nägler T. F., von Blanckenburg F. and Kramers J. D. (2003) Molybdenum isotope records as a potential new proxy for paleoceanography. *Earth Planet. Sci. Lett.* **211**, 159–171.

Siebert C., McManus J., Bice A., Poulson R. and Berelson W. M. (2006) Molybdenum isotope signatures in continental margin marine sediments. *Earth Planet. Sci. Lett.* **241**, 723–733.

Stirling C. H., Andersen M. B., Potter E. K. and Halliday A. N. (2007) Low-temperature isotopic fractionation of uranium. *Earth Planet. Sci. Lett.* **264**, 208–225.

Stylo M., Neubert N., Wang Y., Monga N., Romaniello S. J., Weyer S. and Bernier-Latmani R. (2015) Uranium isotopes fingerprint biotic reduction. *Proc. Natl. Acad. Sci.* **112**, 5619–5624. Available at: http://www.pnas.org/lookup/doi/10.1073/pnas.1421841112.

Tissot F. L. H. and Dauphas N. (2015) Uranium isotopic compositions of the crust and ocean: Age corrections, U budget and global extent of modern anoxia. *Geochim. Cosmochim. Acta* **167**, 113–143.

Tossell J. A. (2005) Calculating the partitioning of the isotopes of Mo between oxidic and sulfidic species in aqueous solution. *Geochim. Cosmochim. Acta* **69**, 2981–2993.

Voegelin A. R., Pettke T., Greber N. D., von Niederhäusern B. and Nägler T. F. (2014) Magma differentiation fractionates Mo isotope ratios: Evidence from the Kos Plateau Tuff (Aegean Arc). *Lithos* **190–191**, 440–448.

Wasylenki L. E., Rolfe B. A., Weeks C. L., Spiro T. G. and Anbar A. D. (2008) Experimental investigation of the effects of temperature and ionic strength on Mo isotope fractionation

during adsorption to manganese oxides. *Geochim. Cosmochim. Acta* **72**, 5997–6005.

Wegwerth A., Eckert S., Dellwig O., Schnetger B., Severmann S., Weyer S., Brüske A., Kaiser J., Köster J., Arz H. W. and Brumsack H. J. (2018) Redox evolution during Eemian and Holocene sapropel formation in the Black Sea. *Palaeogeogr. Palaeoclimatol. Palaeoecol.* **489**, 249–260.

Werne J. P., Hollander D. J., Lyons T. W. and Peterson L. C. (2000) Climate-induced variations in productivity and planktonic ecosystem structure from the Younger Dryas to Holocene in the Cariaco Basin, Venezuela. *Paleoceanography* **15**, 19.

Weyer S., Anbar A. D., Gerdes A., Gordon G. W., Algeo T. J. and Boyle E. A. (2008) Natural fractionation of 238U/235U. *Geochim. Cosmochim. Acta* **72**, 345–359.

Wiederhold J. G. (2015) Metal stable isotope signatures as tracers in environmental geochemistry. *Environ. Sci. Technol.* **49**, 2606–2624.

Wille M., Kramers J. D., Nägler T., Beukes N. J., Schröder S., Meisel T., Lacassie J. P. and Voegelin A. R. (2007) Evidence for a gradual rise of oxygen between 2.6 and 2.5 Ga from Mo isotopes and Re-PGE signatures in shales. *Geochim. Cosmochim. Acta* **71**, 2417–2435.

Wille M., Nägler T. F., Lehmann B., Schröder S. and Kramers J. D. (2008) Hydrogen sulphide release to surface waters at the Precambrian/Cambrian boundary. *Nature* **453**, 767–769. Available at: http://www.nature.com/doifinder/10.1038/nature07072.

Yakushev E. V, Chasovnikov V. K. and Murray J. W. (2007) Vertical Hydrochemical Structure of the Black Sea Vertical Hydrochemical Structure of the Black Sea. **5**.

Zhang J.-Z. and Millero F. J. (1993) The chemistry of the anoxic waters in the Cariaco Trench. *Deep Sea Res. Part I Oceanogr. Res. Pap.* **40**, 1023–1041. Available at: http://linkinghub.elsevier.com/retrieve/pii/096706379390088K.

Supplementary

S 1. Background information on sampling positions

Table S1 summarizes information about sampling in the Black Sea and the Cariaco Basin.

Table S1: Information about sampled cores: cruise names, dates, sampling positions and water depth.

Locality	Cruise	Date	Site	Core no.	Water depth / m	Position
Black Sea	R/V Knorr	April 1988	BSK 1	BC21	2092	43°05.52N, 32°01.56E
			BSK 2	BC25	2217	43°03.33N, 34°01.94E
			BSK 3 / 48	BC55	2164	42°44.91N, 37°34.80E
			STA 27/28	BC43	1861	41°49.38N, 40°12.82E
	M72/5	July 2007	25	25GC-1	418	42°06.2N, 36°37.4E
	MSM33	Nov 2013	22	22MUC-1	1681	44°27.8N, 32°40,3E
			29	29MUC-10	825	44°34.7N, 31°33.3E
			30	30MUC-4	1286	44°16.8N, 31°49.8E
			31	31MUC-4	1660	43°54.3N, 32°10.4E
			32	32MUC-23/24	2069	43°41.9N, 32°30.9E
			42	42MUC-3	2083	43°54.3N, 36°12.3E
			43	43MUC-6	1516	44°16.8N, 36°19.0E
			44	44MUC-1	1273	44°23.4N, 36°03.3E
			45	45MUC-11	283	44°36.2N, 36°24.5E
			46	46MUC-8	150	44°37.7N, 36°24.9E
			47	47MUC-1	214	44°36.6N, 36°24.6E
			49	49MUC-1	845	44°28.4N, 36°12.0E
			51	51MUC-1	429	42°02.4N, 36°43.1E
			54	54MUC-1	382	41°59.0N, 36°43.9E
			55	55MUC-2	362	41°54.0N, 36°47.0E
			59	59MUC-1	312	41°42.9N, 36°55.4E
Cariaco Basin	PLUME07	June 1990	12	12GGC	1039	10°35.53N, 64°56.48W
			22	22BX	656	10°48.11N, 65°8.33W
			67	67BX	400	10°40.36N, 64°42.12W
			69	69BX	545	10°44.22N, 64°36.20W
			70	70GGC	547	10°44.22N, 64°36.20W
			82	82BX	818	10°41.15N, 64°58.05W
			89	89BX	1342	10°35.25N, 64°51.26W
			105	105BX	1296	10°43.28N, 65°39.13W
	ODP leg 165	Feb 1996	1002	1002B	900	10°42.36N, 65°10.17W

S 2. Further information on analytical methods at LUH

Any lab work in Hannover was carried out in a clean-air hood (type 10). Water was provided via a Millipore water purification system that produces 18 MΩ water, called MQ water throughout this study. Acids (HCl and HNO_3) have been cleaned at sub-boiling conditions in a quartz glass or teflon PicoTrace distillation system, respectively. Hydrogen peroxide (30 %) and hydrofluoric acid (40 %) were supplied as suprapure grade by Merck KGaA (Darmstadt, Germany) and perchloric acid (70 %) also in the suprapure grade by Carl Roth GmbH. All analyzer PE tubes and pipette tips have been soaked with 1 mol l^{-1} HNO_3 and MQ water each for 7 days. All Teflon and PE bottles have been cleaned with 6 mol l^{-1} HCl and 1 mol l^{-1} HNO_3 respectively at 50 °C for at least three days. All Savillex® teflon beakers have been cleaned

mechanically with water and a tissue. Then, they have been cleaned further for 24 h in 6 mol l^{-1} HCl, 7.5 mol l^{-1} HNO$_3$ and MQ water, respectively, at 120 °C. All employed resins have been cleaned prior use to minimize any blank contributions. Anion and cation resin (Bio-Rad anion AG1 X8, 100-200 mesh, Dowex cation resin 50Wx8, 200 - 400 mesh) have been cleaned with three resin volumes each using MQ, 2 mol l^{-1} HCl, MQ, and 5 mol l^{-1} HCl. They were stored in cleaned PP bottles in 2 mol l^{-1} HCl. After one usage the resin was discarded. Eichrom UTEVA resin was stored and pre-cleaned in 0.05 mol l^{-1} HCl and further cleaning was carried out immediately prior the separation procedure. The resin was re-used up to ten times.

During the Mo separation, Bio-Rad polypropylene columns (Bio-Rad laboratories, München) with 2 ml bed volume, 10 ml reservoir and porous 30 µm polyethylene frits were used. Moreover, for the U separation method, LDPE (low density polyethylene) Pasteur pipettes (Carl Roth GmbH, Karlsruhe) were customized to have 1 ml bed volumes and 5 ml reservoirs and were employed with 30 µm frits with a height of 1.6 mm (RCT Reichelt Chemietechnik GmbH, Heidelberg). All chromatography columns (devoid of resin) have been soaked in alkaline soap for three days, then were washed carefully with MQ water, and finally soaked in 5 % HCl for another three days. After each separation procedure, used columns were cleaned again with the same procedure to be ready for re-use.

For TOC analyses at LUH ~4 mg of solid powder was weighed into silver boats and moistened with 20 µl of 10 % HCl. The filled boats were put open into a desiccator with a bowl of HCl (37 %) below to destroy any inorganic carbonates (Harris et al., 2001). After 48 h the boats were transferred into a desiccator that had a bowl of NaOH in it so that any remaining acid vapors were neutralized. After another 48 h, the boats were put in a furnace to be dried under ambient air conditions at 60 °C. Then, the silver boats were closed carefully and put within Sn boats and measured on a Vario TOC (Elementar Analysen GmbH). Combustion was performed at 740 °C in a tube with platinum catalyst under synthetic air flow and CO$_2$ was detected by an IR-detector.

S 3. Further information on Rayleigh modeling of U isotopes

A Rayleigh fractionation model can be used to describe the evolution of isotope ratios during incomplete and unidirectional reactions in closed systems (Wiederhold, 2015) by using the following equations.

$$\delta^{238}U_{reactant} = \delta^{238}U_0 + \varepsilon lnf \qquad\qquad \text{Eqn. S1}$$

$$\delta^{238}U_{cum.product} = \delta^{238}U_0 + \varepsilon lnf - (\varepsilon lnf)/(1 - f) \qquad\qquad \text{Eqn. S2}$$

Here, $\delta^{238}U_{reactant}$ is the U isotope composition of remaining seawater, $\delta^{238}U_0$ is the initial composition of seawater, ε is the isotope fractionation factor, f is the fraction of U remaining in the water and $\delta^{238}U_{cum.product}$ is the U isotope composition of sediments. The following table (S2) sums the results for the Black Sea and the Cariaco Basin up.

Table S2: Parameters for Rayleigh distillation model.

Parameter	Black Sea	Cariaco Basin
f	0.6	0.9
$\delta^{238}U_0$	-0.4	-0.4
ε	0.6	0.6
$\delta^{238}U_{reactant}$	-0.71	-0.46
$\delta^{238}U_{cum.product}$	0.06	0.17

S 4. Further information on statistical modeling

Tables S3 to S6 show all parameters and reactions used in the U-Mo isotope reactive transport model.

Table S3: Chemical species and boundary conditions in the model.

Water column		Black Sea	Cariaco basin	Unit
	organic carbon (G)	1 to 20	1 to 20	mmol / m^3
	Sulfate (SO$_4^{2-}$)	1.5e4	1.5e4	mmol / m^3
	H$_2$S	0	0	mmol / m^3
	[Mo] of water	4.5e^{-2}	0.12	mmol / m^3
	[Mo^{98}] of water	Related to δ^{98}Mo	Related to δ^{98}Mo	mmol / m^3
	[Mo] of sediment	0	0	mmol / m^3
	[Mo^{98}] of sediment	0	0	mmol / m^3
sediments	organic carbon (G)	From water column	From water column	mmol / m^3
	MnO$_2$	0	0	mmol / m^3
	Fe(OH)$_3$	0	0	mmol / m^3
	Sulfate (SO$_4$)	Coupled with water column	Coupled with water column	mmol / m^3
	Methane (CH$_4$)	0	0	mmol / m^3
	[U^{235}] of pore-water	Coupled with anoxia of water column	Coupled with anoxia of water column	mmol / m^3
	[U^{238}] of pore-water	Coupled with anoxia of water column	Coupled with anoxia of water column	mmol / m^3
	[U^{235}] of sediment	0	0	mmol / m^3
	[U^{238}] of sediment	0	0	mmol / m^3

Table S4: Model reactions.

	Number	Reactions
Water column	R1	$CH_2O + O_2 \rightarrow CO_2 + H_2O$
	R2	$CH_2O + \frac{1}{2}SO_4^{2-} + \frac{1}{2}H^+ \rightarrow CO_2 + \frac{1}{2}HS^- + H_2O$
	R3	Mo conversion from MoO_4^{2-} to $MoO_nS_{4-n}^{2-}$
Sediments	R1	$CH_2O + O_2 \rightarrow CO_2 + H_2O$
	R2	$CH_2O + 2MnO_2 + 4H^+ \rightarrow CO_2 + 2Mn^{2+} + 3H_2O$
	R3	$CH_2O + 4Fe(OH)_3 + 8H^+ \rightarrow CO_2 + 4Fe^{2+} + 11H_2O$
	R4	$CH_2O + \frac{1}{2}SO_4^{2-} + \frac{1}{2}H^+ \rightarrow CO_2 + \frac{1}{2}HS^- + H_2O$
	R5	$CH_2O \rightarrow \frac{1}{2}CO_2 + \frac{1}{2}CH_4$
	R6	$SO_4^{2-} + CH_4 \rightarrow HS^- + H_2O + CO_3^{2-} + H^+$
	R7	$CH_2O + 2UO_2^{2+} + H_2O \rightarrow CO_2 + 2UO_2 + 4H^+$

Table S5: The laws of reaction rates.

	Number	**reactions**
Water column	R1	$\dfrac{v}{a} \cdot \dfrac{G^{\frac{v+1}{v}}}{G_0^{\frac{1}{v}}}$
	R2	$\dfrac{dG}{dt}\left(\dfrac{[SO_4^{2-}]}{KSO_4 + [SO_4^{2-}]}\right)$
	R3	$k_{Mo}[H_2S]([Mo] - [Mo]_f)$
Sediments	R1	$\dfrac{v}{a} \cdot \dfrac{G^{\frac{v+1}{v}}}{G_0^{\frac{1}{v}}}$
	R2	$\dfrac{dG}{dt}\left(\dfrac{[MnO_2]}{KMnO_2 + [MnO_2]}\right)$
	R3	$\dfrac{dG}{dt}\left(\dfrac{KMnO_2}{KMnO_2 + [MnO_2]}\right)\left(\dfrac{[Fe(OH)_3]}{KFe(OH)_3 + [Fe(OH)_3]}\right)$
	R4	$\dfrac{dG}{dt}\left(\dfrac{KMnO_2}{KMnO_2 + [MnO_2]}\right)\left(\dfrac{KFe(OH)_3}{KFe(OH)_3 + [Fe(OH)_3]}\right)\left(\dfrac{[SO_4^{2-}]}{KSO_4 + [SO_4^{2-}]}\right)$
	R5	$\dfrac{dG}{dt}\left(\dfrac{KMnO_2}{KMnO_2 + [MnO_2]}\right)\left(\dfrac{KFe(OH)_3}{KFe(OH)_3 + [Fe(OH)_3]}\right)\left(\dfrac{KSO_4}{KSO_4 + [SO_4^{2-}]}\right)$
	R6	$k6[SO_4^{2-}][CH_4]$
	R7	$f_U\dfrac{dG}{dt}\left(\dfrac{KMnO_2}{KMnO_2 + [MnO_2]}\right)\left(\dfrac{KFe(OH)_3}{KFe(OH)_3 + [Fe(OH)_3]}\right)\left(\dfrac{[U^{238}]}{KU + [U^{238}]}\right)$

Table S6: Parameters of the model.

	symbol	description	Black Sea value	Cariaco Basin value	unit
Water column	v_{sink}	Sinking rate of particles	1000	1000	m yr^{-1}
	KSO_4	Limiting concentration of SO_4^{2-}	1.6	1.6	mmol l^{-1}
	KU	Limiting concentration of U in pore-water	0.13	0.13	nmol l^{-1}
	α_{Mo}	Isotopic fractionation during the reduction of Mo	0.9973	0.9973	1
	f_U	The rater of U reduction relative to sulfate reduction	5*10^{-6}	5*10^{-6}	1
	a	Average life-time of the more reactive organic matter	0.5	0.5	yr
	v	Shape of organic matter distribution	0.15	0.15	1
	De	Eddy diffusion coefficient	1.4e-5	1.4e-5	m^2 s^{-1}
	k_{Mo}	Rate constant for Mo reduction	1e-4	2e-4	m^3 mmol^{-1}
	Mo$_f$	Limiting concentration for Mo reduction	3/1e3	45/1e3	mmol m^{-3}
Sediments	φ	Porosity	0.8	0.8	1
	ρ	The density of sediment	2.5	2.5	g cm^{-3}
	ω_0	Sediment rate	0.001	0.00035	cm yr^{-1}
	k6	Rate constant for reaction 6	1e4	1e4	cm^3 mmol^{-1}
	a	Average life-time of the more reactive organic matter	4.5	4.5	yr
	v	Shape of organic matter distribution	0.15	0.15	1
	$KMnO_2$	Limiting concentration of MnO_2	32	32	µmol g^{-1}
	$KFe(OH)_3$	Limiting concentration of Fe(OH)$_3$	65	65	µmol g^{-1}
	KSO_4	Limiting concentration of SO_4^{2-}	1.6	1.6	mmol l^{-1}
	KU	Limiting concentration of U in pore-water	0.13	0.13	nmol l^{-1}
	D_U	Diffusion coefficient of U	2.13e-6	2.13e-6	cm^2 yr^{-1}
	α_U	Isotopic fractionation during the reduction of U	1.005-1.009	1.003-1.007	1
	f_U	The rater of U reduction relative to sulfate reduction	1e-6	1e-6	1

S 5. Data

The following tables S7, S8, and S10 show concentration and isotope data for samples measured in this study, partly the data was published previously as cited. Tables S9 and S11 show compared detrital corrections with different elements as detrital monitors. Table S12 summarizes all literature data that is used in this study which was taken from Ravizza et al. (1991), Barling et al. (2001), Weyer et al. (2008), Montoya-Pino et al. (2010), Montoya-Pino (2011), and Arnold et al. (2012).

Table S7: Concentration data for Black Sea and Cariaco Basin samples. Aluminium, Fe, Ti and Mn measured in medium resolution with ICP-MS or measured with ICP-OES, Th measured in low resolution with ICP-MS. Cariaco surface samples data from Gueguen et al. (2016), core 1002B TOC data from Lyons et al. (2003).

Locality	Station	Sample depth / cm	Al / wt%	Fe / wt%	Ti / µg g⁻¹	Mn / µg g⁻¹	Th / µg g⁻¹	TOC / %
Black Sea	29-11	0.5	4.22	2.37		372		4.01
Black Sea	30-4	0.5	3.95	2.32		346		6.62
Black Sea	31-4	0.5	3.09	2.06		358		5.52
Black Sea	22-1	0.5	4.55	2.39		326		3.62
Black Sea	32-23	0.5	2.12	1.6		285		4.09
Black Sea	46-8	0.5	5.75	2.38		395		2.42
Black Sea	47-1	0.5	5.68	2.65		439		3.19
Black Sea	49-1	0.5	4.23	2.18		382		3.83
Black Sea	44-1	0.5	3.61	2.11		389		4.13
Black Sea	43-6	0.5	3.19	2.24		415		5.57
Black Sea	42-3	0.5	2.06	1.6		306		4.86
Black Sea	59-1	0.5	5.88	3.16		488		3.23
Black Sea	55-2	0.5	5.07	2.91		457		4
Black Sea	54-1	0.5	5.04	2.84		456		4.2
Black Sea	51-1	0.5	4.58	2.69		451		5.3
Black Sea	29-11	1.5	4.68	2.5		339		4.89
Black Sea	30-4	1.5	3.58	2.23		378		5.42
Black Sea	31-4	1.5	3.13	2.17		401		6.29
Black Sea	22-1	1.5	5.2	2.69		362		3.5
Black Sea	32-23	1.5	2.49	2.01		389		6.1
Black Sea	46-8	1.5	6.01	2.68		384		1.87
Black Sea	47-1	1.5	5.7	2.66		442		3.25
Black Sea	45-11	1.5	4.43	2.17		324		4.58
Black Sea	49-1	1.5	4.46	2.41		433		4.8
Black Sea	44-1	1.5	4.04	2.4		450		4.95
Black Sea	43-6	1.5	3.44	2.42		450		5.89
Black Sea	42-3	1.5	2.8	2.25		426		6.65
Black Sea	59-1	1.5	5.22	3.08		461		3.18
Black Sea	55-2	1.5	5.36	3.06		507		4.66
Black Sea	54-1	1.5	4.61	2.62		470		4.79
Black Sea	51-1	1.5	4.71	2.73		477		4.85
Black Sea	32MUC24	3.5	2.66	2.04		396		7.17
Black Sea	32MUC24	4.5	3.19	2.26		423		5.88
Black Sea	32MUC24	5.5	3.2	2.13		423		4.36
Black Sea	32MUC24	6.5	3.44	2.35		446		4.71
Black Sea	32MUC24	7.5	3.5	2.48		468		5.72
Black Sea	32MUC24	8.5	3.61	2.61		489		5.74
Black Sea	32MUC24	9.5	3.44	2.52		484		6.1
Black Sea	32MUC24	10.5	2.56	1.97		417		5.54
Black Sea	32MUC24	15.5	1.47	1.17		310		4.16
Black Sea	32MUC24	24.5	2.05	1.65		367		4.74

Locality	Station	Sample depth / cm	Al / wt%	Fe / wt%	Ti / µg g⁻¹	Mn / µg g⁻¹	Th / µg g⁻¹	TOC / %
Black Sea	32MUC24	34.5	6.99	3.4		523		1.32
Black Sea	32MUC24	42.5	5.73	3.15		404		8.88
Cariaco	22BX	surface cm		2.68	2418		8.4	
Cariaco	89BX	surface cm		4.27	3412		8	
Cariaco	82BX	surface cm		3.35	2966		9.6	
Cariaco	105BX	surface cm		4.25	3307		11.1	
Cariaco	67BX	surface cm		3.53	3282		10.8	
Cariaco	69BX	surface cm		3.92	3648		12.1	
Cariaco	12GGC	0.5	5.83	2.91	2765	221	6.5	
Cariaco	70GGC	0.5	6.58	2.65	2457	135	6.7	
Cariaco	12GGC	1.5	5.88	2.91	2655	213	6.44	
Cariaco	12GGC	2.5	6.58	3.01	2805	238	6.75	5.43
Cariaco	12GGC	3.5	7.98	3.38	3198	242	7.48	
Cariaco	12GGC	4.5	7.31	2.99	2723	176	6.97	5.1
Cariaco	12GGC	5.5	6.42	3.05	2874	205	6.76	
Cariaco	12GGC	6.5	7.34	3.48	3425	213	7.33	
Cariaco	12GGC	7.5	6.04	3.25	3105	230	6.68	4.02
Cariaco	12GGC	8.5	7.45	3.47	3301	225	7.23	
Cariaco	12GGC	9.5	6.78	3.41	3292	212	7.3	
Cariaco	12GGC	14.5	6.85	2.89	2861	137	6.54	5.91
Cariaco	12GGC	19.5	4.57	2.17	2150	114	4.89	
Cariaco	12GGC	24.5	8.13	3.58	3062	190	7.97	
Cariaco	12GGC	29.5	5.46	2.79	2539	146	6.43	5.74
Cariaco	12GGC	34.5	5.22	2.5	2431	164	6.07	
Cariaco	12GGC	39.5	5.86	2.79	2767	161	6.79	5.11
Cariaco	12GGC	44.5	5.63	2.87	2668	152	6.41	5.52
Cariaco	12GGC	49.5	5.83	2.83	2711	165	7.01	
Cariaco	70GGC	1.5	7.03	2.79	2605	138	6.99	
Cariaco	70GGC	2.5	6.92	2.64	2555	131	6.92	5.61
Cariaco	70GGC	3.5	6.56	2.51	2500	131	6.58	
Cariaco	70GGC	4.5	7.09	2.75	2605	127	7.07	5.73
Cariaco	70GGC	5.5	6.89	2.64	2538	131	6.85	5.67
Cariaco	70GGC	6.5	6.92	2.7	2542	124	6.86	
Cariaco	70GGC	7.5	7	2.73	2582	134	6.98	
Cariaco	70GGC	8.5	8.24	3.16	3129	143	8.64	4.77
Cariaco	70GGC	9.5	7.44	2.84	2918	127	7.9	
Cariaco	70GGC	14.5	7.48	2.8	2740	133	7.32	5.69
Cariaco	70GGC	24.5	6.88	2.67	2596	148	6.89	5.7
Cariaco	70GGC	29.5	3.02	1.38	1599	72	3.32	
Cariaco	70GGC	34.5	6.18	2.38	2486	130	6.17	5.98
Cariaco	70GGC	39.5	7.02	2.71	2630	134	6.91	5.24
Cariaco	70GGC	44.5	6.65	2.52	2638	139	6.57	5.17
Cariaco	70GGC	49.5	7.33	2.74	2741	137	7.35	
Cariaco	1002B	30	5.44		2867	290	7.7	5.68
Cariaco	1002B	85	6.61		3009	200	8.89	5.25
Cariaco	1002B	105	5.92		2837	210	8.13	5.22
Cariaco	1002B	145	2.57		2762	195	4.97	4.21
Cariaco	1002B	170	6.77		3038	270	8.72	4.33
Cariaco	1002B	200	7.05		3178	252	9.31	4.23
Cariaco	1002B	260	7.02		3189	263	9.43	3.85
Cariaco	1002B	300	6.34		3051	199	8.02	5.15
Cariaco	1002B	340	3.21		3406	200	4.8	6.21
Cariaco	1002B	360	5.05		3399	202	7.5	5.72
Cariaco	1002B	440	4.31		2124	149	6.41	2.89
Cariaco	1002B	450	4.51		2224	151	6.29	2.85
Cariaco	1002B	510	5.38		2847	229	7.12	2.71
Cariaco	1002B	530	6.37		3022	213	7.82	3.2
Cariaco	1002B	590	5.46		3165	335	7.01	5.51

Table S8: Bulk and detritus corrected Mo and δ⁹⁸Mo data.

Locality	Station	Sample depth / cm	Mo$_{bulk}$ / µg g^{-1}	Mo$_{authi.}$ / µg g^{-1}	δ⁹⁸Mo$_{bulk}$ / ‰	δ⁹⁸Mo$_{authi.}$ / ‰	2 s.d. δ⁹⁸Mo / ‰	Mo Detritus / %
Black Sea	29-11	0.5	40.8	41.33	1.98	2.00	0.03	1.38
Black Sea	30-4	0.5	17.5	17.99	1.57	1.60	0.01	2.96
Black Sea	31-4	0.5	29.2	29.61	1.73	1.74	0.06	1.41
Black Sea	22-1	0.5	16.9	17.47	1.72	1.76	0.02	3.52
Black Sea	32-23	0.5	21.9	22.14	1.46	1.47	0.06	1.29
Black Sea	46-8	0.5	1.1	1.86	0.23	0.00	0.03	41.82
Black Sea	47-1	0.5	28.7	29.49	-0.52	-0.55	0.02	2.60
Black Sea	49-1	0.5	29.1	29.72	1.81	1.83	0.09	1.92
Black Sea	44-1	0.5	24.1	24.61	1.70	1.72	0.04	1.98
Black Sea	43-6	0.5	26.2	26.62	1.52	1.54	0.11	1.62
Black Sea	42-3	0.5	20.1	20.33	1.14	1.14	0.19	1.37
Black Sea	59-1	0.5	45.3	46.05	0.56	0.56	0.01	1.72
Black Sea	55-2	0.5	64.0	64.65	1.44	1.45	0.07	1.06
Black Sea	54-1	0.5	44.3	44.97	1.06	1.07	0.08	1.51
Black Sea	51-1	0.5	61.7	62.30	1.51	1.52	0.06	0.99
Black Sea	29-11	1.5	30.1	30.76	0.81	0.82	0.10	2.05
Black Sea	30-4	1.5	35.1	35.58	1.65	1.67	0.01	1.36
Black Sea	31-4	1.5	28.9	29.36	1.68	1.70	0.01	1.44
Black Sea	22-1	1.5	18.5	19.21	1.99	2.04	0.09	3.65
Black Sea	32-23	1.5	28.9	29.25	0.42	0.42	0.06	1.15
Black Sea	46-8	1.5	0.8	1.61	0.02	-0.51	0.02	50.41
Black Sea	47-1	1.5	28.7	29.45	-0.10	-0.12	0.08	2.61
Black Sea	45-11	1.5	48.1	48.69	0.61	0.61	0.04	1.23
Black Sea	49-1	1.5	42.9	43.45	1.97	1.99	0.14	1.39
Black Sea	44-1	1.5	30.1	30.69	1.74	1.76	0.13	1.78
Black Sea	43-6	1.5	28.0	28.42	1.68	1.69	0.18	1.64
Black Sea	42-3	1.5	29.8	30.22	1.55	1.56	0.11	1.25
Black Sea	59-1	1.5	49.3	49.97	0.61	0.61	0.08	1.41
Black Sea	55-2	1.5	55.4	56.16	1.40	1.41	0.04	1.29
Black Sea	54-1	1.5	57.4	58.05	1.20	1.20	0.05	1.07
Black Sea	51-1	1.5	61.7	62.36	1.46	1.47	0.08	1.02
Black Sea	32MUC24	3.5	31.33	30.97	1.69	1.71	0.03	1.14
Black Sea	32MUC24	4.5	30.95	30.52	1.91	1.94	0.03	1.39
Black Sea	32MUC24	5.5	20.51	20.08	1.86	1.89	0.05	2.1
Black Sea	32MUC24	6.5	25.47	25.01	1.94	1.97	0.06	1.82
Black Sea	32MUC24	7.5	25.51	25.04	2.01	2.04	0.06	1.85
Black Sea	32MUC24	8.5	27.75	27.26	1.97	1.99	0.09	1.76
Black Sea	32MUC24	9.5	27.98	27.52	2.00	2.03	0.02	1.66
Black Sea	32MUC24	10.5	23.56	23.21	2.01	2.03	0.02	1.46
Black Sea	32MUC24	15.5	18.61	18.41	2.23	2.24	0.02	1.06
Black Sea	32MUC24	24.5	35.35	35.07	2.38	2.4	0.16	0.78
Black Sea	32MUC24	34.5	17.96	17.02	2.18	2.27	0.02	5.25
Black Sea	32MUC24	42.5	92.69	91.92	1.23	1.23	0.08	0.83
Cariaco	22BX	surface cm	16	15.17	2.8	2.92	0.06	5.19
Cariaco	89BX	surface cm	33.7	32.57	1.53	1.56	0.05	3.34
Cariaco	82BX	surface cm	50.4	49.41	2.03	2.06	0.10	1.97
Cariaco	105BX	surface cm	28.5	27.44	1.16	1.19	0.04	3.71
Cariaco	67BX	surface cm	57.4	56.28	1.6	1.62	0.10	1.94
Cariaco	69BX	surface cm	89.3	88.07	1.83	1.85	0.04	1.37
Cariaco	12GGC	0.5	38.94	38.15	1.51	1.53	0.02	2.02
Cariaco	12GGC	1.5	38.7	37.9	1.55	1.57	0.05	2.05
Cariaco	12GGC	2.5	44.64	43.75	1.47	1.49	0.01	1.99
Cariaco	12GGC	3.5	43.05	41.97	1.48	1.51	0.11	2.5
Cariaco	12GGC	4.5	43.48	42.49	1.53	1.55	0.09	2.27
Cariaco	12GGC	5.5	41.25	40.38	1.53	1.56	0.06	2.1
Cariaco	12GGC	6.5	45.91	44.92	1.34	1.35	0.02	2.16
Cariaco	12GGC	7.5	40.87	40.06	1.5	1.52	0.07	2
Cariaco	12GGC	8.5	47.08	46.08	1.47	1.49	0.07	2.13
Cariaco	12GGC	9.5	55.3	54.38	1.3	1.32	0.08	1.65
Cariaco	12GGC	14.5	109.11	108.19	0.96	0.96	0.04	0.85
Cariaco	12GGC	19.5	47.64	47.02	1.4	1.41	0.03	1.3

Locality	Station	Sample depth / cm	Mo_{bulk} / µg g^{-1}	$Mo_{authi.}$ / µg g^{-1}	$\delta^{98}Mo_{bulk}$ / ‰	$\delta^{98}Mo_{authi.}$ / ‰	2 s.d. $\delta^{98}Mo$ / ‰	Mo Detritus / %
Cariaco	12GGC	24.5	65.66	64.57	1.49	1.5	0.02	1.67
Cariaco	12GGC	29.5	94.22	93.49	1.58	1.59	0.03	0.78
Cariaco	12GGC	34.5	59.43	58.72	1.28	1.29	0.01	1.19
Cariaco	12GGC	39.5	69.19	68.4	1.31	1.31	0.05	1.14
Cariaco	12GGC	44.5	81.19	80.43	1.33	1.34	0.06	0.94
Cariaco	12GGC	49.5	65.47	64.68	1.4	1.41	0.09	1.2
Cariaco	70GGC	0.5	61.81	60.9	1.52	1.53	0.04	1.44
Cariaco	70GGC	1.5	65.55	64.6	1.49	1.51	0.12	1.45
Cariaco	70GGC	2.5	70.79	69.9	1.4	1.41	0.08	1.32
Cariaco	70GGC	3.5	61.93	61	1.43	1.44	0.04	1.43
Cariaco	70GGC	4.5	85.83	84.9	1.38	1.39	0.02	1.11
Cariaco	70GGC	5.5	66.04	65.1	1.55	1.57	0.13	1.41
Cariaco	70GGC	6.5	79.85	78.9	1.48	1.49	0.05	1.17
Cariaco	70GGC	7.5	71.58	70.6	1.77	1.78	0.01	1.32
Cariaco	70GGC	8.5	99.75	98.6	1.44	1.45	0.08	1.11
Cariaco	70GGC	9.5	57.88	56.9	1.79	1.81	0.06	1.74
Cariaco	70GGC	14.5	139.81	138.8	1.03	1.04	0.07	0.72
Cariaco	70GGC	24.5	79.23	78.3	1.56	1.58	0.06	1.17
Cariaco	70GGC	29.5	56.6	56.2	1.58	1.59	0.09	0.72
Cariaco	70GGC	34.5	80.5	79.7	1.61	1.62	0.03	1.04
Cariaco	70GGC	39.5	120.03	119.1	1.28	1.28	0.05	0.79
Cariaco	70GGC	44.5	68.78	67.9	1.76	1.78	0.05	1.31
Cariaco	70GGC	49.5	161.72	160.7	1.1	1.1	0.05	0.61
Cariaco	1002B	30	122.33	121.6	1.17	1.17	0.05	0.6
Cariaco	1002B	85	102.42	101.5	1.08	1.08	0.08	0.87
Cariaco	1002B	105	86.12	85.3	1.15	1.15	0.02	0.93
Cariaco	1002B	145	57.97	57.6	0.98	0.99	0.07	0.6
Cariaco	1002B	170	81.05	80.1	0.91	0.91	0.07	1.13
Cariaco	1002B	200	70.15	69.2	0.9	0.9	0.10	1.36
Cariaco	1002B	260	78.88	77.9	1.05	1.05	0.03	1.2
Cariaco	1002B	300	116.63	115.8	1.2	1.21	0.07	0.73
Cariaco	1002B	340	178.32	177.9	1.3	1.3	0.03	0.24
Cariaco	1002B	360	150.45	149.8	1.18	1.19	0.00	0.45
Cariaco	1002B	440	68.05	67.5	1.62	1.63	0.10	0.86
Cariaco	1002B	450	66.07	65.5	1.58	1.59	0.02	0.92
Cariaco	1002B	510	68.68	68	1.59	1.6	0.07	1.06
Cariaco	1002B	530	107.72	106.9	1.72	1.73	0.05	0.8
Cariaco	1002B	590	189.84	189.1	1.67	1.68	0.01	0.39

Table S9: Comparison of detrital correction with Al and Ti for Mo isotope data from the Cariaco Basin cores 12GGC and 70GGC.

core	sample depth / cm	$\delta^{98}Mo_{bulk}$ / ‰	2 s.d. / ‰	$\delta^{98}Mo_{authi.}$ Al corr. / ‰	$\delta^{98}Mo_{authi.}$ Ti corr. / ‰	difference Al-Ti detr. corr. / ‰
12GGC	0.5	1.51	0.02	1.53	1.53	0.00
	1.5	1.55	0.05	1.57	1.57	0.00
	2.5	1.47	0.01	1.49	1.49	0.00
	3.5	1.48	0.11	1.51	1.50	0.00
	4.5	1.53	0.09	1.55	1.55	0.01
	5.5	1.53	0.06	1.56	1.55	0.00
	6.5	1.34	0.02	1.35	1.35	0.00
	7.5	1.50	0.07	1.52	1.52	0.00
	8.5	1.47	0.07	1.49	1.49	0.00
	9.5	1.30	0.08	1.32	1.32	0.00
	14.5	0.96	0.04	0.96	0.96	0.00
	24.5	1.40	0.03	1.41	1.41	0.00
	29.5	1.49	0.02	1.50	1.50	0.00
	34.5	1.58	0.03	1.59	1.59	0.00
	39.5	1.28	0.01	1.29	1.29	0.00
	44.5	1.31	0.05	1.31	1.31	0.00
	49.5	1.33	0.06	1.34	1.34	0.00

	sample depth / cm	δ^{98}Mo$_{bulk}$ / ‰	2 s.d. / ‰	δ^{98}Mo$_{authi.}$ Al corr. / ‰	δ^{98}Mo$_{authi.}$ Ti corr. / ‰	difference Al-Ti detr. corr. / ‰
	0.5	1.40	0.09	1.41	1.41	0.00
70GGC	1.5	1.52	0.04	1.53	1.53	0.00
	2.5	1.49	0.12	1.51	1.50	0.00
	3.5	1.40	0.08	1.41	1.41	0.00
	4.5	1.43	0.04	1.44	1.44	0.00
	5.5	1.38	0.02	1.39	1.38	0.00
	6.5	1.55	0.13	1.57	1.57	0.00
	7.5	1.48	0.05	1.49	1.49	0.00
	8.5	1.77	0.01	1.78	1.78	0.00
	9.5	1.44	0.08	1.45	1.45	0.00
	14.5	1.79	0.06	1.81	1.81	0.00
	19.5	1.03	0.07	1.04	1.04	0.00
	24.5	1.56	0.06	1.58	1.57	0.00
	29.5	1.58	0.09	1.59	1.59	0.00
	34.5	1.61	0.03	1.62	1.62	0.00
	39.5	1.28	0.05	1.28	1.28	0.00
	44.5	1.76	0.05	1.78	1.78	0.00
	49.5	1.10	0.05	1.10	1.10	0.00

Table S10: Bulk and detritus corrected U and δ^{238}U data.

Locality	Station	Sample depth / cm	U$_{bulk}$ / µg g^{-1}	U$_{authi.}$ / µg g^{-1}	δ^{238}U$_{bulk}$ / ‰	δ^{238}U$_{authi.}$ / ‰	2 s.d. δ^{238}U / ‰	U Detritus / %
Black Sea	29-11	0.5	4.83	4.07	0.03	0.09	0.02	15.74
Black Sea	30-4	0.5	3.09	2.38	-0.08	-0.02	0.01	22.98
Black Sea	31-4	0.5	4.99	4.43	0.01	0.05	0.11	11.15
Black Sea	22-1	0.5	2.92	2.10	0.02	0.15	0.07	28.10
Black Sea	32-23	0.5	3.45	3.07	0.04	0.08	0.06	11.03
Black Sea	46-8	0.5	2.61	1.57	0.05	0.28	0.04	39.71
Black Sea	47-1	0.5	3.43	2.41	0.19	0.39	0.06	29.80
Black Sea	49-1	0.5	2.65	1.88	0.03	0.17	0.03	28.76
Black Sea	44-1	0.5	3.05	2.40	-0.02	0.05	0.02	21.30
Black Sea	43-6	0.5	4.89	4.31	0.01	0.05	0.04	11.76
Black Sea	42-3	0.5	3.67	3.30	0.07	0.11	0.02	10.13
Black Sea	59-1	0.5	2.92	1.86	0.00	0.18	0.06	36.29
Black Sea	55-2	0.5	4.87	3.96	0.17	0.27	0.10	18.73
Black Sea	54-1	0.5	3.26	2.35	0.08	0.22	0.02	27.84
Black Sea	51-1	0.5	6.34	5.51	0.21	0.29	0.04	13.02
Black Sea	29-11	1.5	3.44	2.59	0.00	0.09	0.04	24.51
Black Sea	30-4	1.5	6.07	5.43	0.03	0.07	0.04	10.62
Black Sea	31-4	1.5	7.08	6.51	0.03	0.06	0.08	7.96
Black Sea	22-1	1.5	3.96	3.03	0.01	0.11	0.03	23.61
Black Sea	32-23	1.5	7.04	6.59	0.00	0.02	0.07	6.37
Black Sea	46-8	1.5	4.11	3.03	0.24	0.43	0.07	26.31
Black Sea	47-1	1.5	4.48	3.45	0.26	0.43	0.08	22.92
Black Sea	45-11	1.5	3.12	2.33	-0.07	0.01	0.04	25.51
Black Sea	49-1	1.5						
Black Sea	44-1	1.5	5.60	4.87	0.03	0.08	0.02	13.00
Black Sea	43-6	1.5	6.87	6.25	0.04	0.07	0.03	9.02
Black Sea	42-3	1.5	6.63	6.13	0.08	0.11	0.05	7.61
Black Sea	59-1	1.5	4.24	3.30	0.23	0.38	0.02	22.17
Black Sea	55-2	1.5	6.28	5.31	0.17	0.25	0.05	15.36
Black Sea	54-1	1.5	7.22	6.39	0.35	0.43	0.04	11.50
Black Sea	51-1	1.5	7.41	6.56	0.23	0.30	0.06	11.43
Black Sea	32MUC24	3.5	7.88	7.40	-0.03	-0.01	0.02	6.07
Black Sea	32MUC24	4.5	10.03	9.46	0.03	0.05	0.03	5.72
Black Sea	32MUC24	5.5	12.10	11.53	-0.04	-0.03	0.04	4.76
Black Sea	32MUC24	6.5	11.71	11.09	-0.05	-0.03	0.03	5.28
Black Sea	32MUC24	7.5	14.71	14.08	-0.04	-0.03	0.05	4.28
Black Sea	32MUC24	8.5	15.27	14.62	-0.03	-0.02	0.06	4.25

Locality	Station	Sample depth / cm	U_{bulk} / µg g^{-1}	$U_{authi.}$ / µg g^{-1}	$\delta^{238}U_{bulk}$ / ‰	$\delta^{238}U_{authi.}$ / ‰	2 s.d. $\delta^{238}U$ / ‰	U Detritus / %
Black Sea	32MUC24	9.5	15.03	14.41	-0.08	-0.07	0.04	4.12
Black Sea	32MUC24	10.5	15.63	15.17	-0.25	-0.25	0.08	2.94
Black Sea	32MUC24	15.5	15.04	14.78	-0.17	-0.17	0.06	1.76
Black Sea	32MUC24	24.5	15.46	15.09	0.04	0.05	0.03	2.39
Black Sea	32MUC24	34.5	5.46	4.20	-0.21	-0.18	0.04	23.02
Black Sea	32MUC24	42.5	11.55	10.52	0.47	0.55	0.05	8.93
Cariaco	22BX	surface cm	4.4	2.03	-0.05	0.23	0.01	53.84
Cariaco	89BX	surface cm	6.1	3.84	-0.05	0.09	0.02	36.98
Cariaco	82BX	surface cm	7.7	4.99	0.02	0.19	0.05	35.16
Cariaco	105BX	surface cm	6.0	2.87	-0.03	0.27	0.04	52.17
Cariaco	67BX	surface cm	7.8	4.75	0.02	0.22	0.08	39.05
Cariaco	69BX	surface cm	10.4	6.99	-0.01	0.13	0.04	32.81
Cariaco	12GGC	0.5	5.94	4.89	-0.06	0.04	0.04	17.67
Cariaco	12GGC	1.5	6.59	5.53	0.03	0.15	0.05	16.08
Cariaco	12GGC	2.5	6.67	5.49	0.02	0.15	0.04	17.75
Cariaco	12GGC	3.5	7.42	5.98	0.01	0.13	0.05	19.37
Cariaco	12GGC	4.5	7.19	5.87	0.02	0.13	0.01	18.30
Cariaco	12GGC	5.5	6.76	5.61	0.00	0.12	0.02	17.09
Cariaco	12GGC	6.5	5.95	4.63	0.00	0.16	0.03	22.22
Cariaco	12GGC	7.5	6.06	4.97	-0.01	0.12	0.02	17.95
Cariaco	12GGC	8.5	6.53	5.19	-0.01	0.12	0.02	20.52
Cariaco	12GGC	9.5	6.29	5.07	0.02	0.18	0.05	19.39
Cariaco	12GGC	14.5	11.38	10.15	0.04	0.11	0.03	10.82
Cariaco	12GGC	19.5	3.55	2.72	-0.11	0.01	0.06	23.20
Cariaco	12GGC	24.5	8.34	6.88	-0.17	-0.12	0.02	17.55
Cariaco	12GGC	29.5	7.13	6.15	-0.21	-0.18	0.05	13.78
Cariaco	12GGC	34.5	5.11	4.17	-0.13	-0.04	0.06	18.40
Cariaco	12GGC	39.5	5.69	4.64	-0.11	-0.01	0.01	18.53
Cariaco	12GGC	44.5	7.20	6.18	-0.12	-0.05	0.04	14.09
Cariaco	12GGC	49.5	5.65	4.60	-0.12	-0.02	0.04	18.59
Cariaco	70GGC	0.5	7.79	6.61	-0.08	-0.01	0.05	15.20
Cariaco	70GGC	1.5	8.84	7.58	-0.06	0.01	0.05	14.31
Cariaco	70GGC	2.5	11.30	10.06	0.00	0.06	0.03	11.02
Cariaco	70GGC	3.5	10.46	9.28	0.01	0.07	0.02	11.29
Cariaco	70GGC	4.5	12.30	11.02	0.01	0.06	0.04	10.38
Cariaco	70GGC	5.5	11.50	10.26	0.02	0.08	0.04	10.77
Cariaco	70GGC	6.5	13.00	11.75	0.00	0.05	0.00	9.58
Cariaco	70GGC	7.5	9.49	8.23	-0.03	0.04	0.04	13.28
Cariaco	70GGC	8.5	10.09	8.60	-0.06	0.02	0.01	14.70
Cariaco	70GGC	9.5	9.02	7.68	-0.07	0.01	0.06	14.85
Cariaco	70GGC	14.5	14.03	12.69	-0.06	-0.01	0.02	9.59
Cariaco	70GGC	24.5	10.24	9.00	-0.05	0.01	0.05	12.09
Cariaco	70GGC	29.5	7.08	6.54	-0.01	0.04	0.03	7.67
Cariaco	70GGC	34.5	9.49	8.38	-0.07	-0.02	0.04	11.71
Cariaco	70GGC	39.5	11.94	10.67	0.05	0.12	0.03	10.59
Cariaco	70GGC	44.5	8.38	7.19	-0.14	-0.09	0.02	14.28
Cariaco	70GGC	49.5	20.98	19.66	0.20	0.25	0.02	6.29
Cariaco	1002B	30	11.56	10.58	0.09	0.12	0.05	8.47
Cariaco	1002B	85	13.28	12.09	0.06	0.10	0.07	8.96
Cariaco	1002B	105	11.27	10.20	0.11	0.16	0.00	9.45
Cariaco	1002B	145	12.35	11.89	0.09	0.11	0.04	3.75
Cariaco	1002B	170	11.39	10.17	0.11	0.16	0.00	10.70
Cariaco	1002B	200	11.00	9.73	0.13	0.18	0.07	11.53
Cariaco	1002B	260	9.63	8.37	0.10	0.16	0.05	13.12
Cariaco	1002B	300	12.97	11.83	0.05	0.08	0.03	8.79
Cariaco	1002B	340	18.14	17.56	0.04	0.05	0.06	3.18
Cariaco	1002B	360	20.86	19.95	-0.08	-0.07	0.02	4.36
Cariaco	1002B	440	7.15	6.37	-0.11	-0.08	0.05	10.86
Cariaco	1002B	450	6.62	5.81	-0.14	-0.12	0.06	12.27
Cariaco	1002B	510	7.54	6.58	-0.07	-0.04	0.06	12.83
Cariaco	1002B	530	9.34	8.19	-0.10	-0.07	0.06	12.28
Cariaco	1002B	590	16.93	15.95	-0.09	-0.08	0.04	5.81

Table S11: Comparison of detrital correction with Al and Th for U isotope data from the Cariaco Basin cores 12GGC and 70GGC.

core	depth / cm	$\delta^{238}U_{bulk}$ / ‰	2 s.d. / ‰	$\delta^{238}U_{authi.}$ Al corr. / ‰	$\delta^{238}U_{authi.}$ Th corr. / ‰	difference Al-Th detr. corr. / ‰
12GGC	0.5	-0.06	0.04	-0.01	0.04	-0.06
	1.5	0.03	0.05	0.09	0.15	-0.06
	2.5	0.02	0.04	0.09	0.15	-0.06
	3.5	0.01	0.05	0.08	0.13	-0.05
	4.5	0.02	0.01	0.09	0.13	-0.05
	5.5	0.00	0.02	0.06	0.12	-0.06
	6.5	0.00	0.03	0.08	0.16	-0.07
	7.5	-0.01	0.02	0.05	0.12	-0.07
	8.5	-0.01	0.02	0.06	0.12	-0.06
	9.5	0.02	0.05	0.10	0.18	-0.08
	14.5	0.04	0.03	0.08	0.11	-0.02
	19.5	-0.11	0.06	-0.05	0.01	-0.06
	24.5	-0.17	0.02	-0.14	-0.12	-0.02
	29.5	-0.21	0.05	-0.19	-0.18	-0.02
	34.5	-0.13	0.06	-0.09	-0.04	-0.05
	39.5	-0.11	0.01	-0.06	-0.01	-0.05
	44.5	-0.12	0.04	-0.08	-0.05	-0.03
	49.5	-0.12	0.04	-0.08	-0.02	-0.06
70GGC	0.5	-0.08	0.05	-0.04	-0.01	-0.03
	1.5	-0.06	0.05	-0.02	0.01	-0.03
	2.5	0.00	0.03	0.04	0.06	-0.03
	3.5	0.01	0.02	0.05	0.07	-0.03
	4.5	0.01	0.04	0.04	0.06	-0.02
	5.5	0.02	0.04	0.05	0.08	-0.03
	6.5	0.00	0.00	0.03	0.05	-0.02
	7.5	-0.03	0.04	0.01	0.04	-0.03
	8.5	-0.06	0.01	-0.02	0.02	-0.03
	9.5	-0.07	0.06	-0.03	0.01	-0.04
	14.5	-0.06	0.02	-0.03	-0.01	-0.02
	24.5	-0.05	0.05	-0.01	0.01	-0.02
	29.5	-0.01	0.03	0.02	0.04	-0.02
	34.5	-0.07	0.04	-0.04	-0.02	-0.02
	39.5	0.05	0.03	0.09	0.12	-0.03
	44.5	-0.14	0.02	-0.11	-0.09	-0.02
	49.5	0.20	0.02	0.23	0.25	-0.02

Table S12: Compilation of all literature data on $\delta^{98}Mo$ and $\delta^{238}U$ compared in this study

core	sample name	sample depth / cm	water depth / m	$\delta^{238}U_{authi.}$ / ‰	2 s.d. $\delta^{238}U$ / ‰	$\delta^{98}Mo_{authi.}$ / ‰	2 s.d. $\delta^{98}Mo$ / ‰	$\delta^{238}U$ ref.	$\delta^{98}Mo$ ref.
				Black Sea Unit I					
BC21	BS21-1	0-6	2092	-0.01	0.05	2.27	0.18	Weyer (2008)	Arnold (2012)
BC21	BS21-2	10-14	2092	0.01	0.00	2.28	0.11	Weyer (2008)	Arnold (2012), Barling (2001)
BC25	BS25-1	13-17	2164	0.04	0.01	2.40	0.18	Weyer (2008)	Arnold (2012)
BC43	BS43-1	10-17	1861	0.09	0.06	2.33	0.18	Weyer (2008)	Arnold (2012)
BC43	BS43-2	20-26	1861	0.00	0.06	2.48	0.18	Weyer (2008)	Arnold (2012)
BC55	BS55-4	8-12	2164	0.07	0.10	2.48	0.18	Weyer (2008)	Arnold (2012)
				Black Sea Uni II					
BC25	BS25-2	32-40	2164	0.22	0.10	1.76	0.11	Weyer (2008)	Barling (2001)
25GC1	BS30	62	418	0.33	0.30	1.56	0.16	Montoya-Pino (2010)	Montoya-Pino (2011)
25GC1	BS35	67	418	0.43	0.30	1.51	0.00	Montoya-Pino (2011)	Montoya-Pino (2011)
25GC1	BS40	72	418	0.44	0.30	1.49	0.16	Montoya-Pino (2010)	Montoya-Pino (2011)

core	sample name	sample depth / cm	water depth / m	δ²³⁸U authi. / ‰	2 s.d. δ²³⁸U / ‰	δ⁹⁸Mo authi. / ‰	2 s.d. δ⁹⁸Mo / ‰	δ²³⁸U ref.	δ⁹⁸Mo ref.
25GC1	BS45	77	418	0.00	0.30	1.34	0.16	Montoya-Pino (2010)	Montoya-Pino (2011)
25GC1	BS50	82	418	0.15	0.30	1.51	0.16	Montoya-Pino (2010)	Montoya-Pino (2011)

The figures (S1 to S9) show possible correlations between δ⁹⁸Mo and δ²³⁸U as well as Mo and U versus TOC contents, respectively. Here, only correlation coefficients are shown that are statistically significant (Section S6).
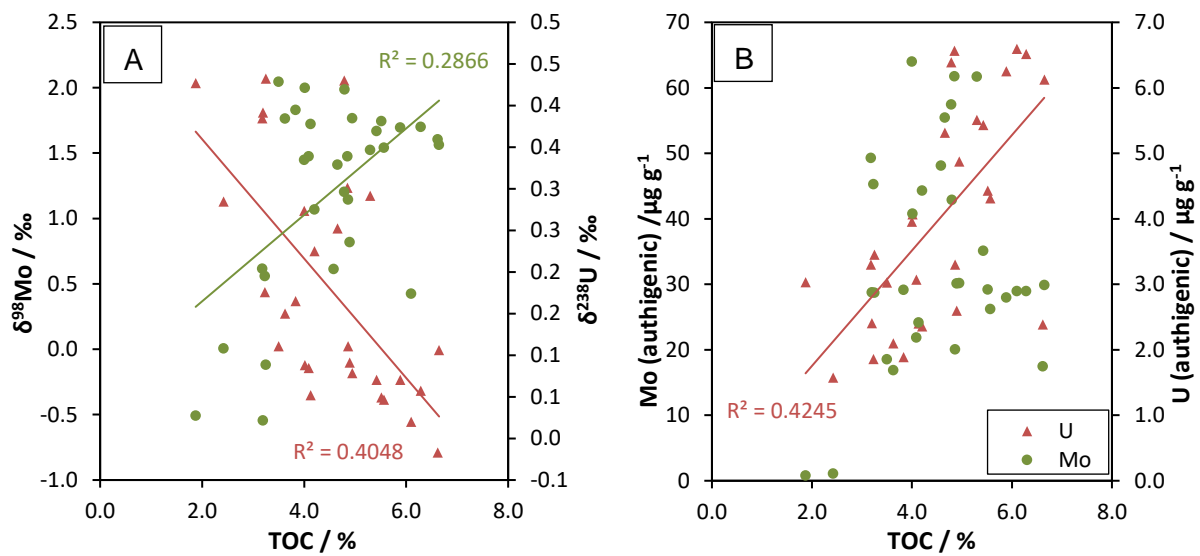
Figure S1: Crossplots of A: δ⁹⁸Mo (NIST-3134+0.25 ‰) and δ²³⁸U (CRM112A) vs. TOC contents and B: Mo and U contents vs. TOC content in surface sediment samples from the Black Sea from 0.5 cm and 1.5 cm depth below seafloor, circles represent Mo values and triangles U values. Error bars depict 2 s.d. values for triplicate isotope measurements.
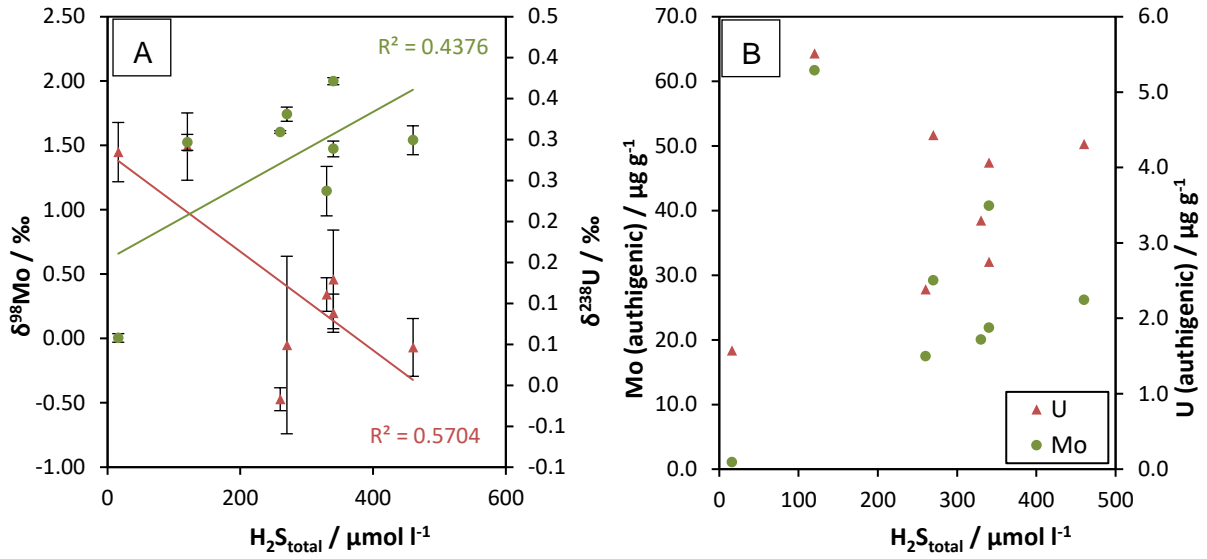
Figure S2: Crossplots of A: δ⁹⁸Mo (NIST-3134+0.25 ‰) and δ²³⁸U (CRM112A) vs. H₂S contents and B: Mo and U contents vs. H₂S concentration in surface sediment samples from the Black Sea from 0.5 cm depth below seafloor, circles represent Mo values and triangles U values. Error bars depict 2 s.d. calculated from triplicate isotope measurements.
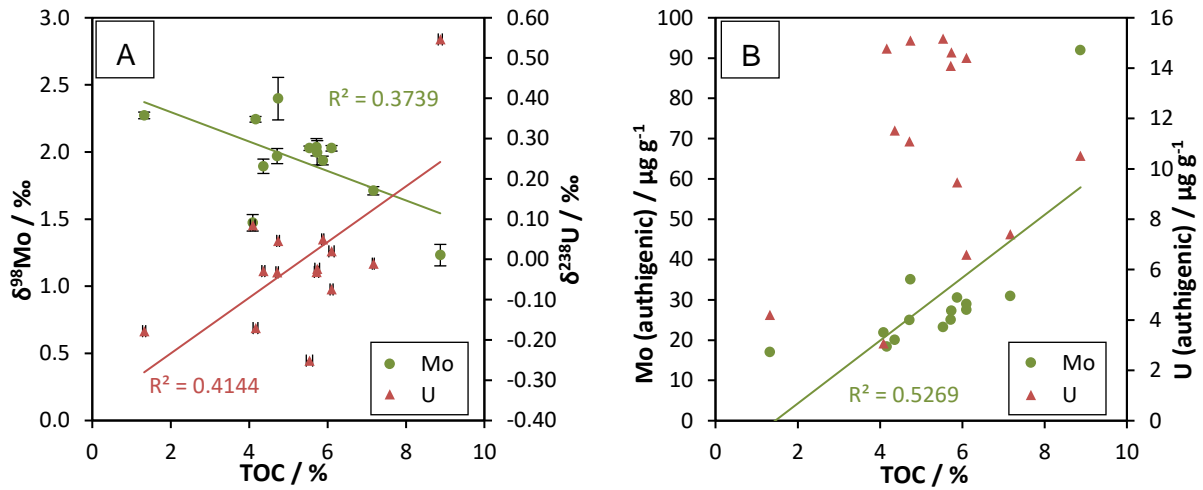
Figure S3: Correlation plots of A: δ⁹⁸Mo (NIST-3134+0.25 ‰) and δ²³⁸U (CRM112A) vs. TOC and B: Mo and U contents vs. TOC in the Black Sea core 32MUC24. Circles represent Mo values and triangles belong to U values. Error bars depict 2 s.d. values for triplicate isotope measurements.
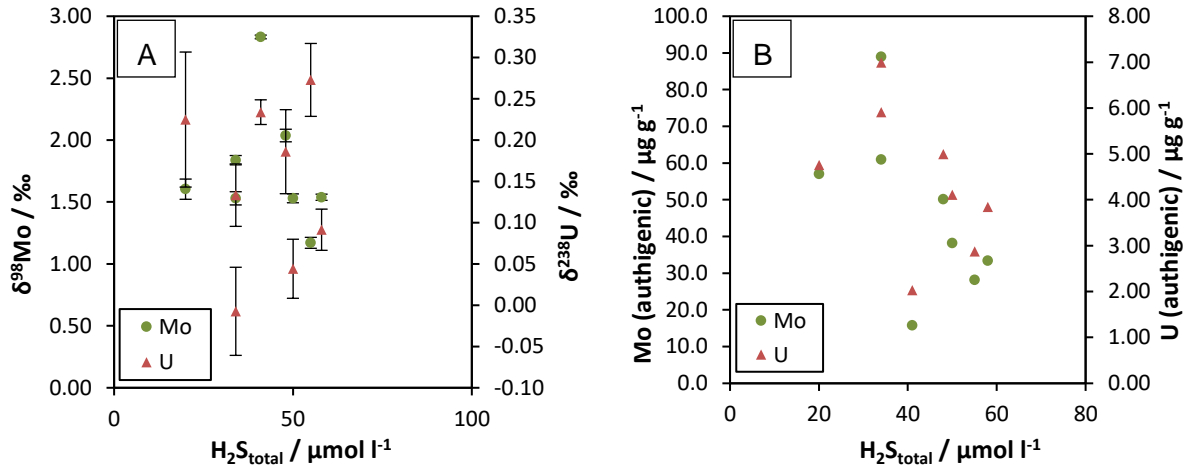
Figure S4: Crossplots of A: δ⁹⁸Mo (NIST-3134+0.25 ‰) and δ²³⁸U (CRM112A) vs. H₂Saq and B: Mo and U contents vs. H₂Saq concentrations in surface sediments from the Cariaco Basin, in A and B: circles represent Mo values and triangles belong to U values. Error bars depict 2 s.d. values for triplicate isotope measurements.
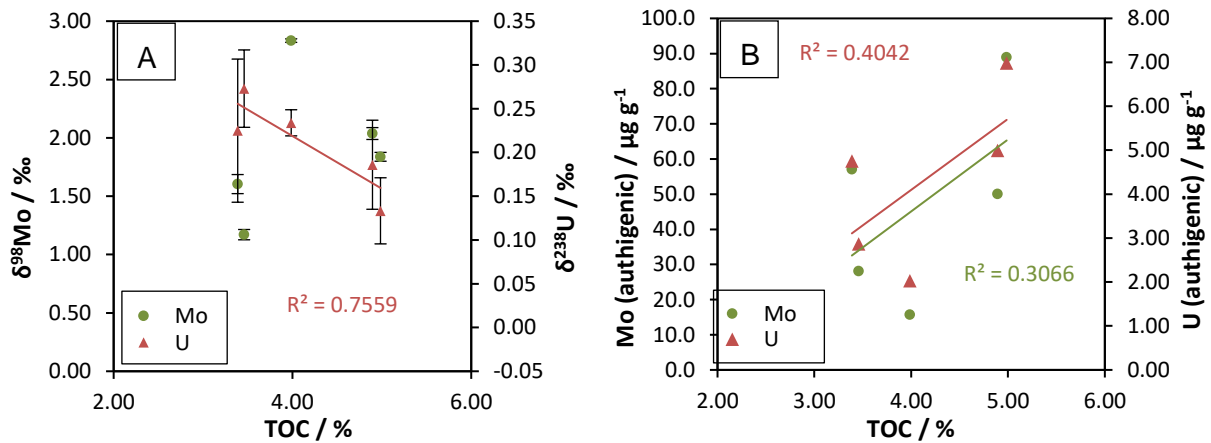
Figure S5: Crossplots of A: δ⁹⁸Mo (NIST-3134+0.25 ‰) and δ²³⁸U (CRM112A) vs. TOC and B: U and Mo contents vs. TOC in core top surface sediments from the Cariaco Basin. Circles represent Mo values and triangles belong to U values. Error bars depict 2 s.d. values for triplicate isotope measurements.
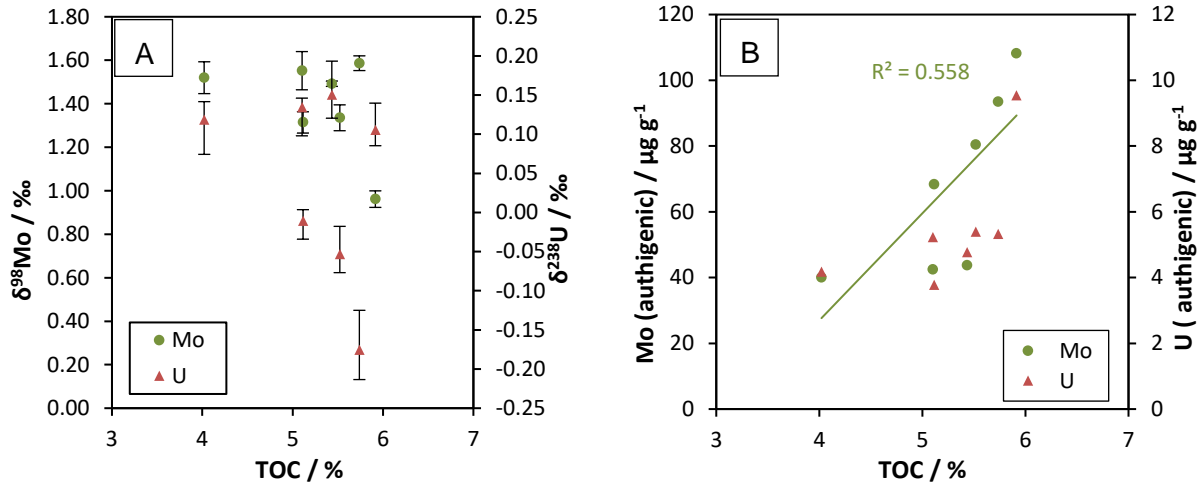
Figure S6: Correlation plots of A: δ^{98}Mo (NIST-3134+0.25 ‰) and δ^{238}U (CRM112A) vs. TOC and B: U and Mo contents vs. TOC in sediments from the 12GGC core from the Cariaco Basin. Circles represent Mo values and triangles belong to U values. Error bars depict 2 s.d. values for triplicate isotope measurements.
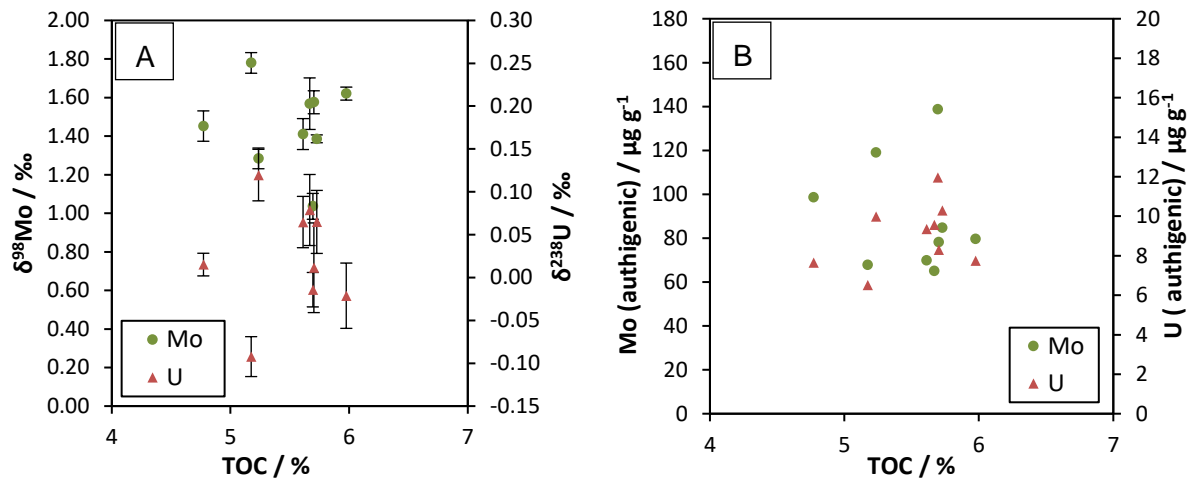
Figure S7: Correlation plots of A: δ^{98}Mo (NIST-3134+0.25 ‰) and δ^{238}U (CRM112A) vs. TOC and B: U and Mo contents vs. TOC in sediments from the 70GGC core from the Cariaco Basin. Circles represent Mo values and triangles belong to U values. Error bars depict 2 s.d. values for triplicate isotope measurements.
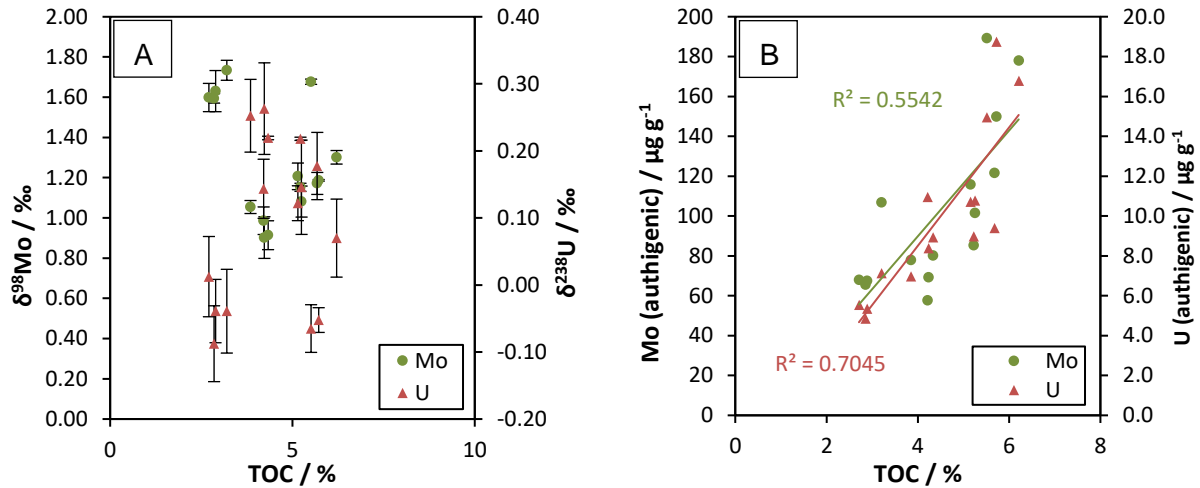
Figure S8: Correlation plots of A: δ⁹⁸Mo (NIST-3134+0.25 ‰) and δ²³⁸U (CRM112A) vs. TOC and B: U and Mo contents vs. TOC in sediments from core 1002B (leg 165) from the Cariaco Basin. Circles represent Mo values and triangles belong to U values. Error bars depict 2 s.d. values for triplicate isotope measurements.
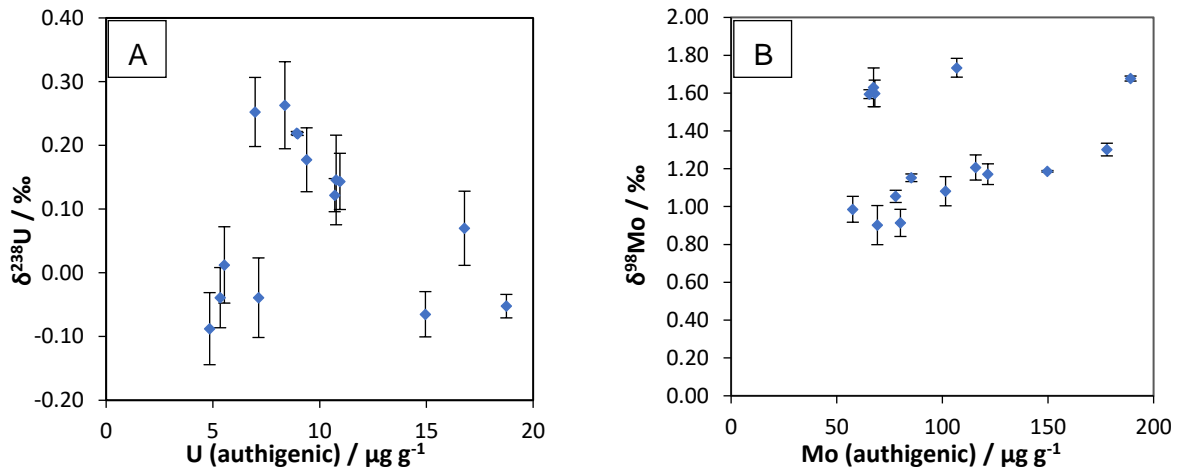

Figure S9: Correlation plots of A: δ²³⁸U (CRM112A) vs. U contents and B: δ⁹⁸Mo (NIST-3134+0.25 ‰) vs. Mo contents in sediments from core 1002B (leg 165) from the Cariaco Basin. Error bars depict 2 s.d. values for triplicate measurements.

S 6. Calculation of significance of correlation coefficients

To mathematically validate any correlations between two parameters, the smallest significant correlation coefficient $\acute{r}^2$ was calculated according to $\acute{r}^2 = \left(\dfrac{t_{\phi;\alpha/2}}{\sqrt{n-2+t_{\phi;\alpha/2}^2}} \right)^2$ using the student-t distribution at a significance level of 97.5 %. This coefficient was compared to the coefficient of determination R^2 (from Excel) in supplementary table S13. If $\acute{r}^2 < R^2$ the correlation is

mathematically significant, however, these coefficients do not necessarily result from causality but must be scientifically proven.

Table S13: Calculation of coefficients of determination.

Sample set	Parameter x	Parameter y	ṙ	R^2 (Excel)
Black Sea 0.5 cm depth	δ^{98}Mo	δ^{238}U	0.2641	0.4782
Black Sea 1.5 cm depth	δ^{98}Mo	δ^{238}U	0.2835	0.5571
Black Sea 0.5 cm depth	[U]	[Mo]	0.2641	0.2994
Black Sea 1.5 cm depth	[U]	[Mo]	0.2835	0.1876
Black Sea 0.5 and 1.5 cm depth	TOC	[Mo]	0.1260	0.0370
Black Sea 0.5 and 1.5 cm depth	TOC	[U]	0.1349	0.4245
Black Sea 0.5 and 1.5 cm depth	TOC	δ^{98}Mo	0.1260	0.2866
Black Sea 0.5 and 1.5 cm depth	TOC	δ^{238}U	0.1349	0.4048
Black Sea 0.5 cm depth	H_2S	[Mo]	0.4995	0.0075
Black Sea 0.5 cm depth	H_2S	[U]	0.4995	0.0694
Black Sea 0.5 cm depth	H_2S	δ^{98}Mo	0.4995	0.4376
Black Sea 0.5 cm depth	H_2S	δ^{238}U	0.4995	0.5704
Black Sea 32MUC24	δ^{98}Mo	δ^{238}U	0.2835	0.5558
Black Sea 32MUC24	TOC	[Mo]	0.2835	0.5269
Black Sea 32MUC24	TOC	[U]	0.2835	0.0604
Black Sea 32MUC24	TOC	δ^{98}Mo	0.3057	0.3739
Black Sea 32MUC24	TOC	δ^{238}U	0.2835	0.3924
Black Sea 32MUC24	[Mo]	[U]	0.4572	0.0011
Cariaco surface sediments	δ^{98}Mo	δ^{238}U	0.4995	0.0641
Cariaco surface sediments	[Mo]	[U]	0.4995	0.9462
Cariaco surface sediments	H_2S	[Mo]	0.4995	0.3187
Cariaco surface sediments	H_2S	[U]	0.4995	0.2151
Cariaco surface sediments	H_2S	δ^{98}Mo	0.4995	0.0304
Cariaco surface sediments	H_2S	δ^{238}U	0.4995	0.0011
Cariaco surface sediments	TOC	[Mo]	0.7714	0.3066
Cariaco surface sediments	TOC	[U]	0.7714	0.4042
Cariaco surface sediments	TOC	δ^{98}Mo	0.7714	0.1109
Cariaco surface sediments	TOC	δ^{238}U	0.7714	0.7559
Cariaco 12GGC 0-10 cm depth	δ^{98}Mo	δ^{238}U	0.3993	0.2722
Cariaco 12GGC 15-50 cm depth	δ^{98}Mo	δ^{238}U	0.4995	0.7810
Cariaco 12GGC 0-10 cm depth	TOC	[Mo]	0.3993	0.0509
Cariaco 12GGC 15-50 cm depth	TOC	[Mo]	0.4995	0.7565
Cariaco 12GGC	TOC	[Mo]	0.5280	0.5580
Cariaco 12GGC	TOC	[U]	0.5280	0.3717
Cariaco 12GGC	TOC	δ^{98}Mo	0.5280	0.1933
Cariaco 12GGC	TOC	δ^{238}U	0.5280	0.1382
Cariaco 70GGC 0-10 cm depth	δ^{98}Mo	δ^{238}U	0.3625	0.0275
Cariaco 70GGC 15-50 cm depth	δ^{98}Mo	δ^{238}U	0.6583	0.9682
Cariaco 70GGC	[Mo]	[U]	0.2289	0.7006
Cariaco 70GGC	TOC	[Mo]	0.4441	0.0261
Cariaco 70GGC	TOC	[U]	0.4441	0.1337
Cariaco 70GGC	TOC	δ^{98}Mo	0.4441	0.0036
Cariaco 70GGC	TOC	δ^{238}U	0.4441	0.0031
Cariaco 1002B	δ^{98}Mo	δ^{238}U	0.2614	0.7363
Cariaco 1002B	[Mo]	[U]	0.2614	0.6690
Cariaco 1002B	TOC	[Mo]	0.2614	0.5542
Cariaco 1002B	TOC	[U]	0.2614	0.7045
Cariaco 1002B	TOC	δ^{98}Mo	0.2614	0.1662
Cariaco 1002B	TOC	δ^{238}U	0.2614	0.0621
Cariaco > 10 cm bsf	δ^{98}Mo	δ^{238}U	0.1629	0.3913
Black Sea > 3 cm depth	δ^{98}Mo	δ^{238}U	0.1303	0.5795

Chapter IV:

The onset of oxidative weathering traced by

uranium isotopes

A. Neddermeyer[a*], P. Rammensee[b], S. Eroglu[c], A. Martin[a], M. Lazarov[a], G. Albut[c], S. Schuth[a], S. Aulbach[b], R. Schoenberg[c], N. Beukes[d], A. Hofmann[d], T. Nägler[e] & S. Weyer[a]

[a]Leibniz University Hannover, Institute of Mineralogy, Germany

[b]Goethe-University Frankfurt, Institute of Geosciences, Germany

[c]University Tübingen, Dept. of Geosciences, Germany

[d]University of Johannesburg, DST-NRF CIMERA, Dept. of Geology, South Africa

[e]University of Bern, Institute of Geological Sciences, Switzerland

Abstract

The invention of photosynthesis was a key moment in Earth's history, initiating major changes in the evolution of the oceans and atmosphere. An increasing number of studies provide evidence that enhanced oxygen levels already existed before the Paleoproterozoic Great Oxidation Event (GOE, 2.45 Ga to 2.32 Ga). However, the onset of photosynthetic oxygenation, as well as spatial and temporal fluctuations of atmospheric and oceanic oxygen levels are highly debated. Here, we present U isotope data from black shales, carbonates and iron-rich sedimentary rocks from the Hamersley Basin (Western Australia), Kaapvaal (South Africa) and Zimbabwe Cratons ranging in depositional ages from 3.2 to 2.2 Ga. Sub-recent U mobilization was monitored by simultaneous analyses of $\delta^{234}U$, and detrital contribution was monitored with [Al]/[U] or [Th]/[U] ratios. Samples with significant authigenic U enrichment ($EF_U > 2$, relative to post-Archean Australian Shale) show variations in authigenic $\delta^{238}U$ ranging from -0.96 to -0.02 ‰, which significantly deviates from typical $\delta^{238}U$ of the continental crust (-0.4 to -0.2 ‰). Remarkably, we observed a significant increase in $\delta^{238}U$ variability in the upper Ghaap group (2.47 – 2.64 Ga) toward samples from the lower Pretoria Group (2.42 Ga, Duitschland formation), both from the Kaapvaal craton, South Africa. The predominantly light U isotope composition of the latter samples is best explained by U isotope fractionation related to the onset of partial U mobilization during oxidative weathering of uraninite, just before the GOE at around 2.5 Ga. Low $\delta^{238}U$ values were not observed in the Timeball Hill formation (overlying the Duitschland formation), deposited after the GOE, indicative of the onset of modern-style weathering of uraninite and other U-bearing minerals, with quantitative U mobilization, resulting in very limited U isotope fractionation. The very limited U isotope variations in the oceanic sediments furthermore imply, that the mobilized U was quantitatively reduced in the overall still rather anoxic oceans.

1. Introduction

The evolution of oxygen concentrations in the atmosphere and oceans on Earth shaped and likely was shaped by the evolution of life. However, the driving mechanisms and the timing are still highly debated (Anbar et al., 2007; Crowe et al., 2013; Lyons et al., 2014; Planavsky et al., 2014). The so-called Great Oxidation Event (GOE) is assumed to be the turning point in atmospheric oxygen evolution with a prominent change from overall anoxic to slightly oxic conditions, and began roughly between 2.45 Ga and 2.32 Ga (Bekker et al., 2004; Hannah et al., 2004; Luo et al., 2016; Gumsley et al., 2017). It was first indicated by the loss of detrital pyrite and uraninite grains in rocks younger than 2.22 Ga (Cloud, 1972; Johnson et al., 2014 and references therin). Further proof came from mass-independent sulfur isotope signatures (MIF), which disappeared after the GOE indicating $p(O_2) > 10^{-5}$ PAL (present atmospheric levels, Farquhar, 2000; Pavlov and Kasting, 2002; Bekker et al., 2004). Also the appearance of oxidized Fe^{3+} in redbeds and paleosols on land provide proof that oxygen was around inducing Fe immobilization and preventing Fe loss (Rye and Holland, 1998). However, it is not yet clear if O_2 levels changed progressively or erratic and their spatial and temporal variations remain poorly defined. Enhanced levels and characteristic isotope signatures of redox-sensitive metals (including e.g. Cr, Fe, Mo and U) in oceanic sediments, indicate that oxidative weathering and metal mobilization may significantly predate the GOE by several hundred Ma (Siebert et al., 2005; Anbar et al., 2007; Wille et al., 2007; Scott et al., 2008; Voegelin et al., 2010; Czaja et al., 2012; Crowe et al., 2013; Kendall et al., 2013; Partin et al., 2013a; Wille et al., 2013; Lyons et al., 2014; Eroglu et al., 2015; Kendall et al., 2015; Kurzweil et al., 2015; Satkoski et al., 2015; Frei et al., 2016; Kurzweil et al., 2016; Eroglu et al., 2017; Eroglu et al., 2018; Wang et al., 2018; Wille et al., 2018). It is, however, unclear whether metal mobilization was temporally and locally restricted or of global significance.

Redox-sensitive metals, for example Mo and U, show conservative behavior and very long ocean residence times under oxidizing conditions which result in their enrichment in present day oxidized oceans. In contrast, at the reducing conditions of the Archean atmosphere, they are assumed to have been poorly mobilized during weathering, resulting in low concentration levels in oceans and sediments. Traces of oxygen may have been sufficient to mobilize and transport those elements to the anoxic ocean, resulting in moderate enrichment in sediments above the lithologic background. This hypothesis relies on the fact that both Mo or U are bound in their tetravalent form in continental crust minerals (broadly speaking uraninite, UO_2 and molybdenite, MoS_2) and that these are affected by oxidative dissolution through release of oxidized hexavalent ions to the environment. This approach has been widely used to account for trace metal enrichment in Archean sediments (Anbar et al., 2007; Wille et al., 2007; Scott et al., 2008; Partin et al., 2013a).

Scott et al. (2008) investigated the authigenic Mo enrichment in sulfidic shales and found evidence for this process since 2.65 Ga. Strong Mo enrichment occurred since 2.15 Ga, roughly 200 - 300 Ma after the initial rise in atmospheric oxygen. A similar compilation for authigenic U enrichment has been published by Partin et al. (2013). These authors show that organic-rich shales deposited prior to 2.32 Ga do not show significant U enrichment and explain the data with anoxic surface conditions that result in low dissolved U concentrations in terrestrial and marine waters. These different onsets of Mo and U redox cycling may be related to their different sensitivity to oxygen concentrations during oxidative weathering.

Molybdenum's main host minerals in the Archean and present-day continental crust are not clearly identified as its behavior during igneous differentiation and crust formation is not precisely known. A recent study identifies volcanic glasses and weathering-resistant titaniferous phases to be main hosts of Mo in the upper Archean continental crust (basaltic, andesitic, and granitic rocks) in addition to molybdenite (MoS_2), whereas other sulfides are apparently only minor primary Mo hosts (Greaney et al., 2018). It is under debate, however, if molybdenite can account for the missing Mo phase from mass-balance calculations in Archean and modern continental crust, as it could not directly be detected in the samples by Greaney et al. (2018). Molybdenite is particularly sensitive to the oxygen levels during continental weathering and may be responsible for the release of Mo in the Archean followed by subsequent enrichment in marine sediments. Alternatively, sub-marine weathering of volcanic glasses should be considered as a possible source of Mo into Archean oceans as well (Greaney et al., 2018) where it was either immobilized with S or accumulated in the ocean until enough reductants were available. Only few constraints on the sensitivity of molybdenite to oxygen are available, however, Greber et al. (2015) experimentally predict oxygen levels of 5.4×10^{-5} atm to 9.6×10^{-5} atm for oxidative dissolution of molybdenite (translates into 2.6 to 4.6×10^{-4} of the present atmospheric level (PAL)).

In contrast, U was mainly hosted in uraninite (ideally UO_2) in the Archean continental crust (Hazen et al., 2009) and uraninite has been shown to be stable until oxygen levels of 3.2×10^{-5} atm in a conservative model approach under combined chemical and physical weathering (Johnson et al., 2014), i.e. similar to slightly lower than those values required for molybdenite. However, it remains difficult to identify the secular distribution of uraninite and its general sensitivity to combined physical and chemical weathering as weathering of detrital mineral grains depends on provenance, climate, transportation, lithologic background, and secondary alteration (Rasmussen and Buick, 1999) and cannot be easily modeled nor easily experimentally constrained. Hence, a direct comparison of the Mo and U sensitivity to oxygen is complicated based on the few data available from modelling and experiments.

Recently, the isotope fractionation of redox-sensitive trace metals has emerged to be an additional powerful proxy to define the oxygen evolution on Earth in combination with

authigenic enrichments. Molybdenum isotopes have been used as one of the first isotope proxies in addition to the authigenic Mo enrichment in Archean sediments (Siebert et al., 2005; Wille et al., 2007; Duan et al., 2010; Voegelin et al., 2010; Czaja et al., 2012; Wille et al., 2013; Planavsky et al., 2014). These isotope results compare very well with the observation of Mo enrichment, that before ~2.7 Ga no Mo geochemical redox cycling occurred (Fig. 4 in Wille et al., 2013 and Fig. 5 in Duan et al., 2010).

Uranium isotopes have been analyzed in Archean sediments by Kendall et al. (2013) and Wang et al. (2018) to define the onset of oxidative geochemical U cycling. Kendall et al. (2013) showed that U isotopes were fractionated towards heavier δ^{238}U values in a distinct unit of the 2.5 Ga old Mt. McRae black shales from Western Australia, going along with significant enrichment in Mo-, although not in U concentrations (Anbar et al., 2007). These observations were explained by either oxidative weathering in an oxygen lagoon and subsequent partial reduction in anoxic deep ocean water or by a shift of δ^{238}U in the water column by preferential adsorption of light U isotopes elsewhere in the ocean. Wang et al. (2018) even pinpoint the onset of oxidative weathering of U minerals to 3.0 Ga by analyzing U isotope signatures in iron-rich formations, organic rich shales and paleosols from various ages and formations around the globe. The principal idea behind both studies is that oxidative weathering of U minerals at a certain oxygen concentration either in the atmosphere or in shallow water would mobilize U that could be partially reduced and thus isotopically fractionated in anoxic deep oceans. To date, the U isotope signature of detrital Archean uraninite is not known which the source for mobilized U in the Archean environment would be. Analyses of a wide range of granitic and basaltic crustal rocks throughout Earth's history show rather homogenous U isotope signatures of -0.29 ± 0.03 ‰ (Tissot and Dauphas, 2015; Noordmann et al., 2016), indicating that δ^{238}U of Archean uraninite is likely well represented by that of the average continental crust.

In this study, we analyzed black shales, carbonates, and iron-rich sediments from the Archean and Proterozoic crossing the GOE. We focus specifically on the time period before the GOE to gain a better understanding of local or global processes and environmental changes that induced first U isotope fractionation. Therefore, we chose mainly drill core samples that show low alteration grades and select samples carefully based on their authigenic U enrichment. We use samples from the meso-Archean as references to compare with younger deposited units.

2. The U isotope proxy

In this study, we use the fractionation of $^{238}U/^{235}U$ to identify and better constrain the onset of oxidative geochemical U cycling. $^{234}U/^{238}U$ ratios were also analyzed, using deviations from the secular equilibrium (Cheng et al., 2000) as an indicator for sub-recent U mobilization. Naturally, U occurs in three oxidation states, U^{IV}, U^{V} and U^{VI}, however, U^{V} disproportionates quickly and is therefore uncommon in nature (Renshaw et al., 2005). Under ambient aqueous conditions U mainly occurs as uranyl cation (UO_2^{2+}) which preferably forms carbonate complexes (e.g. $((UO_2)(CO_3)_3)^{4-}$) and has a long ocean residence time of 320 - 560 ky (Ku et al., 1977; Dunk et al., 2002). In general, the redox-sensitivity of U results in isotopic offsets between oxidized and reduced reservoirs. Oxidized ambient seawater shows a very homogenous signature of -0.4 ‰ (Stirling et al., 2007; Weyer et al., 2008; Tissot and Dauphas, 2015; Rolison et al., 2017).

Under reducing conditions, U^{VI} is reduced to U^{IV} that forms solid uraninite (UO_2, U_3O_7, U_3O_8). Uranium reduction is thought to take place mainly in the sediment porewater rather than in the water column (Anderson et al., 1989; Klinkhammer and Palmer, 1991; Algeo and Tribovillard, 2009) and may be catalyzed by enzymes from iron or sulfate reducing bacteria. Uranium has two primordial isotopes with highly different abundances; ^{238}U with 99.28 % and ^{235}U with 0.71 %. The isotope ^{234}U is a decay product of ^{238}U that also occurs in nature in very low abundances (0.0054 %, Berglund and Wieser, 2011 and Cheng et al., 2013). Due to alpha-recoil processes during the decay of ^{238}U to ^{234}U, the crystal lattice in minerals can be damaged. This process results in preferential mobilization of loosely bound ^{234}U and fractionation of the $^{234}U/^{238}U$ ratio from secular equilibrium (atomic $^{234}U/^{238}U_{sec.eq.} = 54.891*10^{-6} \pm 0.094*10^{-6}$; Cheng et al. (2000). Thus, precise measurements of $^{234}U/^{238}U$ may be used to track weathering processes, in order to reject respective samples for paleo-redox studies (Andersen et al., 2004; Stirling et al., 2007; Andersen et al., 2014). The volume-dependent fractionation of ^{238}U and ^{235}U leads to the enrichment of the heavy isotope ^{238}U in U^{IV} species relative to U^{VI} species during reduction processes, as archived e.g. by black shales (Stirling et al., 2007; Weyer et al., 2008). During U^{IV} oxidation isotopic fractionation between U^{IV} and U^{VI} only occurs when both species are equilibrium, e.g. in acidic solution. In this case, U^{VI} is depleted in ^{238}U, similar to U reduction (Wang et al., 2015). However, during mobilization of solid U^{IV}, i.e. uraninite, under excess oxygen only minor isotope fractionation occurs, likely as the result of a "rind effect", i.e. quantitative layer-by-layer dissolution of the uranniite grains (Wang et al., 2015). The observed shift in dissolved $\delta^{238}U$ even towards slightly heavier values may have been the result of preferential adsorption of ^{235}U. Apart from redox-driven processes, U isotopes fractionate only minor during adsorption onto oxides which has been shown by experimental and natural studies revealing that oxides preferably take the light isotopes, resulting in ~0.2 ‰ isotope fractionation (Stirling et al., 2007; Weyer et al., 2008; Gregory A. Brennecka et al., 2011; Goto et al., 2014; Wang et al., 2016).

3. Sample description

In this study shales and carbonate rock samples from different drill cores and outcrops from South Africa, Zimbabwe, and Western Australia were analyzed (Figure 1 and table 1). The samples originate from the DP-16 (shales) and KMF-5 cores (shales and carbonates from the main and diversion core, respectively) from the Transvaal Basin (South Africa) that expose the Pretoria and Chuniespoort groups (~2.22 Ga to ~2.55 Ga; for detailed lithostratigraphic description and geochemical data of KMF-5 diversion core see Eroglu et al., 2015 and Eroglu et al., 2017). Additionally, BH-1 core carbonate rocks from the Ghaap group were analyzed as well as GKP-01 core samples, which consist of carbonates and black shales from the Ghaap group (~2.47 Ga to ~2.7 Ga; for BH-1 additional geochemical data see Eroglu et al., 2015 and Eroglu et al., 2018; for geochemical data about GKP-01 see Schröder et al., 2006, Wille et al., 2007, Voegelin et al., 2010, and Czaja et al., 2012). An outcrop black shale sample from the Black Reef group (~2.5 Ga, Kaapvaal craton) was analyzed as well (Siebert et al., 2005). A black shale sample from the Ngezi group (~2.7 Ga), Zimbabwe craton, was analyzed (Nercmar core). From the core PDP-1 (~2.72 Ga), Fortescue group in the Hamersley Basin in Western Australia, stromatolitic limestones were analyzed (see also Thomazo et al., 2009 and Thomazo et al., 2011). From cores BARB-3 and BARB-5 (~3.22 to ~3.44 Ga; Kaapvaal craton, Barberton Greenstone Belt) black shales and Fe-rich sediments from the Fig Tree and Onverwacht groups were analyzed (for additional geochemical data see Rammensee, 2016). Apart from drill cores, different outcrop samples from the Moodies and Fig Tree groups from the Barberton Greenstone Belt were anlyzed as well (~3.15 to ~3.23 Ga; for additional geochemical data see Siebert et al., 2005 and Wille et al., 2007). These samples comprise black shales and cherts, siltstone and banded iron formations. Further information about the lithology and stratigraphy can be found in the supplementary section S 2.

Table 1: Summary of all sampled areas, SA=South Africa, ZB=Zimbabwe, WA=Western Australia.

Sampling area	Super-group	Group	Age / Ga	Core / Origin	Lithology	References about stratigraphy
Transvaal Basin (SA)	Transvaal	Pretoria	2.22 – 2.42	DP-16, KMF-5	Black shale, siltstone	This study, supplementary S 2
Transvaal Basin (SA)	Transvaal	Chunies-poort	2.43 – 2.55	KMF-5	Carbonate	(Eroglu et al., 2015)
Transvaal Basin (SA)	Transvaal	Black Reef	2.5	outcrop	Black shale	(Siebert et al., 2005)
Griqualand West Basin (SA)	Transvaal	Ghaap, Black Reef	2.47 – 2.64	GKP-01, BH-1	Black shale, carbonate	(Voegelin et al., 2010; Czaja et al., 2012; Eroglu et al., 2017)
Zimbabwe craton (ZB)	Belingwe	Ngezi	2.7	Nercmar core	Black shale	(Siebert et al., 2005; Wille et al., 2007)
Hamersley Basin (WA)	Pilbara	Fortescue	2.72	PDP-1	Stromatolitic limestone	(Thomazo et al., 2009; Thomazo et al., 2011; Hickman and Van Kranendonk, 2012)
Barberton Greenstone Belt (SA)	Barberton	Moodies, Fig Tree, Onverwacht	3.15 – 3.44	Outcrop, mines, BARB-3, BARB-5	Black shale, BIF, siltstone, carbonate	(Hofmann, 2005; Siebert et al., 2005; Lowe and Byerly, 2007; Wille et al., 2007; Rammensee, 2016)
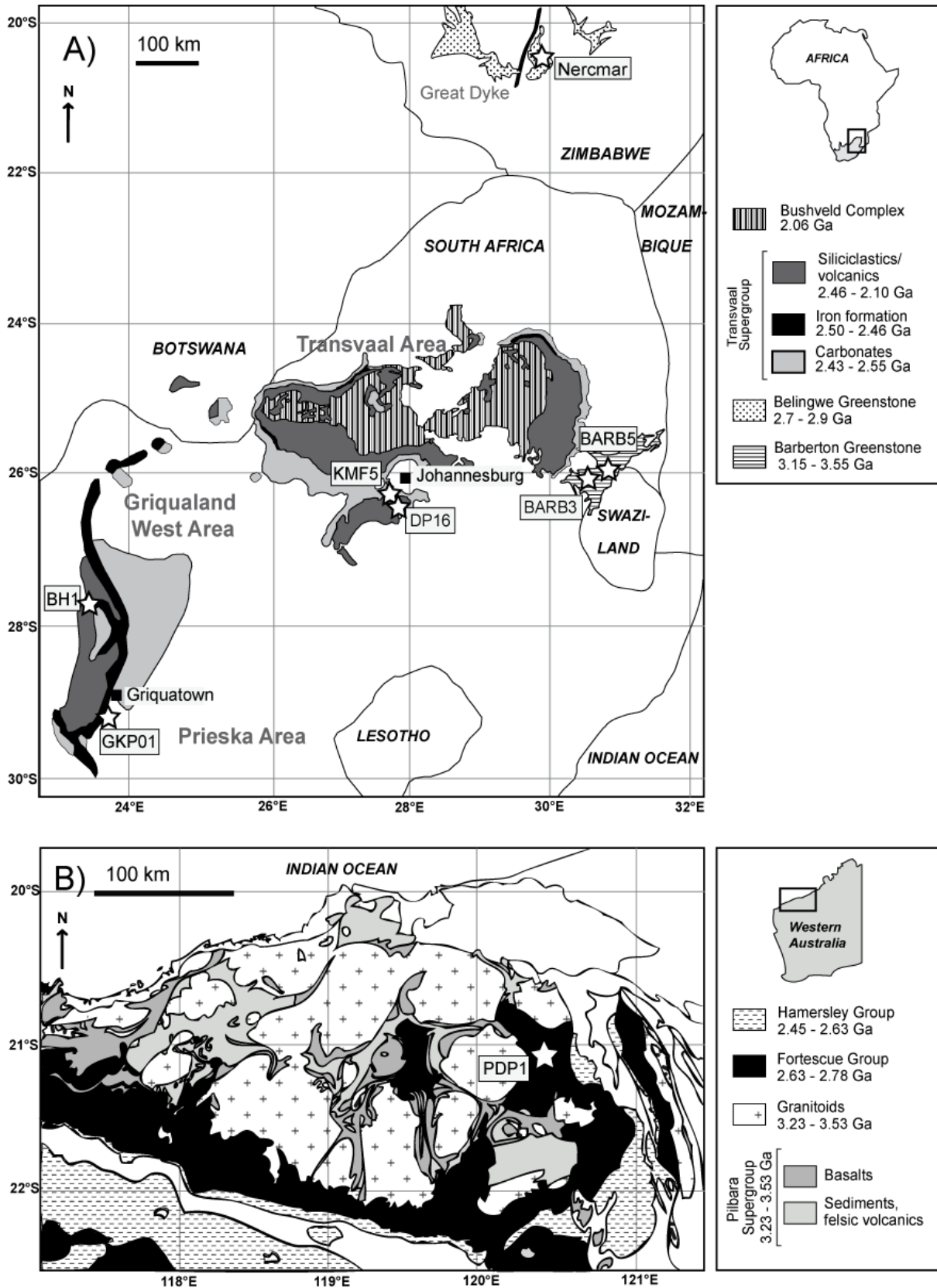
Figure 1: Geological map of sampling positions of drillcores in A) South Africa and Zimbabwe, and B) Western Australia. Modified from Thomazo et al. (2009) and Eroglu et al. (2017). Drilled cores are highlighted with asterisks and labelled with names.

4. Analytical Methods

4.1 Sample preparation

Samples from drillcores BARB-3 and BARB-5 were prepared at Goethe-University Frankfurt. The data is published in Rammensee (2016). Between 1 – 2 g of sample powder was ashed for 8 h at 550 °C (determine loss on ignition, LOI). Samples were digested as bulk rocks and additionally mildly leached to check whether this method appropriately dissolves the authigenic U fractions (see supplementary chapter S 1 for comparison of both methods). Both methods were applied to the certified reference materials SDO-1 and SBC-1 and some samples. For bulk digestion, around 100 mg of ashed sample powder was digested with 3 ml 28 M HF and 4 ml 15 $MHNO_3$ in a 15 ml PFA vial with screw cap at 180 °C on a hot plate for at least 2 days while being jacketed with Al foil to minimize the temperature gradient from PFA bottom to top. After the first day, the vial was opened to decrease internal pressure and 100 – 200 µl $HClO_4$ was added. The mixture was evaporated slowly at 140 °C for 4 h to ensure complete dryness of the whole vial before proceeding. Then, 2 ml 15 M HNO_3 was added, the vial was closed, and heated at 140 °C for one day. To destroy fluorides, the solution was evaporated gently and taken up in 2 ml 10 M HCl. This solution was evaporated to complete dryness again and re-dissolved in weighed 4 ml 6 $MHNO_3$ for trace element and U isotope analyses. The leaching method was processed according to Xu et al. (2012). Thus, ~1 g of non-ashed sample was mixed with 2 ml 10 M HCl, shaken, and sonicated for 10 minutes in a 15 ml PP centrifuge vial. After resting 20 minutes, 5 ml of 14 $MHNO_3$ was added. The closed vials were placed in a ca. 85 °C hot water bath for 150 minutes. The supernatant was then transferred to a 15 ml PFA vial and dried at 120 °C. The samples were re-dissolved in weighed 4 ml 6 M HCl for trace element and U isotope analyses.

Samples from drillcores of DP-16, BH-1, and lower KMF-5 (Chuniespoort group) were prepared at University of Tübingen for major and trace element analyses with X-ray fluorescence analyses (XRF). KMF-5 and BH-1 major and trace element data is published in Eroglu et al. (2015). Roughly 1 to 2 cm thick homogeneous sections were cut, crushed and powdered with avoiding secondary veins. Samples were ground with a tungsten carbide mill for 3 min. Loss on ignition (LOI) was determined at 1000 °C. For the fused beads 1.5 g of dried sample powder (at 105 °C) was mixed with 7.5 g MERCK spectromelt A12 (mixture of 66 % Li-tetraborate and 34 % Li-metaborate) and melted at 1200 °C to fused beads using an Oxiflux system from CBR analytical service.

Samples from drillcores of upper KMF-5 (Pretoria group), GKP-01, Nercmar, and all outcrop samples were prepared at Leibniz University Hannover for complementary trace metal measurements and U isotope analyses (also BH-1, DP-16, and lower KMF-5 samples). Rock samples were crushed and, for total digestion, were weighed into ceramic crucibles and ashed.

Carbonate powders were oxidized at 750 °C and other sediments at ~500 °C each for 8 - 10 hours to destroy any volatiles and organics (determine loss on ignition, LOI). Between 50 mg and 250 mg of ashed black shales were weighed in Savillex® PFA screw top beakers for dissolution. The certified black shale reference material SDO-1 was processed in several batches as well. Black shale digestion followed a multi-acid approach beginning with 6 M HCl for 24 h at 140 °C, then evaporating the solution. 6 ml of a 1:1 mixture of HNO_3 (65 %) and HF (40 %) were added afterwards and heated at 140 °C for 5 to 6 days. After evaporating this solution again, 6 ml of a 3:1 mixture of HCl (37 %) and HNO_3 (65 %) were added and heated at 140 °C for 24 h. This solution was again evaporated and 5 ml HNO_3 (3 N) were added gravimetrically. After heating this solution to 120 °C for a few hours all samples were completely dissolved. These solutions were split for concentration and isotope measurements of U isotopes. The carbonate rock standard materials JDo-1 and JLs-1 were processed to test carbonate leaching approaches and different ashing temperatures (see supplementary chapter S 1 for detailed method testing results) to assure reproducibility and recovery of authigenic U. Between 1 g and 2 g of carbonate powder of all samples from cores KMF-5, BH-1, and GKP-01 as well as three samples from PDP-1 were weighed into centrifuge tubes to leach the authigenic U fraction. Therefore, 40 g of 3 M HNO_3 was added gravimetrically. All tubes were left open overnight, then closed and shook in a shaker for ~7 hours and then centrifuged at 4500 rpm for 15 minutes. The supernatant was diluted further to be measured concerning U concentrations and following U isotope analyses.

All carbonate samples from core PDP-1 were analyzed at Leibniz University of Hannover as whole-rocks for U isotope analyses and for comparison with results from leached samples. For whole-rock digestion for U isotope analyses, between 1 g and 2 g of powder was weighed in Savillex® teflon screw top beakers and after that 20 - 30 ml of 6 M HCl was added. The supernatant was removed, and the residual solids were treated with a 1:1 mixture of HNO_3 (65 %) and HF (40 %). After evaporating this solution, the supernatant HCl solution was given back into the beaker. After that, some drops of a 1:1 mixture of HNO_3 (65 %) and H_2O_2 (30 %) were added. These solutions were heated over night at 100°C and then evaporated. Finally, the samples were re-dissolved in ~20 ml 3 M HNO_3 for U isotope measurements. For trace metal analyses of these samples, approximately 100 mg of ashed powder was weighed into PFA beakers. The acid-soluble fraction was first removed by the addition of 4 ml 1.5 M HNO_3 and heating at 80°C for 6 h. The aqueous phase was then removed by centrifugation and stored in a centrifuge tube for later use. To dissolve the remaining solid phase, 0.5 ml HNO_3 (65 %) and 2 ml HF (40 %) were added and heated at 120°C overnight. These solutions were then evaporated at 100°C. To ensure complete dissolution of the solid phase, 0.5 ml HNO_3 (65 %) and 1.5 ml HCl (37 %, aqua regia) were added and heated overnight at 120°C. The solutions were then evaporated at 100°C. The 1.5 M HNO_3 solution removed during the first

step was then added to the solid residues and evaporated at 100°C. Finally, 0.1 ml HNO_3 (65 %) was added to the solid residues and evaporated at 100°C until the solid residue reached incipient dryness. The solid residue was then re-dissolved in 3 % HNO_3 for ICP-MS analyses.

4.2 Major and trace element analyses

Trace element concentrations of drillcores BARB-3 and BARB-5 were measured on a Thermo Fisher Scientific ELEMENT 2 ICP-MS at the Goethe-University Frankfurt (Rammensee, 2016). Sample uptake was done with a 100 μl PFA nebulizer attached to a glass spray chamber and machine settings were tuned for maximum sensitivity with an UO formation rate of 3 – 5 %. Samples were diluted in 2 % HNO_3 and doped with 10 ng g^{-1} Indium as internal standard. A mixed plasma standard solution was produced from AAS plasma standard multi and single solutions with concentration of 10 μg g^{-1} Mg and 1 μg g^{-1} (all other elements), gravimetrically. Each measurement session, an aliquot of this solution was diluted by 1:100, 1:1000 and 1:10,000 doped with Indium in 2 % HNO_3 and was measured repeatedly in between 4 to 5 samples following a blank in 2 % HNO_3 solution for external calibration. In each session, a reference standard material (digested in the same way than the samples) was repeatedly measured. Within-run uncertainties of individual elements usually are lower than 5 % rsd. Full procedural blank was in average lower than 0.01 of sample concentrations. USGS Reference sample materials (SDO-1 and SBC-1) have been digested, diluted 1:4,000 and 1:9,000, measured and quantified against the plasma standard multi element solutions. Within error, the results were mostly identical and fit well to the published recommended values. Thus, all samples have been diluted 1:5,000 and each analytical session SDO-1 or SBC-1 was measured repeatedly.

Wavelength dispersive X-ray fluorescence analyses (XRF) at University of Tübingen were performed on the Bruker AXS S4 Pioneer spectrometer (Rh-tube at 4 kW) of the Isotope Geochemistry Group, University of Tübingen, with 32 standardized samples (Potts and Webb, 1992). Core DP-16 data can be found in supplementary table S 6. Analytical error and detection limits vary and depend on element and sample composition uncertainties. Generally, uncertainties for all major elements are better than 1 % (1SD) and for trace elements better than 5 % (1SD). The used international standards are compiled in Govindaraju (1989).

All concentration measurements in Hannover (samples from cores PDP-1, main KMF-5, GKP-01, nercmar, and outcrop samples from the BGB, see supplementary tables S 5, S 7 to S 9) were performed with a Thermo Fisher Scientific Element XR single-collector mass spectrometer (Noordmann et al., 2015) using Rhodium for internal standardization and applying a 5-point external calibration diluted from pure standard solutions in the range from 1 ng g^{-1} to 100 ng g^{-1}. Standard and sample solutions were diluted to yield 3 vol% HNO_3. All

concentration data was corrected for loss on ignition. The river water standard TMDA-51.3 was measured repeatedly to check in-house accuracy and precision. The certified Devonian Ohio shale SDO-1 was processed and measured for comparison. Isotopes that were out of the certified range of both reference materials during a session were not taken for further evaluation of concentration data. Results and comparison with literature data for TMDA-51.4 and SDO-1 can be found in supplementary tables S 10 and S 11.

Enrichment factors were calculated for all samples according to $EF_U=([U]/[X]_{sample})/([U]/[X]_{PAAS})$ either with X = [Al] or [Th] using the $[U]/[Al]_{PAAS} = 0.11 \times 10^{-4}$ g g^{-1} or $[U]/[Th]_{PAAS} = 0.212$ g g^{-1} of post-Archean Australian Shale (PAAS, Taylor and McLennan, 1985) for all samples. The $[U]/[Al]_{PAAS}$ value is lower than present day upper crust and thus may reflect the lithogenic background of the analyzed samples well. The [U]/[Th] has not changed much over geologic times (Taylor and McLennan, 1985; Rudnick and Fountain, 1995; Rudnick and Gao, 2003; Cole et al., 2017). For bulk black shales or carbonates these values describe true enrichments in solid samples, whereas for leached carbonates these factors describe the ratio of U versus Al in leached samples. Consequently, in bulk carbonates the true EF_U would be lower because not all the bulk Al is leached compared to the authigenic U.

4.3 U isotope analyses

U isotope analyses followed the protocol of Noordmann et al., 2015 and Weyer et al., 2008. From all dissolved samples an aliquot of ~ 100 to 500 ng U was subsampled and equilibrated with the IRMM-3636a U double spike (Richter et al., 2008) prior to separating U from the remaining matrix by using Eichrom UTEVA resin (Weyer et al., 2008) or right before measuring the isotopes (only BARB-3 and BARB-5 samples). The purified U fraction was treated with a 1:1 solution of hydrogen peroxide (30 %) and HNO_3 (65 %) and was then diluted between ~30 ng g^{-1} and ~70 ng g^{-1} U with 3 vol % HNO_3 depending on the respective instrument tuning. All measurements were performed with the Thermo Fisher Scientific Neptune in Hannover at dry plasma conditions using a Cetac Aridus 2. Nickel H sampler and X skimmer cones were used. In detail, the ion beams of ^{233}U, ^{235}U and ^{236}U were measured on faraday detectors attached to 10^{11} Ω resistors and ^{238}U with a 10^{10} Ω resistor. The low abundant ^{234}U was measured on a 10^{12} Ω (BARB-3 and BARB-5 measurements) or a 10^{13} Ω resistor (all other samples). The 10^{13} Ω resistor resulted in a 1-sigma reproducibility of ~100 µg g^{-1} on the $^{234}U/^{238}U$. Abundance sensitivity of ^{238}U on ^{236}U was < 1 µg g^{-1} and thus negligible, however, was monitored throughout all sessions. An electronic baseline was measured each day and subtracted from all data. Isotope data was integrated each 4 s in 60 - 80 cycles resulting in a total data collection time of max. 5.33 minutes. An acid blank was measured every ~20 samples and those values were subtracted automatically during any sequence. Instrumental

mass bias was corrected using mass discrimination factors calculated from $^{233}U/^{236}U$ with the exponential law. All sequences were performed using a double standard-sample-bracketing method relative to a CRM-112A standard solution that matched the U concentration of samples within 10 %. Results for $\delta^{238}U$ are given in the delta notation relative to CRM-112A (eqn. 1). Results for $\delta^{234}U$ are given according to eqn. 2 relative to the secular equilibrium of $^{234}U/^{238}U = 54.891 \pm 0.094 *10^{-6}$ (2σ) (Cheng et al., 2000).

$$\delta^{238}U = \left[\left(\left(^{238}U/^{235}U\right)_{sample}/\left(^{238}U/^{235}U\right)_{CRM-112A}\right) - 1\right] * 1000 \ [‰] \qquad \text{Eqn. 1}$$

$$\delta^{234}U = \left[\left(\left(^{234}U/^{238}U\right)_{sample}/\left(^{234}U/^{238}U\right)_{sec.Eq.}\right) - 1\right] * 1000 \ [‰] \qquad \text{Eqn. 2}$$

In addition to SDO-1, the reference materials IRMM-184 and Reimep-18a were measured repeatedly during any sequence to check instrument performance. During a time period of 28 month, SDO-1 gave $\delta^{238}U = -0.08 \pm 0.05$ ‰ (n = 55) and $\delta^{234}U = -0.66 \pm 3.22$ ‰ (n = 43) and IRMM-184 gave $\delta^{238}U = -1.17 \pm 0.05$ ‰ (n = 131) and $\delta^{234}U = -33.43 \pm 2.69$ ‰ (n = 103). Two different batches of Reimep-18a gave $\delta^{238}U = -0.25 \pm 0.06$ ‰ (n = 89) and $\delta^{234}U = 28.11 \pm 2.44$ ‰ (n = 61) as well as $\delta^{238}U = -0.13 \pm 0.06$ ‰ (n = 33) and $\delta^{234}U = 29.44 \pm 2.40$ ‰ (n = 33). All of these values are in good agreement with previously reported values (Richter et al., 2005; Weyer et al., 2008; Richter et al., 2010; Asael et al., 2013; Goldmann et al., 2015; Andersen et al., 2017; Lu et al., 2017). All samples were usually measured as triplicates and given errors are two standard deviations of these measurements (2 s.d.) both for $\delta^{238}U$ and $\delta^{234}U$. Isotope measurements were used afterwards to calculate U concentrations by isotope dilution to compare to concentration measurements by SF-ICP-MS (except for samples from PDP-1, BARB-3 and BARB-5). Both methods agreed in average within 11 %, however, all isotope dilution data was used for further calculations because they are more precise. Total procedure blanks varied between 0.4 - 3.9 ng that included digestion, matrix separation and measurement and were considered as negligible compared to processed U from samples, so no procedure blank correction was applied to the data.

All $\delta^{238}U$ ratios of black shales and bulk carbonates were corrected for detrital contribution by using eqn. 3 and 4, assuming an average continental crust composition of $\delta^{238}U_{detritus} = -0.3$ ‰ for the detritus (Tissot and Dauphas, 2015; Noordmann et al., 2016) and lithogenic background $[U]/[Al]_{PAAS}$ of 0.000011 g g^{-1} or $[U]/[Th]_{PAAS}$ of 0.212 g g^{-1} (Taylor and McLennan, 1985), whereby Th was only used for BARB-3 and BARB-5 samples because no Al contents were available (Rammensee, 2016). In most carbonate samples the authigenic U fraction was directly leached so that no detritus correction needed to be applied.

$$\delta^{238}U_{auth.} = \frac{(\delta^{238}U_{bulk}*[U]_{bulk} - \delta^{238}U_{detr.}*[U]_{detr.})}{[U]_{auth.}} \qquad \text{Eqn. 3}$$

$$[U]_{auth.} = [U]_{bulk} - [U]_{detritus} = [U]_{bulk} - \left(\frac{[U]_{PAAS}}{[Al]_{PAAS}} * [Al]_{sample}\right) \qquad \text{Eqn. 4}$$

Table 2: Results for U concentration, $\delta^{238}U_{raw}$ and $\delta^{238}U_{authigenic}$, $\delta^{234}U_{Sec.EQ.}$ and detrital amount. 2 s.d. either out of replicate measurements or long-term reproducibility of processed SDO-1 (0.05 ‰), whichever is higher.

Core, origin	Sample	Formation, group	Lithology	U_{bulk} / µg g^{-1}	EF_U (PAAS)	$\delta^{238}U_{raw}$ / ‰	$\delta^{238}U_{authigenic}$ / ‰	2 s.d. $\delta^{238}U$ / ‰	$\delta^{234}U_{Sec.EQ.}$ / ‰	2 s.d. $\delta^{234}U$ / ‰	Detritus / %
KMF-5	346.1	Timeball Hill	shale+siltstone	6.92	4.80	-0.29	-0.28	0.05	-2.37	0.52	20.8
KMF-5	383.6	Timeball Hill	shale+siltstone	27.49	19.32	-0.25	-0.24	0.05	-3.40	0.70	5.2
KMF-5	453.1	Timeball Hill	shale+siltstone	5.84	3.05	-0.30	-0.30	0.07	0.41	0.98	32.8
KMF-5	487	Timeball Hill	shale+siltstone	4.92	3.65	-0.37	-0.39	0.05	-0.19	0.34	27.4
KMF-5	521.4	Timeball Hill	shale+siltstone	6.97	5.78	-0.35	-0.36	0.05	0.98	1.70	17.3
KMF-5	551.3	Timeball Hill	shale+siltstone	6.47	4.34	-0.34	-0.35	0.07	-0.79	1.86	23.0
KMF-5	570.9	Timeball Hill	shale+siltstone	7.89	6.22	-0.35	-0.35	0.05	1.39	0.38	16.1
KMF-5	579.4	Timeball Hill	black shale	5.81	4.62	-0.36	-0.37	0.05	3.21	0.40	21.7
KMF-5	590.3	Timeball Hill	shale+siltstone	8.08	7.57	-0.34	-0.35	0.05	-2.79	0.21	13.2
KMF-5	592.8	Timeball Hill	black shale	7.76	17.41	-0.32	-0.32	0.06	9.03	0.59	5.7
KMF-5	593.3	Timeball Hill	black shale	13.71	16.44	-0.21	-0.20	0.05	-3.63	0.84	6.1
KMF-5	594.1	Timeball Hill	black shale	6.21	7.73	-0.35	-0.36	0.05	-1.64	0.61	12.9
KMF-5	595.6	Duitschland	black shale	2.96	11.39	-0.47	-0.49	0.07	-3.62	0.17	8.8
KMF-5	599.3	Duitschland	black shale	1.88	1.42	-0.33		0.05	-0.84	0.17	70.6
KMF-5	601	Duitschland	black shale	2.76	1.94	-0.31		0.05	-2.50	1.22	51.6
KMF-5	601.6	Duitschland	black shale	4.56	2.73	-0.42	-0.50	0.05	0.28	0.73	36.6
DP-16	744.5	Timeball Hill	black shale	9.56	10.74	-0.26	-0.25	0.05	-0.49	0.84	9.3
DP-16	748	Duitschland	black shale	12.20	6.03	-0.15	-0.12	0.05	-1.03	0.44	16.6
DP-16	751.60	Duitschland	shale	1.95	3.52	-0.39	-0.43	0.05	36.62	1.18	28.4
DP-16	753.40	Duitschland	shale	2.18	2.20	-0.37	-0.43	0.05	-1.97	0.36	45.4
DP-16	754.70	Duitschland	shale	2.10	2.12	-0.28	-0.26	0.05	-0.20	0.38	47.2
DP-16	756.20	Duitschland	shale	3.13	2.67	-0.34	-0.36	0.05	0.06	0.11	37.4
DP-16	761.40	Duitschland	mudstone	3.54	3.15	-0.33	-0.35	0.05	-0.59	0.51	31.7
DP-16	764.7	Duitschland	quartzite	3.41	9.34	-0.52	-0.54	0.05	74.30	2.84	10.7
DP-16	767.5	Duitschland	quartzite	2.86	4.46	-0.45	-0.50	0.08	25.08	0.12	22.4
DP-16	769.5	Duitschland	shale	9.27	9.49	-0.10	-0.08	0.05	-1.07	0.44	10.5
DP-16	774.1	Duitschland	quartzite	2.61	4.18	-0.62	-0.72	0.05	0.57	0.19	23.9
DP-16	777.40	Duitschland	marly shale	1.39	1.92	-0.47		0.05	-0.78	0.59	52.0
DP-16	781.1	Duitschland	shale	3.39	3.33	-0.41	-0.45	0.05	-0.85	0.32	30.0
DP-16	789.1	Duitschland	mudst./shale	3.74	4.02	-0.41	-0.44	0.06	-0.03	0.78	24.9
DP-16	792	Duitschland	shale	5.65	4.89	-0.36	-0.38	0.05	-0.53	1.76	20.4
DP-16	800	Duitschland	silicified shale	7.55	18.51	-0.17	-0.16	0.05	33.85	4.58	5.4
DP-16	803.5	Duitschland	black shale	4.95	3.33	-0.42	-0.47	0.05	-2.09	0.59	30.0
GKP-01	185.16	Kuruman	black shale	0.90	6.17	-0.23	-0.21	0.05	-1.28	1.14	16.2
GKP-01	190.97	Kuruman	black shale	0.74	5.68	-0.55	-0.61	0.13	-4.21	0.67	17.6
GKP-01	264	Klein Naute	black shale	2.32	5.15	-0.39	-0.42	0.09	-4.14	0.74	19.4
GKP-01	280	Klein Naute	black shale	3.53	5.70	-0.23	-0.22	0.06	-20.71	1.54	17.6
GKP-01	317.6	Klein Naute	black shale	10.25	4.87	-0.20	-0.17	0.05	-1.91	0.56	20.5

Core, origin	Sample	Formation, group	Lithology	U_{bulk} / µg g^{-1}	EF_U (PAAS)	$\delta^{238}U_{raw}$ / ‰	$\delta^{238}U_{authigenic}$ / ‰	2 s.d. $\delta^{238}U$ / ‰	$\delta^{234}U_{sec.EQ.}$ / ‰	2 s.d. $\delta^{234}U$ / ‰	Detritus / %
GKP-01	322.02	Klein Naute	black shale	1.17	3.08	-0.25	-0.22	0.05	0.46	0.29	32.5
GKP-01	344.54	Upper Nauga	black shale	0.81	11.17	-0.41	-0.42	0.07	-5.18	0.39	9.0
GKP-01	346.9	Upper Nauga	Dolomite	0.204	17.74	-0.53	-0.53	0.15	50.89	1.14	
GKP-01	410.85	Upper Nauga	black shale	1.96	1.61	-0.41		0.05	-6.18	1.18	62.0
GKP-01	444	Upper Nauga	black shale	0.43	8.00	-0.20	-0.18	0.09	-17.69	0.60	12.5
GKP-01	460.3	Upper Nauga	Dolomite	0.227	7.54	-0.35	-0.35	0.07	48.63	0.82	
GKP-01	480.64	Upper Nauga	Dolomite	0.39	13.19	-0.35	-0.35	0.05	29.28	0.78	
GKP-01	485	Upper Nauga	black shale	1.98	1.27	-0.29		0.08	-2.33	2.00	78.6
GKP-01	485.23	Upper Nauga	black shale	1.85	0.79	-0.40		0.05	-4.94	0.73	100.0
GKP-01	489.01	Upper Nauga	black shale	1.39	0.71	-0.31		0.16	-0.34	0.55	100.0
GKP-01	561.95	Upper Nauga	Dolomite	0.662	4.24	-0.30	-0.30	0.05	128.84	0.44	
GKP-01	619	Upper Nauga	Dolomite	0.389	9.28	-0.22	-0.22	0.07	45.81	0.30	
GKP-01	634.45	Upper Nauga	Dolomite	0.278	12.89	-0.20	-0.20	0.06	40.02	0.16	
GKP-01	637	Upper Nauga	black shale	1.17	0.86	-0.31		0.05	0.20	0.39	100.0
GKP-01	667	Upper Nauga	Dolomite	0.167	8.29	-0.38	-0.38	0.05	28.54	0.35	
GKP-01	693.84	Lower Nauga	Dolomite	0.185	8.65	-0.45	-0.45	0.06	41.09	0.07	
GKP-01	696.3	Lower Nauga	black shale	11.04	6.39	-0.22	-0.20	0.05	-10.77	1.80	15.7
GKP-01	699.23	Lower Nauga	Dolomite	0.256	34.23	-0.12	-0.12	0.05	34.06	0.31	
GKP-01	755.51	Lower Nauga	Dolomite	0.232	10.34	-0.41	-0.41	0.07	13.47	0.57	
GKP-01	796.22	Lower Nauga	Dolomite	0.228	8.45	-0.39	-0.39	0.05	31.94	0.14	
GKP-01	830.9	Lower Nauga	black shale	0.29	5.48	-0.29	-0.28	0.07	3.55	0.15	18.2
GKP-01	859.9	Lower Nauga	Dolomite	0.195	14.77	-0.21	-0.21	0.08	23.75	1.37	
GKP-01	871.83	Lower Nauga	black shale	1.61	1.34	-0.42		0.08	-0.02	1.05	74.8
GKP-01	890.7	Lower Nauga	black shale	2.35	2.46	-0.13	-0.02	0.07	2.68	1.56	40.6
GKP-01	892.4	Lower Nauga	black shale	0.22	0.24	-0.20		0.10	-19.30	0.78	
GKP-01	911.8	Lower Nauga	Dolomite	0.148	38.71	-0.24	-0.24	0.05	9.74	0.62	
GKP-01	959.9	Monteville	Dolomite	0.214	6.36	-0.31	-0.31	0.05	52.01	1.10	
GKP-01	980.12	Monteville	black shale	1.42	1.33	-0.38		0.06	3.33	0.17	74.9
GKP-01	1022.12	Monteville	black shale	1.18	0.91	-0.26		0.08	-1.16	4.66	100.0
GKP-01	1049.1	Monteville	black shale	0.91	8.18	-0.42	-0.44	0.05	0.81	1.26	12.2
GKP-01	1079.9	Lokammona	black shale	1.24	1.48	-0.38		0.05	-0.07	0.49	67.4
GKP-01	1132.15	Boomplaas	Limestone	0.082	12.85	-0.13	-0.13	0.07	61.83	2.54	
GKP-01	1150.9	Boomplas	black shale	1.81	1.81	-0.32		0.08	0.83	0.88	55.3
GKP-01	1200.95	Vryburg	black shale	2.37	2.62	-0.30	-0.31	0.05	0.99	0.53	38.1
GKP-01	1262.1	Vryburg	black shale	3.09	3.71	-0.23	-0.21	0.05	-1.39	0.86	27.0
BH-1	340	Gamohaan	calcite	0.156	2.72	-0.19	-0.19	0.05	12.49	0.17	
BH-1	670	Kogelbeen	calcite	0.027	11.02	-0.05	-0.05	0.05	8.00		
BH-1	751	Kogelbeen	dolomite	0.010	11.85	-0.96	-0.96	0.05	-4.16		
BH-1	1400	Papkuil	dolomite	0.054	7.48	-0.43	-0.43	0.05	1.00	1.26	
BH-1	1620	Fairfield	dolomite	0.062	17.58	-0.50	-0.50	0.05	-1.40	1.66	
BH-1	1750	Fairfield	dolomite	0.127	3.68	-0.32	-0.32	0.12	-2.04	2.22	

Core, origin	Sample	Formation, group	Lithology	U_{bulk} / µg g^{-1}	EF_U (PAAS)	$\delta^{238}U_{raw}$ / ‰	$\delta^{238}U_{authigenic}$ / ‰	2 s.d. $\delta^{238}U$ / ‰	$\delta^{234}U_{sec.EQ.}$ / ‰	2 s.d. $\delta^{234}U$ / ‰	Detritus / %
BH-1	1914	Fairfield	dolomite	0.010	4.42	-0.23	-0.23	0.06	-13.35	1.37	
BH-1	2098	Reivilo	pure carb.	0.211	5.64	-0.31	-0.31	0.05	6.72	0.61	
BH-1	2131	Reivilo	detr. carb.	0.145	1.54	-0.93		0.16	4.99	0.41	
BH-1	2400	Reivilo	pure carb.	0.026	11.83	-0.52	-0.52	0.05	3.22		
KMF-5	875.5	Eccles	pure carb.	0.016	15.22	-0.19	-0.19	0.15	1.69	0.57	
KMF-5	1136.6	Lyttleton	pure carb.	0.159	13.21	-0.28	-0.28	0.05	7.87	1.49	
PDP-1	42.65	Tumbiana	strom. limest.	0.119	1.21	-0.27		0.05	126.61	1.80	82.8
PDP-1	65.75	Tumbiana	strom. limest.	0.990	2.11	-0.33	-0.36	0.05	2.61	1.49	47.3
PDP-1	67.55	Tumbiana	strom. limest.	2.003	2.85	-0.31	-0.31	0.05	-14.22	1.48	35.1
PDP-1	68.19	Tumbiana	strom. limest.	0.909	2.43	-0.30	-0.29	0.05	-66.16	0.97	41.1
PDP-1	71.55	Tumbiana	strom. limest.	0.209	1.54	-0.27		0.05	53.32	1.74	65.0
PDP-1	72.05 Si-rich	Tumbiana	strom. limest.	0.136	1.01	-0.30		0.05	62.98	2.08	99.2
PDP-1	72.05 C-rich	Tumbiana	strom. limest.	0.187	1.27	-0.33		0.05	-6.14	1.13	79.0
PDP-1	78.65 Si-rich	Tumbiana	strom. limest.	0.886	2.06	-0.32	-0.35	0.05	-54.14	0.87	48.5
PDP-1	78.65 C-rich	Tumbiana	strom. limest.	0.375	1.12	-0.36		0.05	90.01	1.27	89.2
PDP-1	79.18	Tumbiana	strom. limest.	1.269	2.40	-0.31	-0.32	0.07	6.26	1.11	41.7
PDP-1	67.55	Tumbiana	strom. limest.	2.003	2.85	-0.31	-0.31	0.10	-14.22	1.48	35.1
PDP-1	68.19	Tumbiana	strom. limest.	0.909	2.43	-0.30	-0.29	0.05	-66.16	0.97	41.1
outcrop	99/02	Black Reef	black shale	14.59	5.26	-0.32	-0.33	0.05	-107.10	2.78	19.0
nercmar	BES-7	Manjeri	black shale	1.97	2.31	-0.29	-0.28	0.09	-1.78	0.91	43.3
outcrop	01/018	Moodies	Graywacke	2.99	3.65	-0.26	-0.24	0.08	-93.92	1.31	27.4
outcrop	01/032	Moodies	BIF	0.17	8.43	-0.44	-0.46	0.05	25.89	0.62	11.9
outcrop	01/073	Moodies	BIF	1.18	1.71	-0.54		0.07	-144.16	0.89	58.4
outcrop	01/078Fe	Moodies	BIF	0.65	5.92	-0.40	-0.42	0.07	8.93	0.70	16.9
outcrop	284.5 a	Fig Tree	black shale	1.87	1.93	-0.07		0.08	-4.41	0.82	51.9
outcrop	284.5 b	Fig Tree	black shale	1.87	1.93	-0.08		0.05	-2.81	1.15	51.9
outcrop	435.75	Fig Tree	black shale	3.20	6.57	-0.26	-0.26	0.05	-8.98	0.80	15.2
outcrop	496.3	Fig Tree	black shale	1.13	2.00	-0.22	-0.13	0.05	-4.48	1.40	50.1
outcrop	99/029	Fig Tree	gray mudst.	1.92	2.87	-0.25	-0.23	0.05	-40.98	0.38	34.9
outcrop	99/034	Fig Tree	black siltstone	2.49	3.11	-0.17	-0.11	0.07	7.47	0.87	32.2
outcrop	99/038	Fig Tree	black shale	1.18	1.50	-0.22		0.05	-20.52	0.21	66.7
outcrop	99/039	Fig Tree	black shale	1.92	2.11	-0.17	-0.06	0.05	-10.99	0.23	47.3
BARB-5	205.17	Mapepe	sandy shale	1.699	1.58	-0.36		0.05	1.21	1.42	63.36
BARB-5	265.3	Mapepe	sandy shale	1.311	1.99	-0.39		0.05	2.85	1.85	50.37
BARB-5	289.65	Mapepe	carb. shale	1.203	1.49	-0.37		0.08	-7.14	0.56	67.07
BARB-5	290.9	Mapepe	carb. shale	1.16	1.52	-0.39		0.07	-17.09	1.94	65.71
BARB-5	304.77	Mapepe	carb. shale	2.01	1.93	-0.35		0.05	-8.30	2.77	51.87
BARB-5	389.515	Mapepe	carb. shale	0.544	1.26	-0.32		0.05	-7.52	6.81	79.23
BARB-5	500.1	Mapepe	shale (with IF)	0.228	1.47	-0.30		0.05	6.56	1.00	67.98
BARB-5	515.345	Mapepe	carb. shale	0.834	1.69	-0.33		0.06	-1.96	1.11	59.07
BARB-5	560	Mapepe	carb. shale	0.772	2.32	-0.42	-0.51	0.09	4.66	2.04	43.18

Core, origin	Sample	Formation, group	Lithology	U_{bulk} / µg g^{-1}	EF_U (PAAS)	$\delta^{238}U_{raw}$ / ‰	$\delta^{238}U_{authigenic}$ / ‰	2 s.d. $\delta^{238}U$ / ‰	$\delta^{234}U_{sec.EQ.}$ / ‰	2 s.d. $\delta^{234}U$ / ‰	Detritus / %
BARB-5	599.83	Mapepe	carb. shale	0.893	2.49	-0.33	-0.35	0.08	2.17	1.40	40.18
BARB-5	630.425	Mapepe	carb. shale	0.643	1.62	-0.31		0.06	4.89	2.20	61.75
BARB-5	675.22	Mapepe	carb. shale	0.889	5.44	-0.41	-0.43	0.05	0.71	0.75	18.39
BARB-5	686.13	Mapepe	carb. shale	0.856	3.88	-0.41	-0.45	0.05	2.56	2.32	25.80
BARB-5	700.01	Mapepe	carb. shale	0.993	1.86	-0.31		0.05	-12.58	0.52	53.88
BARB-5	730.51	Mapepe	shale	1.282	1.89	-0.36		0.05	-4.52	2.83	53.00
BARB-5	744.74	Mapepe	carb. shale	0.759	1.63	-0.31		0.05	-16.07	0.58	61.26
BARB-5	760.15	Mapepe	carb. shale	0.872	1.81	-0.35		0.05	-1.57	2.27	55.27
BARB-5	760.95	Mapepe	carb. shale	0.823	1.44	-0.36		0.04	-0.13	4.70	69.66
BARB-5	761.8	Mapepe	carb. shale	0.496	1.57	-0.28		0.05	-8.36	0.03	63.78
BARB-3	208.9	Kromberg	carb. shale	0.946	1.27	-0.36		0.05	7.17	1.96	79.01
BARB-3	211.44	Kromberg	shale+chert	0.091	2.14	-0.86		0.10	105.16	10.00	46.67
BARB-3	212.1	Kromberg	carb. shale	1.639	1.26	-0.32		0.05	8.87	0.32	79.54
BARB-3	212.24	Kromberg	carb. shale	1.624	0.96	-0.26		0.05	-25.49	1.52	100.00
BARB-3	212.45	Kromberg	carb. shale	1.131	1.24	-0.30		0.08	6.26	0.44	80.54
BARB-3	212.7	Kromberg	carb. shale	0.969	1.06	-0.27		0.05	6.05	0.69	100.00

5. Results

U enrichment factors (EF_U) were calculated versus Post-Archean Average Shale (PAAS, Taylor and McLennan, 1985). Samples with EF_U lower than two are excluded from further interpretation and these samples are not shown in figure 2 as their bulk U content and isotope signature is controlled by ≥ 50 % detritus which would result in inacceptable high uncertainties for further interpretation. Doing so, the total sample number is reduced from 134 to 89 (Figure 3). This criterion favors younger samples over older ones simply because with increasing weathering-induced U mobilization authigenic U concentrations in sediments increased. In figure 2, EF_U of leached carbonate samples are not plotted because they only show enrichment in leached fractions and not bulk sediments.

5.1 Pretoria group, ~2.22 Ga to ~2.55 Ga

In the Pretoria group (upper KMF-5 and DP-16 core), the Timeball Hill and Duitschland samples (whole-rock) show EF_U between 1.42 to 19.32 relative to PAAS with the Timeball Hill showing generally higher EF_U (in average twice as high as the Duitschland formation). The U isotope ratios vary between $\delta^{238}U_{authigenic}$ = -0.08 ‰ to -0.72 ‰ with samples from the Timeball Hill formation varying roughly around continental crust with an average of -0.32 ‰ ($\delta^{238}U_{cont.\ crust}$ = -0.3 ‰, (Tissot and Dauphas, 2015; Noordmann et al., 2016). In contrast, samples from the Duitschland formation show significantly larger variations, in particular, towards lower than crustal values, resulting in a lighter average $\delta^{238}U$ of -0.39 ‰. In the Timeball Hill formation all but one sample (with slightly higher $\delta^{234}U$ of +9 ‰) are close to secular equilibrium within $\delta^{234}U$ of ± 3.6 ‰. In the Duitschland formation, all except four samples (751.6, 764.7, 767.5 and 800 m) are within secular equilibrium of $\delta^{234}U$ = 0 ±2.1 ‰. These four samples show significantly enriched $\delta^{234}U$, that might hint at secondary weathering-induced U mobilization.

5.2 Chuniespoort group, ~2.43 Ga to ~2.55 Ga

From the Malmani subgroup only two carbonate samples from the Eccles and Lyttleton formations were analyzed. Both show high EF_U of 15.22 and 13.21 in the leached fraction and thus indicate that only minor detrital components were leached. This was also inferred by Eroglu et al. (2015), who defined carbonates with less than 1 % Al_2O_3 as 'pure' carbonates mainly derived from authigenic sources. The two samples show $\delta^{238}U_{authigenic}$ values of -0.19 ‰ and -0.28 ‰ and $\delta^{234}U$ of 1.69 ‰ and 7.87 ‰, respectively.

5.3 Ghaap and Black Reef groups, ~2.47 Ga to ~2.7 Ga

In the Asbestos, Campbellrand, and Schmidtsdrift subgroups black shales (whole-rock) and carbonates (leach digest) were sampled that show EF_U between 0.24 to 38.71. The $\delta^{238}U_{authigenic}$ values vary from -0.96 ‰ to -0.02 ‰. The $\delta^{234}U$ values show a high variability that generally encompasses values from -20.7 ‰ to 128.8 ‰ that results mostly from leached carbonate samples. The outcrop black shale sample from the lower-most Black Reef group shows EF_U of 5.26, a $\delta^{238}U_{authigenic}$ of -0.33 ‰ and a $\delta^{234}U$ values of -107.1 ‰ which may be due to its outcrop origin.

5.4 Fortescue group, ~2.72 Ga

Stromatolitic limestone samples (whole-rock) from the Fortescue group show EF_U between 1.01 and 2.85, note that for these carbonates these values describe true enrichment as they were analyzed as whole-rocks and also corrected for detrital contamination. Their $\delta^{238}U_{authigenic}$ (-0.36 ‰ to -0.26 ‰) all agree with the range assumed for the continental crust. The $\delta^{234}U$ values are highly variable and deviate from secular equilibrium and range from +126.6 ‰ to -66.2 ‰.

5.5 Barberton and Belingwe core, outcrop, and mine samples, ~2.7 Ga to ~3.4 Ga

From the Belingwe Greenstone Belt in Zimbabwe only one sample shows an EF_U of > 2 with $\delta^{238}U_{authigenic}$ of -0.28 ‰ and $\delta^{234}U$ of -1.78 ‰ (as whole-rock). Samples from the Moodies group from the Barberton Greenstone Belt comprise only outcrops, in detail we have analyzed three Banded Iron Formations (BIF) and one graywacke. These samples show EF_U of 1.71 to 8.43, $\delta^{238}U_{authigenic}$ values of -0.46 ‰ to -0.24 ‰ and highly variable $\delta^{234}U$ values between -144.16 ‰ to 25.89 ‰, indicating weathering-induced U mobilization. From the Fig Tree group seven black shales or black mudstone outcrop samples have EF_U from 1.50 to 6.57, $\delta^{238}U_{authigenic}$ values of -0.26 ‰ to -0.06 ‰ and $\delta^{234}U$ values between -40.98 ‰ to 7.47 ‰. Additionally, shale samples from the drillcore BARB-5 (Mapepe formation, 19 samples) in general show very low EF_U mostly below 2 (whole-rocks), except for four samples (BARB-5 560.00, 599.83, 675.22, and 686.13) that have slightly higher EF_U and also show minor variations in their $\delta^{238}U_{authigenic}$ values. From the lowermost unit of the Barberton Greenstone Belt, the Onverwacht group, six shale samples from the drillcore BARB-3 were analyzed. All samples show EF_U below 2 and hence, no authigenic U enrichment.
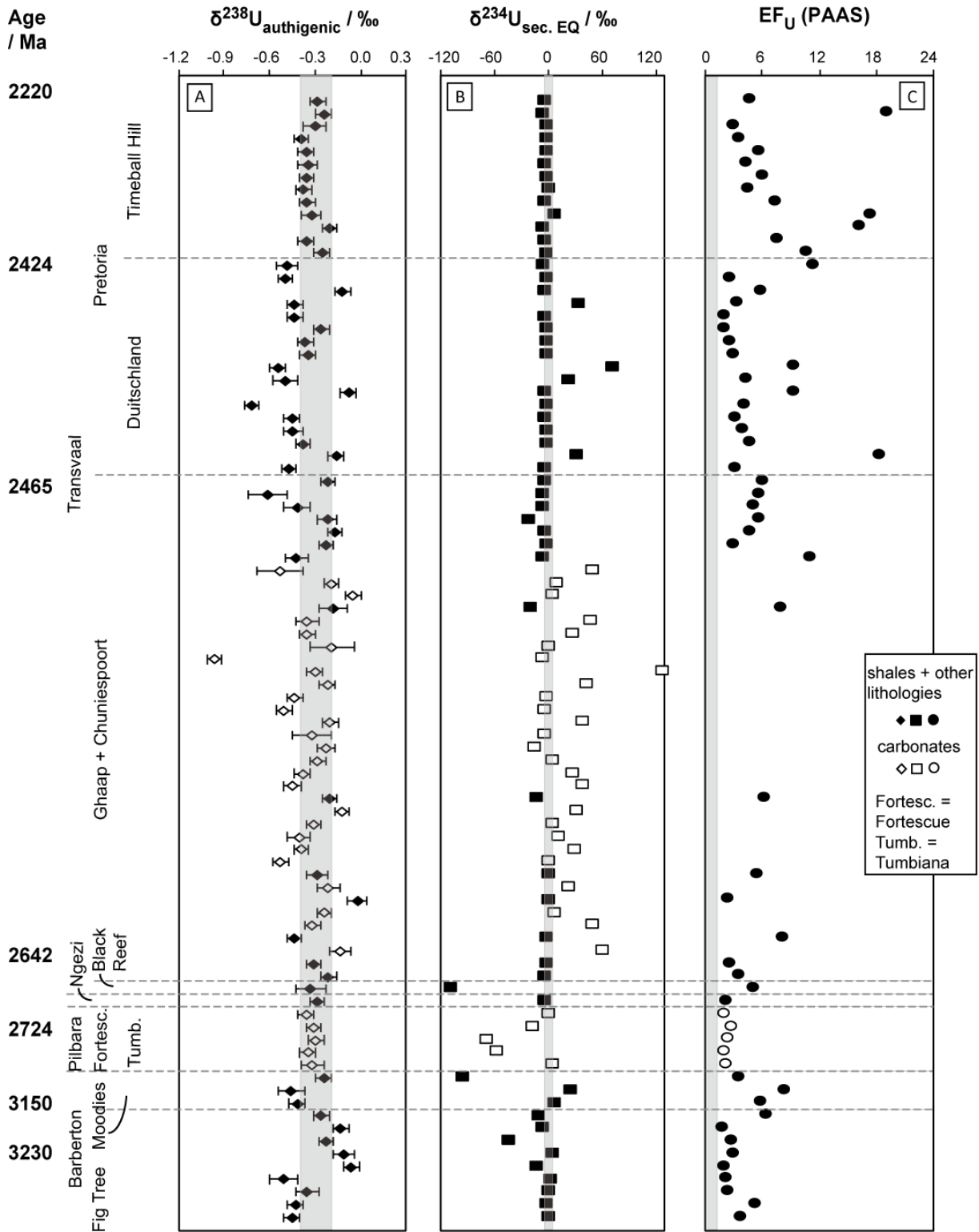
Figure 2: Variation in chronological order of A) $\delta^{238}U_{authigenic}$ (2 s.d. either out of replicate measurements or long-term reproducibility of processed SDO-1, whichever is higher), B) $\delta^{234}U_{secular\ equilibrium}$, and C) EF_U (only whole rock digests). Ages are indicated on the left-hand side according to table 1. In A) the vertical grey bar represents the $\delta^{238}U$ signature of present continental crust (Tissot and Dauphas, 2015; Noordmann et al., 2016). In B) the vertical bar represents secular equilibrium ($\delta^{234}U = 0$ ‰, Cheng et al., 2000). In C) the vertical bar represents $EF_U < 2$.

6. Discussion

6.1 Detrital contribution and authigenic U enrichment

In the black shale samples, the detritus makes up between 5 % and 100 % of total sample content and thus exerts major influence on the bulk U isotope composition. By correcting the detrital contribution, the bulk $\delta^{238}U$ is changed by up to ± 0.11 ‰ (in samples with $EF_U > 2$; this translates into maximal 50 % detritus). This is significant compared to the total sample variability, suggesting the need of a detritus correction, which was applied to all whole-rock digested black shale and carbonate samples. On the other hand, it shows that the detritus, according to its unknown U concentration and isotope composition, also represents a major source of uncertainty. Also, the choice of the detrital background [U]/[Al] or [U]/[Th] either from present-day or Archean crust is highly important and may change the final signature. Here, we chose the value for post-Archean Average Shale as reference which might reflect the Archean crust closely as it is lower than present day continental crust (Taylor and McLennan, 1985; Rudnick and Fountain, 1995; Rudnick and Gao, 2003; Tribovillard et al., 2006). Alternatively, the authigenic U fraction can be leached directly so that any detrital compounds are left in the residue. This method was tested on carbonate reference materials and then applied to some carbonate samples (see supplementary chapter S 1). Application of such a technique requires that the authigenic U fraction is entirely dissolved, while none of the detrital U is leached, as any partial U mobilization may lead to isotope fractionation. According to these requirements, only carbonate samples can be reliably processed with a partial U extraction technique. The detrital calculation highlights that in early and mid-Archean times only a limited amount of U was mobilized during continental weathering, resulting in low authigenic U enrichment in sediments.

No correlation can be observed between $\delta^{238}U_{authigenic}$ and EF_U (Figure 3) which highlights that U isotope fractionation is generally decoupled from authigenic U enrichment in these samples. This may indicate that not the deposition itself is responsible for U isotope fractionation but rather processes during weathering and U mobilization or a combination of the latter with depositional effects. Both, the calculated EF_U and $\delta^{238}U_{authigenic}$ are based on the assumption that [U]/[Al] or [U]/[Th] of the lithogenic input to the sediments are represented by PAAS which may bear a considerable uncertainty. On the other hand, corrections of $\delta^{238}U$ result in changes of maximal ± 0.11 ‰ and the overall observed variability of both, corrected and uncorrected values is larger than that typically observed for the continental crust (-0.4 ‰ to -0.2 ‰, Tissot and Dauphas, 2015; Noordmann et al., 2016), indicating U isotope fractionation during U cycling.
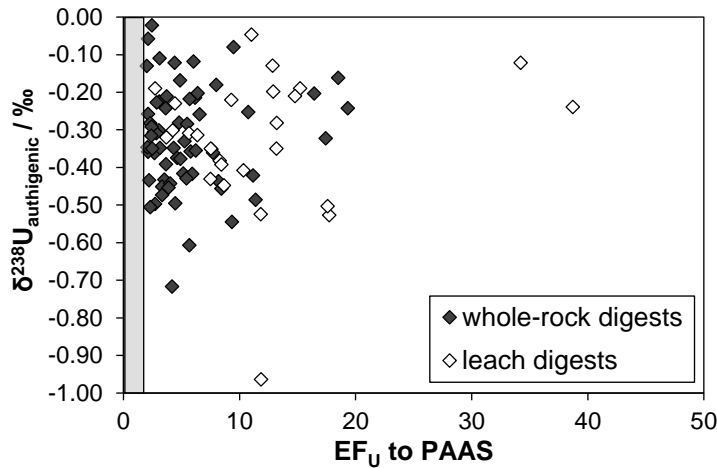
Figure 3: U enrichment factor vs. δ^{238}U$_{authigenic}$ in whole-rock (filled diamonds) and leached (empty diamonds) samples, grey bar denotes area with EF$_U$ < 2.

6.2 Recent weathering signatures indicated by δ^{234}U

In this study, 10 outcrop samples with different lithologies (black shale, graywacke, BIF, siltstone, mudstone) were analyzed and compared to 82 black shale, siltstone, mudstone, black chert, and carbonate drillcore samples. Most of all samples show δ^{234}U values within secular equilibrium ± 10 ‰. The δ^{234}U signature is used as a hint to indicate secondary alteration during sub-recent weathering, which may also have affected the ^{238}U/^{235}U signature, in theory. Thus, these samples may be considered with caution for paleo redox reconstruction. Disequilibrium of ^{234}U with ^{238}U is generated by alpha-recoil processes, resulting in damage of the crystal lattice and preferential loss of the more labile bound ^{234}U compared to its mother nuclide ^{238}U. Additional ^{234}U variability in sediments may stem from enrichment by U-bearing fluids. Hence, δ^{234}U out of secular equilibrium can be used to track recent weathering and alteration processes in ancient rocks. In our data set, mainly the outcrop and carbonate samples deviate from secular equilibrium (Figure 4 A+B). For the outcrop samples, the rather low δ^{234}U signatures can be best explained by preferential ^{234}U leaching during sub-recent weathering (Andersen et al., 2010). However, processes affecting the ^{234}U/^{238}U ratio may not necessarily affect the ^{238}U/^{235}U ratio of the samples, which is indicated by the non-existence of any correlation between δ^{234}U and δ^{238}U. We therefore decided not to generally reject samples based on their disequilibrium δ^{234}U signatures, rather we investigated whether these samples show systematically different δ^{238}U compared to undisturbed samples.
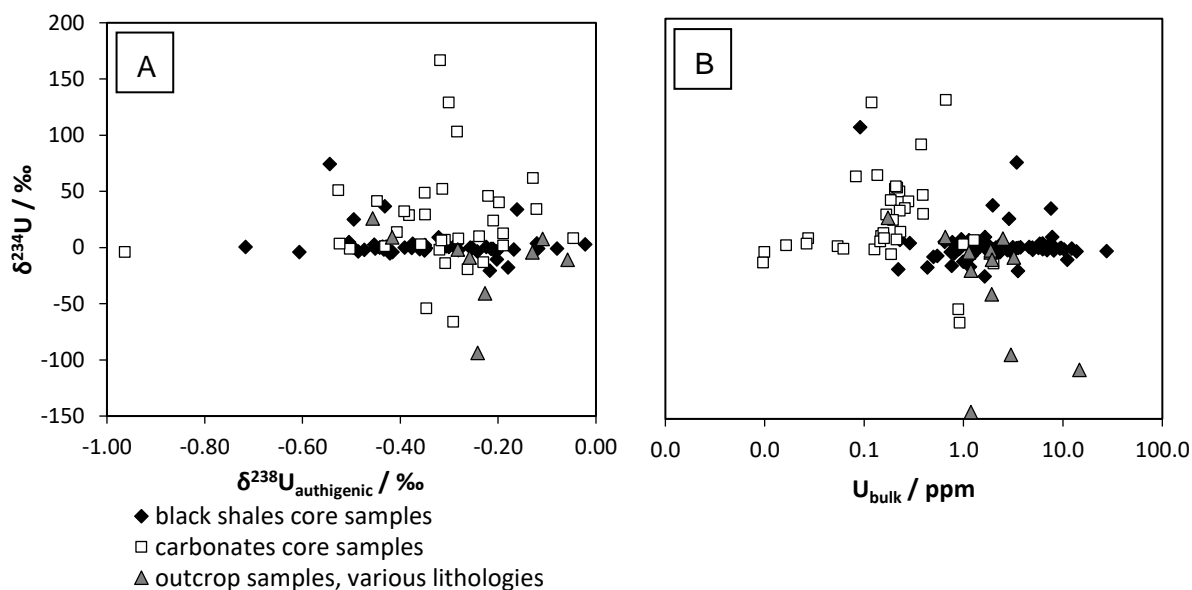
Figure 4: Variation of δ²³⁴U values vs. A) δ²³⁸U_authigenic values, only samples with EF_U > 2, and B) U bulk concentration of all samples, note log scale on x-axis in B). Carbonate samples include whole-rock and leach digests.

In all Paleo-Proterozoic and Neo-Archean black shale samples (including Duitschland and Timeball Hill formations, as well as Ghaap and Chuniespoort groups (Figure 2), only a few samples show variable δ²³⁴U signatures, while the rest of the samples is in secular equilibrium. The deviating samples may indicate that even in drillcores some fluids circulate locally at depth and may affect the ²³⁴U/²³⁸U ratio. In the older stratigraphically lower samples, all other drillcore samples (Ngezi, BARB-3, BARB-5) show δ²³⁴U signatures within secular equilibrium and thus show no indication for sub-recent weathering (Table 2).

The rather heavy δ²³⁴U signatures of most carbonate drillcore samples (Ghaap and Chuniespoort group), may be related to sample treatment. During the leaching of authigenic U from carbonate samples with 3 mol l⁻¹ nitric acid, additional ²³⁴U can be leached from the silicate fraction. This is indicated by the results of a leaching test (supplementary section S 1) where δ²³⁴U signatures of leached fractions are either in secular equilibrium or enriched in ²³⁴U. Notable however, the δ²³⁸U of the same samples show no variability between different leachates (see supplementary section S 1) demonstrating that the isotopes ²³⁵U and ²³⁸U are not affected by leaching artifacts with our method. Accordingly, we cannot distinguish if variations of δ²³⁴U in the investigated natural carbonate samples are pristine or whether they are artificial and origin from sample treatment in the laboratory. However, we exclude that sample treatment affected the analyzed δ²³⁸U values.

On the other hand, three out of five of the carbonates from the Tumbiana formation are also not in secular equilibrium. As these samples are analyzed as bulk digests, the variable δ²³⁴U of these samples cannot be a method artefact. However, as shown by our leaching

experiments, leaching-induced fractionation of $\delta^{234}U$ does not necessarily affect $\delta^{238}U$ values. Similarly, weathering-induced U leaching may also affect $\delta^{234}U$, but not necessarily $\delta^{238}U$ values. Accordingly, secular equilibrium of ^{234}U may be used as indicator for sub-recent U mobilization, however, it does not indicate weathering-induced fractionation of $\delta^{238}U$.

6.3 U isotope ratios

Due to the low number of samples and generally low U enrichment in Barberton Greenstone Belt samples, we use those samples (outcrops and drillcores BARB-3 and BARB-5 and Tumbiana carbonates) as reference for the Meso- and Paleoarchean. Most of those samples show no deviation from continental crust within their analytical errors which indicates that no or very little oxygen was around to induce redox-driven mobilization and cycling of U in the Archean. Similarly, most samples from the Ghaap and Chuniespoort groups show only minor U isotope variability and only a few samples exceed the typical range of the continental crust. In the Duitschland formation of the Pretoria group, there is a significant shift towards more variable and in average lower $\delta^{238}U$. Notably, 8 out of 17 samples have lower - and 3 out of 17 samples higher $\delta^{238}U$ (outside analytical uncertainties), as compared to the typical range observed for the continental crust (Tissot and Dauphas, 2015; Noordmann et al., 2016). This variability disappears in the overlaying Timeball Hill formation where all except two samples show crustal signatures.

6.3.1 Interpreting low $\delta^{238}U_{authigenic}$ values

The only two BIF samples, with significant authigenic U enrichment from the Barberton Greenstone Belt, show a slightly lower $\delta^{238}U_{authigenic}$ signature than continental crust. As shown by previous authors, these signatures are common among banded iron formations (Weyer et al., 2008; Wang et al., 2018) and may be explained by preferential adsorption of ^{235}U onto iron oxides (Stirling et al., 2007; Weyer et al., 2008; Brennecka et al., 2011; Goto et al., 2014; Wang et al., 2016). Alternatively, the BIF signature was inherited from an isotopically light water column, either as the result of a weathering induced low-$\delta^{238}U$ input to the ocean, or because the dominant sinks from ocean water preferentially removed heavy U isotopes from ocean water. Because of the overall anoxic ocean, U likely behaved non-conservative, which may have resulted in locally variable isotope signatures.

In the Ghaap group, four carbonate samples have lower signatures than continental crust (outside their 2 s.d. uncertainties), one of which shows a very light value of $\delta^{238}U$ = -0.96 ‰. Recent studies have shown that particularly biogenic carbonates may record seawater U isotope signatures without significant isotope fractionation during their formation, thus making them a promising archive for past seawater U isotope variations (Romaniello et al., 2013; Chen

et al., 2017; Elrick et al., 2017). However, other studies have also shown that depending on environmental conditions during carbonate deposition and during subsequent diagenetic activity and alteration carbonates can fractionate U isotope composition by up to 0.4 ‰ relative to seawater (Romaniello et al., 2013; Hood et al., 2016; Chen et al., 2017; Chen et al., 2018). However, the average $\delta^{238}U_{authigenic}$ of the carbonates analyzed in this study does not deviate from that of the analyzed shales, indicating U incorporation into both reservoirs without significant U isotope fractionation, potentially during quantitative U removal from seawater.

Black shales have been found to comprise heavy isotope signatures compared to overlaying seawater due to isotope fractionation during U reduction (Stirling et al., 2007; Weyer et al., 2008). However, quantitative U reduction in anoxic water likely resulted in isotopically unfractionated sediments. Of the here analyzed black shales, in particular one sample of the uppermost Ghaap group, as well as several samples from the overlaying Duitschland formation (roughly 80 Ma years younger) show $\delta^{238}U$ significantly lower than the typical crustal range. As isotope fractionation towards lower values is unlikely, the observed low signatures of the black shale samples are likely a result of quantitative capture of isotopically light seawater.

Two scenarios may explain a low U isotope signature in late-Archean seawater. These include 1) preferential removal of heavy U isotopes into black shales, which may have represented the dominant U sink in the overall anoxic oceans and 2) a weathering induced isotopically light U source to the oceans. In the first scenario, isotope fractionation during non-quantitative U reduction in an anoxic ocean may have resulted in preferential removal of heavy U isotopes from seawater. As the U residence time in the mostly anoxic water column during the Archean and Paleoproterozoic was likely short, this process may have produced a temporally and/or locally low-$\delta^{238}U$ residual seawater composition (reservoir effect) and thus, isotopically heavy signatures in the sediments. However, this process would require a significant amount of dissolved U^{VI} in the water column, allowing for partial U-reduction and expressed isotope fractionation, which is rather unlikely because oxygen consuming chemical compounds likely used up oxidized metals as electron acceptors, quantitatively. Furthermore, also heavy U isotope signatures in black shales should be expected, however, are only rarely observed.

The second scenario assumes input of isotopically light detritus to the oceans, as a result of preferential leaching of U-bearing minerals during weathering, likely associated with mildly oxidative atmospheric conditions. Those signatures may then simply be captured by the sediments during quantitative U removal from ocean water. As shown by Wang et al. (2015) oxidation of solid U^{IV} may induce an isotope fractionation with the resulting solution being lower in $\delta^{238}U$. However, experiments under excess oxygen, showed essentially no net isotope fractionation, likely because each mineral layer is oxidized quantitatively (described as "rind effect" by Wang et al. (2015). As, however, the pre-GOE atmosphere had only very low oxygen levels, U of U-bearing minerals, such as uraninite, may have been only partially mobilized,

either on land or in shallow more oxygen rich water on the continental shelfs, which may have generated more significant U isotope fractionation because of preferential oxidation of light U isotopes (Wang et al., 2015). Notably, the light U isotope signature disappeared in the overlying Timeball Hill formation, which was deposited during and after the GOE. In case of the second scenario, this may be explained by an increase in atmospheric oxygen levels, resulting in more quantitative, i.e. more similar to modern-style weathering of U minerals with insignificant U isotope fractionation. Unfortunately, no experimental data about the effect of mildly oxidative conditions during weathering of U minerals on U isotope fractionation are available. Such data may enable a calibration of the increase of atmospheric oxygen levels during the early Paleoproterozoic, using sedimentary U isotope signatures.

6.3.2 Interpreting high $\delta^{238}U_{authigenic}$ values

Two carbonate samples from the Ghaap group, as well as four black shales, one from the Ghaap group and three from the Pretoria group, show higher U isotope signatures than typical continental crust. These signatures may either be the result of a temporarily heavy water column or of isotope fractionation during deposition of the sediments. As discussed above, preferential weathering of heavy U isotopes is unlikely, independent from atmospheric oxygen levels. Thus, the U isotopic input to the oceans is expected to be either unfractionated, relative to the continental crust, or has slightly lower $\delta^{238}U$ than the latter. To date, only adsorption to oxides are known to preferentially remove light isotopes from seawater (potentially adsorption to other e.g. organic particles has a similar effect). However, oxides are unlikely the dominant U sink in Archean and Paleoproterozoic oceans in general, excluding shelf regions with extensive BIF formations. Thus, even a temporally heavy U isotopic water column is unlikely at this time, unless may be very locally and the heavy black shale signatures are more likely generated during or after deposition of the sediments.

As discussed above, $\delta^{238}U$ of carbonates may be fractionated towards seawater as the result of deposition or during diagenesis, e.g. during partial U reduction at anoxic conditions, resulting in an average U isotope fractionation between carbonates and seawater of ~0.2 ‰ in modern carbonates (Romaniello et al., 2013; Chen et al., 2018). Modern black shales show even higher $\delta^{238}U$ in the order of 0.0 ‰, i.e. ~0.4 ‰ higher than modern seawater (Stirling et al., 2007; Weyer et al., 2008; Andersen et al., 2014; Noordmann et al., 2016; Andersen et al., 2017). These signatures are interpreted to be generated during partial U reduction, likely both in the water column in sediment pore water (see chapter III of this thesis). Also, in other Archean black shales, heavy U isotope signature have been observed already, e.g. from Mount McRae (Western Australia, Kendall et al., 2013) which have been interpreted to likely result from partial U reduction during the deposition of the sediments. According to these findings, the observed

δ^{238}U higher than crustal average in some sediments are likely the result of incomplete U reduction during the deposition or early diagenesis of the sediments.

6.4 Weathering and the marine U cycle in the Archean and Early Proterozoic

The δ^{238}U signatures of samples from the Archean and Early Proterozoic times, show systematically different distribution patterns. In the Archean only minor U isotope fractionation and U enrichment can be observed (Figure 5). The only light δ^{238}U signatures are observed for two BIF samples and may be related to minor U isotope fractionation during U adsorption onto Fe oxides. Atmospheric oxygen levels, however, were not high enough for significant weathering-induced U input to the oceans, and to build up a sizable U^{VI} reservoir in the uppermost, potentially slightly oxidized oceans.
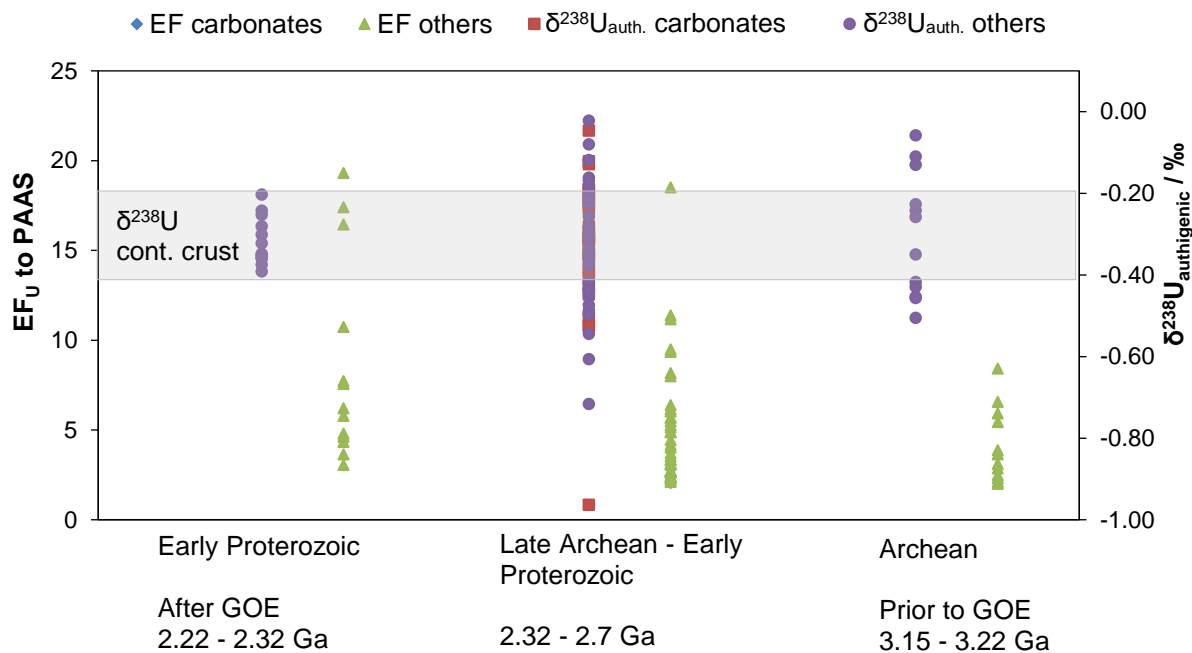
Figure 5: Summary of all δ^{238}U$_{auth.}$ (squares and circles) and EF$_U$ (diamonds and triangles) in sediments sorted by time intervals and into two lithologic groups: carbonates and other lithologies which include black shales, gray shales, and Fe-rich sediments. Grey horizontal bar denotes the δ^{238}U of present-day continental crust. Note that EF$_U$ of carbonates are only whole-rock digests, whereas δ^{238}U$_{auth.}$ is shown for leach and whole-rock digests.

The time period from the late Archean to the Early Proterozoic (2.32 to 2.7 Ga) is characterized by more variability and in average lower δ^{238}U signatures in black shales as well as in carbonates and an increase in EF$_U$ values. The data indicates the onset of weak oxidative

weathering of reduced U minerals on land or in shallow water around 2.5 Ga. This process probably involved preferential release of light ^{235}U isotopes resulting in a fractionated upper water column. The variable U isotope compositions can be best explained by a stratified water column with comparably higher oxygen levels in shallow water and at the same time an anoxic deep ocean. In such an environment, U isotope fractionation may only be induced during partial U reduction in the uppermost slightly oxidized water column and locally result in some variable U isotope compositions within black shales and carbonates deposited along the shelf region whereas otherwise, the overall anoxic water column likely resulted in quantitative capture of U isotope compositions from seawater with absence of U isotope fractionation.

After the Great Oxidation Event, our data from the early Proterozoic Timeball Hill formation show unfractionated δ^{238}U signatures, however, still associated with enhanced U enrichment, as compared to the Archean black shales. In general, these data may be explained by a general increase of oxygen levels in the atmosphere resulting in more quantitative U mobilization during oxidative weathering with essentially no isotope fractionation. Interestingly, also heavy U isotope signatures are almost absent in the Timeball Hill formation (with only one exception), although enhanced oxidative U mobilization should have resulted in the built up of a larger U^{VI} reservoir in the upper water column, enhancing the possibility of partial U reduction with isotope fractionation, in theory. However, as mentioned above, such conditions were likely restricted to some oxygen lagoons in the shelf regions (Anbar et al., 2007; Kendall et al., 2013), which was not sampled by the Timeball Hill formation samples.

6.5 Implications for reconstructing Archean environments

Significantly fractionated U isotope compositions can be found in parts of the Ghaap group (ca. 2.5 – 2.6 Ga) and in the Duitschland formation (ca 2.3 Ga). This observation pre-dates the onset of U weathering defined by U enrichment in shales from 2.32 Ga on (Partin et al., 2013a) by roughly hundred million years, however, goes along with the significant U enrichment found in iron formations (Partin et al., 2013b). As shown by Kendall et al. (2013) U enrichment and U isotope fractionation do not always go along because U isotope signatures appear to be more sensitive than U enrichment factors to minor changes in environmental conditions, affecting the weathering-induced U delivery to the oceans or the U enrichment in oceanic sinks.

Our results thus confirm previous findings (Siebert et al., 2005; Anbar et al., 2007; Wille et al., 2007; Scott et al., 2008; Voegelin et al., 2010; Czaja et al., 2012; Crowe et al., 2013; Kendall et al., 2013; Partin et al., 2013a; Wille et al., 2013; Lyons et al., 2014; Eroglu et al., 2015; Kendall et al., 2015; Kurzweil et al., 2015; Satkoski et al., 2015; Frei et al., 2016; Kurzweil et al., 2016; Eroglu et al., 2017; Eroglu et al., 2018; Wang et al., 2018; Wille et al., 2018) that atmospheric oxygen levels likely started to rise before the Great Oxidation Event, in detail

some 100 – 200 Ma indicated by our data and triggered weathering induced partial U mobilization and isotope fractionation. Interestingly, Wang et al. (2018) found fractionated U isotopes in much older sediments from 3.0 Ga, thus, implying the onset of oxidative U weathering may have been even earlier. However, the statistical variability is mainly based on the Sinqeni iron formation samples (Pongola group). This formation needs to be considered carefully as this setting has been found to have been overprinted by modern weathering proven in outcrop samples by trace elements and Cr isotopes (Albut et al., 2018). In contrast, drillcore samples did not show fractionated Cr isotopes, hence indicating the absence of free oxygen during their deposition (Planavsky et al., 2014; Albut et al., 2018). This is in agreement with the absence of significant U isotope fractionation in samples older than ~ 2.5 Ga in drillcore samples analyzed in this study. Apart from that, comparison of sensitivities to oxygen of Cr and U isotopes is not straightforward. Additionally, Wang et al. (2018) found a second statistical turning point in their dataset at ~2.4 Ga which is in agreement with implications from our data. Hence, either the Sinqeni locality was overprinted by modern alteration resulting in U isotope fractionation which may be tested for example with $^{234}U/^{238}U$ ratios and trace element data. Alternatively, this locality may have experienced locally restricted oxygen enrichment coupled with U isotope fractionation and thus, the global increase in atmospheric oxygen levels with U mobilization by mildly oxidative weathering occurred later as indicated by our data and in accordance with the second turning point of Wang et al. (2018). Locally restricted free oxygen containing lagoons have also been indicated by other redox-sensitive isotope proxies at other localities for the same times (Eickmann et al., 2018).

Apart from U and Cr, Mo abundances and isotopes have been used widely to constrain the onset of weathering-induced oxidative mobilization of Mo, implying an increase in atmospheric oxygen levels (Siebert et al., 2005; Wille et al., 2007; Duan et al., 2010; Voegelin et al., 2010; Czaja et al., 2012; Wille et al., 2013; Planavsky et al., 2014). The findings of these studies implies that the onset of enhanced Mo mobilization pre-dates that of U mobilization, as indicated by the results of this study. In general, the sensitivity of an redox-sensitive element during weathering to oxygen partial pressures in the atmosphere critically depends on its host mineral stability. As Mo and U resided in different host minerals, e.g. likely mostly uraninite for U and molybdenite for Mo (Hazen et al., 2009; Greaney et al., 2018) different oxygen levels for the onsets of oxidative weathering processes are sampled by (the isotope signatures of) different elements. To this end, combining the signatures of different redox-sensitive elements of the isotopic tool box, may be very powerful in reconstructing a stepwise evolution of atmospheric oxygen, at local and temporal scales, assuming the mineral host and their resistance to weathering at different oxygen levels are precisely known. The U isotope results of this study indicate that Mo and Cr both are more sensitive to oxidative weathering than U. The power of U isotopes is that U mobilization by oxidative weathering appears to result in a

different isotope signature (low δ^{238}U) than that typically generated during reductive U removal from seawater (high δ^{238}U) and that this isotope signature may be restricted to a certain atmospheric oxygen levels, which has to be defined by experiments. By all means, the absence of light U isotope signatures in post-GOE sediments is in agreement with quantitative weathering-induced U mobilization, as also indicated by the absence of detrital uraninite in such sediments.

7. Conclusions

Our U isotope data from different sediments throughout the Archean and Early Proterozoic indicate that the onset of oxidative weathering of U minerals dates to ~2.5 Ga. Thus, it predates the Great Oxidation Event by 100-200 Ma and in agreement with findings from other isotope proxy studies (Duan et al., 2010; Voegelin et al., 2010; Kendall et al., 2013; Wille et al., 2013).

First U oxidative weathering resulted most likely in the preferential release of light ^{235}U isotopes which were accumulated in the uppermost slightly oxic water column of a stratified ocean. In the anoxic deeper water column, U isotopes were either partially reduced, resulting in isotope fractionation towards higher δ^{238}U, or quantitatively reduced to capture light isotope compositions.

Archean oxygen concentrations most likely rose step-wise and fluctuated at local and temporal scales, possibly generating locally and temporally variable U isotope compositions. The disappearance of light U isotope signatures in sediments deposited after the GOE are indicative of quantitative oxidative U mobilization during weathering at low but constant atmospheric oxygen partial pressures. The mobilized U was quantitatively reduced without isotope fractionation in the still overall anoxic oceans.

Acknowledgements

References (including supplementary)

Albut G., Babechuk M. G., Kleinhanns I. C., Benger M., Beukes N. J., Steinhilber B., Smith A. J. B., Kruger S. J. and Schoenberg R. (2018) Modern rather than Mesoarchaean oxidative weathering responsible for the heavy stable Cr isotopic signatures of the 2.95 Ga old Ijzermijn iron formation (South Africa). *Geochim. Cosmochim. Acta* **228**, 157–189. Available at: https://doi.org/10.1016/j.gca.2018.02.034.

Algeo T. J. and Tribovillard N. (2009) Environmental analysis of paleoceanographic systems based on molybdenum–uranium covariation. *Chem. Geol.* **268**, 211–225. Available at: http://linkinghub.elsevier.com/retrieve/pii/S0009254109003805.

Anbar A. D., Duan Y., Lyons T. W., Arnold G. L., Kendall B., Creaser R. A., Kaufman A. J., Gordon G. W., Scott C., Garvin J. and Buick R. (2007) A Whiff of Oxygen Before the Great Oxidation Event? *Science (80-.).* **317**, 1903–1906. Available at: http://www.sciencemag.org/cgi/doi/10.1126/science.1140325.

Andersen M. B., Romaniello S., Vance D., Little S. H., Herdman R. and Lyons T. W. (2014) A modern framework for the interpretation of 238U/235U in studies of ancient ocean redox. *Earth Planet. Sci. Lett.* **400**, 184–194. Available at: http://dx.doi.org/10.1016/j.epsl.2014.05.051.

Andersen M. B., Stirling C. H., Potter E. K. and Halliday A. N. (2004) Toward epsilon levels of measurement precision on 234U/ 238U by using MC-ICPMS. *Int. J. Mass Spectrom.* **237**, 107–118.

Andersen M. B., Stirling C. H. and Weyer S. (2017) Uranium Isotope Fractionation. *Rev. Mineral. Geochemistry* **82**, 799–850. Available at: http://rimg.geoscienceworld.org/lookup/doi/10.2138/rmg.2017.82.19.

Andersen M. B., Stirling C. H., Zimmermann B. and Halliday A. N. (2010) Precise determination of the open ocean 234U/238U composition. *Geochemistry, Geophys. Geosystems* **11**.

Armstrong R. A., Compston W., de Wit M. J. and Williams I. S. (1990) The stratigraphy of the 3.5-3.2 Ga Barberton Greenstone Belt revisited: a single zircon ion microprobe study. *Earth Planet. Sci. Lett.* **101**, 90–106.

Arndt N. (2012) Peering into the Cradle of Life : Scientific Drilling in the Barberton Greenstone Belt , South Africa. *EGU Gen. Assem. Conf. Abstr.* **14**, 6976.

Asael D., Tissot F. L. H., Reinhard C. T., Rouxel O., Dauphas N., Lyons T. W., Ponzevera E., Liorzou C. and Chéron S. (2013) Coupled molybdenum, iron and uranium stable isotopes as oceanic paleoredox proxies during the Paleoproterozoic Shunga Event. *Chem. Geol.* **362**, 193–210. Available at: http://dx.doi.org/10.1016/j.chemgeo.2013.08.003.

Azmy K., Kendall B., Brand U., Stouge S. and Gordon G. W. (2015) Redox conditions across the Cambrian-Ordovician boundary: Elemental and isotopic signatures retained in the GSSP carbonates. *Palaeogeogr. Palaeoclimatol. Palaeoecol.* **440**, 440–454. Available at: http://dx.doi.org/10.1016/j.palaeo.2015.09.014.

Bekker A., Holland H. D., Wang P. L., Rumble D., Stein H. J., Hannah J. L., Coetzee L. L. and Beukes N. J. (2004) Dating the rise of atmospheric oxygen. *Nature* **427**, 117–120.

Bekker A., Kaufman A. J., Karhu J. A., Beukes N. J., Swart Q. D., Coetzee L. L. and Eriksson K. A. (2001) Chemostratigraphy of the Paleoproterozoic Duitschland Formation, South Africa: Implications for coupled climate change and carbon cycling. *Am. J. Sci.* **301**, 261–

285.

Berglund M. and Wieser M. E. (2011) Isotopic compositions of the elements 2009 (IUPAC Technical Report). *Pure Appl. Chem.* **83**, 397–410. Available at: http://www.degruyter.com/view/j/pac.2011.83.issue-2/pac-rep-10-06-02/pac-rep-10-06-02.xml.

Blake T. S., Buick R., Brown S. J. A. and Barley M. E. (2004) Geochronology of a Late Archaean flood basalt province in the Pilbara Craton, Australia: constraints on basin evolution, volcanic and sedimentary accumulation, and continental drift rates. *Precambrian Res.* **133**, 143–173. Available at: https://www.sciencedirect.com/science/article/pii/S0301926804000828 [Accessed January 18, 2019].

Brennecka G. A., Herrmann A. D., Algeo T. J. and Anbar A. D. (2011) Rapid expansion of oceanic anoxia immediately before the end-Permian mass extinction. *Proc. Natl. Acad. Sci.* **108**, 17631–17634. Available at: http://www.pnas.org/cgi/doi/10.1073/pnas.1106039108.

Brennecka G. A., Wasylenki L. E., Bargar J. R., Weyer S. and Anbar A. D. (2011) Uranium isotope fractionation during adsorption to Mn-oxyhydroxides. *Environ. Sci. Technol.* **45**, 1370–1375.

Byerly G. R., Kröner A., Lowe D. R., Todt W. and Walsh M. M. (1996) Prolonged magmatism and time constraints for sediment deposition in the early Archean Barberton greenstone belt: evidence from the Upper Onverwacht and Fig Tree groups. *Precambrian Res.* **78**, 125–138. Available at: http://linkinghub.elsevier.com/retrieve/pii/0301926895000739.

Catuneanu O. and Eriksson P. G. (2002) Sequence stratigraphy of the precambrian Rooihoogte-Timeball Hill rift succession, Transvaal basin, South Africa. *Sediment. Geol.* **147**, 71–88.

Chen X., Romaniello S. J. and Anbar A. D. (2017) Uranium isotope fractionation induced by aqueous speciation: Implications for U isotopes in marine CaCO3 as a paleoredox proxy. *Geochim. Cosmochim. Acta* **215**, 162–172. Available at: http://dx.doi.org/10.1016/j.gca.2017.08.006.

Chen X., Romaniello S. J., Herrmann A. D., Hardisty D., Gill B. C. and Anbar A. D. (2018) Diagenetic effects on uranium isotope fractionation in carbonate sediments from the Bahamas. *Geochim. Cosmochim. Acta* **237**, 294–311. Available at: https://www.sciencedirect.com/science/article/pii/S0016703718303417 [Accessed December 14, 2018].

Cheng H., Edwards R. L., Hoff J., Gallup C. D., Richards D. A. and Asmerom Y. (2000) The half-lives of uranium-234 and thorium-230. *Chem. Geol.*, 17–33.

Cheng H., Lawrence Edwards R., Shen C. C., Polyak V. J., Asmerom Y., Woodhead J., Hellstrom J., Wang Y., Kong X., Spötl C., Wang X. and Calvin Alexander E. (2013) Improvements in 230Th dating, 230Th and 234U half-life values, and U-Th isotopic measurements by multi-collector inductively coupled plasma mass spectrometry. *Earth Planet. Sci. Lett.* **371**–**372**, 82–91. Available at: http://dx.doi.org/10.1016/j.epsl.2013.04.006.

Cloud P. (1972) A working model of the primitive Earth. *Am. J. Sci.*

Cole D. B., Zhang S. and Planavsky N. J. (2017) A new estimate of detrital redox-sensitive metal concentrations and variability in fluxes to marine sediments. *Geochim. Cosmochim. Acta* **215**, 337–353.

Crowe S. A., Døssing L. N., Beukes N. J., Bau M., Kruger S. J., Frei R. and Canfield D. E. (2013) Atmospheric oxygenation three billion years ago. *Nature* **501**, 535–538. Available at: http://www.nature.com/doifinder/10.1038/nature12426.

Czaja A. D., Johnson C. M., Roden E. E., Beard B. L., Voegelin A. R., Nägler T. F., Beukes N. J. and Wille M. (2012) Evidence for free oxygen in the Neoarchean ocean based on coupled iron-molybdenum isotope fractionation. *Geochim. Cosmochim. Acta* **86**, 118–137.

Duan Y., Anbar A. D., Arnold G. L., Lyons T. W., Gordon G. W. and Kendall B. (2010) Molybdenum isotope evidence for mild environmental oxygenation before the Great Oxidation Event. *Geochim. Cosmochim. Acta* **74**, 6655–6668. Available at:

http://dx.doi.org/10.1016/j.gca.2010.08.035.

Dunk R. M., Mills R. A. and Jenkins W. J. (2002) A reevaluation of the oceanic uranium budget for the Holocene. *Chem. Geol.* **190**, 45–67.

Eickmann B., Hofmann A., Wille M., Bui T. H., Wing B. A. and Schoenberg R. (2018) Isotopic evidence for oxygenated Mesoarchaean shallow oceans. *Nat. Geosci.* **11**, 133–138. Available at: http:https://doi.org/10.1038/s41561-017-0036-x.

Elrick M., Polyak V., Algeo T. J., Romaniello S., Asmerom Y., Herrmann A. D., Anbar A. D., Zhao L. and Chen Z. Q. (2017) Global-ocean redox variation during the middle-late Permian through Early Triassic based on uranium isotope and Th/U trends of marine carbonates. *Geology* **45**, 163–166.

Eroglu S., Schoenberg R., Pascarelli S., Beukes N. J., Kleinhanns I. C. and Swanner E. D. (2018) Open ocean vs. continentally-derived iron cycles along the neoarchean campbellrand-malmani carbonate platform, South Africa. *Am. J. Sci.* **318**, 367–408.

Eroglu S., Schoenberg R., Wille M., Beukes N. and Taubald H. (2015) Geochemical stratigraphy, sedimentology, and Mo isotope systematics of the ca. 2.58-2.50Ga-old Transvaal Supergroup carbonate platform, South Africa. *Precambrian Res.* **266**, 27–46. Available at: http://dx.doi.org/10.1016/j.precamres.2015.04.014.

Eroglu S., van Zuilen M. A., Taubald H., Drost K., Wille M., Swanner E. D., Beukes N. J. and Schoenberg R. (2017) Depth-dependent δ13C trends in platform and slope settings of the Campbellrand-Malmani carbonate platform and possible implications for Early Earth oxygenation. *Precambrian Res.* **302**, 122–139. Available at: http://dx.doi.org/10.1016/j.precamres.2017.09.018.

Farquhar J. (2000) Atmospheric Influence of Earth's Earliest Sulfur Cycle. *Science (80-.).* **289**, 756–758. Available at: http://www.sciencemag.org/cgi/doi/10.1126/science.289.5480.756.

Frei R., Crowe S. A., Bau M., Polat A., Fowle D. A. and Døssing L. N. (2016) Oxidative elemental cycling under the low O2 Eoarchean atmosphere. *Sci. Rep.* **6**, 21058. Available at: http://www.nature.com/articles/srep21058.

Godfrey L. V and Falkowski P. G. (2009) The cycling and redox state of nitrogen in the Archaean ocean. *Nat. Geosci.* **2**, 725. Available at: https://doi.org/10.1038/ngeo633.

Goldmann A., Brennecka G., Noordmann J., Weyer S. and Wadhwa M. (2015) The uranium isotopic composition of the Earth and the Solar System. *Geochim. Cosmochim. Acta* **148**, 145–158. Available at: http://dx.doi.org/10.1016/j.gca.2014.09.008.

Goto K. T., Anbar A. D., Gordon G. W., Romaniello S. J., Shimoda G., Takaya Y., Tokumaru A., Nozaki T., Suzuki K., Machida S., Hanyu T. and Usui A. (2014) Uranium isotope systematics of ferromanganese crusts in the Pacific Ocean: Implications for the marine 238U/235U isotope system. *Geochim. Cosmochim. Acta* **146**, 43–58. Available at: http://dx.doi.org/10.1016/j.gca.2014.10.003.

Govindaraju K. (1989) 1989 Compilation of Working Values and Sample Description for 272 Geostandards. *Geostand. Newsl.* **13**, 1–113.

Greaney A. T., Rudnick R. L., Gaschnig R. M., Whalen J. B., Luais B. and Clemens J. D. (2018) Geochemistry of molybdenum in the continental crust. *Geochim. Cosmochim. Acta* **238**, 36–54.

Greber N. D., Mäder U. and Nägler T. F. (2015) Experimental dissolution of molybdenum-sulphides at low oxygen concentrations: A first-order approximation of late Archean atmospheric conditions. *Earth Sp. Sci.* **2**, 173–180.

Gumsley A. P., Chamberlain K. R., Bleeker W., Söderlund U., de Kock M. O., Larsson E. R. and Bekker A. (2017) Timing and tempo of the Great Oxidation Event. *Proc. Natl. Acad. Sci.* **114**, 1811–1816. Available at: http://www.pnas.org/lookup/doi/10.1073/pnas.1608824114.

Hannah J. L., Bekker A., Stein H. J., Markey R. J. and Holland H. D. (2004) Primitive Os and 2316 Ma age for marine shale: implications for Paleoproterozoic glacial events and the rise of atmospheric oxygen. *Earth Planet. Sci. Lett.* **225**, 43–52. Available at: http://linkinghub.elsevier.com/retrieve/pii/S0012821X04004029.

Hazen R. M., Ewing R. C. and Sverjensky D. A. (2009) Evolution of uranium and thorium minerals. *Am. Mineral.* **94**, 1293–1311.

Heubeck C., Engelhardt J., Byerly G. R., Zeh A., Sell B., Luber T. and Lowe D. R. (2013) Timing of deposition and deformation of the Moodies Group (Barberton Greenstone Belt, South Africa): Very-high-resolution of Archaean surface processes. *Precambrian Res.* **231**, 236–262. Available at: http://dx.doi.org/10.1016/j.precamres.2013.03.021.

Hickman A. H. and Van Kranendonk M. J. (2012) Early Earth evolution: evidence from the 3.5-1.8 Ga geological history of the Pilbara region of Western Australia. *… Geol. Sci.*, 283–297. Available at: http://scholar.google.com/scholar?hl=en&btnG=Search&q=intitle:Revised+lithostratigraphy+of+Archean+supracrustal+and+intrusive+rocks+in+the+northern+Pilbara+Craton,+Western+Australia#0%5Cnhttp://aca.unsw.edu.au/sites/default/files/publications/Pilbara_Epis.

Hofmann A. (2005) The geochemistry of sedimentary rocks from the Fig Tree Group, Barberton greenstone belt: Implications for tectonic, hydrothermal and surface processes during mid-Archaean times. *Precambrian Res.* **143**, 23–49.

Hofmann A., Karykowski B., Mason P., Chunnet G. and Arndt N. (2013) Barberton drilling project – Buck Reef Chert core BARB3. **15**, 12227.

Hofmann A. and Kusky T. (2004) The Belingwe Greenstone Belt: Ensialic or Oceanic? *Dev. Precambrian Geol.* **13**, 487–538.

Hood A. V. S., Planavsky N. J., Wallace M. W., Wang X., Bellefroid E. J., Gueguen B. and Cole D. B. (2016) Integrated geochemical-petrographic insights from componentselective δ238U of Cryogenian marine carbonates. *Geology* **44**, 935–938.

Hunter M. A., Bickle M. J., Nisbet E. G., Martin A. and Chapman H. J. (1998) Continental extensional setting for the Archean Belingwe Greenstone Belt. *Geology* **26**, 883–886.

Imai N., Sakuramachi H., Terashima S., Itoh S. and Ando A. (1996) 1996 Compilation of analytical data on nine GSJ geochemical reference samples, "sedimentary rock series." *Geostand. Newsl.* **20**, 165–216.

Johnson J. E., Gerpheide A., Lamb M. P. and Fischer W. W. (2014) O 2 constraints from Paleoproterozoic detrital pyrite and uraninite. *Geol. Soc. Am. Bull.* **126**, 813–830. Available at: https://pubs.geoscienceworld.org/gsabulletin/article/126/5-6/813-830/126042.

Kendall B., Brennecka G. A., Weyer S. and Anbar A. D. (2013) Uranium isotope fractionation suggests oxidative uranium mobilization at 2.50Ga. *Chem. Geol.* **362**, 105–114. Available at: http://dx.doi.org/10.1016/j.chemgeo.2013.08.010.

Kendall B., Creaser R. A., Reinhard C. T., Lyons T. W. and Anbar A. D. (2015) Transient episodes of mild environmental oxygenation and oxidative continental weathering during the late Archean. *Sci. Adv.* **1**, 1–7.

Klinkhammer G. P. and Palmer M. R. (1991) Uranium in the oceans: Where it goes and why. *Geochim. Cosmochim. Acta* **55**, 1799–1806.

de Kock M. O., Evans D. A. D. and Beukes N. J. (2009) Validating the existence of Vaalbara in the Neoarchean. *Precambrian Res.* **174**, 145–154.

Kröner A. and Todt W. (1988) Barberton Greenstone Belt, Southern Africa. *J. Geophys. Res.* **93**, 15329–15337.

Ku T., Knauss K. G. and Mathieu G. G. (1977) Uranium in open ocean: concentration and isotopic composition. *Deep Sea Res.* **24**, 1005–1017.

Kurzweil F., Wille M., Gantert N., Beukes N. J. and Schoenberg R. (2016) Manganese oxide shuttling in pre-GOE oceans ??? evidence from molybdenum and iron isotopes. *Earth Planet. Sci. Lett.* **452**, 69–78. Available at: http://dx.doi.org/10.1016/j.epsl.2016.07.013.

Kurzweil F., Wille M., Schoenberg R., Taubald H. and Van Kranendonk M. J. (2015) Continuously increasing δ98Mo values in Neoarchean black shales and iron formations from the Hamersley Basin. *Geochim. Cosmochim. Acta* **164**, 523–542. Available at: http://dx.doi.org/10.1016/j.gca.2015.05.009.

Lau K. V., Maher K., Altiner D., Kelley B. M., Kump L. R., Lehrmann D. J., Silva-Tamayo J. C., Weaver K. L., Yu M. and Payne J. L. (2016) Marine anoxia and delayed Earth system recovery after the end-Permian extinction. *Proc. Natl. Acad. Sci.* **113**, 2360–2365. Available at: http://www.pnas.org/lookup/doi/10.1073/pnas.1515080113.

Lowe D. R. and Byerly G. R. (2007) Chapter 5.3 An Overview of the Geology of the Barberton

Greenstone Belt and Vicinity: Implications for Early Crustal Development. *Dev. Precambrian Geol.* **15**, 481–526.

Lowe D. R. and Byerly G. R. (1999) Stratigraphy of the west-central part of the Barberton Greenstone Belt, South Africa. *Spec. Pap. Soc. Am.*, 1–36.

Lu X., Kendall B., Stein H. J., Li C., Hannah J. L., Gordon G. W. and Ebbestad J. O. R. (2017) Marine redox conditions during deposition of Late Ordovician and Early Silurian organic-rich mudrocks in the Siljan ring district, central Sweden. *Chem. Geol.* **457**, 75–94. Available at: http://linkinghub.elsevier.com/retrieve/pii/S0009254117301407.

Luo G., Ono S., Beukes N. J., Wang D. T., Xie S. and Summons R. E. (2016) Rapid oxygenation of Earth's atmosphere 2 . 33 billion years ago. *Sci. Adv.* **2**, e1600134.

Lyons T. W., Reinhard C. T. and Planavsky N. J. (2014) The rise of oxygen in Earth's early ocean and atmosphere. *Nature* **506**, 307–315. Available at: http://www.nature.com/doifinder/10.1038/nature13068.

Mason P., Galic A., Montinaro A., Strauss H. and Hofmann A. (2013) Barberton Drilling Project – Barite Valley Core BARB5. **15**, 13902.

Noordmann J., Weyer S., Georg R. B., Jöns S. and Sharma M. (2016) 238U/235U isotope ratios of crustal material, rivers and products of hydrothermal alteration: new insights on the oceanic U isotope mass balance. *Isotopes Environ. Health Stud.* **52**, 141–163.

Noordmann J., Weyer S., Montoya-Pino C., Dellwig O., Neubert N., Eckert S., Paetzel M. and Böttcher M. E. (2015) Uranium and molybdenum isotope systematics in modern euxinic basins: Case studies from the central Baltic Sea and the Kyllaren fjord (Norway). *Chem. Geol.* **396**, 182–195. Available at: http://dx.doi.org/10.1016/j.chemgeo.2014.12.012.

Partin C. A., Bekker A., Planavsky N. J., Scott C. T., Gill B. C., Li C., Podkovyrov V., Maslov A., Konhauser K. O., Lalonde S. V., Love G. D., Poulton S. W. and Lyons T. W. (2013a) Large-scale fluctuations in Precambrian atmospheric and oceanic oxygen levels from the record of U in shales. *Earth Planet. Sci. Lett.* **369**–**370**, 284–293.

Partin C. A., Lalonde S. V., Planavsky N. J., Bekker A., Rouxel O. J., Lyons T. W. and Konhauser K. O. (2013b) Uranium in iron formations and the rise of atmospheric oxygen. *Chem. Geol.* **362**, 82–90. Available at: http://dx.doi.org/10.1016/j.chemgeo.2013.09.005.

Pavlov A. A. and Kasting J. F. (2002) Mass-Independent Fractionation of Sulfur Isotopes in Archean Sediments: Strong Evidence for an Anoxic Archean Atmosphere. *Astrobiology* **2**, 27–41. Available at: http://www.liebertonline.com/doi/abs/10.1089/153110702753621321.

Planavsky N. J., Asael D., Hofmann A., Reinhard C. T., Lalonde S. V., Knudsen A., Wang X., Ossa Ossa F., Pecoits E., Smith A. J. B., Beukes N. J., Bekker A., Johnson T. M., Konhauser K. O., Lyons T. W. and Rouxel O. J. (2014) Evidence for oxygenic photosynthesis half a billion years before the Great Oxidation Event. *Nat. Geosci.* **7**, 283–286.

Potts P. J. and Webb P. C. (1992) X-ray fluorescence spctrometry. *J. Geochemical Explor.* **44**, 251–296.

Puchtel I. S., Walker R. J., Touboul M., Nisbet E. G. and Byerly G. R. (2014) Insights into early Earth from the Pt-Re-Os isotope and highly siderophile element abundance systematics of Barberton komatiites. *Geochim. Cosmochim. Acta* **125**, 394–413. Available at: http://dx.doi.org/10.1016/j.gca.2013.10.013.

Rammensee P. (2016) A multiple isotope and trace element approach to constrain the oxygenation and metal cycling. .

Rasmussen B. and Buick R. (1999) Redox state of the Archean atmosphere : Evidence from detrital heavy minerals in ca . 3250 – 2750 Ma sandstones from the Pilbara Craton , Australia : Comment and Reply. *Geology* **27**, 115–118. Available at: http://geology.gsapubs.org/content/27/2/115.abstract.

Renshaw J. C., Butchins L. J. C., Livens F. R., May I., Charnock J. M. and Lloyd J. R. (2005) Bioreduction of uranium: Environmental implications of a pentavalent intermediate. *Environ. Sci. Technol.* **39**, 5657–5660.

Richter S., Alonso-Munoz A., Eykens R., Jacobsson U., Kuehn H., Verbruggen A., Aregbe Y., Wellum R. and Keegan E. (2008) The isotopic composition of natural uranium samples-Measurements using the new n(233U)/n(236U) double spike IRMM-3636. *Int. J. Mass*

Spectrom. **269**, 145–148.

Richter S., Alonso A., Bolle W. De, Kühn H., Verbruggen A., Wellum R. and Taylor P. D. P. (2005) Re-certification of a series of uranium isotope reference materials: IRMM-183, IRMM-184, IRMM-185, IRMM-186 and IRMM-187. *Int. J. Mass Spectrom.* **247**, 37–39.

Richter S., Eykens R., Kühn H., Aregbe Y., Verbruggen A. and Weyer S. (2010) New average values for the n(238U)/n(235U) isotope ratios of natural uranium standards. *Int. J. Mass Spectrom.* **295**, 94–97.

Rolison J. M., Stirling C. H., Middag R. and Rijkenberg M. J. A. (2017) Uranium stable isotope fractionation in the Black Sea: Modern calibration of the 238 U/ 235 U paleo-redox proxy. *Geochim. Cosmochim. Acta* **203**, 69–88. Available at: http://linkinghub.elsevier.com/retrieve/pii/S0016703716307116.

Romaniello S. J., Herrmann A. D. and Anbar A. D. (2013) Uranium concentrations and238U/235U isotope ratios in modern carbonates from the Bahamas: Assessing a novel paleoredox proxy. *Chem. Geol.* **362**, 305–316.

Rudnick R. L. and Fountain D. M. (1995) <Rudnick-1995.pdf>. , 267–309.

Rudnick R. L. and Gao S. (2003) The composition of the continental crust. In *Treatise on Geochemistry* pp. 1–64.

Rye R. and Holland H. D. (1998) Paleosols and the evolution of atmospheric oxygen: a critical review. *Am. J. Sci.* **298**, 621–72. Available at: http://www.ncbi.nlm.nih.gov/pubmed/11542256.

Satkoski A. M., Beukes N. J., Li W., Beard B. L. and Johnson C. M. (2015) A redox-stratified ocean 3.2 billion years ago. *Earth Planet. Sci. Lett.* **430**, 43–53. Available at: http://dx.doi.org/10.1016/j.epsl.2015.08.007.

Schröder S., Beukes N. J. and Armstrong R. A. (2016) Detrital zircon constraints on the tectonostratigraphy of the Paleoproterozoic Pretoria Group, South Africa. *Precambrian Res.* **278**, 362–393. Available at: https://linkinghub.elsevier.com/retrieve/pii/S0301926816300298.

Schröder S., Lacassie J. P. and Beukes N. J. (2006) Stratigraphic and geochemical framework of the Agouron drill cores, Transvaal Supergroup (Neoarchean-Paleoproterozoic, South Africa). *South African J. Geol.* **109**, 23–54.

Scott C., Lyons T. W., Bekker A., Shen Y., Poulton S. W., Chu X. and Anbar A. D. (2008) Tracing the stepwise oxygenation of the Proterozoic ocean. *Nature* **452**, 456–459. Available at: http://www.nature.com/doifinder/10.1038/nature06811.

Siebert C., Kramers J. D., Meisel T., Morel P. and Nägler T. (2005) PGE, Re-Os, and Mo isotope systematics in Archean and early Proterozoic sedimentary systems as proxies for redox conditions of the early Earth. *Geochim. Cosmochim. Acta* **69**, 1787–1801. Available at: http://linkinghub.elsevier.com/retrieve/pii/S001670370400794X.

Stirling C. H., Andersen M. B., Potter E. K. and Halliday A. N. (2007) Low-temperature isotopic fractionation of uranium. *Earth Planet. Sci. Lett.* **264**, 208–225.

Sumner D. Y. and Beukes N. J. (2006) Sequence Stratigraphic Development of the Neoarchean Transvaal carbonate platform, Kaapvaal Craton, South Africa. *South African J. Geol.* **109**, 11–22. Available at: https://dx.doi.org/10.2113/gssajg.109.1-2.11.

Taylor S. R. and McLennan S. M. (1985) S. R. Taylor & S. M. McLennan 1985. The Continental Crust: Its Composition and Evolution. xvi + 312 pp. Oxford, London, Edinburgh, Boston, Palo Alto, Melbourne: Blackwell Scientific. Price £16.80 (paperback). ISBN 0 632 01148 3. *Geol. Mag.* **122**, 673. Available at: http://www.journals.cambridge.org/abstract_S0016756800032167.

Thomazo C., Ader M., Farquhar J. and Philippot P. (2009) Methanotrophs regulated atmospheric sulfur isotope anomalies during the Mesoarchean (Tumbiana Formation, Western Australia). *Earth Planet. Sci. Lett.* **279**, 65–75. Available at: http://dx.doi.org/10.1016/j.epsl.2008.12.036.

Thomazo C., Ader M. and Philippot P. (2011) Extreme 15N-enrichments in 2.72-Gyr-old sediments: Evidence for a turning point in the nitrogen cycle. *Geobiology* **9**, 107–120.

Thorne A. M. and Trendall A. F. (2001) *Geology of the Fortescue Group, Pilbara Craton, Western Australia.*, Geological Survey of Western Australia, Department of Minerals and Energy.

Tissot F. L. H. and Dauphas N. (2015) Uranium isotopic compositions of the crust and ocean: Age corrections, U budget and global extent of modern anoxia. *Geochim. Cosmochim. Acta* **167**, 113–143.

Tribovillard N., Algeo T. J., Lyons T. W. and Riboulleau A. (2006) Trace metals as paleoredox and paleoproductivity proxies: An update. *Chem. Geol.* **232**, 12–32.

Voegelin A. R., Nägler T. F., Beukes N. J. and Lacassie J. P. (2010) Molybdenum isotopes in late Archean carbonate rocks: Implications for early Earth oxygenation. *Precambrian Res.* **182**, 70–82. Available at: http://dx.doi.org/10.1016/j.precamres.2010.07.001.

Wang X., Johnson T. M. and Lundstrom C. C. (2015) Isotope fractionation during oxidation of tetravalent uranium by dissolved oxygen. *Geochim. Cosmochim. Acta* **150**, 160–170. Available at: http://dx.doi.org/10.1016/j.gca.2014.12.007.

Wang X., Planavsky N. J., Hofmann A., Saupe E. E., De Corte B. P., Philippot P., LaLonde S. V., Jemison N. E., Zou H., Ossa Ossa F., Rybacki K., Alfimova N., Larson M. J., Tsikos H., Fralick P. W., Johnson T. M., Knudsen A. C., Reinhard C. T. and Konhauser K. O. (2018) A Mesoarchean Shift in Uranium Isotope Systematics. *Geochim. Cosmochim. Acta* **238**, 438–452. Available at: https://linkinghub.elsevier.com/retrieve/pii/S0016703718304101.

Wang X., Planavsky N. J., Reinhard C. T., Hein J. R. and Johnson T. M. (2016) A cenozoic seawater redox record derived from238U/235U in ferromanganese crusts. *Am. J. Sci.* **315**, 64–83.

Weyer S., Anbar A. D., Gerdes A., Gordon G. W., Algeo T. J. and Boyle E. A. (2008) Natural fractionation of 238U/235U. *Geochim. Cosmochim. Acta* **72**, 345–359.

Wille M., Kramers J. D., Nägler T., Beukes N. J., Schröder S., Meisel T., Lacassie J. P. and Voegelin A. R. (2007) Evidence for a gradual rise of oxygen between 2.6 and 2.5 Ga from Mo isotopes and Re-PGE signatures in shales. *Geochim. Cosmochim. Acta* **71**, 2417–2435.

Wille M., Nebel O., Van Kranendonk M. J., Schoenberg R., Kleinhanns I. C. and Ellwood M. J. (2013) Mo-Cr isotope evidence for a reducing Archean atmosphere in 3.46-2.76Ga black shales from the Pilbara, Western Australia. *Chem. Geol.* **340**, 68–76. Available at: http://dx.doi.org/10.1016/j.chemgeo.2012.12.018.

Wille M., Schoenberg R., Bui T. H., Wing B. A., Eickmann B. and Hofmann A. (2018) Isotopic evidence for oxygenated Mesoarchaean shallow oceans. *Nat. Geosci.* **11**, 133–138. Available at: http://dx.doi.org/10.1038/s41561-017-0036-x.

Xu G., Hannah J. L., Bingen B., Georgiev S. and Stein H. J. (2012) Digestion methods for trace element measurements in shales: Paleoredox proxies examined. *Chem. Geol.* **324**–**325**, 132–147. Available at: http://dx.doi.org/10.1016/j.chemgeo.2012.01.029.

Supplementary

S 1. Further information on methods

S.1.1 Method testing and lab work at Leibniz University of Hannover

Any lab work in Hannover was carried out in a clean-air hood (type 10). Water used in this study was provided via a Millipore water purification system that produces 18 MΩ water, called MQ water throughout this study. Acids (HCl and HNO_3) used in this study have been cleaned at sub-boiling conditions in a quartz glass or teflon PicoTrace distillation system, respectively. Hydrogen peroxide (30 %) and hydrofluoric acid (40 %) were supplied as suprapure grade by Merck KGaA (Darmstadt, Germany). All analyzer PE tubes and pipette tips have been soaked with 1 M HNO_3 and MQ water each for 7 days. All Teflon and PE bottles have been cleaned with 6 M HCl and 1 M HNO_3 respectively at 50 °C for at least three days. All Savillex® teflon beakers have been cleaned mechanically with water and a tissue. Then, they have been cleaned further for 24 h in 6 M HCl, 7.5 M HNO_3 and MQ water, respectively, at 120 °C. Eichrom UTEVA resin was stored and pre-cleaned in 0.05 M HCl and further cleaning was carried out immediately prior the separation procedure.

Carbonate leaching methods were tested on reference materials JLs-1 and JDo-1 (Imai et al., 1996) for leaching acids 1 M HCl, 6 M HCl and 3 M HNO_3 in comparison to previously published methods (Brennecka et al., 2011; Romaniello et al., 2013; Azmy et al., 2015; Lau et al., 2016). Therefore, both materials were ashed at 500 °C and 750 °C and leached in respective acid at 60 °C for roughly 20 hours. The remaining residue (fraction called 'R' in figure S 1) was dissolved with a multi-acid approach. First, 14 ml of a 3:1 mixture of HCl (37 %) and HNO_3 (65 %) was added and heated overnight at 140 °C. Any remaining solids were then treated with a 1:1 mixture of HF (40 %) and HNO_3 (65 %). The dissolved fractions were evaporated and refluxed with 3 M HNO_3. All fractions (Uranium leachate and residues) were measured concerning their U concentrations with the Thermo Fisher Scientific Element XR single-collector mass spectrometer (Noordmann et al., 2015). Rhodium was used for internal standardization and a 5-point external calibration, diluted from pure standard solutions, in the range from 1 ng g^{-1} to 100 ng g^{-1} was applied. Standard and sample solutions were diluted to yield 3 vol% HNO_3. Results for leaching tests are shown in figure S 1. Remarkably, 1 M HCl is not an appropriate leaching acid for U, however, 6 M HCl and 3 M HNO_3 both yielded good results within analytical error. As nitric acid is used in the further chemical separation of U from any remaining matrix, it was chosen as leaching acid for all following samples to avoid further evaporating steps. The ashing temperature of 750 °C was found to be appropriate in removing all volatile compounds from carbonate samples and was adopted for further analyses.
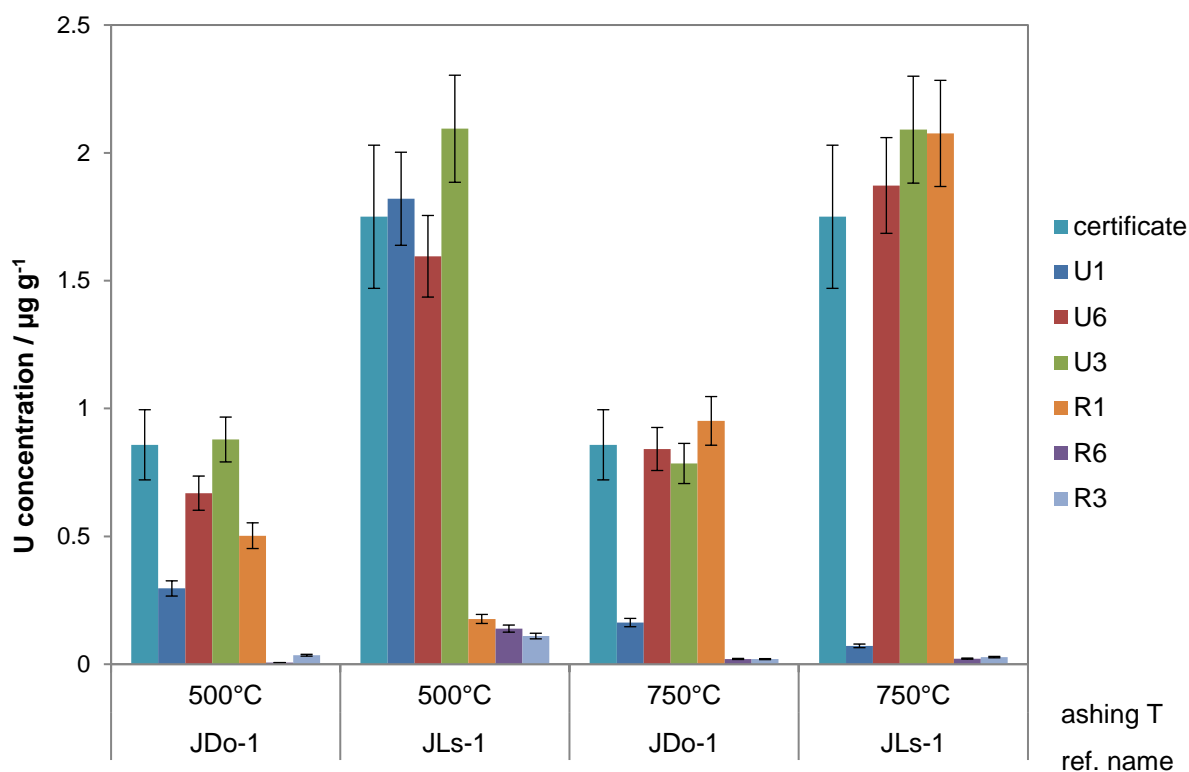
Figure S 1: Uranium yield during leaching tests for different acids. Error bars denote standard deviation; for our measurements they are ~10% (compare table S 10 and S 11). Certificate values (SD and concentration) are from Imai et al. (1996). 'U' describes the respective U fraction, whereas 'R' describes the residuum, '1', '6', and '3' describe leaching with 1 M HCl, 6 M HCl, and 3 M HNO$_3$, respectively.

All fractions were measured concerning their U isotope ratios according to the described method from the main text except for the 1 M HCl leach. Here, only JLs-1 ashed at 500°C was measured because the others did not successfully leach (see figure S 1). During the sequence, the reference materials SDO-1, IRMM-184, and Reimep-18a were measured repeatedly. SDO-1 gave δ^{238}U = -0.08 ± 0.05 ‰ and δ^{234}U = -5.70 ± 2.11 ‰ (n = 13), IRMM-184 gave δ^{238}U = -1.17 ± 0.04 ‰ and δ^{234}U = -26.22 ± 1.65 ‰ (n = 28), and Reimep-18a gave δ^{238}U = -0.26 ± 0.04 ‰ and δ^{234}U = 36.34 ± 1.70 ‰ (n = 28). Variability in δ^{234}U values was high due to a badly calibrated 10^{13} Ω amplifier attached to the faraday cup for measurements of the low abundant ^{234}U. However, resulting higher 2 s.d. values and a lower accuracy do not change results significantly compared to the high natural variability in the δ^{234}U values (Table S 1).

Additionally, JDo-1 and JLs-1 were leached during sample processing again. In total, the leached reference materials gave the following results. All JDo-1 fractions gave δ^{238}U = -0.17 ‰ ± 0.11 ‰ (n = 25) and all JLs-1 fractions δ^{238}U = -0.25 ‰ ± 0.05 ‰ (n = 31). Detailed results are shown in the following table S 1.

Table S 1: Detailed results for δ²³⁸U and δ²³⁴U$_{sec.EQ}$ in leached reference materials. 2 s.d. values are for replicate measurements.

Sample	Ashing T / °C	Leaching acid	δ²³⁸U / ‰	δ²³⁴U$_{sec.EQ}$ / ‰	Average δ²³⁸U / ‰	2 s.d. δ²³⁸U / ‰	Average δ²³⁴U$_{sec.EQ.}$ / ‰	2 s.d. δ²³⁴U$_{sec.EQ.}$ / ‰	n
JDo-1	500	6 M HCl	-0.18	37.86	-0.19	0.01	38.12	0.47	3
JDo-1	500	6 M HCl	-0.19	38.32					
JDo-1	500	6 M HCl	-0.20	38.17					
JDo-1	500	3 M HNO3	-0.12	21.47	-0.13	0.05	21.58	0.21	3
JDo-1	500	3 M HNO3	-0.16	21.68					
JDo-1	500	3 M HNO3	-0.11	21.59					
JDo-1	750	6 M HCl	-0.11	-2.68	-0.12	0.05	-2.49	0.34	3
JDo-1	750	6 M HCl	-0.10	-2.41					
JDo-1	750	6 M HCl	-0.15	-2.38					
JDo-1	750	3 M HNO3	-0.15	-2.86	-0.15	0.01	-2.76	0.30	2
JDo-1	750	3 M HNO3	-0.16	-2.65					
JLs-1	500	1 M HCl	-0.21	26.79	-0.23	0.04	26.88	0.29	3
JLs-1	500	1 M HCl	-0.24	26.79					
JLs-1	500	1 M HCl	-0.25	27.04					
JLs-1	500	6 M HCl	-0.24	22.48	-0.25	0.02	22.44	0.56	3
JLs-1	500	6 M HCl	-0.24	22.69					
JLs-1	500	6 M HCl	-0.26	22.14					
JLs-1	500	3 M HNO3	-0.24	13.10	-0.23	0.01	13.08	0.10	3
JLs-1	500	3 M HNO3	-0.23	13.12					
JLs-1	500	3 M HNO3	-0.23	13.03					
JLs-1	750	6 M HCl	-0.25	6.68	-0.25	0.03	6.89	0.42	3
JLs-1	750	6 M HCl	-0.24	6.90					
JLs-1	750	6 M HCl	-0.27	7.10					
JLs-1	750	3 M HNO3	-0.22	7.20	-0.26	0.05	7.37	2.03	19
JLs-1	750	3 M HNO3	-0.22	6.95					
JLs-1	750	3 M HNO3	-0.27	6.85					
JLs-1	750	3 M HNO3	-0.26	9.26					
JLs-1	750	3 M HNO3	-0.29	9.32					
JLs-1	750	3 M HNO3	-0.28	6.28					
JLs-1	750	3 M HNO3	-0.28	6.44					
JLs-1	750	3 M HNO3	-0.23	6.61					
JLs-1	750	3 M HNO3	-0.22	6.43					
JLs-1	750	3 M HNO3	-0.28	5.47					
JLs-1	750	3 M HNO3	-0.24	6.84					
JLs-1	750	3 M HNO3	-0.30	7.05					
JLs-1	750	3 M HNO3	-0.27	7.68					
JLs-1	750	3 M HNO3	-0.28	7.65					
JLs-1	750	3 M HNO3	-0.25	7.88					
JLs-1	750	3 M HNO3	-0.28	7.85					
JLs-1	750	3 M HNO3	-0.27	7.39					
JLs-1	750	3 M HNO3	-0.27	8.66					
JLs-1	750	3 M HNO3	-0.28	8.27					
JDo-1-1	750	3 M HNO3	-0.32	-1.31	-0.19	0.13	-3.38	1.70	14
JDo-1-1	750	3 M HNO3	-0.21	-2.49					
JDo-1-1	750	3 M HNO3	-0.21	-4.49					
JDo-1-1	750	3 M HNO3	-0.14	-4.60					
JDo-1-1	750	3 M HNO3	-0.16	-4.15					
JDo-1-1	750	3 M HNO3	-0.15	-4.13					
JDo-1-2	750	3 M HNO3	-0.33	-3.50					
JDo-1-2	750	3 M HNO3	-0.19	-3.34					
JDo-1-2	750	3 M HNO3	-0.13	-3.37					
JDo-1-2	750	3 M HNO3	-0.13	-3.22					
JDo-1-2	750	3 M HNO3	-0.14	-3.61					
JDo-1-2	750	3 M HNO3	-0.22	-3.20					
JDo-1-2	750	3 M HNO3	-0.14	-2.86					
JDo-1-2	750	3 M HNO3	-0.14	-3.12					

Comparison between δ²³⁸U of bulk and leached fractions of core PDP-1 samples revealed no isotopic difference within analytical errors between both methods for all of three samples and

the reference material JDo-1 (table S 2). This also applies to two of the three tested samples (67.55 and 68.19), however, the third sample, 42.65, shows a significantly heavier signature in the corrected fraction compared to the leached and bulk ones. This offset can be explained with the very low EF_U of only 1.21 (vs. PAAS) which results in an overestimation of the authigenic $\delta^{238}U$ portion compared to the detrital one. Hence, a detrital correction should not be applied to samples with these low EF_U. For samples 67.55 and 68.19 the main fractions hosting U are authigenic phases that overcome detrital contributions. Also, the leaching method itself does not produce isotope offsets in $^{238}U/^{235}U$. Nevertheless, we find the $\delta^{234}U_{sec.EQ.}$ value sample 68.19 being higher in the leached fraction compared to the bulk value, which may hint at incomplete dissolution. On the other hand, the two other samples (42.66 and 67.55) are higher in the leached fractions compared to whole-rocks. This is indicative of preferential leaching of ^{234}U compared to ^{238}U and is in accordance with our previous method testing on JDo-1 and JLs-1. Here, however, JDo-1 did not fractionate $^{234}U/^{238}U$ nor $^{238}U/^{235}U$ during the whole leaching method.

Table S 2: Comparison of EF_U, $\delta^{234}U_{sec.EQ}$, and $\delta^{238}U$ of leached (index L) and whole-rock digests (bulk and detritus corrected, indexed by authigenic) of samples from core PDP-1. 2 s.d. values are for replicate measurements.

sample	EF_U	$\delta^{238}U_{leached}$ / ‰	$\delta^{238}U_{bulk}$ / ‰	$\delta^{238}U_{authigenic}$ / ‰	$\delta^{238}U$ 2 s.d. / ‰	$\delta^{234}U_{sec.EQ.}$ / ‰	$\delta^{234}U_{sec.EQ.}$ 2 s.d. / ‰
42.65 L		-0.32			0.05	166.65	2.41
42.65	1.21		-0.27	-0.15	0.02	126.61	1.80
67.55 L		-0.28			0.02	103.11	2.11
67.55	2.85		-0.28	-0.31	0.03	-14.22	1.48
68.19 L		-0.26			0.01	-19.37	1.94
68.19	2.43		-0.30	-0.29	0.03	-66.16	0.97
JDo-1 L		-0.19			0.05	-8.46	2.56
JDo-1			-0.19		0.00	-7.65	1.07

S.1.2 Method testing at Goethe-University of Frankfurt

Inverse aqua regia leaching and bulk digestion was tested on reference materials SDO-1, SBC-1, and some samples for trace element concentrations and U isotope compositions (Rammensee, 2016). Uranium concentration yielded 117.62 % recovery in bulk digested SDO-1 and 69.06 % in the leached fraction (both n=8). For SBC-1, U was recovered with 97.22 % in the bulk digested aliquots (n=6) and with 34.72 % in the leached fractions (n=7). In total, SDO-1 was digested three times as bulk sample and four times as leached samples for U isotope measurements. SBC-1 was digested each three times as bulk and leached samples. All those aliquots were measured as triplicates (n=3) during U isotope measurements. The results show, that even with varying U recovery, the U isotope composition is reproducible and indifferent of the used dissolution method (Table S 3). It strikes that the $\delta^{234}U$ values in the leached fractions are highly out of secular equilibrium, however, for both reference materials,

the δ^{238}U values are in accordance with previously published values (Tissot and Dauphas, 2015). This implies that the leaching method does not affect the isotopes ^{238}U and ^{235}U and can be well used to attack only one component in sedimentary rocks. For SDO-1 the δ^{238}U value is highly depleted whereas for SBC-1 it is highly enriched indicative of a differing and uncommon process affecting the isotope ^{234}U. Also, compared with the other reference materials JDo-1 and JLs-1, only SDO-1 fractionated δ^{234}U into negative values.

Table S 3: Comparison of U isotope composition of bulk and leached SDO-1 and SBC-1 reference materials.

sample	n	δ^{238}U / ‰	δ^{238}U 2 s.d. / ‰	δ^{234}U / ‰	δ^{238}U 2 s.d. / ‰
			bulk digest		
SDO-1 a	3	-0.07	0.02	3.26	1.42
SDO-1 b	3	-0.09	0.05	-2.20	1.20
SDO-1 c	3	-0.08	0.05	2.86	0.75
Average	12	-0.08	0.04	1.31	1.12
SBC-1 a	3	-0.35	0.02	-1.21	0.44
SBC-1 b	3	-0.28	0.06	-0.26	2.24
SBC-1 c	3	-0.27	0.02	-1.23	1.64
Average SBC-1	12	-0.30	0.03	-0.90	1.44
leached digest					
SDO-1 a	3	0.19	0.06	-188.51	1.36
SDO-1 b	3	-0.10	0.02	-196.80	0.82
SDO-1 c	3	-0.08	0.01	-226.90	0.13
SDO-1 d	3	-0.12	0.05	-206.33	1.02
Average SDO-1	15	-0.03	0.03	-204.63	0.83
SBC-1 a	3	-0.26	0.01	224.71	2.45
SBC-1 b	3	-0.29	0.06	306.74	0.68
SBC-1 c	3	-0.30	0.03	308.39	0.55
Average SBC-1	12	-0.28	0.04	279.95	1.23
difference between both methods					
SDO-1		-0.05		205.94	
SBC-1		-0.02		-280.85	

In table S 4, the results from leaching and whole-rock digests (bulk and detritus corrected) of samples from the BARB-3 and BARB-5 cores are shown. They reveal, that except for one sample (BARB-5-761.80) the δ^{238}U values of leach digest are lower or the same as bulk digest within analytical error. This indicates that the leaching method either attacks the authigenic fraction which has a lower δ^{238}U signatures or it fractionates the bulk signature with preferential release of lighter ^{235}U. The values for bulk digest were corrected for their detrital component and this calculation resulted in a shift of the bulk values toward lower authigenic δ^{238}U values or did not change the value within analytical errors. However, and most likely due to the very low U contents in those samples (EF$_U$ < 2 for 18 out of 22 samples), the detrital correction generally produces a high offset between bulk and authigenic δ^{238}U signatures and for three samples (BARB3-208.90, BARB3-211.44, and BARB3-212.10) did not produce reasonable values at all. Hence, the detrital correction should only be applied to samples with adequate U contents which applies to four samples with EF$_U$ > 2 (BARB5-560.00, BARB5-599.83, BARB5-

675.22, and BARB5-686.13). The $\delta^{234}U$ values of the inverse aqua regia leach show a significant offset to bulk digested samples with the leached fractions being highly enriched in ^{234}U. Such values can only be explained with an method artefact that preferentially releases ^{234}U. In comparison to the other leaching tests with 3 M HNO_3, aqua regia leaching produces higher artefacts in $\delta^{234}U$ values. Hence, for interpretation of $\delta^{234}U$ values only bulk digests are applicable.

Table S 4: Comparison of EF_U, $\delta^{234}U_{sec.EQ}$, and $\delta^{238}U$ of leached and whole-rock digests (bulk and detritus corrected, indexed by auth) of samples from cores BARB-3 and BARB-5. Values in brackets are not reasonably corrected. 2 s.d. values are for replicate measurements.

sample	EF_U	$\delta^{238}U$ leach / ‰	$\delta^{238}U$ bulk / ‰	$\delta^{238}U_{auth}$ / ‰	$\delta^{238}U$ 2 s.d. / ‰	$\delta^{234}U_{sec.EQ}$. leach / ‰	$\delta^{234}U_{sec.EQ}$ leach 2 s.d. / ‰	$\delta^{234}U_{sec.EQ}$ bulk / ‰	$\delta^{234}U_{sec.EQ}$ bulk 2 s.d. / ‰
BARB5-205.17	1.58	-0.47	-0.36	-0.58	0.02	183.8	1.23	1.2	1.42
BARB5-265.30	1.99	-0.38	-0.39	-0.53	0.01	479.4	0.36	2.8	1.85
BARB5-289.65	1.49	-0.34	-0.37	-0.69	0.04	548.7	2.12	-7.1	0.56
BARB5-304.77	1.93	-0.36	-0.35	-0.43	0.01	479.5	4.41	-8.3	2.77
BARB5-389.515	1.26	-0.41	-0.32	-0.81	0.04	369.1	0.36	-7.5	6.81
BARB5-500.10	1.47	-0.56	-0.30	-0.27	0.06	882.2	1.11	6.6	1.00
BARB5-515.345	1.69	-0.37	-0.33	-0.40	0.05	600.0	0.81	-2.0	1.11
BARB5-560.00	2.32	-0.40	-0.42	-0.55	0.03	802.4	1.95	4.7	2.04
BARB5-599.83	2.49	-0.41	-0.33	-0.36	0.02	729.8	1.30	2.2	1.40
BARB5-630.425	1.62	-0.41	-0.31	-0.34	0.01	999.1	0.97	4.9	2.20
BARB5-675.22	5.44	-0.44	-0.41	-0.44	0.05	806.8	2.92	0.7	0.75
BARB5-686.13	3.88	-0.40	-0.41	-0.47	0.04	1061.0	0.97	2.6	2.32
BARB5-700.01	1.86	-0.40	-0.31	-0.34	0.03	753.1	1.00	-12.6	0.52
BARB5-730.51	1.89	-0.37	-0.36	-0.46	0.00	1085.3	1.85	-4.5	2.83
BARB5-744.74	1.63	-0.48	-0.31	-0.33	0.09	738.5	1.62	-16.1	0.58
BARB5-760.15	1.81	-0.31	-0.35	-0.47	0.04	482.5	2.03	-1.6	2.27
BARB5-761.80	1.57	-0.10	-0.28	-0.23	0.10	1087.0	20.00	-8.4	0.03
BARB3-208.90	1.27	-0.51	-0.36	(-2.07)	0.03	410.3	0.47	7.2	1.96
BARB3-211.44	2.14	-1.04	-0.86	(-1.60)	0.05	221.6	2.19	105.2	10.00
BARB3-212.10	1.26	-0.40	-0.32	(-1.24)	0.02	1195.8	0.43	8.9	0.32
BARB3-212.45	1.24	-0.44	-0.30	-0.41	0.00	1051.7	2.27	6.3	0.44
BARB3-212.70	1.06	-0.46	-0.27	-0.48	0.06	779.3	0.55	6.0	0.69

S 2. Stratigraphy and lithologic information

S 2.1 Cores DP-16 and KMF-5, Pretoria and Chuniespoort Group, ~2.22 Ga to ~2.55 Ga

The Timeball Hill formation stratigraphically overlies the Duitschland formation and both belong to the Pretoria group that is part of the Transvaal supergroup and is exposed in the Transvaal basin in South Africa. The Duitschland formation has been dated by single zircon analyses to have a depositional age of 2424 ± 24 Ma whereas the youngest single grain age of the Timeball Hill formation is 2324 ± 17 Ma (Schröder et al., 2016). The contact between both units is reconsidered to be conformable to para-conformable with a minor time gap and places the

top of the Duitschland formation at about 2320 Ma (Bekker et al., 2001; Schröder et al., 2016). The Duitschland formation is divided into two parts that are separated by a distinct conglomerate boundary and has been deposited in a marine depositional environment (Bekker et al., 2001). The Lower Duitschland formation consists mainly of chert, finely-laminated carbonaceous shale and interbedded layers of limestone, marl and breccia. The Upper Duitschland formation consists of fine- to coarse-grained quartzite, conglomerates and shale, that is intercepted by carbonate layers (Bekker et al., 2001). The Timeball Hill formation is mainly composed of shale, conglomerate and a sandstone/quartzite unit and has been deposited in a marine to marginal marine environment (Catuneanu and Eriksson, 2002). The cores DP-16 and KMF-5 (main core) comprise both units (Figure S 2), however, in KMF-5 the Duitschland formation has several hiatuses. From DP-16 we sampled eleven (black) shales, one marly shale, one mudstone/shale, one mudstone, and three quartzites. From the KMF-5 main core, we chose 8 laminated shale/siltstones and 8 black shales for analyses.

Stratigraphically beneath the Pretoria Group lies the Chuniespoort group. These sediments were sampled with the KMF-5 diversion core, which was drilled ~40° from the bottom of the KMF-5 main core to optimize the sedimentary thickness of the Chuniespoort group. In downward order, this unit consists of the Tongwane formations, the Penge iron formation and the Malmani subgroup. The latter consists of the Frisco, Eccles, Lyttleton, Monte Christo, and Oaktree formations in downward order and can be stratigraphically correlated with the GKP-01 and BH-1 cores (section S 2.2). The Malmani subgroup is stratigraphically above the Black Reef formation. In the KMF-5 diversion core, the Penge iron formation is not exposed due to an erosional surface (Eroglu et al., 2015). The Malmani subgroup represents a carbonate platform that can be stratigraphically correlated with the Campbellrand platform in the Griqualand West Basin (Bekker et al., 2001; Sumner and Beukes, 2006; Eroglu et al., 2015). It comprises mainly peritidal dolomitic stromatolites with varying degrees of silicification (Eroglu et al., 2017). We picked two pure carbonate samples, one from the Eccles and one from the Lyttleton formation for analyses.
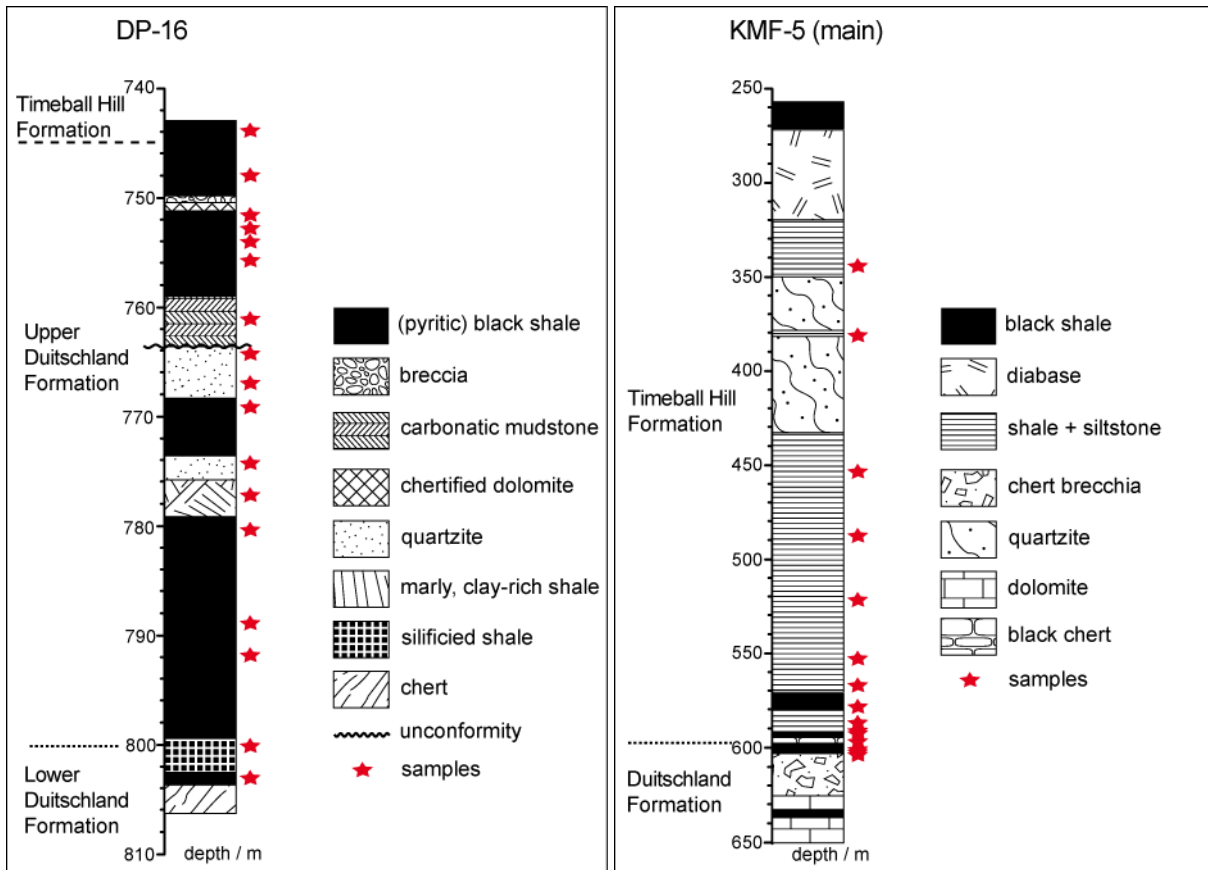
Figure S 2: Stratigraphy of cores DP-16 and KMF-5 (main core). Asterisks highlight sample positions.

S 2.2 Cores BH-1 and GKP-01, Ghaap Group, ~2.47 Ga to ~2.64 Ga

The Ghaap Group is stratigraphically beneath the Potsmasburg Group and above the Vryburg formation. It is exposed in the Griqualand West Basin, Prieska area and Griqualand West area, in South Africa and can be stratigraphically correlated with the Chuniespoort Group in the Eastern Transvaal Basin (Schröder et al., 2006; Wille et al., 2007; Voegelin et al., 2010; Eroglu et al., 2015; Eroglu et al., 2017). The Ghaap Group consists of several subgroups and formations, that are in downward order: the Koegas subgroup, regionally either the Griquatown or Kuruman iron formation, and the lowermost Campbellrand subgroup. Our samples from drillcores BH-1 and GKP-01 (Figure S 3) originate from the Campbellrand subgroups and depending on their drilling locality, the subgroup is divided into different formations that can be correlated with the Kamden Member (Bekker et al., 2001). Also, both cores can be stratigraphically correlated with the KMF-5 core, Chuniespoort Group (Figure S 3) (Bekker et al., 2001; Sumner and Beukes, 2006; Eroglu et al., 2015). In the Griqualand West area, the drillcore BH-1 exposes the Gamohan, Kogelbeen, Klippan, Papkuil, Klipfontein-Heuwel, Fairfield, Kamden Member, Reveilo, and Monteville formations in downward order. We chose two calcites, five dolomites, two pure carbonates, and one detritus-containing carbonate to be

analyzed for U isotopes, that have been previously analyzed (Eroglu et al., 2015; Eroglu et al., 2017). In the Prieska area, the drillcore GKP-01 contains sediments from the Klein Naute, Upper Nauga, Kamden Member, Lower Nauga and Monteville formations in downward order. Our samples comprise black shales (n = 25), dolomites (n = 14), and one limestone (Figure S 3, Siebert et al., 2005; Wille et al., 2007; Voegelin et al., 2010). The Campbellrand subgroup belongs to the Neoarchean shallow marine Malmani-Campbellrand carbonate platform that has been found to be an early environment with enriched oxygen concentrations based on Mo isotopes, redox-sensitive trace metals, N isotopes, and microbial facies (Wille et al., 2007; Godfrey and Falkowski, 2009; Voegelin et al., 2010; Eroglu et al., 2015). It consist mainly of stromatolitic carbonate rocks that have been deposited under shallow subtidal conditions (Eroglu et al., 2017).
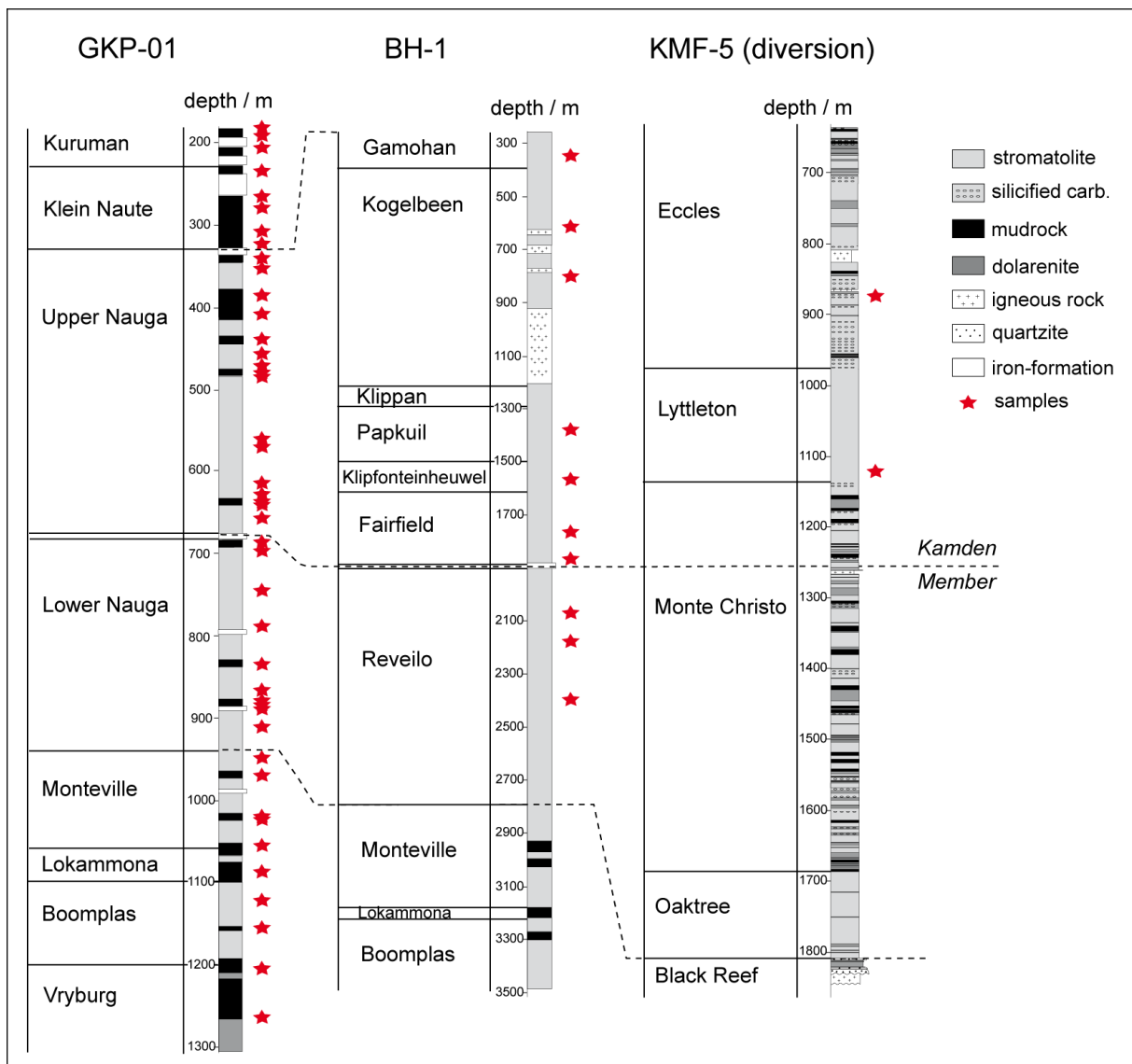
Figure S 3: Stratigraphy of cores GKP-01, BH-1, and KMF (diversion core) modified from Schröder et al., (2006) and Eroglu et al. (2017). Asterisks highlight sample positions.

S 2.3 Nercmar core, Ngezi Group, ~2.7 Ga

The sedimentary Manjeri formation belongs to the 2.7 Ga Ngezi Group of the Belingwe Greenstone Belt in Zimbabwe (Hunter et al., 1998; Hofmann and Kusky, 2004; Planavsky et al., 2014). The Manjeri formation can be subdivided into three members; the basal Spring Valley Member, Rubweruchena Member and the upper Jimmy Member. The Spring Vallley unit consists of conglomerate interbedded with sandstone beneath layers of ironstone-shale-siltstone (Hunter et al., 1998). Our black shale samples originate from the Nercmar core that covers the entire Manjeri formation as well as above and below laying horizons (see Hunter et al. (1998) for desription of drillcore).

S 2.4 Core PDP-1, Fortescue Group

The Tumbiana formation is part of the Fortescue group (Mount Bruce supergroup) and is exposed in the Fortescue Basin in Western Australia (Hickman and Van Kranendonk, 2012) which unconformably overlies the Archean Pilbara craton. This craton has been found to be correlative with the Kaapvaal craton in south Africa as both presumably were connected in the Archean times (de Kock et al., 2009). Thus, the Australian samples can be used to gain additional information on marine depositional conditions together with South African samples. The Fortescue basin consists of volcanic and sedimentary rocks that were deposited during 2.78 Ga and 2.63 Ga on top of the granitoid-greenstone basement of the craton. The Tumbiana formation itself has a depositional age of 2.727 - 2.715 Ga (Blake et al., 2004; Hickman and Van Kranendonk, 2012) and consists of large-scale cross-bedded calcareous sandstone, stromatolitic and fenestrate carbonate (limestone) associated with mudstone (Figure S 4), and micaceous sandstone, which are interlayered with volcanic fine-grained siltstone (Thorne and Trendall, 2001). The drillcore PDP-1 was drilled in 2004 and covers the upper Tumbiana and overlying Maddina formations (Thomazo et al., 2009). Its mineral assemblage consists mainly of quartz, green chlorite, carbonate and pyrite (Thomazo et al., 2009). For our analyses, we picked eight stromatolitic samples, of which two were separated each into a silicate and a carbonate and organic rich layer, respectively (samples from 78.6 m and 72 m, Figure S 4).
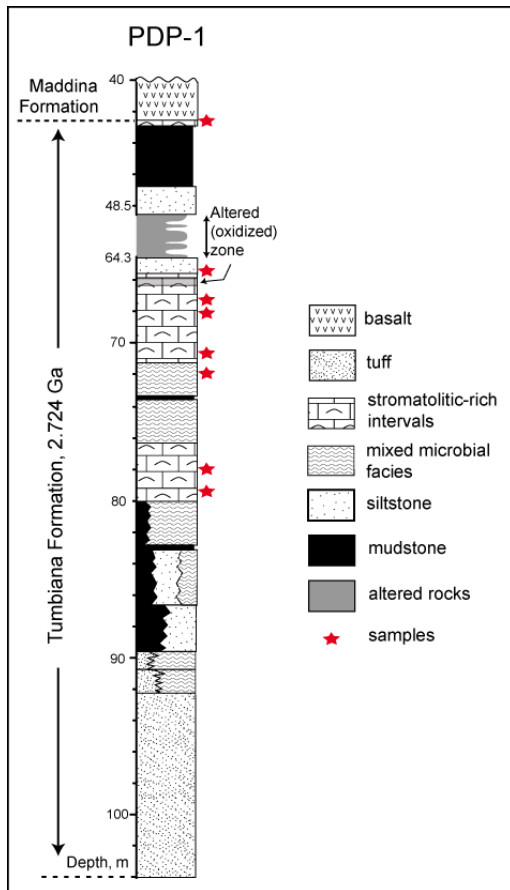
Figure S 4: Stratigraphy of core PDP-1 from Western Australia. Modified from Thomazo et al. (2009).

S 2.5 Cores BARB-3 and BARB-5, Fig Tree and Onverwacht groups, ~3.22 to 3.44 Ga

The relevant stratigraphic units of the Barberton Greenstone Belt (BGB) in this study are the volcano-sedimentary Fig Tree Group and the sediments of the Onverwacht Group. Age constraints of the deposition of the Fig Tree Group are provided by radiometric zircon dating (3243 ± 4 Ma to 3225 ± 5 Ma Pb-Pb, Kröner and Todt, 1988; 3259 ± 3 Ma to 3255 ± 3 Ma Pb-Pb, Byerly et al., 1996; 3223.4 ± 0.3 Ma CA-ID-TIMS U-Pb, Heubeck et al., 2013) of zircons found in tuff near stratigraphic boundaries. Direct Re-Os dating of the Fig Tree Group sediments has been tried on samples collected at surface outcrops but failed due to alteration and Re-loss (Siebert et al., 2005). Constraints on sedimentary parts of the Onverwacht Group are given e.g. for the Kromberg Fm. (top: 3334 ± 4 Ma Pb-Pb, Byerly et al., 1996) and the older thick succession of chert, the so-called Buck reef chert (base: 3416 ± 3 Ma Pb-Pb, Kröner and Todt, 1988). Komatiite flow events have been dated using Pb-Pb on zircons (top Komati Fm. 3445 ± 3 Ma, Komati Fm. 3482 ± 5 Ma, Kröner and Todt, 1988; Armstrong et al., 1990) and Re-Os isochrones (Komati formation 3484 ± 38 Ma and Weltevreden formation 3263 ± 12 Ma, Puchtel et al., 2014). The Barberton Drilling Project (Arndt, 2012) gave the opportunity to investigate samples free of recent surface alteration. The BARB-5 drill core was obtained from

the Barite Valley and was driven in Mapepe formation rocks (Mason et al., 2013). The BARB-3 drill core obtained among other units a >700 m thick, incomplete transection of the Buck Reef Chert. A <10 m thin carbonaceous shale unit is located directly on top of the chert sequence underneath a ca. 150 m ultramafic sill (Hofmann et al., 2013). The shale unit probably is a lower part of the Kromberg formation that is dominated by subaerial komatiitic lava flows interlayered with clastic sediments.

BARB-5 core was sampled with a resolution of approximately 2.5 m stratigraphic depth and 24 samples from stratigraphic units 1 – 3 were chosen to be analyzed in this study. Samples from unit 1 are described as carbonaceous shales (n=13), shale (n=1) and shale with iron formation clasts (n=1). Samples from unit 2 are carbonaceous shale (n=7) and sandy shale (n=1). The single sample of unit 3 is sandy shale.

From BARB-3 core, a small interval was sampled by 8 to 9 quarter core pieces of 3 cm to 32 cm length from depths of 208.90 m to 212.70 m. These six samples consist of carbonaceous shale (n=5) and shale with iron formation (n=1) with a (sedimentary) lamination plane circa perpendicular to the drilling direction. Stratigraphically, they are between the Buck Reef Chert formation and Komatiite flows of Kromberg Formation (Hofmann et al., 2013). Their appearance is grey to black, with few light veinlets in the mm-scale. One sample shows additional features: in BARB3-211.44 a 1 cm wide light band and a 0.5 cm wide yellow-brownish band with white rim are visible as well as pyrite veins (sub mm).

S 2.6 Various outcrop samples, ~2.5 to 3.23 Ga

Several outcrop samples from South Africa were analyzed to complement drillcore data in this study. The black shale sample 99-02 originates from the 2.5 Ga upper part of the Black Reef formation that is accessible in an open pit gold mine in Randfontein (Siebert et al., 2005). The Black Reef formation underlies the Chuniespoort Group and belongs to the Transvaal Supergroup. Outcrop samples from the Barberton Greenstone Belt comprise three Banded Iron Formations (BIF) and one graywacke from the Moodies group with an approximate age of 3.15 Ga (Lowe and Byerly, 1999; Siebert et al., 2005). They originate from the following localities sample 01/018 from S25°42'52'', E31°05'05'', samples 01/032, 01/073, and 01/078 separated into a Fe and Si layer from S25°50'05'', E31°00'59'' (Siebert et al., 2005). From the Fig Tree group (3.22 Ga to 3.23 Ga, Lowe and Byerly, 1999) four black shales originate from the Fairview mine, one black mudstones was sampled at Louws Creek Road and one black siltstone comes from the Consort Mine PL-shaft ca. -1200 m. Additionally, two black shales were sampled at S25°44'12'', E031°16'34'' (99/038) and S25°44'31'', E031°16'18'' (99/039) (Siebert et al., 2005).

S 3. Data

The following tables show concentration data for samples measured in this study. DP-16 data was obtained at University of Tübingen (only Al_2O_3). All other data was obtained at University of Hannover, however, for PDP-1 only Al_2O_3 is presented.

Table S 5: Aluminiumoxide contents in bulk PDP-1 core samples.

Sample depth / m	Group	Formation	Lithology	Al_2O_3 / wt%
42.65	Fortescue	Tumbiana	strom. limestone	1.71
65.75	Fortescue	Tumbiana	strom. limestone	8.17
67.55	Fortescue	Tumbiana	strom. limestone	12.27
68.19	Fortescue	Tumbiana	strom. limestone	6.52
71.55	Fortescue	Tumbiana	strom. limestone	2.37
72.05 Si-rich	Fortescue	Tumbiana	strom. limestone	2.35
72.05 C-rich	Fortescue	Tumbiana	strom. limestone	2.57
78.65 Si-rich	Fortescue	Tumbiana	strom. limestone	7.49
78.65 C-rich	Fortescue	Tumbiana	strom. limestone	5.83
79.18	Fortescue	Tumbiana	strom. limestone	9.23

Table S 6: Aluminiumoxide data for DP-16 core samples.

Sample depth / m	Group	Formation	Lithology	Al_2O_3 / wt%
744.5	Pretoria	Timeball Hill	black shale	15.52
748	Pretoria	Duitschland	black shale	35.31
751.60	Pretoria	Duitschland	shale	9.67
753.40	Pretoria	Duitschland	shale	17.2
754.70	Pretoria	Duitschland	shale	17.31
756.20	Pretoria	Duitschland	shale	20.44
761.40	Pretoria	Duitschland	mudstone	19.60
764.7	Pretoria	Duitschland	quartzite	6.37
767.5	Pretoria	Duitschland	quartzite	11.20
769.5	Pretoria	Duitschland	shale	17.03
774.1	Pretoria	Duitschland	quartzite	10.9
781.1	Pretoria	Duitschland	shale	17.77
789.1	Pretoria	Duitschland	mudstone/shale	16.20
792	Pretoria	Duitschland	shale	20.15
800	Pretoria	Duitschland	silicified shale	7.11
803.5	Pretoria	Duitschland	black shale	25.9

Table S 7: Geochemical data for GKP-01 core black shale samples (Ghaap group).

Sample depth	Formation	Lithology	Al₂O₃	TiO₂	V	Cr	Mn	Co	Ni	Cu	Sr	Y	Zr	Mo	Ba	W	Re	Th
m			wt%	wt%	µg g⁻¹	µg g⁻¹	µg g⁻¹	µg g⁻¹	µg g⁻¹	µg g⁻¹	µg g⁻¹	µg g⁻¹	µg g⁻¹	µg g⁻¹	µg g⁻¹	µg g⁻¹	µg g⁻¹	µg g⁻¹
185.16	Kuruman	black shale	2.56	0.57	28.59	52	545	5	38	12	74.50	30.30	84.13	1.56	205.77	2.22	0.08	3.35
190.97	Kuruman	black shale	2.29	0.10	51.68	27	5063	5	30	10	31.69	8.65	26.38	1.48	428.44	0.60	0.08	2.32
264	Klein Naute	black shale	7.88	0.43	130.41	82	774	18	102	34	56.87	21.46	129.77	7.23	314.98	54.51	0.09	10.33
280	Klein Naute	black shale	10.80	0.73	76.46	151	3188	27	72	51	69.82	43.05	209.67	3.27	589.67	88.52	0.13	22.36
317.6	Klein Naute	black shale	36.71	1.05	51.37	13	89	9	22	40	54.31	59.54	645.01	0.74	115.68	1.96	0.10	46.00
322.02	Klein Naute	black shale	6.65	0.31	57.61	46	1171	131	400	552	25.12	12.15	87.53	3.87	110.86	170.13	0.12	4.39
344.54	Upper Nauga	black shale	1.26	0.04	18	15	12963	10	37	49	24.73	20.33	17.92	3.86	25.30	2.97	1.14	0.76
410.85	Upper Nauga	black shale	21.18	1.54	300	826	1756	29	96	186	18.84	9.86	109.10	3.02	340.27	39.39	0.12	5.87
444	Upper Nauga	black shale	0.94	0.04	15	12	7864	7	18	10520	31.13	7.60	12.49	2.52	12.21	17.65	1.16	0.42
485	Upper Nauga	black shale	27.19	1.90	365	249	5673	49	126	200	20.76	25.51	159.90	1.60	145.18	15.05	0.12	6.54
485.23	Upper Nauga	black shale	40.61	2.24	394	290	5738	42	141	243	27.70	35.00	184.85	1.57	330.53	16.55	0.12	11.97
489.01	Upper Nauga	black shale	34.34	2.21	453	322	21253	38	144	235	19.14	33.34	146.86	1.13	222.87	1.01	0.13	4.53
637	Upper Nauga	black shale	23.61	0.58	150	369	2389	24	132	43	40.66	17.27	78.83	1.14	179.41	1.33	0.15	6.53
696.3	Lower Nauga	black shale	30.14	0.71	8	7	114	6	38	20	22.51	126.40	1454.28	4.34	167.19	3.94	1.03	62.57
830.9	Lower Nauga	black shale	0.92	0.04	19	14	8146	6	29	9	20.42	6.21	12.43	2.96	3.90	24.08	1.18	0.39
871.83	Lower Nauga	black shale	21.06	0.72	162	345	202	31	163	62	12.61	16.73	138.67	2.03	209.30	2.42	0.14	7.54
890.7	Lower Nauga	black shale	16.61	1.35	259	184	237	264	223	201	18.15	16.98	152.61	5.84	160.51	41.16	1.01	5.85
892.4	Lower Nauga	black shale	15.76	1.69	331	166	1446	71	127	215	30.40	22.18	102.44	2.81	495.46	3.63	1.39	0.31
980.12	Monteville	black shale	18.57	0.81	173	319	97	22	116	60	15.64	12.20	145.35	3.70	194.36	32.13	1.18	5.13
1022.12	Monteville	black shale	22.72	0.48	126	294	4827	43	205	51	37.12	16.28	89.90	2.70	251.27	49.41	0.11	4.69
1049.1	Monteville	black shale	1.95	0.08	13	20	8965	45	36	12	23.57	6.56	29.07	1.04	19.96	49.95	0.12	1.63
1079.9	Lokammona	black shale	14.59	0.94	151	235	1282	26	88	74	34.96	15.56	132.44	1.14	254.77	1.14	0.15	4.19
1150.9	Boomplas	black shale	17.47	0.93	160	310	1104	21	124	104	70.26	19.25	154.42	1.79	321.10	0.82	0.16	5.41
1200.95	Vryburg	black shale	15.76	0.84	144	330	680	36	142	91	29.01	15.58	168.79	1.66	243.47	1.46	0.13	5.17
1262.1	Vryburg	black shale	14.52	0.88	139	362	418	39	176	79	40.15	19.58	182.25	4.51	311.54	41.68	1.23	5.67

Table S 8: Geochemical data for main core KMF-5.

Sample depth	Group	Formation	Lithology	Al₂O₃	TiO₂	V	Cr	Mn	Co	Ni	Cu	Sr	Y	Zr	Mo	Ba	W	Re	Th
m				wt%	wt%	µg g⁻¹	µg g⁻¹	µg g⁻¹	µg g⁻¹	µg g⁻¹	µg g⁻¹	µg g⁻¹	µg g⁻¹	µg g⁻¹	µg g⁻¹	µg g⁻¹	µg g⁻¹	µg g⁻¹	µg g⁻¹
346.1	Pretoria	Timeball Hill	shale+ siltstone	25.15	0.67	114.87	123.98	598.41	26.25	48.34	99.26	81.91	26.37	208.79	4.41	399.15	7.90	0.04	26.35
383.6	Pretoria	Timeball Hill	shale+ siltstone	24.82	0.64	168.82	130.23	320.17	57.61	57.39	83.83	76.88	57.17	112.17	159.64	377.22	6.10	1.24	20.31
453.1	Pretoria	Timeball Hill	shale+ siltstone	33.41	0.78	141.42	157.54	471.02	19.88	70.12	126.50	103.41	19.72	117.72	1.83	635.59	7.27	1.21	21.43

Sample depth	Group	Formation	Lithology	Al$_2$O$_3$	TiO$_2$	V	Cr	Mn	Co	Ni	Cu	Sr	Y	Zr	Mo	Ba	W	Re	Th
m				wt%	wt%	µg g^{-1}	µg g^{-1}	µg g^{-1}	µg g^{-1}	µg g^{-1}	µg g^{-1}	µg g^{-1}	µg g^{-1}	µg g^{-1}	µg g^{-1}	µg g^{-1}	µg g^{-1}	µg g^{-1}	µg g^{-1}
487	Pretoria	Timeball Hill	shale+ siltstone	23.50	0.68	104.56	113.93	138.26	21.82	71.32	26.13	86.15	17.02	139.17	5.60	541.86	6.84	1.12	17.35
521.4	Pretoria	Timeball Hill	shale+ siltstone	21.04	0.72	130.22	145.69	245.25	17.42	52.99	42.29	100.89	24.49	165.84	2.71	558.11	7.22	0.07	27.39
551.3	Pretoria	Timeball Hill	shale+ siltstone	26.02	0.71	145.72	153.30	244.61	29.68	57.60	39.19	94.13	22.02	142.10	4.43	595.09	7.29	0.06	24.28
570.9	Pretoria	Timeball Hill	shale+ siltstone	22.13	0.67	146.93	155.12	235.47	27.84	66.91	20.19	110.02	23.73	140.30	2.12	583.75	7.56	0.08	30.03
579.4	Pretoria	Timeball Hill	black shale	21.93	0.61	130.36	126.85	281.36	24.46	81.49	38.94	89.84	20.45	132.02	2.66	478.01	6.94	0.05	18.31
590.3	Pretoria	Timeball Hill	shale+ siltstone	18.63	0.66	124.44	138.36	87.62	88.29	106.67	69.52	94.17	36.76	165.13	1.86	761.83	8.25	1.89	25.49
592.8	Pretoria	Timeball Hill	black shale	7.78	0.29	97.77	66.17	1309.52	15.22	206.95	80.99	53.49	32.18	100.42	0.97	278.78	3.41	0.06	9.52
593.3	Pretoria	Timeball Hill	black shale	14.54	0.60	156.62	115.54	114.65	11.17	47.51	216.46	89.76	38.70	163.73	2.32	745.49	9.43	2.27	20.13
594.1	Pretoria	Timeball Hill	black shale	14.02	0.69	108.05	119.01	73.37	1.09	51.77	85.62	89.29	27.82	201.68	1.65	945.58	5.84		19.56
595.6	Pretoria	Duitschland	black shale	4.53	0.16	60.28	37.45	7361.09	1.53	30.67	49.08	20.65	17.60	52.04	1.13	176.78	1.26		2.68
599.3	Pretoria	Duitschland	black shale	23.13	0.99	119.94	152.94	85.47	4.63	24.92	14.50	85.93	24.77	203.23	0.73	473.20	4.75		23.11
601	Pretoria	Duitschland	black shale	24.80	1.66	240.95	163.53	102.65	54.23	104.51	23.69	76.80	26.41	284.05	1.54	372.92	12.99	0.81	20.42
601.6	Pretoria	Duitschland	black shale	29.15	1.51	170.79	186.30	38.09	6.50	42.25	59.63	93.85	26.34	243.66	3.39	451.89	15.58	0.95	24.18

Table S 9: Geochemical data for outcrop samples (Black Reef and Barberton Greenstone Belt) and Nercmar core sample.

Sample name	Group	Lithology	Al$_2$O$_3$	TiO$_2$	V	Cr	Mn	Co	Ni	Cu	Sr	Y	Zr	Mo	Ba	W	Re	Th
			wt%	wt%	µg g^{-1}	µg g^{-1}	µg g^{-1}	µg g^{-1}	µg g^{-1}	µg g^{-1}	µg g^{-1}	µg g^{-1}	µg g^{-1}	µg g^{-1}	µg g^{-1}	µg g^{-1}	µg g^{-1}	µg g^{-1}
99/02	Black Reef	black shale	48.38	1.47	267.72	1020	11	2	9	32	685.21	37.59	285.02	1.49	602.73	5.70	0.16	22.80
BES-7	Ngezi	black shale	14.89	0.50	109.83	412	834	28	254	196	42.80	12.48	77.13	2.26	327.78	1.88	0.18	6.51
01/018	Moodies	Graywacke siltstone	14.29	0.69	133.08	827	2240	46	378	48	77.71	15.85	111.77	2.20	358.89	4.56	1.54	5.98
01/032	Moodies	BIF	0.36	0.02	6.50	21	1774	6	18	15	3.24	1.88	2.82	0.70	65.73	1.42	0.16	0.41
01/073	Moodies	BIF	12.05	0.81	478.82	1747	70	113	1747	491	16.83	4.06	46.83	2.96	314.29	9.05	0.17	0.75
01/078 Fe	Moodies	BIF	1.92	0.09	19.38	92	8528	8	55	6	6.65	4.04	17.69	1.01	230.06	3.51	0.16	1.26
284.5 a	Fig Tree	black shale	16.97	0.64	166.83	1347	6970	36	579	55	23.46	23.58	80.20	1.09	215.61	14.04	0.15	6.42
435.75	Fig Tree	black shale	8.49	0.38	62.59	493	948	21	191	54	133.61	14.06	106.92	1.45	423.29	2.35	0.17	8.94
496.3	Fig Tree	black shale	9.87	0.36	110.97	607	2089	58	475	217	274.71	11.67	46.80	2.58	325.40	3.97	0.98	2.11
99/029	Fig Tree	gray to black mudstone	11.68	0.67	150.03	849	379	35	342	50	14.91	18.59	90.03	3.05	338.96	5.68	1.42	3.37
99/034	Fig Tree	black siltstone	13.99	0.69	132.28	900	1608	47	402	106	99.98	22.33	111.36	3.05	511.74	3.11	1.21	5.14
99/038	Fig Tree	black shale	13.72	0.67	173.86	907	449	52	478	150	14.71	18.78	84.11	0.71	170.68	1.47	0.16	4.76
99/039	Fig Tree	black shale	15.88	0.71	186.92	1009	127	19	410	114	13.14	23.34	99.50	2.71	341.11	5.35	1.86	5.56

Tables S 10 and S 11 show the results for measurements of reference materials TMDA-51.4 and SDO-1 and their comparison with certified values.

Table S 10: Results for TMDA-51.4 measurements and comparison with certified values.

isotope	resolution	TMDA-51.4 certified / ng g^{-1}	± 2-sigma certified / ng g^{-1}	# measured	average measured / ng g^{-1}	1 s.d. / ng g^{-1}	1 s.d. / %
^{47}Ti	low	14.2	0.99	3	14.54	0.29	1.98
^{49}Ti	low	14.2	0.99	3	15.67	0.14	0.87
^{55}Mn	low	84.3	6.6	10	84.82	3.06	3.61
^{59}Co	low	70.6	4.5	21	72.44	1.46	2.02
^{60}Ni	low	65.7	4.5	21	68.85	3.20	4.64
^{62}Ni	low	65.7	4.5	11	69.58	3.54	5.09
^{63}Cu	low	80.7	6.9	21	88.06	8.28	9.41
^{65}Cu	low	80.7	6.9	21	86.65	8.91	10.28
^{88}Sr	low	116	8.5	21	117.44	2.01	1.71
^{95}Mo	low	57.6	4.5	45	57.61	1.35	2.34
^{97}Mo	low	57.6	4.5	45	57.86	1.33	2.30
^{135}Ba	low	73.1	5.1	21	73.84	1.00	1.36
^{137}Ba	low	73.1	5.1	21	73.69	1.53	2.08
^{238}U	low	29.1	2.5	45	30.99	2.96	9.55
^{27}Al	medium	95.1	9.6	41	97.65	11.39	11.66
^{47}Ti	medium	14.2	0.99	39	14.07	1.75	12.42
^{49}Ti	medium	14.2	0.99	41	14.44	1.40	9.70
^{51}V	medium	48	3.7	45	48.95	1.99	4.07
^{52}Cr	medium	66.2	4.7	45	67.31	2.66	3.96
^{53}Cr	medium	66.2	4.7	45	67.37	2.76	4.10
^{55}Mn	medium	84.3	6.6	45	87.23	7.42	8.51
^{56}Fe	medium	118	15.2	39	135.97	21.15	15.56
^{57}Fe	medium	118	15.2	42	137.02	21.46	15.66
^{60}Ni	medium	65.7	4.5	13	68.90	3.12	4.53
^{62}Ni	medium	65.7	4.5	13	69.02	3.36	4.86
^{66}Zn	medium	140	13.6	24	126.95	19.89	15.67
^{68}Zn	medium	140	13.6	24	127.82	19.88	15.55

Table S 11: Results for SDO-1 measurements and comparison with certificate.

Isotope	resolution	TMDA-51.4 certified / µg g^{-1}	± 2-sigma certified / µg g^{-1}	average measured / µg g^{-1}	stabw / µg g^{-1}	stabw / %	# measured
^{27}Al	medium	64939.78	1217.29	57368	7630.82	13.30	34
^{47}Ti	medium	4255.32	185.80	3684	361.67	9.82	34
^{49}Ti	medium	4255.32	185.80	3707	329.61	8.89	34
^{51}V	medium	160.00	21.00	148.09	12.29	8.30	34
^{52}Cr	medium	66.40	7.60	56.08	5.13	9.16	34
^{53}Cr	medium	66.40	7.60	55.85	4.97	8.90	34
^{55}Mn	medium	325.27	38.72	276.91	22.79	8.23	34
^{55}Mn	low	325.27	38.72	283.24	1.89	0.67	9
^{59}Co	low	46.80	6.30	40.86	3.59	8.78	18
^{60}Ni	medium	99.50	9.90	89.92	1.76	1.96	9
^{62}Ni	medium	99.50	9.90	90.13	2.52	2.80	9
^{60}Ni	low	99.50	9.90	85.07	8.00	9.40	18
^{62}Ni	low	99.50	9.90	150.39	14.24	9.47	9
^{63}Cu	low	60.20	9.60	54.02	3.65	6.76	18
^{65}Cu	low	60.20	9.60	57.27	3.57	6.24	18
^{88}Sr	low	75.10	11.00	70.41	5.71	8.11	18
^{89}Y	low	40.60	6.50	31.88	2.53	7.95	18
^{90}Zr	low	165.00	24.00	106.63	7.82	7.33	34
^{91}Zr	low	165.00	24.00	105.49	7.59	7.20	34
^{95}Mo	low	134.00	21.00	141.86	12.01	8.47	34
^{97}Mo	low	134.00	21.00	141.74	11.70	8.25	34
^{135}Ba	low	397.00	38.00	358.01	27.74	7.75	18
^{137}Ba	low	397.00	38.00	362.70	28.43	7.84	18
^{182}W	low	3.30		4.06	0.98	24.14	15
^{183}W	low	3.30		3.93	0.75	19.13	15
^{232}Th	low	10.50	0.55	8.75	1.74	19.93	31
^{238}U	low	48.80	6.50	43.87	5.57	12.70	31

Chapter V: Synopsis

Outlook

This thesis shows that the application of metal isotope fractionation of Mo, U, and V is a powerful tool in geo-scientific research to gain information about geochemical cycling and removal pathways in modern and past marine samples (sediments and seawater). Especially the combination of different proxies results in fundamental understanding of the processes and helps to interpret environmental conditions in detail.

The V isotope composition of North Sea seawater was measured successfully and revealed only minor differences to recently published values for the open ocean. The process of developing a method for the separation of V from a complex matrix, such as seawater, showed that V isotope analyses are not trivial and need rigorous organization and handling to avoid any contamination and loss of V during the procedure. Here, additional work may be spent on further optimizing the method and increasing V recovery. Moreover, it must be ensured that measured isotope ratios are trustworthy, and this can only be achieved by replicate analyses of the same seawater. Finally, the V isotope composition of additional seawater samples, such as deep water compared to surface water, of restricted basins, such as the Black Sea or other temporarily anoxic basins, and river water as a major V source to the oceans must be investigated to understand the global V isotope cycling in more detail.

The application of Mo and U on the same samples from the anoxic basins Black Sea and Cariaco Basin revealed an inversely correlated inter-relationship irrespective of the different removal pathways of Mo and U. These findings will help in future paleo-redox studies and form a solid basis to understand stable metal isotope fractionation in detail. It is highly recommended to apply multi-proxy approaches whenever possible as shown in this study because they may complement each other and strengthen interpretations. Further detailed analyses, for example of the speciation of both metals and their bonding environments in anoxic sediments may further enhance the understanding of specific immobilization processes. As the Cariaco Basin and Black Sea both exhibit an individual inverse correlation trend of δ^{238}U vs. δ^{98}Mo, further research may help to understand how these local signatures translate into global signals and influence global mass balance calculations.

The use of U isotope ratios to decipher the onset of oxidative weathering of U minerals in Archean and Early Proterozoic times reveals this process to begin at roughly ~2.5 Ga, hence, pre-dating the Great Oxidation Event (GOE) by 100 – 200 Ma years. The observed U isotope compositions can be explained by U isotope fractionation because of partial U mobilization during oxidative weathering of uraninite and isotope fractionation in a stratified ocean. After the GOE, the observed unfractionated δ^{238}U values indicate the onset of modern-style

weathering of uraninite and other U-bearing minerals. An open question remains on the local vs. global extent of oxidative weathering of U. Other studies have shown that U is isotopically fractionated in sediments in older sections and at other localities. Hence, it remains to be investigated whether from ~2.5 Ga on, the oxidative weathering occurred on a global style indicating a global increase in atmospheric oxygen concentrations. Additionally, further experimental studies are needed to investigate the sensitivity of host minerals, not only of U, but also other redox-sensitive elements, such as Mo or Cr, to oxygen and to quantify the amounts of needed free atmospheric oxygen for oxidative weathering. The isotope fractionation of U during oxidation under very low atmospheric oxygen pressures may be also subject to further experimental studies. Nevertheless, U isotope fractionation is well suited to understand the past oxygen evolution and may be enhanced by combination with other studied isotope systems in the Archean and Early Proterozoic times.

Curriculum Vitae Annika Neddermeyer

■ Personal data

Date and place of birth: 09/25/1989 in Hannover

Email: a.neddermeyer@outlook.de

■ Work experience

Since 08/2015	**Research Associate**
	Leibniz University of Hannover, Institute of Mineralogy, Geochemistry
	Mass-spectrometric analyses, sample preparation in clean-lab, data evaluation, supervision of Bachelor or Master thesis's
11/2012 - 07/2015	**Student / research assistant**
	Leibniz University of Hannover, Institute of Mineralogy, Geochemistry

■ Education

Since 09/2015	**PhD student**
	Leibniz University of Hannover, Institute of Mineralogy, Geochemistry Title of dissertation: The development and application of Uranium, Molybdenum and Vanadium stable isotope ratios as redox-proxies in samples from modern times and the Early Earth
04/2013 – 07/2015	**Studies of geosciences**
	Leibniz University of Hannover
	Graduation to **Master of Science** in July 2015 with **Grade 1.3**
	Title of Master's thesis: Vanadium Isotopes, a potential new proxy for paleo-oceanography
09/2009 – 03/2013	**Studies of chemistry**
	Leibniz University of Hannover
	Graduation to **Bachelor of Science** in April 2013 with **Grade 1.8**
	Title of Bachelor's thesis: Quantifizierung ozeanischer Anoxia an der Perm-Trias Grenze anhand von Uran Isotopen in Schwarzschiefern
07/2009	**Higher Education certificate (A-levels)** with **grade 1.4**
	Integrierte Gesamtschule Garbsen

■ **Advanced Education**

Graduate Academy of the Leibniz University of Hannover

Oct. 2017 - June 2018 Program "PhD and beyond" (in German and English)

e.g. seminars: Basics and practice of project management, entrepreneurial strategies, (social) interactions in a team and communication, career perspectives

November 2017 Workshop "Time- and Self-management"

April 2016 Workshop "Say it right - how to make yourself better understood"

March 2016 Workshop "Management of scientific data"

Priority program 1833 of the German Research Foundation

April 2017 Workshop "Archean Surface Environments" (in English)
Friedrich-Schiller University Jena

March 2017 Workshop "Isotope-analytics" (in English)
Goethe University Frankfurt (Main), scholarship of SPP 1833

June 2016 Workshop "Geomicrobiology" (in English)
Eberhardt Karls University Tuebingen

April 2016 Workshop about themes of the SPP 1833 "Building a habitable Earth"
University of Cologne

■ **Knowledge and skills**

- o Professional competence in mass spectrometric analyses, work in clean-lab
- o Analytical, cross-linked thinking (Development of new scientific methods)
- o Effective processing, evaluation and presentation of big data
- o Presentation and discussion of data on international scientific conferences
- o Inter-disciplinary collaboration with other scientists in international projects
- o Publication of scientific data in professional journals
- o Audience-orientated lectures of expert knowledge (at scientific conferences and students at the University)
- o English language skills C1 – fluent in written and spoken word
- o Very good knowledge of Microsoft Office programs Excel, Word and Powerpoint
- o Driving license B, BE und A
- o Technically and artistically gifted (own production of jewelry)

Publications

Journals

2018

A. Wegwerth, S. Eckert, O. Dellwig, B. Schnetger, S. Severmann, S. Weyer, **A. Brüske**, L. Kaiser, J. Köster, H.-W. Arz, H.-J. Brumsack (2018): Redox evolution during Eemian and Holocene sapropel formation in the Black Sea, Paleogeography Paleoclimatology Paleoecology 489, p. 249-260.

2017

M. Weyrauch, M. Oeser, **A. Brüske**, S. Weyer (2017): In situ high-precision Ni isotope analysis of metals by femtosecond-LA-MC-ICP-MS, Journal of Analytical Atomic Spectrometry 32, p. 1312-1319.

S. Schuth, I. Horn, **A. Brüske**, P. E. Wolff, S. Weyer (2017): First vanadium isotope analyses of V-rich minerals by femtosecond laser ablation and solution-nebulization MC-ICP-MS, Ore Geology Reviews 81, p. 1271-1286.

Abstracts

2019

A. Martin, M. Lazarov, **A. Brüske**, S. Weyer (2019): Uranium isotope fractionation in Archean Carbonates: Insights from the Tumbiana Formation, Western Australia, General Meeting of SPP 1833 Building a habitable Earth, Cologne, oral presentation by A. Martin.

2018

A. Brüske, G. Albut, S. Schuth, R. Schoenberg, N. Beukes, A. Hofmann, T. Nägler and S. Weyer (2018): Uranium isotopes track oxidative weathering of U minerals in Archean sediments, General Meeting of SPP 1833 Building a habitable Earth, Goettingen, oral presentation.

A. Brüske, G. Albut, S. Schuth, R. Schoenberg, N. Beukes, A. Hofmann, T. Nägler and S. Weyer (2018): The onset of oxidative weathering traced by uranium isotopes, Goldschmidt conference, Boston, USA, oral presentation.

A. Brüske, G. Albut, S. Schuth, R. Schoenberg, N. Beukes, A. Hofmann, T. Nägler and S. Weyer (2018): Determining the onset of oxidative weathering with Uranium isotopes, Uranium-Bio-Geo conference, Ascona, Switzerland, oral presentation.

A. Brüske, S. Weyer, N. Pierau, O. Dellwig, N. Planavsky, T. Lyons (2018): Coupled U and Mo isotope signatures in modern anoxic sediments, Uranium-Bio-Geo conference, Ascona, Switzerland, oral presentation by S. Weyer.

2017

A. Brüske, N. Neubert, V. Schulte, D. Zok, O. Dellwig, N. Planavsky, T. Lyons, S. Weyer (2017): Deciphering the relationship between Molybdenum and Uranium isotope signatures in modern anoxic sediments from the Black Sea and the Cariaco Basin, GeoBremen conference, Bremen, oral presentation.

A. Brüske, S. Schuth, G. Albut, R. Schoenberg, N. Beukes, A. Hofmann, T. Nägler and S. Weyer (2017): Constraints on metal mobilization in Archean and early Proterozoic marine sediments from uranium isotopes, Goldschmidt conference, Paris, France, poster presentation.

S. Weyer, **A. Brüske**, N. Neubert, V. Schulte, D. Zok, O. Dellwig, N. Planavsky, T. Lyons (2017): Correlated Mo and U isotope signatures in sediments from the Black Sea and the Cariaco Basin, Goldschmidt conference, Paris, France, oral presentation by S. Weyer.

A. Brüske, S. Schuth, G. Albut, R. Schoenberg, S. Weyer (2017): Constraints on metal mobilization in early Proterozoic marine sediments from Uranium isotopes, General Meeting of SPP 1833 Building a habitable Earth, Jena, poster presentation.

2016

S. Weyer, **A. Brüske**, C. Montoya Pino, L. Xu, N. Neubert, S. Schuth, B. van de Schootbrugge, J. Pross, W. Oschmann & B. Lehmann (2016): Towards an Improved Understanding of the Mo and U Isotope Proxies Using Correlated Mo-U Isotope Signatures, Goldschmidt conference, Yokohama, Japan, oral presentation by S. Weyer.

A. Brüske, S. Schuth, S. Weyer (2016): Vanadium and Uranium isotope signatures in Archean sediments: Evidence for metal mobilization and enzymatic reduction in an overall anoxic world, General Meeting of SPP 1833 Building a habitable Earth, Cologne, poster presentation.

2015

A. Brüske, S. Schuth, L. Xu, M.C. Arnold, N. Pierau & S. Weyer (2015): Stable Vanadium isotopes as a potential new proxy for paleo-oceanography, DMG sectional meeting geochemistry and petrology, Potsdam, oral presentation.

A. Brüske, S. Schuth, L. Xu, M.C. Arnold, N. Pierau & S. Weyer (2015): Vanadium isotopes – a potential new proxy for paleo-oceanography, Goldschmidt conference, Prague, Czech Republic, oral presentation.

A. Brüske, S. Schuth, L. Xu, M.C. Arnold, N. Pierau & S. Weyer (2015): Stable vanadium isotopes – a potential new proxy for paleo-oceanography, GeoBerlin meeting, Berlin, oral presentation.